

PRISMA I

Final report



PRISMA I
Final report

Author(s)

Alex Kirichek
Katherine Cronin
Lynnyrd de Wit
Ebi Meshkati
Daan van Keulen
Jarno Terwindt

PRISMA I
Final report

Client	TKI
Contact	Edwin Hupkes
Reference	
Keywords	Fluid mud, WID, rheology, 1DV, PoR, port maintenance

Document control

Version	1.0
Date	12-08-2021
Project nr.	11203928-000
Document ID	11203928-000-ZKS-0004
Pages	198
Classification	public
Status	final

Author(s)

Alex Kirichek		
Katherine Cronin		
Lynyrd de Wit		
Ebi Meshkati		
Daan van Keulen		
Jarno Terwindt		

Doc. version	Author	Reviewer	Approver	Publish
1.0	Katherine Cronin <i>KC</i>	Thijs van Kessel <i>TJK</i>	Toon Segeren Dirk-Jan Walstra (i/a) <i>[Signature]</i>	

Summary

The navigation in ports and waterways must be safeguarded by maintenance dredging, i.e. removing of deposited sediments. The dredged sediment is typically reallocated offshore. As maintenance dredging and relocation of these deposits can be highly expensive, port authorities seek for tailor-made solutions to reduce the costs and at the same time guarantee safe navigation.

Water injection dredging (WID) is an example of a technique to reduce dredging costs on the short term. WID is a technique to fluidize sediment deposits with water jets. After fluidization, sediment may flow away as a density-driven current and its transport may be further enhanced by tidal currents, notably if WID is carried out during an appropriate tidal window. The efficiency of this dredging method has been recognized over the past 30 years, however, the successful application of WID can be only achieved by combining technical approaches with knowledge of the system where WID is to be applied. Obtained knowledge of the sediment distribution after WID can be a powerful tool that can help to define the timeframe for maintenance dredging requirements. Furthermore, having reliable in-situ measurements is important because the thickness of WID-induced fluid mud layers is often larger than the thickness of original mud layer resulting in a reduced draft for the incoming vessels. In this case, WID is often combined with the nautical bottom approach defined by PIANC for navigation. Therefore, the objective of this TKI research project is on developing new knowledge and tools, that can potentially facilitate WID in ports and waterways with severe siltation problems. This research is generic, but most examples and applications are for the Port of Rotterdam, partner in this TKI project.

The project is divided into 4 work packages (WP). The goal of WP1 is to generate new knowledge on fluid mud deposits via in-situ monitoring surveys at the Port of Rotterdam. Particularly spatial and temporal variations of mud properties (grain size, density, strength, organic matter content, etc) are investigated. WP2 is focused on validation of recently developed in-situ tools (Graviprobe and Rheotune), that can be used for measuring thickness, density and strength of fluid mud layers for applying the nautical bottom concept. WP3 is aiming to further develop and test a high-resolution fine sediment/mud transport model of the Maasmond and port basins. The model can help to predict far-field WID plume movement after WID. Finally, within WP4 the near field behaviour of WID plumes is investigated. Two different model tools have been tested for WID: a rapid assessment Lagrangian 1DV model and a 3D multiphase CFD model. The models can be applied for predicting the behaviour of sediment plumes in the WID area.

In-situ monitoring surveys have identified natural fluid mud deposits in the port areas. The strength and density of these deposits have been measured for applying the nautical bottom concept in these areas. The developed models have been applied for predicting WID plume movement in the Calandkanaal within Port of Rotterdam. The model outcomes are consistent with available field observations suggesting that the developed models can be applied for predicting plume movement after conducting WID in other areas of the port.

Contents

	Summary	4
1	Introduction	9
1.1	Background	9
1.2	Dredge more efficiently (SHORT-TERM)	10
1.3	Reduce return flow (SHORT-TERM)	13
1.4	Modify intervention protocol (LONG-TERM)	13
1.5	Objectives	15
1.6	Outline	15
2	WP1: System knowledge	16
2.1	Introduction	16
2.2	Spatial and temporal variation of fluid mud deposits	17
2.3	Yield stress and density variation	19
2.4	Laboratory characterization	20
2.4.1	Particle size analysis	20
2.4.2	Floc morphology	21
2.4.3	Organic matter	24
3	WP2: Monitoring tools	25
3.1	Introduction	25
3.2	Test Setup and Procedure	25
3.2.1	Test Setup	25
3.2.2	Deployment of the GraviProbe	26
3.2.3	Deployment of the RheoTune	27
3.3	Sample Preparation	27
3.3.1	Field Sampling from the Port	27
3.3.2	Mixing	28
3.4	Test Program	29
3.4.1	Test Program	29
3.4.2	Probe Deployment Positions	31
3.5	Probe Depth Registration	32
3.5.1	GraviProbe	32
3.5.2	RheoTune	33
3.5.3	Beaker Sampler	34
3.6	Test Results	35
3.6.1	Beaker Sampler	35
3.6.2	GraviProbe	38
3.6.3	Results versus Depth	38
3.6.4	Summarized Results	40
3.6.5	Parameter Plots	41

3.6.6	RheoTune	42
3.6.7	Results versus Depth	42
3.6.8	Summarized Results	45
3.6.9	Parameter Plots	48
3.7	Comments on Test Results	48
4	WP3: Far-field modelling tools	50
4.1	Introduction	50
4.1.1	Objective of the modelling work in PRISMA	51
4.1.2	Background of the existing models	52
4.1.3	Development of TKI HBR model	53
4.2	Model set-up	55
4.2.1.1	Delft3D model	55
4.2.2	Water Injection Dredging Investigations	56
4.2.2.1	Set-up	56
4.2.2.2	Implementation of WID in the Delft3D model	56
4.2.2.3	Implementation of sediment trap	59
4.2.3	Scenarios	59
4.2.3.1	Type 1: Simulating single HW or LW release	59
4.2.3.2	Type 2: Week of water injection dredging	60
4.3	Insights gained from model results	62
4.3.1	Hydrodynamics near the WID area.	62
4.3.2	WID plume dispersion	64
4.3.2.1	Influence of HW or LW release on the sediment plume	64
4.3.2.2	Influence of HW or LW release on the sediment footprint	66
4.3.2.3	Influence of a week of water injection modelling on sediment plume dispersion	68
4.3.2.4	Influence of a week of water injection modelling on the sediment footprint	71
4.3.3	Mixing over the vertical	73
4.3.3.1	Influence of HW or LW release on vertical mixing of the plume	73
4.3.3.2	Influence of a week of water injection modelling on vertical mixing of the plume	76
4.3.4	Fate of the WID sediment and return flows	77
4.3.5	Recommendations from WP3	79
5	WP 4: near field modelling tools	81
5.1	Introduction	81
5.1.1	WID characteristics	81
5.1.2	Working definition of 'near field' within PRISMA	82
5.2	1DV modelling of WID	83
5.2.1	Brief description 1DV model	83
5.2.2	Application of 1DV model for a turbidity current on an erodible bed (experiment of Parker et al. 1987)	84
5.2.3	Input parameter study	86
5.2.4	Results 1DV parameter study	87
5.2.5	Conclusions 1DV	89
5.3	3D CFD modelling of WID	90
5.3.1	Brief description 3D CFD model TUDflow3d	90
5.3.2	Application of TUDflow3d for a turbidity current on an erodible bed (experiment of Parker et al. 1987)	90
5.3.3	3D CFD of WID in real Port of Rotterdam bathymetry	92
5.3.4	Conclusions 3D CFD modelling of WID	95

5.4	Comparison CFD and 1Dv model	95
5.4.1	Introduction	95
5.4.2	Results of the comparison	95
5.4.3	Conclusion	98
5.5	Linking PRISMA WP3 and WP4	99
5.6	Conclusions of WP4	99
6	Conclusions	101
	References	103
A	In-situ and lab measurements	107
B	Graviprobe and Rheotune	165
B.1	Working Principle of Measurement and Monitoring Tools	165
B.1.1	GraviProbe 2.0	165
	Conclusions and recommendations	166
B.1.2	RheoTune	166
	Rheology	166
	Calibration:	168
	Yield stress:	169
	Evaluation:	169
	Conclusions and recommendations:	170
B.1.3	Beeker Sampler	170
	Rheological Measurements	171
	Density Measurements	171
C	Far-field modelling	172
C.1	Analysis of the turbulent-laminar transition	172
C.2	LW and HW mid column plume spreading	174
C.3	Near bed plume spreading - One week of WID	176
C.4	Influence of HW or LW release on the sediment footprint of individual fractions	180
C.5	Influence of the production rate on the sediment footprint	182
C.6	Influence of the production rate on the sediment footprint of individual fractions	184
D	Description and validation TUDflow3d	188
D.1	Introduction	188
D.2	TUDflow3d	188
D.2.1	Flow Equations	188
D.2.2	Turbulence	189
D.2.2.1.	LES	189
D.2.2.2.	RANS	189
D.2.3	Sediment	189
D.2.4	Bed update	190
D.3	Verification TUDflow3d for WID plumes	190
D.3.1	Introduction verification	190
D.3.2	Front speed of density current at sloping bed (experiment of Britter and Linden 1980)	190

D.3.3	Radial spreading of density driven overflow plume at bed (experiment of Boot 2000)	191
D.3.4	Density current including deposition (experiment of Hallworth et al. 1998)	192
D.3.5	Turbidity current on erodible bed (experiment of Parker et al. 1987)	193
D.3.6	Conclusions verification TUDflow3d for WID plumes	197

1 Introduction

1.1 Background

The navigation in ports and waterways has to be safeguarded by maintenance dredging, removing sediments deposited by tide, river flows and currents. The volumes of dredged material have been substantially increased over the last 5 years (see Figure 1-1). As maintenance dredging and relocation of these deposits can be highly expensive, port authorities seek for tailor-made solutions to reduce the costs and at the same time guarantee safe navigation in ports and waterways.

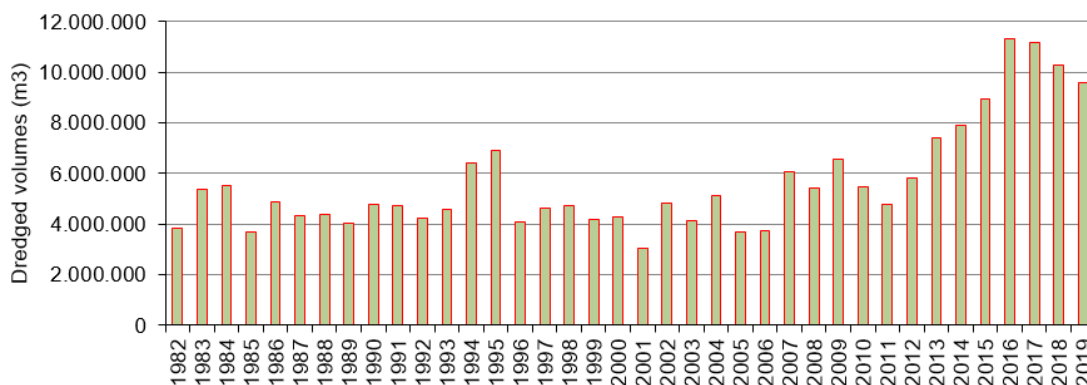


Figure 1-1. Dredged sediment volumes at the Port of Rotterdam from 1987 till 2019, excluding dredging by RWS in the access channels.

In order to keep ports and waterways accessible, more than 11 million m³ of sediment were dredged in 2017 (twice more than the volumes dredged in 2011). In 2017, about 77% of deposited sediment was mainly dredged by a hopper dredger at Maasvlakte, Europoort and Botlek areas (see Figure 1-2). The dredged sediment in these areas consists mainly of fine cohesive minerals forming silt layers.

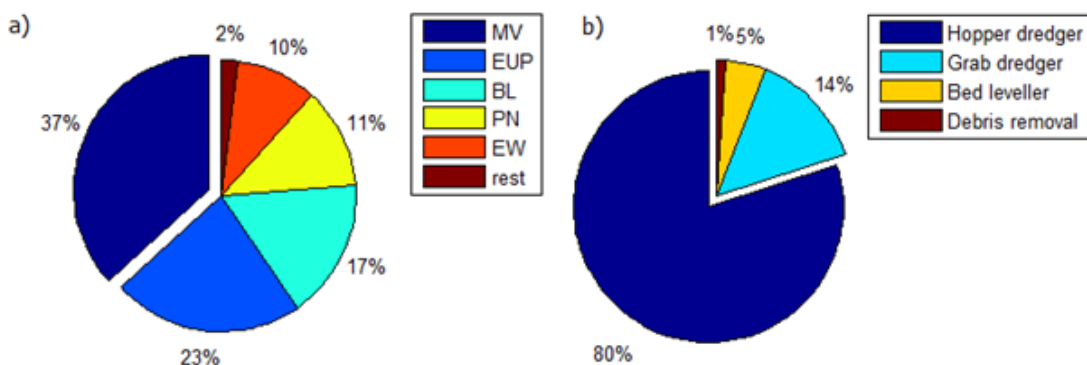


Figure 1-2. a) Dredged volumes at the port areas (MV: Maasvlakte, EUP: Europoort, BL: Botlek, PN: Pernis, EW: Eem-Waalhaven) in 2017. b) Dredging methods by means of costs in 2017. From Kirichek et al., 2018a.

There are several options to reduce dredging costs:

1. SHORT-TERM: dredge more efficiently & reduce sediment return flow
2. LONG-TERM: modify intervention protocol

Water Injection Dredging (WID) is an example of the 1st option. WID entails the fluidization of sediment deposits by water jets; the fluidized sediment may subsequently flow away under influence of gravity and tidal currents. To avoid additional siltation in the vicinity and/or strong return flows, this option should be applied in combination with a favourable bed slope, ebb currents and/or a sediment trap from which sediment can be dredged more efficiently. The main beneficial application of a WID is foreseen for locations, which are not easily accessible by hopper dredgers. At short term the benefits may be large, but care should be taken that this is not counteracted by long term costs in the form of increasing dredging volumes.

Smart sediment release is another example of the 1st option. The ongoing SURICATES project (Masson et al, 2018) is aiming to optimize locations and conditions in which sediment is released. Thus, the return flow to harbour basins may be minimized. At short term the costs may be large, but long-term benefits may be substantial in the form of reduced dredging volumes.

Revising the criterium for nautical bottom is an example of the 2nd option. Instead of removing sediment, its presence is accepted as ships may sail through mud. Local sediment conditioning may be required to avoid that mud layers become too strong to allow sailing through it.

All options have their pros and cons and may be feasible at different time scales. In all cases, insight into the local redistribution of sediment within the harbour area, the import from the river and the import from and export to sea is essential to properly assess the effects of these options on the sediment balance, dredging volumes and for cost-benefit analysis.

Such insight is acquired from a combination of monitoring with modelling and from validation of the models in combination with in-situ pilots. This is aimed at fluid mud behaviour and transport, but also at suspended transport, as both mechanisms are important, depending on hydrodynamic conditions. In the previous joint Deltares – PoR TKI project about modelling local mud dynamics the relative importance of both mechanisms has already been investigated (Cronin et al., 2019).

1.2 Dredge more efficiently (SHORT-TERM)

Water Injection Dredging (WID) methods can be efficiently applied for fluidizing and transporting the sediment over long distances within the port area. By applying the WID methods, it is proposed to keep port locations, which are not easily accessible by hopper dredgers, at required nautical depth.

The principle of the water injection process is based on fluidization the sediment bed using a water jet (see Figure 1-3). Water injection is performed by injecting large volumes of water under relatively low-pressure water jet nozzles. The injected water loosens the whole structure of the bed and the water-sediment mixture forms a fluid mud layer right above the bed. Field studies show that this dense fluid mud layer hardly mixes upwards and therefore transport of the mud layer remains close to the bed (Kirichek et al., 2021).

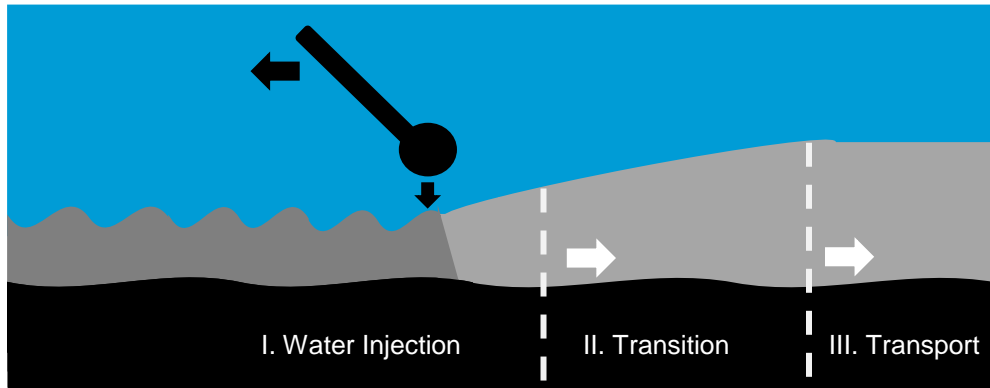


Figure 1-3 Phases of WID: I. Water injection and fluidization; II. Transition zone, where a density flow is created; III. Transport of the density flow. Adapted from Verhagen HJ. Water injection dredging. In: Proceedings of the 2nd International Conference Port Development and Coastal Environment (PDCE 2000); 5-7 June 2000, Varna, Bulgaria, 2000.

In a navigational channel with a fine-grained cohesive sediment bed this may result in a sequence as shown in Figure 1-4. The near bed fluidized sediment deposit generates a gravity driven density flow up to 2 metres high (PIANC, 2013; Kirichek and Rutgers, 2020) (b), transporting the sediment in a horizontal direction as a result of the density difference. This density flow is a homogeneous suspension layer with a sediment concentration of up to 200 g/l (c). Due to the density difference between the fluid mud layer and the surrounding water, the fluid mud is transported under the effects of gravity and momentum. Different transport distances from a few hundred meters to a few kilometres are reported for fluidized sediment. Based on the hydrodynamic conditions in a port basin, WID-conditioned sediment can either settle over time in a low-energy area or be transported by means of gravity currents to deeper areas such as sediment traps (Kirichek et al., 2020). This method can greatly reduce the cost for dredging at locations (e.g. at berths), which are not easily accessible by hopper dredgers.

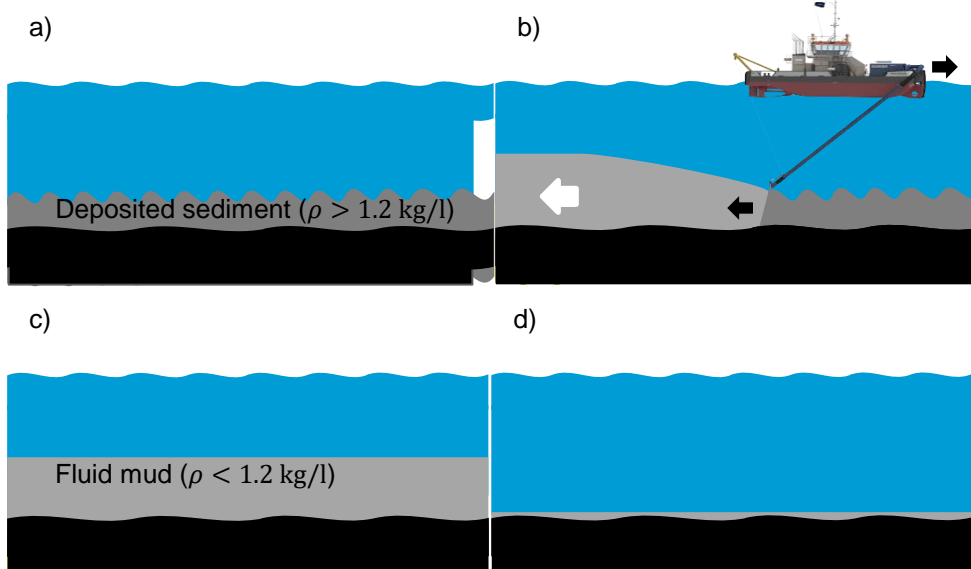


Figure 1-4 Illustration of WID performed in a navigational channel during the ebb tide. a) Initial conditions for WID. b) Fluidization of deposited sediment during WID. c) WID-induced fluid mud layer. d) Final result after WID in case WID is conducted for sediment reallocation purposes.

In recent years, different tools have been developed for optimizing WID processes and better prediction of sediment plume movement during WID. Numerical modelling tools can be used for estimating sediment dynamics in ports and waterways after WID.

Near-field modelling is often used for calculating the sediment footprint on the areas up to about 1 km away from WID. The obtained knowledge on sedimentation can help to better design WID operations including real bathymetry of a navigational channel. Existing and hypothetical infrastructure can be included in mid-field modelling allowing for testing of WID in combination with sediment transport steering management solutions such as sediment traps, sills and current-deflection walls (Kirichek et al, 2021).

Far-field modelling evaluates the impact of WID on the scale of the entire port or estuary area and simulates the plume when it is at a lower density and hence transported due to advection and dispersion processes. This kind of modelling is used for estimating WID reallocation strategies of sediment from the port basins to the sea and for assessing return flows. Simulations can demonstrate the transport of the WID plume during different phases of the tide and the impact of river and sea conditions. Based on the obtained information, the authorities can decide if conducting WID for reallocation purposes is effective in the port.

WID is most efficient if the following conditions are met:

- a. Most WID sediments deposit in a sediment trap, which is a deepening in a local bathymetry used for mitigation of siltation rates.
- b. The remainder is transported away as much as possible (although still substantially higher return flows are expected compared to sediment release at the present relocation area Loswal)
- c. As little sediment as possible deposits in other maintenance areas (as it has then to be re-dredged again)
- d. Additional siltation of background sediment in the sediment trap is desirable if the additional volume is compensated with a reduction of the same volume elsewhere in the harbour (where dredging is more costly than in the trap)
- e. Additional siltation is undesirable if it is not compensated elsewhere and the total trapping is increased.

In order to gradually change to and optimize the new maintenance method, that is based on WID and sediment trapping, the following knowledge has to be developed:

Related to WID:

- 1a) What are the most efficient locations for WID applications? Technically speaking, what is the shear strength (the yield stress) profile at PoR (especially at Maasvlakte, Europoort and Botlek)? What type of sediment is present in those areas? We need system knowledge to answer these questions.
- 2a) Where does the fluidized (by WID) sediment go to? Where does it settle? Does it consolidate or stays in a fluid phase? We need a combination of sediment models and in-situ measurements for reliable predictions.
- 3a) What are the most favourable current conditions (ebb or flood) for WID? We need current/flow models for predictions of the right time for WID.
- 4a) What is the environmental impact of WID? We need to know the impact of WID on existing flora and fauna for keeping a 'green port' status.

5a) How to optimize WID? We need WID models for improving/advancing the WID actions (optimal slopes, flows, angle, etc.).

Related to sediment traps:

1b) What are the most optimal locations for sediment traps at PoR?

2b) What are the most efficient dimensions of sediment traps (depth, size, shape, etc.)?

3b) Does the sediment settle and consolidate or remain fluid in the sediment trap and is this behaviour location-specific?

What are additional measures that can increase/decrease sediments settling velocities at sediment traps?

1.3 Reduce return flow (SHORT-TERM)

Reducing the return flow of dredged material can be done by:

- optimizing the release locations (linked to ongoing SURICATES project),
- optimizing the tidal window for release,
- alternative re-use of sediment, e.g. for wetland reconstruction or clay for dikes (i.e. extraction from the sedimentary system).

An alternative area for sediment relocation at the Maasmond and natural transport by the ebb flow to the open sea are currently investigated by ongoing SURICATES project (Masson et al, 2018).

Reducing the return flow of dredged material has already been investigated with regard to the first point in a previous TKI-project (Hendrix and Schuurman, 2017). Herein the return flow from the Loswal has been quantified and alternative locations have been proposed and assessed.

There is less focus on this aspect in the present proposal. However, this aspect can't be ignored completely as a local assessment of sediment (return) flows is essential to evaluate the effectiveness of WID, local sediment traps and to evaluate occurrence of fluid layers for nautical depth. The local sediment dynamic model in combination with observations on suspended sediment and fluid mud forms the basis for such assessment.

1.4 Modify intervention protocol (LONG-TERM)

A conventional way to estimate the navigability in ports and waterways with fluid mud layers is done through the estimation of the nautical depth. This criterion ensures that vessels can safely navigate through areas where thick layers of fluid mud are detected. For practical reasons, the nautical depth is defined as a critical density (1.2 t/m^3 at PoR). The current nautical depth concept applied at PoR is shown in Figure 1-5.

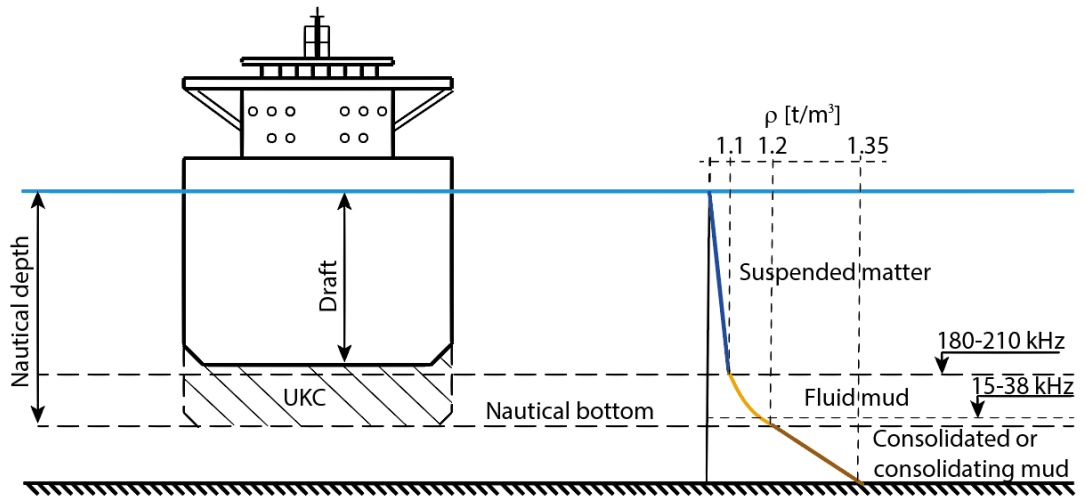


Figure 1-5 . The nautical bottom concept at the Port of Rotterdam for the density limit of 1.2 t/m³.

The difference between consolidated and fluid mud is shown in Figure 1-6. From Kirichek et. al., 2018b.



Figure 1-6. Left: stiff consolidated mud. Right: weak fluid mud.

It has long been recognized that a practical definition of nautical bottom should be based on considerations not only of density, but should also include the so-called rheological properties of the water-sediment mixture (Wurpts and Torn, 2005). Rheological properties (i.e. yield stress) provide a reliable criterion for nautical depth definition since they are related to the stress history and shear of the mud (Kirichek, 2016). Currently, the yield stress serves as a critical parameter for nautical depth in the Port of Emden (PIANC, 2014).

Until a few years ago, rheological properties could only be determined in the laboratory or by in-situ point measurements. Recently developed penetrometers (see Figure 1-7) can measure rheological signatures in-situ using empirical correlations between the mechanical properties of the penetrated medium (Kirichek et al., 2018, 2020). Even though such tools are capable of showing an acceptable depth profile of the waterways and harbours by means of rheological characteristics, the nature of measurements and empirical relations behind the outputs have to be verified. Laboratory measurements cannot serve as a direct indication of in-situ rheological properties of mud due to mud penetration during the sampling. Hence, laboratory measurements show significant deviations from the in-situ survey recordings (McAnally, et al., 2007).



Figure 1-7 Left: the Graviprobe. Right: the Rheotune

Even though the existing measuring methods can provide useful information about the rheological properties of the fluid mud, the utilization of these methods is cumbersome and impractical. One reason is that the relations between the rheological properties and the tools' measuring output are based on empirical relations. As a result, the tools must be calibrated for the specific location and conditions of the survey. Another reason is that the available measuring techniques provide only point measurements; hence, the penetrometer measurements have low repeatability (Diaferia, et al., 2013; Kirichek et al., 2018). This drawback makes it difficult to monitor the temporal changes of the mud properties in the mud layer caused by a storm or dredging activities, for instance. Finally, common measuring devices penetrate the mud, and, thus, alter the properties of the medium during the survey. This means that the rheological result obtained from these devices will be different before, during, and after the survey even when measuring at the same location.

All these arguments suggest that new continuous and non-invasive monitoring methods have to be developed, which would allow conducting continuous reliable surveys (Kirichek, 2016).

For revising the current criterion of nautical depth, the following key questions have to be answered through knowledge development:

- 1c) How does fluid mud influence the ship navigation and manoeuvrability?
- 2c) How rheological properties of mud can be continuously monitored in non-destructive way?
- 3c) What are the boundary conditions (limits) for safe ship navigation through fluid mud?

1.5 Objectives

The project aimed to deliver the tools, which are necessary to successfully employ, quantitatively assess and generically improve WID actions and sediment trapping and can be further used for optimizing in-situ pilots at PoR. In addition to the research questions listed above, the following methods, knowledge and experience have been gained:

- Generated system knowledge: spatial and temporal variability of mud (WP1)
- Reliability of measuring devices: Graviprobe and Rheotune (WP2)
- Improved flow model and calibrated by in-situ measurements sediment model (WP3)
- WID actions model (WP4)

1.6 Outline

This report summarizes the research conducted for developing the tools that can be used for quantitatively assessment and generic improvement of WID actions and sediment trapping. The results of monitoring campaigns are introduced in Chapter 2, followed by the testing of monitoring tools (Graviprobe and Rheotune) in Chapter 3. Developed sediment modelling tools are described in Chapter 4. The models that were developed for WID actions are presented in Chapter 5. Finally, the conclusions and recommendations are presented in Chapter 6.

2 WP1: System knowledge

2.1 Introduction

The goal of this Work Package is to generate new knowledge on fluid mud deposits at the Port of Rotterdam by conducting 4 monitoring campaigns. In particular, in-situ measurements are conducted in order to analyse spatial and temporal distribution of fluid mud deposits. The core samples are collected for further analysis in the laboratory. Rheological properties (yield stresses), density, particle size distribution (PSD), properties of flocs (size, density and settling velocity), Total Organic Carbon and zeta potential are measured for better understanding of fluid mud variability in different port locations.

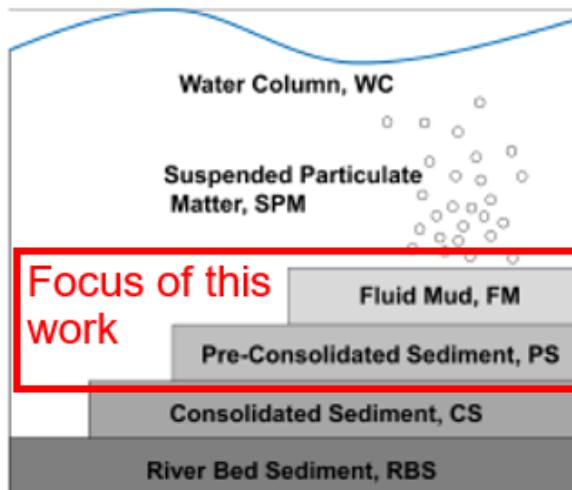


Figure 2.1. Stratified transition from suspended sediment to river bed sediment. The focus of this research is fluid mud and a transient state of fluid mud, that is referred as pre-consolidated sediment.

The research is focused on fluid mud deposits and on a transient state of fluid mud, that is referred to as pre-consolidated sediment in this study (see Figure 2.1.). Mud is a cohesive material consisting of a mixture of clay minerals, water, organic matter, and some amounts of sand. The particles forming the fluid mud layer, to be found at the bottom of some port channels, may be kept in suspension by tidal motion in combination with wave motion generated by wind, ship motion (Ross and Mehta 1989; Mehta 2013), human activities like dredging and fishing (Gordon 1974), or bioturbation (Harrison and Wass 1965; Ross and Mehta 1989). Fluid mud is usually defined as a fluid having a density within the range of 1030–1300 kg/m³, in which settling is considerably hindered by the presence of flocs (Inglis and Allen, 1957; Whitehouse et al, 2000; McAnally et al, 2007, Shakeel et al., 2019). The transient state of mud from fluid mud to consolidated stiff bed is referred as pre-consolidated sediment.

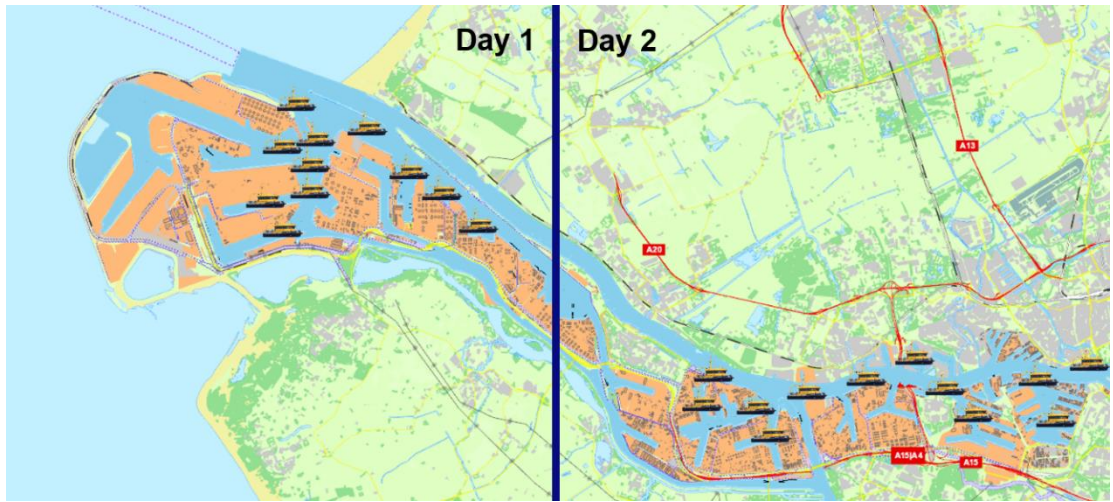


Figure 2.2. Locations of monitoring surveys conducted in 2019/2020

In total, 4 monitoring campaigns have been conducted in the Port of Rotterdam in 2019/2020 on the following days:

- I campaign: the 27th and the 28th of June 2019
- II campaign: the 13th and the 14th of November 2019
- III campaign: the 27th and the 28th of January 2020
- IV campaign: the 18th and the 25th of March 2020

Each monitoring campaign consists of 2 monitoring days. During the first day, the surveys are carried out in downstream of the port basin (see Figure 2.2). The Calandkanaal, the Nijlhaven, the Beerkanaal, the 8th Petroleumhaven and the Amazonehaven are surveyed during the monitoring campaigns. During the second day, the upstream of the port basin is monitored. The 3rd Petroleumhaven, Botlek, Scheurkade, Koolenkade, the Waalhaven, the Eemshaven, the Schiehaven are surveyed in order to detect fluid mud deposits.

2.2 Spatial and temporal variation of fluid mud deposits

The port basins area is divided into 2 parts: upstream and downstream (Figure 2.2). The downstream and upstream areas are surveyed during Day 1 and Day 2 of every monitoring campaigns.

Fluid mud deposits at the Port of Rotterdam are detected in the following way. First, the areas of potential fluid mud deposits are defined based on the bathymetry charts and dredging maps. Second, the SILAS system (Diaferia et al, 2013) is used for detecting the fluid mud deposits at the location shown in Figure 2.2. Figure 2.3. shows the online SILAS measurements of fluid mud deposits. Fluid mud can be distinguished from consolidated bed by the contrast in SILAS measurements resulting from a density gradient between fluid mud and consolidated bad (shown in the right panel of Figure 2.3). Another indication of the presence of fluid mud layers is the observation of a flat lutocline that is common for fluid mud layers.

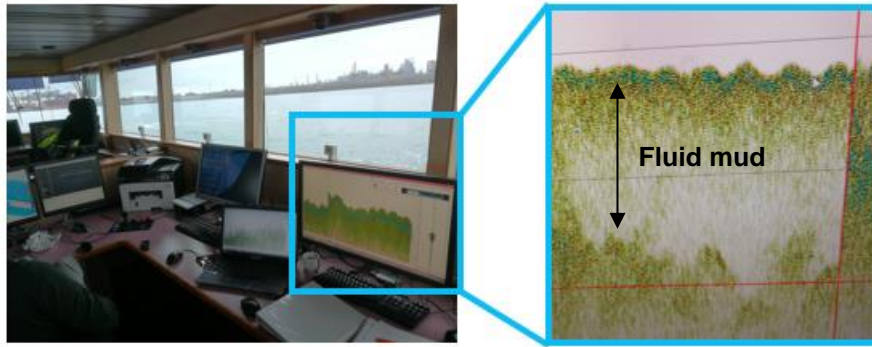


Figure 2.3. Detecting fluid mud with SILAS system during monitoring campaigns in 2019/2020

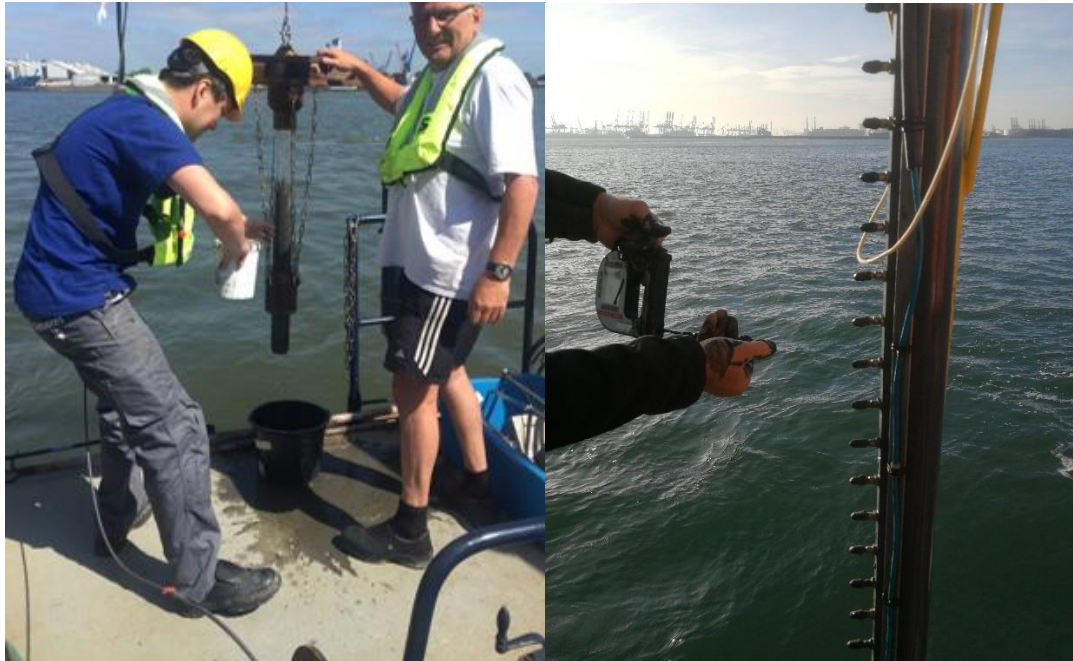


Figure 2.4. Collecting the core samples during the monitoring campaign in 2019/2020

When fluid mud is detected, we collect a core sample at the potential fluid mud location, either with so-called “falling bomb” (the left panel of Figure 2.4.) or with silt sampler (the right panel of Figure 2.4.) depending on the thickness of fluid mud layer. Based on the visual observation from core samples and density measurements (conducted by Anton Paar density meter or Rheotune), it is concluded if a collected core sample contains fluid mud or not. The detected fluid mud samples are brought to the laboratory for further analysis.

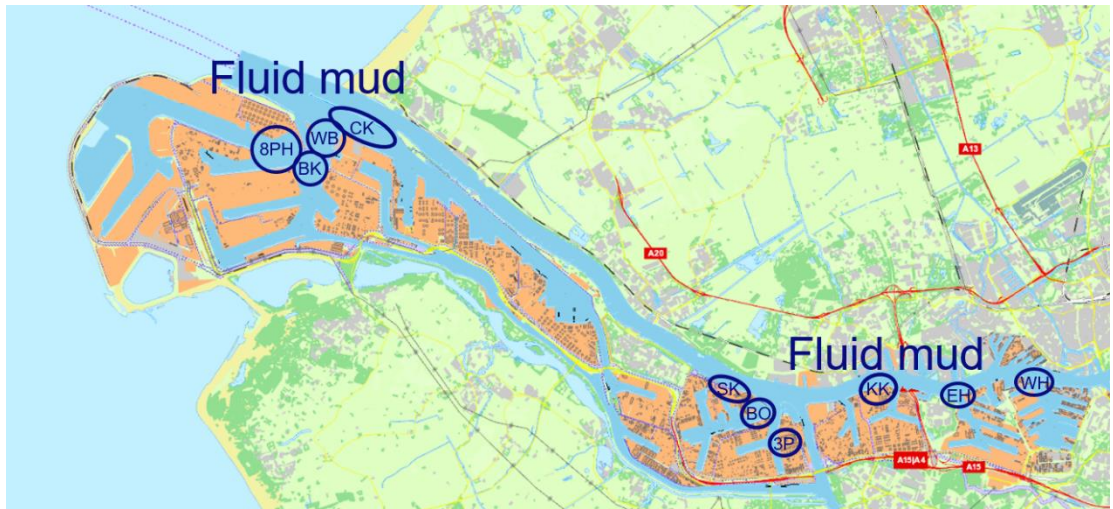


Figure 2.5. Detected fluid mud deposits during the monitoring campaign in 2019/2020. Fluid mud is observed mainly in a close proximity to the coastal area (CK: the Calandkanaal, BK: the Beerkanaal, WB: the Westbocht, 8PH: the 8th Petroleumhaven), near the quay walls (SK: the Scheurkade, KK: the KTM kade and 3P: the 3rd Petroleumhaven) and in the sediment traps (BO: Botlek, EH: the Eemhaven, WH: the Waalhaven)

The results of all four monitoring campaigns show that fluid mud layers are detected mainly in proximity to the coastal area, near the quay walls and in the sediment traps (see Figure 2.5). Particularly, fluid mud layers are observed in the Calandkanaal, the Beerkanaal, Westbocht, and the 8th Petroleumhaven during all 4 monitoring campaigns. The result of the monitoring campaign in March 2020 are exceptional because of detecting thick (up to 2.5 m) fluid mud layers in the Calandkanaal, in the Beerkanaal, in Westbocht and in the 8th Petroleumhaven. The large thickness of the fluid mud layers observed during this campaign are likely related to storms, as the campaign was carried out just after a storm period. As for regular conditions during the monitoring campaigns in June 2019, November 2019 and January 2020, the thickness of observed fluid mud layers is ranging from 0.3 m to 1.5 m in the Calandkanaal, from 0.3 m to 2.4 m in the Beerkanaal, from 0.3 m to 1.2 m in the Westbocht and from 0.3 m to 2.8 m in the 8th Petroleumhaven.

Furthermore, the fluid mud deposits are found near the Scheurkade, the KTM kade and the Koolenkade, where the fluid mud layer thicknesses are ranging from 0.3 m to 0.9 m in the Scheurkade, from 0.4 m to 1.2 m in the KTM kade and from 0.3 m to 0.7 m in the 3rd Petroleumhaven.

The thickness of fluid mud layers in the sediment traps is ranging from 0.30 m to 1.2 m in Botlek, from 0.5 m to 1.5 m in the Waalhaven and from 0.30 m to 1 m in the Eemhaven.

2.3 Yield stress and density variation

Following the protocol of Shakeel et al, 2019, the yield stress – density relationship is confirmed to be non-linear. Laboratory analysis of collected fluid mud samples shows that the samples from the Calandkanaal, the Beerkanaal, the Westbocht, the 8th Petroleumhaven, the KTM kade, the 3rd Petroleumhaven, the Eemhaven and the Waalhaven exhibit similar yield behaviour with density variation. However, the samples from the Scheurkade is dissimilar with the other samples: low yield stress values (<100 Pa) are corresponding to high densities (>1.25 Pa) of the Scheurkade samples (see Figure 2.6). The same yield stress – density behaviour is also observed in the field (see Appendix A). The difference of the yield stress – density variation in the Scheurkade can be due to higher fine sand content in this area of the port (Figure 2.7).

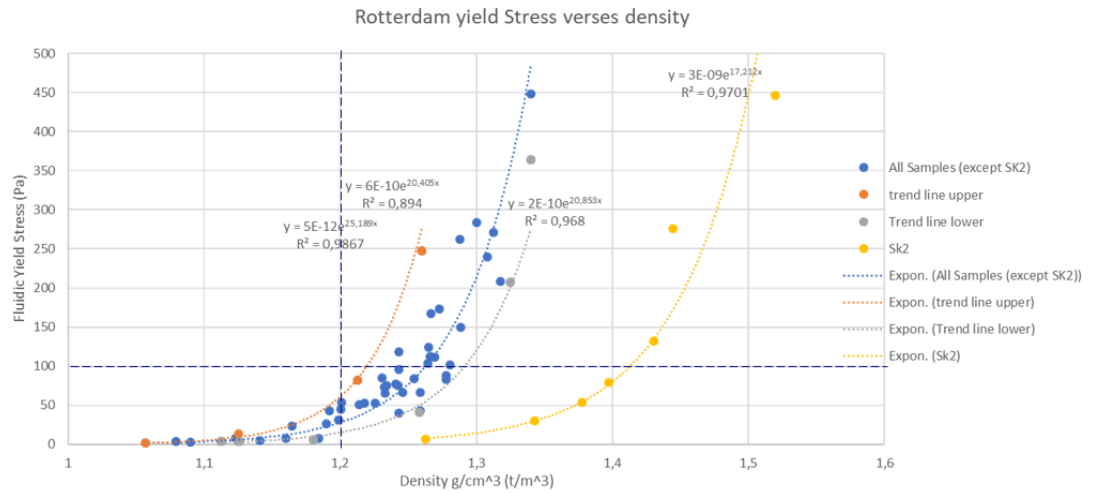


Figure 2.6. Yield stress-density variation of samples collected during the monitoring campaign in 2019/2020

2.4 Laboratory characterization

2.4.1 Particle size analysis

The particle size analysis showed that all fluid mud samples exhibit similar grain size except the sample from the Scheurkade (see Figure 2.7). Most particles fall within the silt size class (between 2 and 63 μm). They are typically no primary particles, but particle aggregates or flocs. The sample from the Scheurkade contains more sand than the samples from other locations.

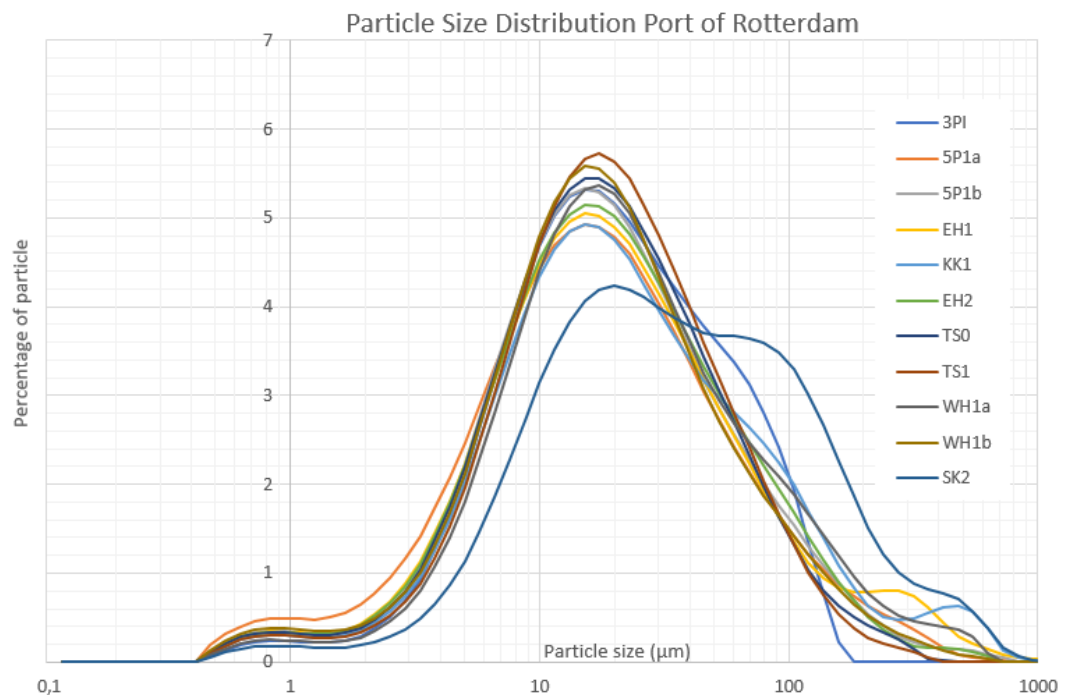


Figure 2.7. PSD analysis of samples collected during the monitoring campaign in 2019/2020

2.4.2 Floc morphology

Floc morphology analysis is conducted for estimating the size, settling velocity and density of flocs. The measurements and analysis are conducted by Prof. Andrew J. Manning (University of Plymouth, HR Wallingford). The population of flocs is divided into macroflocs (diameter > 160 microns) and microflocs (diameter < 160 microns) based on the floc diameter.

Figure 2.8 shows a floc morphology analysis of a 1 g/l water sample collected 1 m above a fluid mud layer at the Calandkanaal on 27-06-2019. The size of the flocs ranges from 20 to 408 microns, settling velocities varies from 0.04 to 18 mm/s and the effective density is from 3 to 2318 kg/m³. Macroflocs have average size of 240 microns, average settling velocity of 7.8 mm/s and average density of 274 kg/m³. Microflocs have average size of 82 microns, average settling velocity of 1.15 mm/s and average density of 300 kg/m³. Macroflocs have a mean size 3-times that of the microflocs and are just 25 kg/m³ less dense, but collectively settle nearly 7-times quicker than the microflocs. Macroflocs only constitute just over quarter of the individual flocs, but represent nearly more than half (53.7%) of the floc mass. That implies that the macroflocs settling dynamics represent ~89% of the sample Mass Settling Flux.

Figure 2.9 shows a floc morphology analysis of a 1 g/l water sample collected 1 m above a fluid mud layer at the KTM-kade on 28-06-2019. The size of the flocs ranges from 24 to 363 microns, settling velocities varies from 0.1 to 8 mm/s and the effective density is from 16 to 1756 kg/m³. Macroflocs have average size of 215 microns, average settling velocity of 7.8 mm/s and average density of 274 kg/m³. Microflocs have average size of 87 microns, average settling velocity of 1 mm/s and average density of 265 kg/m³. Macroflocs only constitute just over quarter of the individual flocs (total 2,677 flocs), but represent 43% of the floc mass. That implies that the macroflocs settling dynamics represent ~71% of the sample Mass Settling Flux.

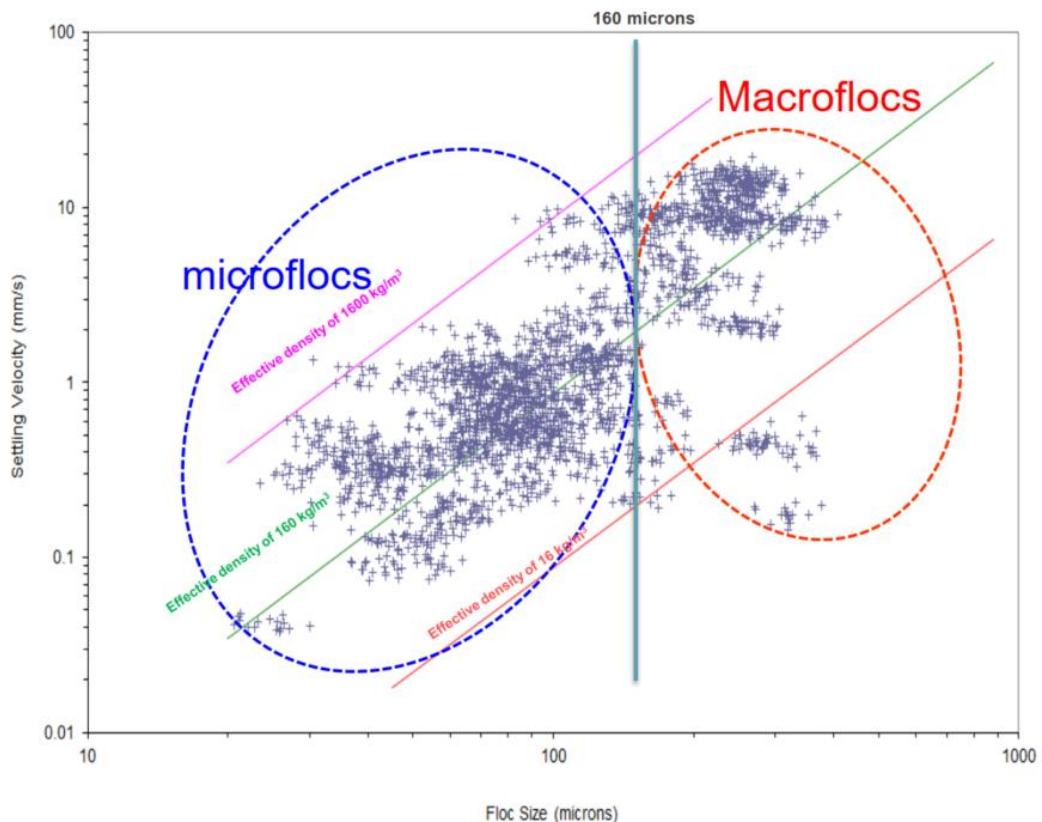


Figure 2.8. Floc morphology analysis of 1g/l water sample collected 1 m above fluid mud layer at the Calandkanaal on 27-06-2019

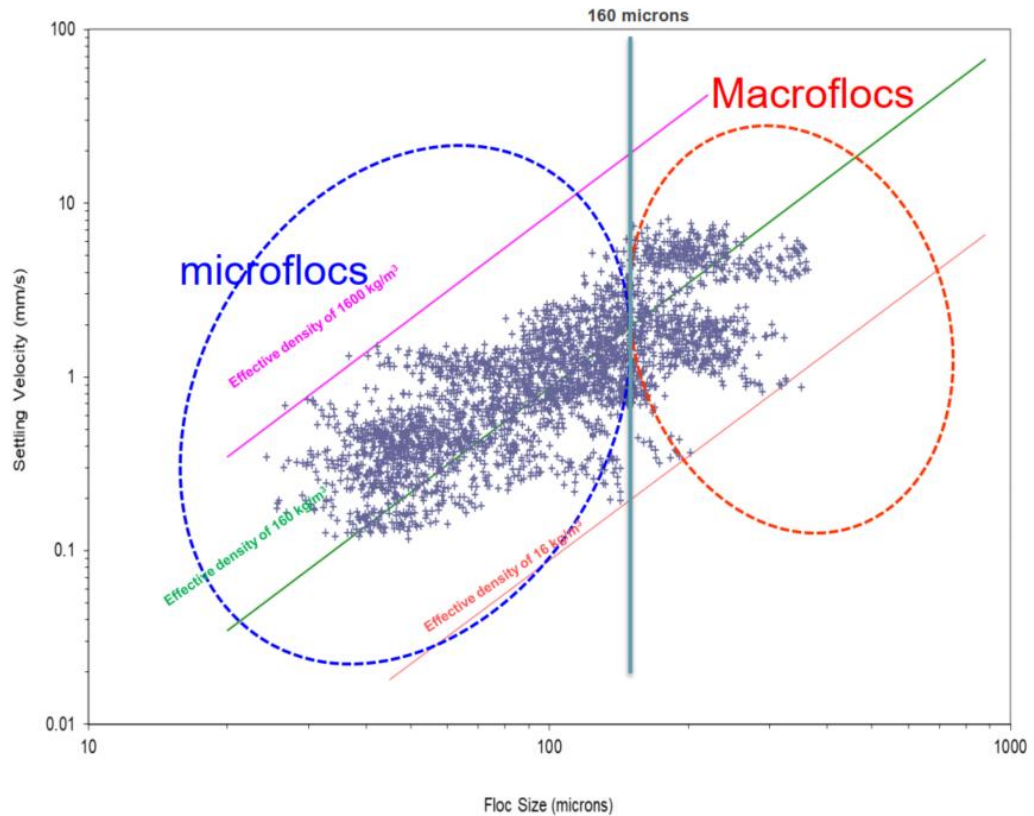


Figure 2.9. Floc morphology analysis of 1g/l water sample collected 1 m above fluid mud layer at the KTM Kade on 28-06-2019

Figure 2.10 shows a floc morphology analysis of a 5 g/l water sample collected approx. 10 cm above a fluid mud layer at the KTM Kade on 28-06-2019. The size of the flocs ranges from 23 to 1325 microns, settling velocities varies from 0.03 to 20 mm/s and the effective density is from 13 to 677 kg/m³. Macroflocs have average size of 275 microns, average settling velocity of 3.5 mm/s and average density of 85 kg/m³. Microflocs have average size of 97 microns, average settling velocity of 0.5 mm/s and average density of 106 kg/m³. Macroflocs only constitute over 40% of the individual flocs (total 9,457 flocs), but represent nearly 2/3 of the floc mass (64.3%). That implies that the macroflocs settling dynamics represent 89% of the sample Mass Settling Flux.

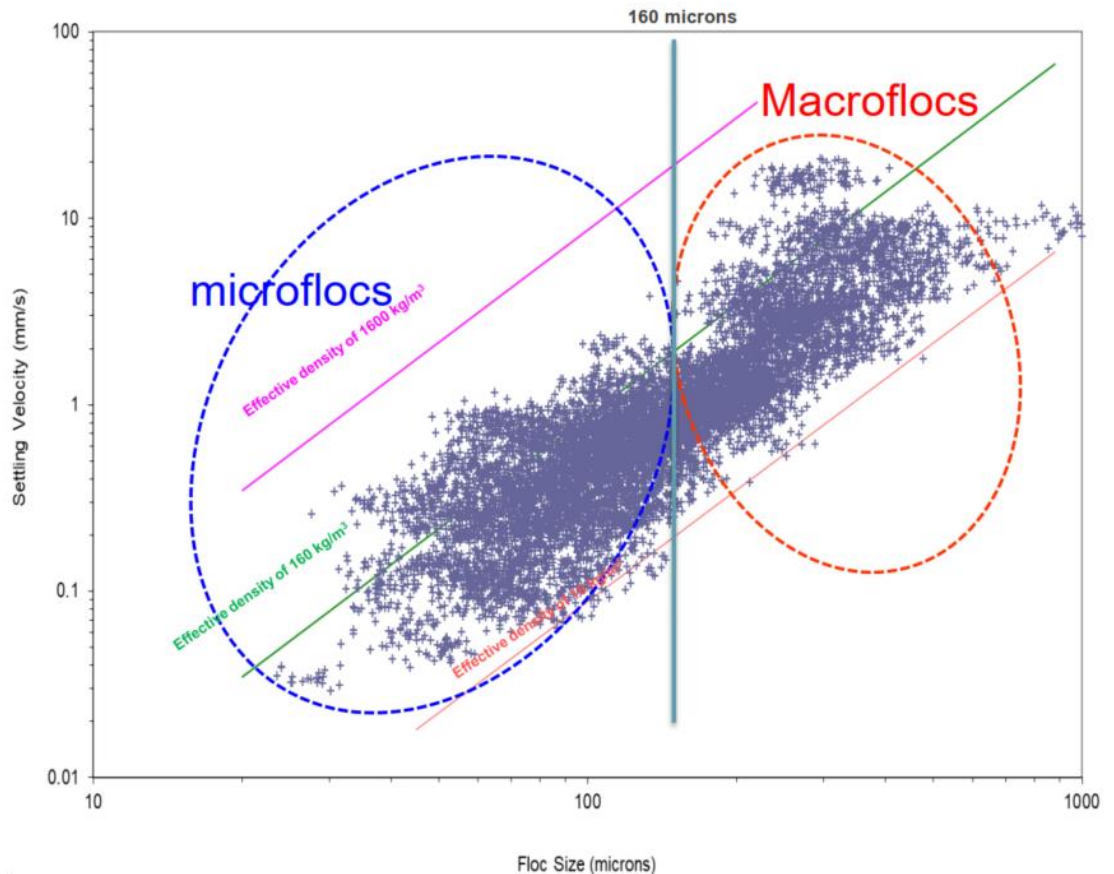


Figure 2.10. Floc morphology analysis of 5g/l water sample collected approx. 10 cm above fluid mud layer at the KTM Kade on 28-06-2019

The following preliminary conclusions can be made from population comparisons of samples collected 1 m above the fluid mud layer (FKK1) and approx. 10 cm above the fluid mud layer (FKK2) at the KTM kade:

- SSC of FKK2 is higher than SSC of FKK1 (5 g/l vs 1 g/l);
- The diameter of FKK2 is 1000 microns larger than FKK1;
- The settling velocity of FKK2 is 12 mm/s larger than FKK1 (20 mm/s vs 8 mm/s);
- The effective density of FKK2 is 1,000 kg/m³ less dense than FKK1 (700 kg/m³ vs 1756 kg/m³);
- Both FKK2 and FKK1 have similar settling velocities of microflocs (~3-3.5 mm/s);
- The settling velocity of FKK2 microflocs is half of FKK1 microflocs;
- The effective density of FKK2 (both microflocs and macroflocs) is significantly less than FKK1;
- The porosity of FKK2 (both microflocs and macroflocs) is bigger than FKK1;
- At FKK2 the macrofloc mass (65%) dominates and is 20% higher than at FKK1;
- The FKK2 macroflocs contribution to the mass settling flux is 93%, which is 21% higher than for FKK1.

So, although most flocs in the water column are micro flocs that contribute most to turbidity, macro flocs are the dominant fraction for sedimentation, as they have a larger settling velocity and contain relatively more mass and volume than micro flocs.

2.4.3 Organic matter

The results of the Total Organic Carbon (TOC) analysis show that TOC is between 2.3% to 2.5% for downstream locations (the Calandkanaal, the Westbocht, the 8th Petroleumhaven) and between 3.5% and 3.8% for upstream locations (the Scheurkade, the KTM kade, the 3rd Petroleumhaven, the Eemhaven and Waalhaven).

3 WP2: Monitoring tools

3.1 Introduction

This chapter describes the test results performed for the PRISMA TKI Project, Work Package 2: Monitoring Tools. The purpose of this study is to evaluate the performance of two monitoring tools; the GraviProbe (dotOcean, Brugge, Belgium) and the RheoTune (Stema Systems, Geldermalsen, the Netherlands). These tools are known to as devices to measure the mud strength (in terms of undrained shear strength, yield stress) and/or density and are typically used to establish mud properties in ports for navigation and dredging purposes. The working principles of both tools can be found in Appendix B.

The output of these tools is compared to the undrained shear strength, determined by a novel rheological protocol for defining navigable fluid mud layers. This protocol comprises rheological measurements, whereby a quick stress sweep curve is applied to the mud. This means that the strain or shear rate response of mud to a fast and transient application of shear stress is measured. The undrained shear strength is identified by a steep decline in apparent viscosity, when plotted as a function of the shear strain applied. Details are provided in Shakeel et al. (2019).

Mud was sampled from two ports; the Port of Rotterdam and the Port of Hamburg, was transported to Deltares, Delft, the Netherlands, where it was mixed, and diluted to a specified density, and prepared into a container for testing purposes. The testing consisted of deployment of the monitoring tools into the mud-filled container. After deployment the mud was subsampled using a Beeker Sampler (a 1.5 m long tube sampler, manufactured by Eijkelkamp, Giesbeek, the Netherlands). The subsamples were transported to Deltares' Physical Laboratory for the rheological testing (performed with a HAAKE MARS rheometer, Thermo Fisher, Karlsruhe, Germany) and density measurements (performed with an Anton Paar DMA 35, Graz, Austria), which served as independent reference measurements. The details of the reference measurements are provided in Appendix B.

3.2 Test Setup and Procedure

3.2.1 Test Setup

The test setup consisted of a mud reservoir, a mixer and a positive displacement screw type pump (also known as a water screw) and a test container. An overview is shown in Figure 3-1. The test container consisted of four steel cell rings mounted on top of each other. The inner diameter was 1250 mm and the height of a single cell ring was 500 mm, resulting in a 2 m-high container. The bottom cell ring was filled with a 0.3 m thick sand layer. This layer was in place in order to prevent damage to the probes, particularly the GraviProbe.

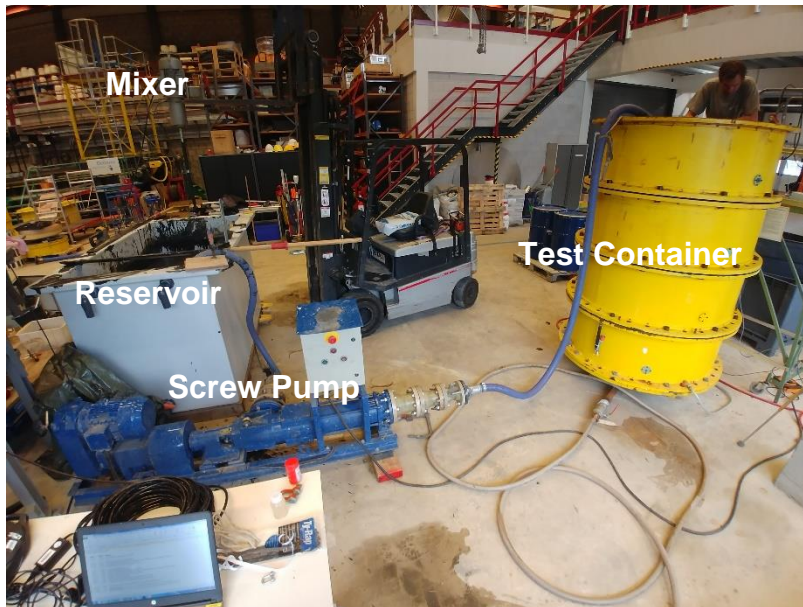


Figure 3-1: Overview of the test setup.

3.2.2 Deployment of the GraviProbe

For testing with the GraviProbe, an additional 4 m of water column was required for the probe to function correctly. This was realized by adding a 4 m high acrylate cylinder. The cylinder had an inner diameter of 280 mm and was made up of two 2000 mm high segments. These were mounted on a top cover, which in turn was mounted on top of the steel cell rings. The assembly is shown in Figure 3-2. The GraviProbe was positioned inside the cylinder using an overhead crane. Free-fall was initiated by an electronically operated magnetic release. A nylon rope was attached to the end of the GraviProbe for retrieval, with enough excess rope to ensure a smooth, uninterrupted free-fall.

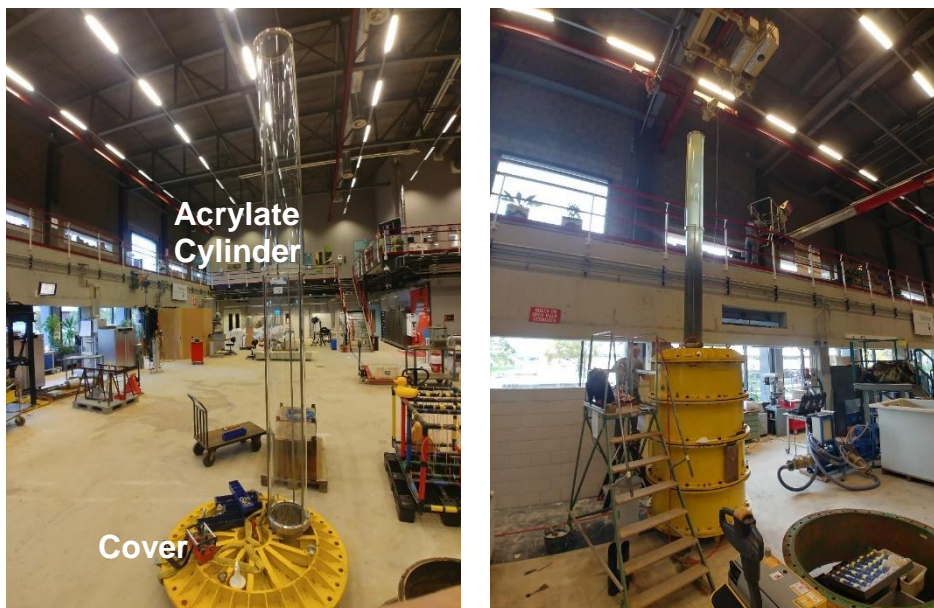


Figure 3-2: Container cover with additional acrylate cylinder.

3.2.3 Deployment of the RheoTune

The RheoTune was positioned just above mudline with an overhead crane. A 1.6 m long, 7.4 kg weighing steel profile was positioned on top of the RheoTune in order to ensure a vertical penetration path. Upon lowering the overhead crane, the RheoTune penetrated the mud under its self-weight from the mudline. The probe was retrieved by simply hoisting the crane back up.

3.3 Sample Preparation

3.3.1 Field Sampling from the Port

Sampling in the Port of Rotterdam was done from the quay Oosthavenkade, Vlaardingen, the Netherlands. Fourteen 200L barrels were filled with a grab crane, shown in Figure 3-3. No specific control was exercised with respect to the sampling depth or volume. After filling the containers, they were sealed off and transported to Delft, the Netherlands.

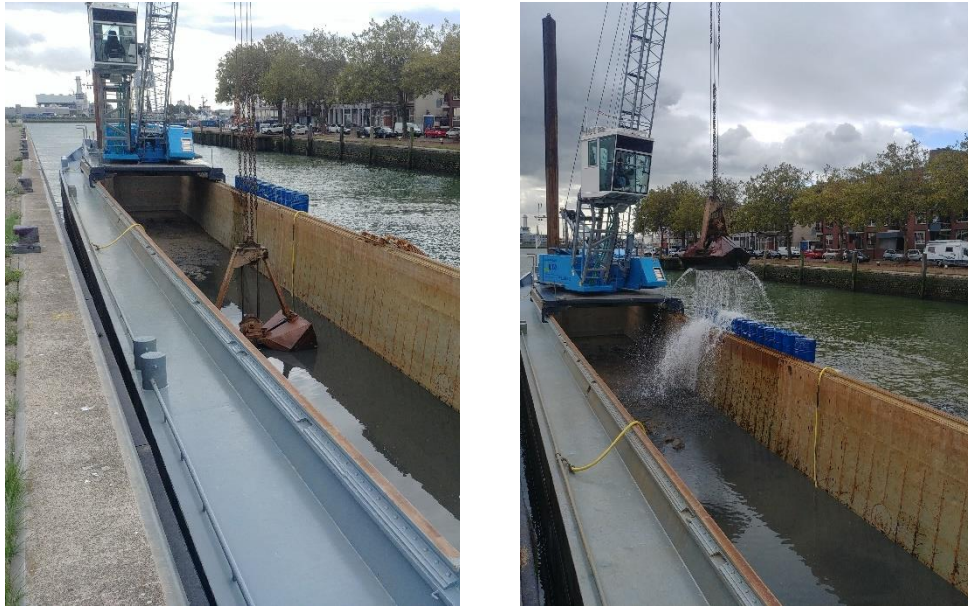


Figure 3-3: Sampling Operations in the Port of Rotterdam

Sampling operations for the Port of Hamburg were done without any Deltares' personnel present but are assumed to have been performed in a similar manner. The containers used for the port of Hamburg were smaller in volume (about 60L). The total amount of mud was also less than from the Port of Rotterdam. Therefore, it was opted to dilute the mud to $1.20 \text{ g}\cdot\text{cm}^{-3}$ for the first test series (instead of $1.25 \text{ g}\cdot\text{cm}^{-3}$ as for the Port of Rotterdam). Even so, the total thickness of the mud layer was less when compared to the Port of Rotterdam (about 1.0 m compared to 1.5 m). A particle size distribution of the sampled mud is shown in Figure 3-4.

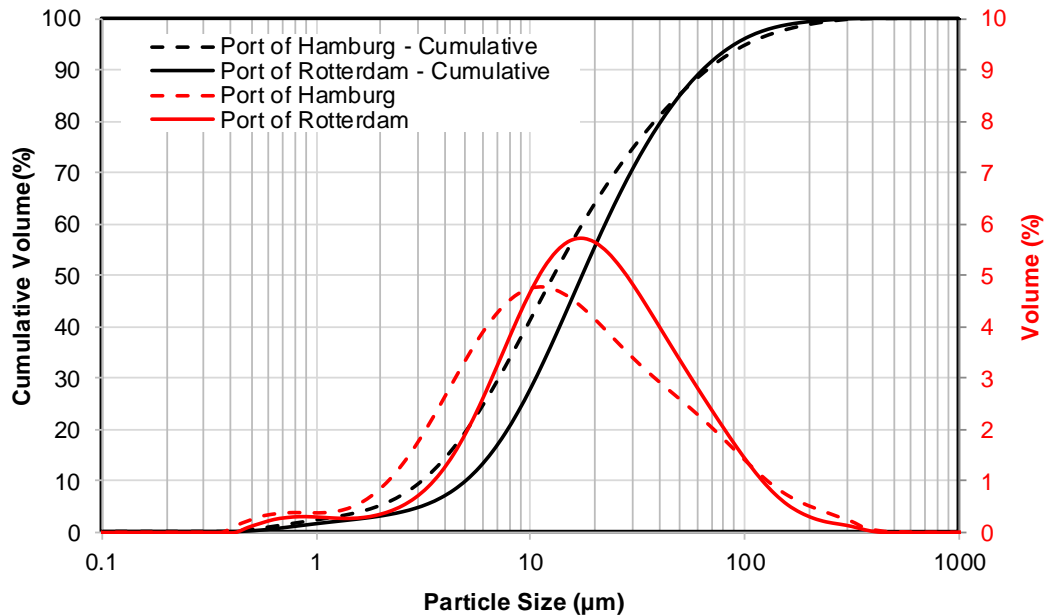


Figure 3-4: Particle size distribution for mud from the Port of Rotterdam (solid line) and Port of Hamburg (dashed line), both cumulative (black) and as non-cumulative (red).

3.3.2 Mixing

The mixing of the mud was done in two stages. The first stage consisted of pre-mixing the mud in the original containers by use of a marine blade electrical mixer until the mixture appeared homogeneous upon visual inspection (shown on the left-hand side of Figure 3-5). In the next stage the containers were emptied into a larger container, as shown in the right-hand side of Figure 3-5 and Figure 3-6. The purpose of the larger container was to act as a reservoir for the mud from the different barrels. In this reservoir the mud was diluted with tap water to a specified density. Tap water was chosen because the initial salinity (measured with an electrical conductivity probe) was higher than expected (about $40 \text{ mS}\cdot\text{cm}^{-1}$, where $20 \text{ mS}\cdot\text{cm}^{-1}$ was expected). Table 3.2 provides further details.

Mixing in the large container was done by the same electrical mixer and an additional screw type pump, which circulated the mud inside the reservoir. The same screw type pump was used to transport the mud from the reservoir to the test container (shown in the right-hand side of Figure 3-6).



Figure 3-5: Pre-mixing of mud (left-hand side) and deposition of mud into a larger container for dilution.



Figure 3-6: Mixing of the mud in the large collection container (left-hand side) and filling of the test container (right-hand side).

3.4 Test Program

3.4.1 Test Program

The test program consisted of using two different mud densities, two different mud rest times, and two types of mud (i.e. mud from the port of Rotterdam and mud from the port of Hamburg), for three measurement devices the GraviProbe, the RheoTune and direct measurement using the Beaker sampler. Upon completion of the GraviProbe and/or RheoTune deployments, a sample was taken using the Beaker sampler at a location which was not disturbed by the penetration of the other two probes. The first few tests were taken without a piston applied in the Beaker sampler. For one test with the Rotterdam mud (GP 1, see Table 3.1), the Beaker sampler was not available. Therefore, a syringe with a 1.5 m long hollow tube was used to sample mud at specified depth.

The amount of mud available from the Port of Hamburg was not enough to create a 1.5 m thick layer, as for the Port of Rotterdam. Therefore, it was decided to dilute the mud to $1.20 \text{ g}\cdot\text{cm}^{-3}$ instead of $1.25 \text{ g}\cdot\text{cm}^{-3}$ for the first tests. Although dilution resulted in a larger mud layer thickness, it was still significantly less than 1.5 m, about 0.9 m. The resulting mud layer thickness for the Port of Hamburg at a density of $1.15 \text{ g}\cdot\text{cm}^{-3}$ was about 1.1 m. An overview of the test program is shown in Table 3.1.

Table 3.1- Overview of Test Program

Probe Type ¹	Test No.	Date ²	Mud Origin ³	Target Density	Rest Time	Mud Layer Thickness	Mud Sampling ⁴
(-)	(-)	(dd/mm)	(-)	($\text{g}\cdot\text{cm}^{-3}$)	(hours)	(m)	
RT	1	10/10	PoR	1.25	24	1.52	No piston
RT	2	14/10	PoR	1.25	72	1.53	No piston
RT	3	27/11	PoR	1.15	24	1.53	With piston
RT	4	02/12	PoR	1.15	72	1.53	With piston
GP	1	12/11	PoR	1.25	24	1.52	Syringe
GP	2	18/11	PoR	1.25	72	1.53	With piston
GP	3	20/11	PoR	1.15	24	1.52	With piston
GP	4	25/11	PoR	1.15	72	1.53	With piston
RT	5	04/12	PoH	1.20	24	0.87	With piston
RT	6	06/12	PoH	1.15	24	1.12	With piston
GP	5	04/12	PoH	1.20	24	0.87	With piston
GP	6	06/12	PoH	1.15	24	1.12	With piston

Note 1) RT refers to RheoTune, GP refers to GraviProbe.

Note 2) All tests were done in 2019.

Note 3) PoR refers to the Port of Rotterdam, PoH refers to the Port of Hamburg.

Note 4) All sampling was done with the Beeker sampler, except for the test noted "Syringe".

The mud samples were diluted with tap-water. Table 3.2 provides an overview of electrical conductivity of free water on top.

Table 3.2- Overview of Electrical Conductivity measurements.

Port	Date ¹	EC ²	T ³	Comment
	(dd/mm)	($\text{mS}\cdot\text{cm}^{-1}$)	(°C)	
Rotterdam	07/10	40.5	19	Sample from free water on top of mud in barrels
Rotterdam	10/10	21.8 – 23.2	20	Sample from filtered water of mud RT 1
Rotterdam	10/10	0.85	21	Free water on top pre-test of RT 1
Rotterdam	10/10	0.86	21	Free water on top post-test of RT 1
Rotterdam	11/10	0.74	19	Free water on top mudbed for RT 2
Rotterdam	14/10	0.74	19.5	Free water on top pre-test of RT 2
Rotterdam	14/10	0.74	19.4	Free water on top post-test of RT 2
Rotterdam	18/11	0.79	17.5	Free water on top post-test of GP 2
Rotterdam	22/11	11.51	16.8	EC of mud (density 1.15)
Rotterdam	25/11	1.64	16.5	Free water on top post-test of GP 4
Rotterdam	27/11	1.19	18.7	Free water on top post-test of RT 3

Port	Date ¹	EC ²	T ³	Comment
Rotterdam	02/12	0.62	16.5	Free water on top post-test of RT 4
Hamburg	06/12	0.49	17.7	Free water on top post-test of GP 6

Note 1) All tests were done in 2019.

Note 2) EC refers to Electrical Conductivity.

Note 3) T refers to Temperature.

3.4.2 Probe Deployment Positions

During testing for the mud from the Port of Rotterdam, the test container was filled with newly remoulded mud before each different probe type was tested, allowing for three GraviProbe or two RheoTune deployments in a single test container, in addition to the deployment of the Beaker sampler. This was not possible for the mud from the Port of Hamburg due to time constraints. Here, a single GraviProbe and a single RheoTune deployment were done in a single prepared test container. A top-view of the lay-outs is shown in Figure 3-7 to Figure 3-9.

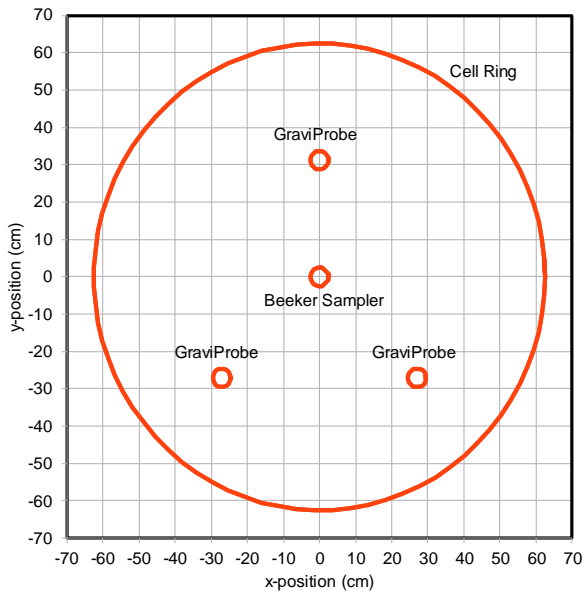


Figure 3-7: Top-view of test layout for the Port of Rotterdam GraviProbe deployments.

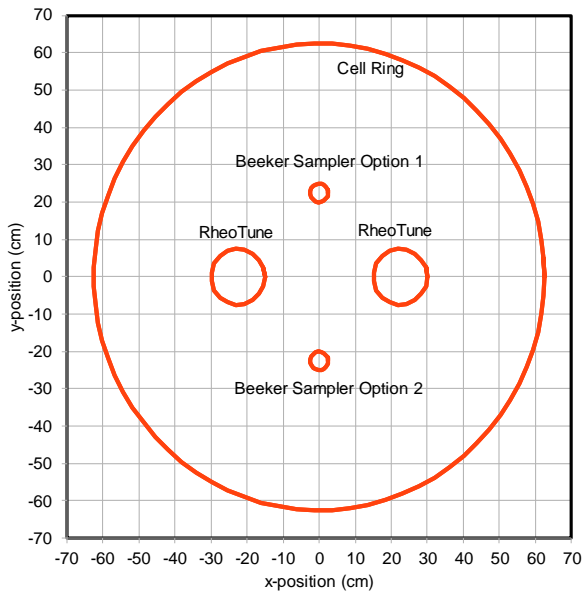


Figure 3-8: Top-view of test layout for the Port of Rotterdam RheoTune deployments.

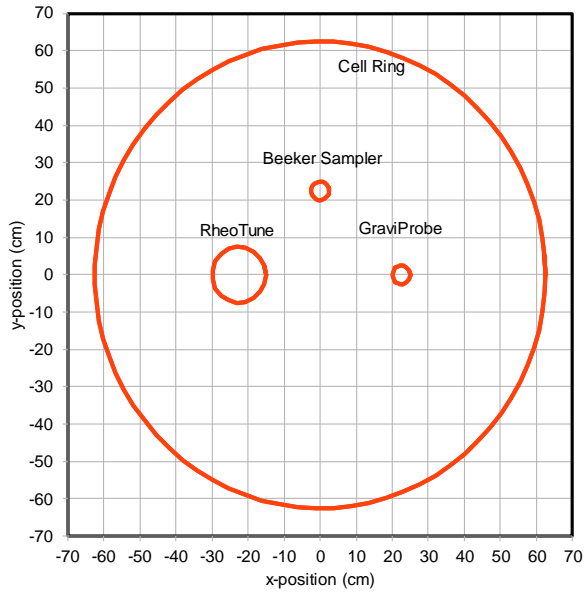


Figure 3-9: Top-view of test layout for the Port of Hamburg tests.

3.5 Probe Depth Registration

3.5.1 GraviProbe

In order to validate the measured depth from the GraviProbe, a visual check was performed on the pictures taken from the penetration of probe in the acrylate cylinder. By manually selecting the position of the probe in the column from a high-speed time lapse series (a selection is shown in Figure 3-10), and referencing the pixel values to vertical distance, a depth versus velocity profile could be made. This was then compared to the probe output, shown in Figure 3-11.

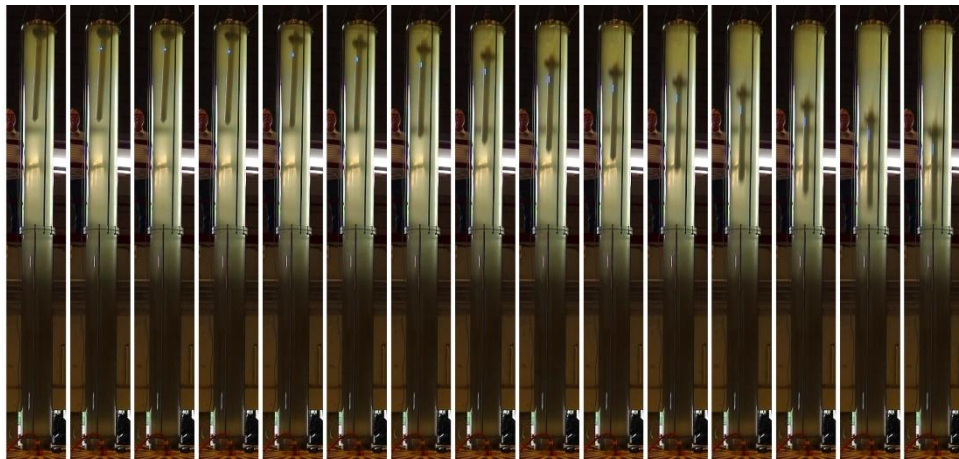


Figure 3-10: Selection from the time-lapse series for the GraviProbe drop in water.

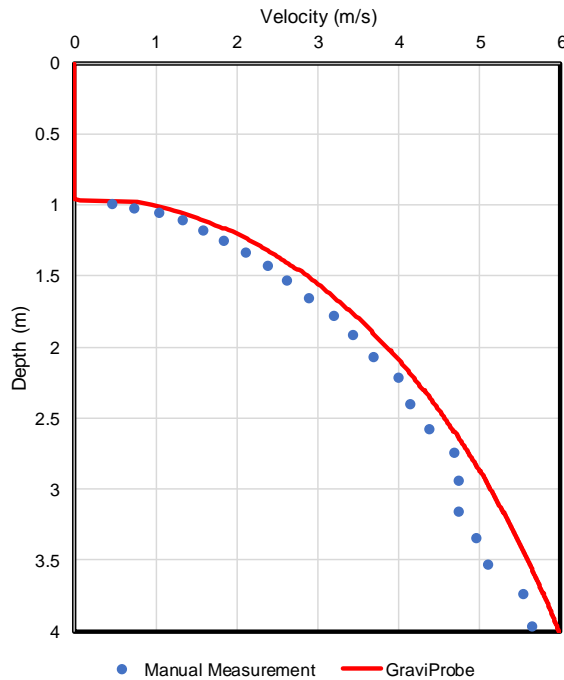


Figure 3-11: Validation of the velocity of the GraviProbe.

The discrepancies between the manual check and the output of probe are most likely attributed to uncertainty in finding the probe position in the time-lapse picture series due to blur and turbidity. Therefore, it can be assumed that the depth measurement for the GraviProbe is correct.

3.5.2 RheoTune

During the first deployment, the RheoTune indicated a penetration depth of about 1 m, while the visually observed penetration was about 1.5 m. This penetration was verified by a tape measure. Inspection of the depth-time series showed non-linear penetration rate with time, while the winch speed of the overhead crane was constant.

The depth measurement of the RheoTune is calculated with data from the pressure sensor at the top of the probe. Clogging of the pressure sensor by mud is most likely the cause of the discrepancy in depth reading (according to Stema Systems, this discrepancy can be solved by batch processing in RheoEdit). In order to correct for the discrepancy in depth, we used the winch speed to establish the probe depth in time. An example of the correction is shown in Figure 3-12. This procedure was applied to all tests.

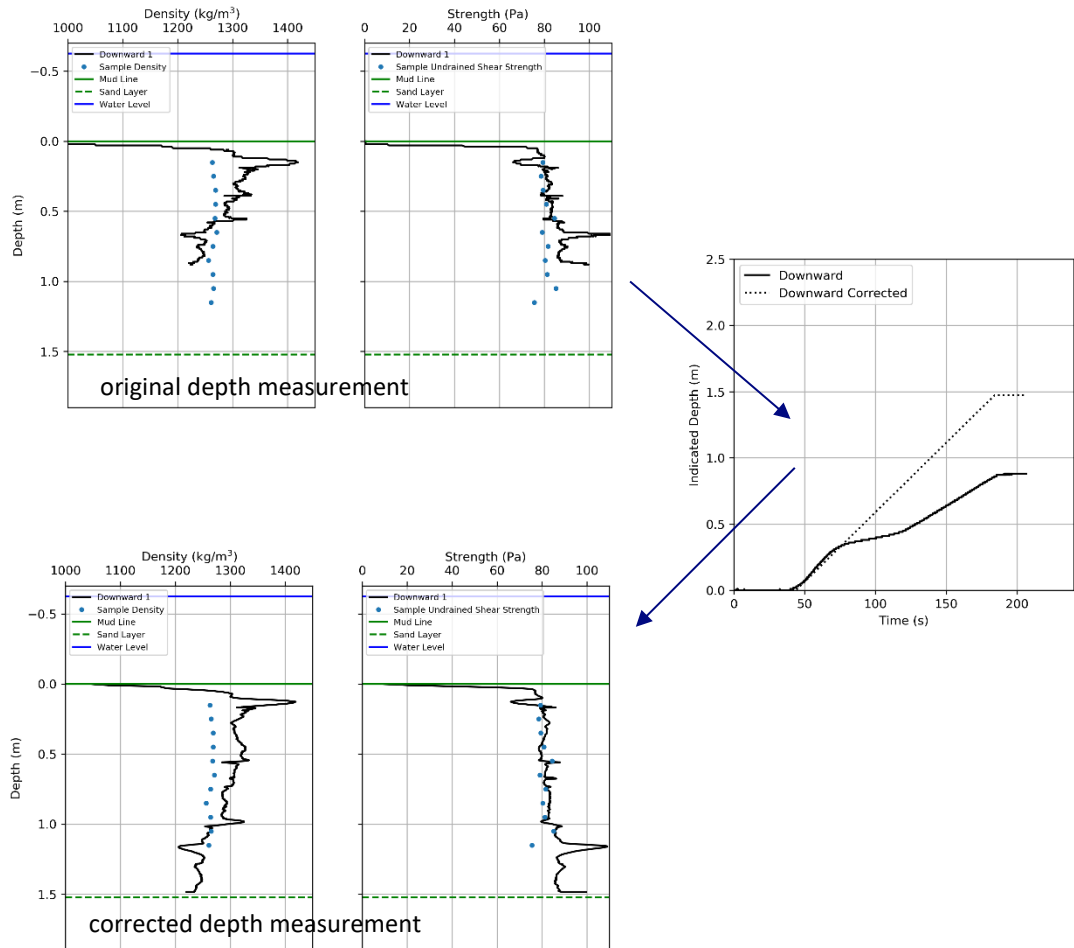


Figure 3-12: Depth correction for RheoTune Measurements.

3.5.3 Beeker Sampler

While the penetration length of the Beeker sampler was always 1.5 m, the recovered samples typically yielded only 1.1 m to 1.2 m of sample material. This can be attributed to:

- Sample compression, although this is unlikely due to the high water-content of the mud and the incompressibility of water.
- Sample material flowing out of the sample during retrieval, but visual inspection of the balloon-type seal at the cutting shoe did not reveal any gaps.
- Under-sampling; under-sampling occurs during penetration of the sampler into the mud when material flows around the cutting shoe rather than inside it. The underlying cause is plugging of the sampler: the accumulated soil material inside the liner is subject to frictional drag. When the drag force becomes larger than the mobilized bearing capacity of the soil which is about to be sampled, the soil is being pushed out in front of the sampler, instead of entering the barrel. (Park and Sills, 1990, Skinner and McCave, 2003, Wegener and Kalumba, 2016). It is checked if this could happen, with the most realistic values of the undrained shear strength, this seems not very likely.

Because it is unclear where exactly the discrepancy between penetration and recovery originates from, it was decided to apply no depth correction or shift; i.e. sample 1 was assumed to originate from 0.0 m to 0.1 m below mudline, sample 2 from 0.1 m to 0.2 m and so forth.

3.6 Test Results

3.6.1 Beaker Sampler

Figure 3-13 to Figure 3-15 provide an overview of the measured reference parameters i.e. density (measured by DMA35) and undrained shear strength (measured with the Rheometer) after direct (core) sampling using the Beaker sampler. In this study we assume that density and strength measurements on the samples taken by the Beaker sampler are the reference values and hence, the output from GraviProbe and RheoTune are compared against them. For the two tests on mud from the Port of Rotterdam the direct density measurement was not done due to time constraints. These two tests were GraviProbe deployments, in which the density was of limited value for comparison as the GraviProbe has no density measurement. The rheograms of the undrained shear strength measurements are shown in Figure 3-16 to Figure 3-18. The values presented in these rheograms are the median values of all the sub-samples of the shown test.

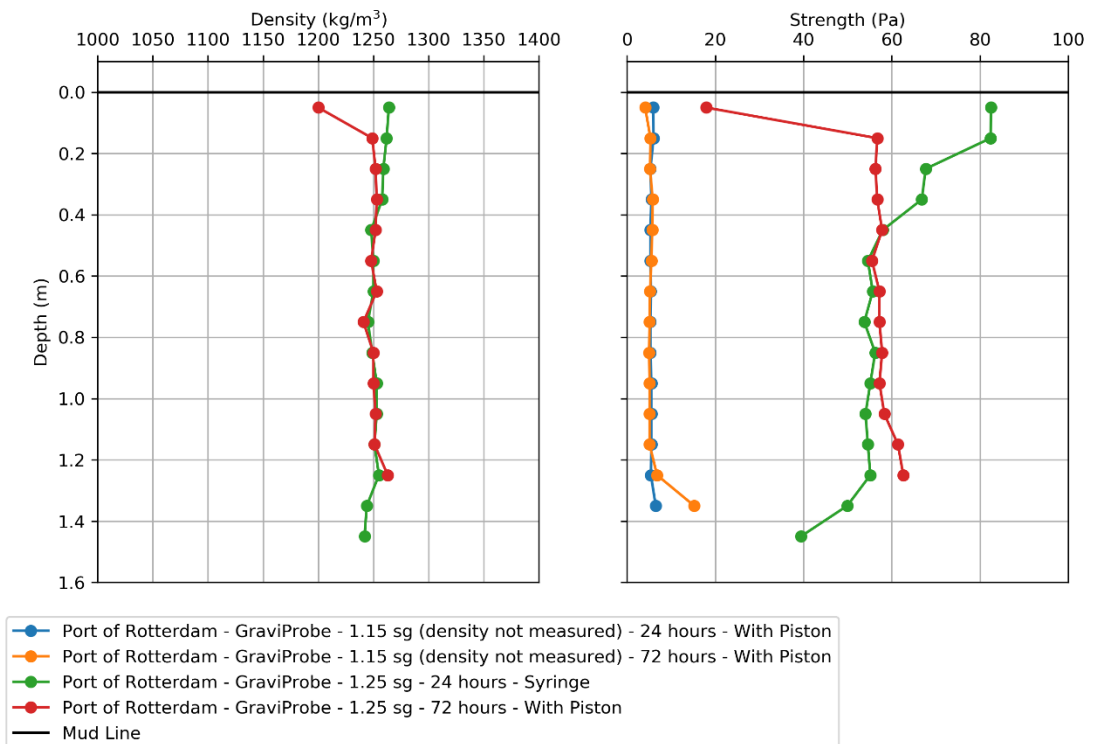


Figure 3-13: Overview of measured reference parameters from PoR's mud sampled from the test container after GraviProbe tests.

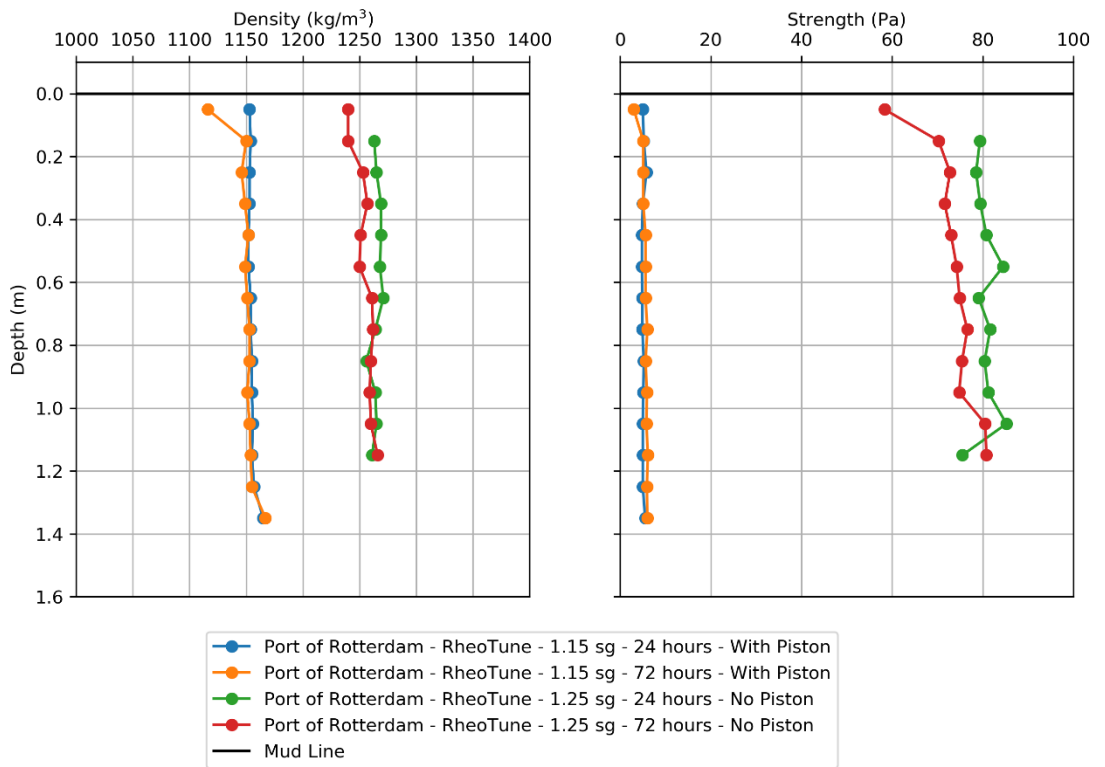


Figure 3-14: Overview of measured reference parameters from PoR's mud sampled from the test container after RheoTune tests.

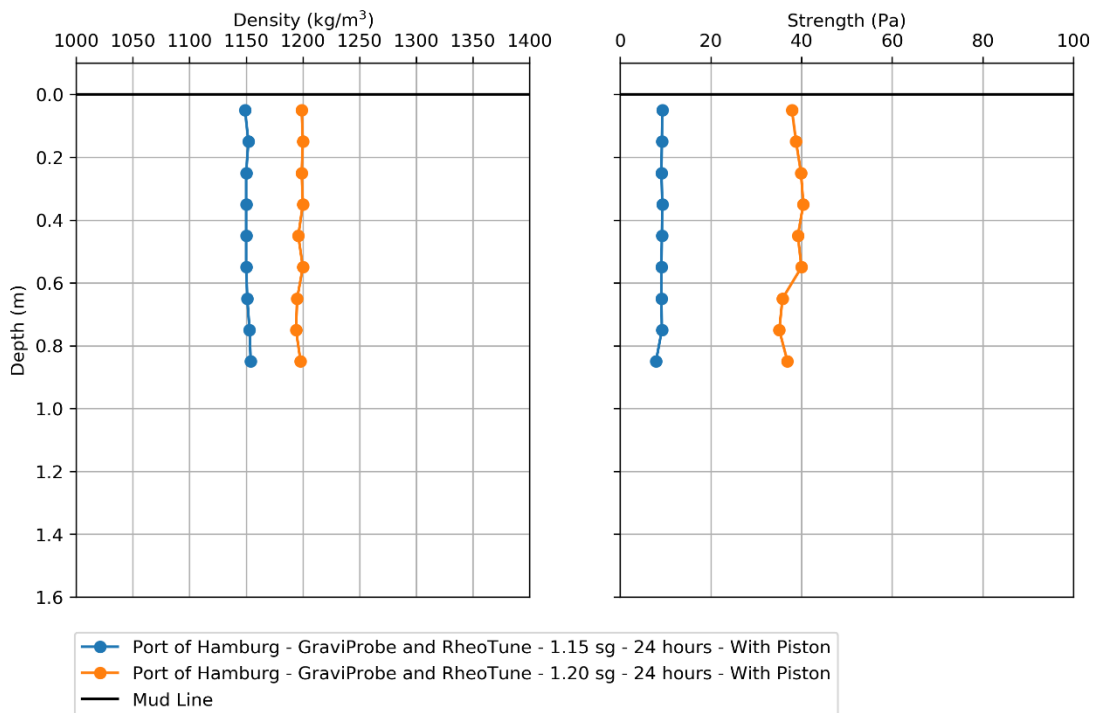


Figure 3-15: Overview of measured reference parameters from PoH mud sampled from the test container after GraviProbe and RheoTune Tests.

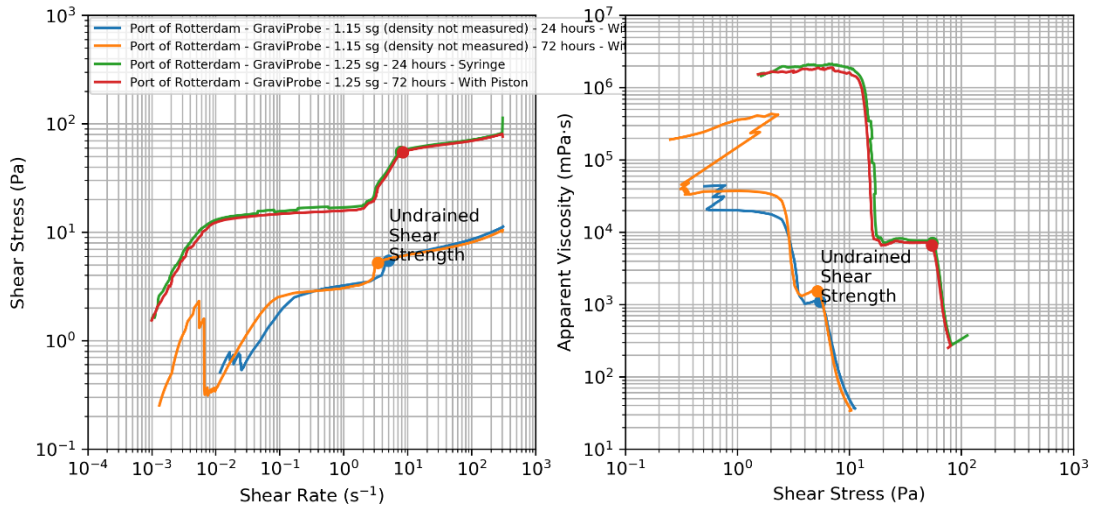


Figure 3-16: Overview of measured reference undrained shear strength from PoR's mud sampled from the test container after GraviProbe tests. Values are median from all depths.

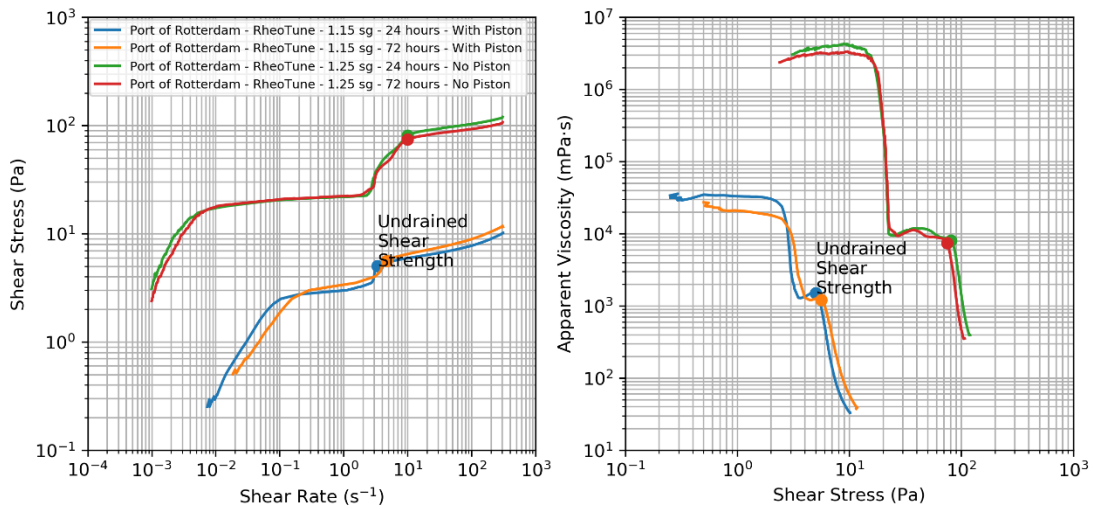


Figure 3-17: Overview of measured reference undrained shear strength from PoR's mud sampled from the test container after RheoTune tests. Values are median from all depths.

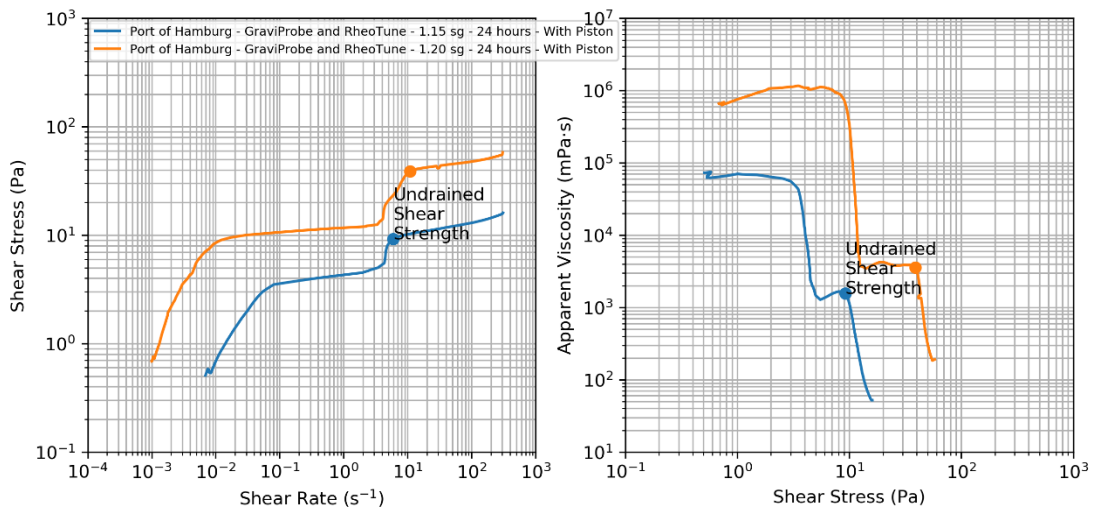


Figure 3-18: Overview of measured reference undrained shear strength from PoH's mud sampled from the test container after GraviProbe and RheoTune tests. Values are median from all depths.

3.6.2
3.6.3

**GraviProbe
Results versus Depth**

GraviProbe test results are shown in Figure 3-19 -Figure 3-24. These figures each consists of three sub-plots, on the left-hand side: the acceleration versus depth, in the middle: velocity versus depth and on the right-hand side: the strength versus depth. Both reference and GraviProbe measurements are shown, where available. Please note that, for optimal detail, the x-axis ranges may differ per plot. The data is presented “as-is”, i.e. no further processing was performed other than converting the raw data to text files using the manufactures software.

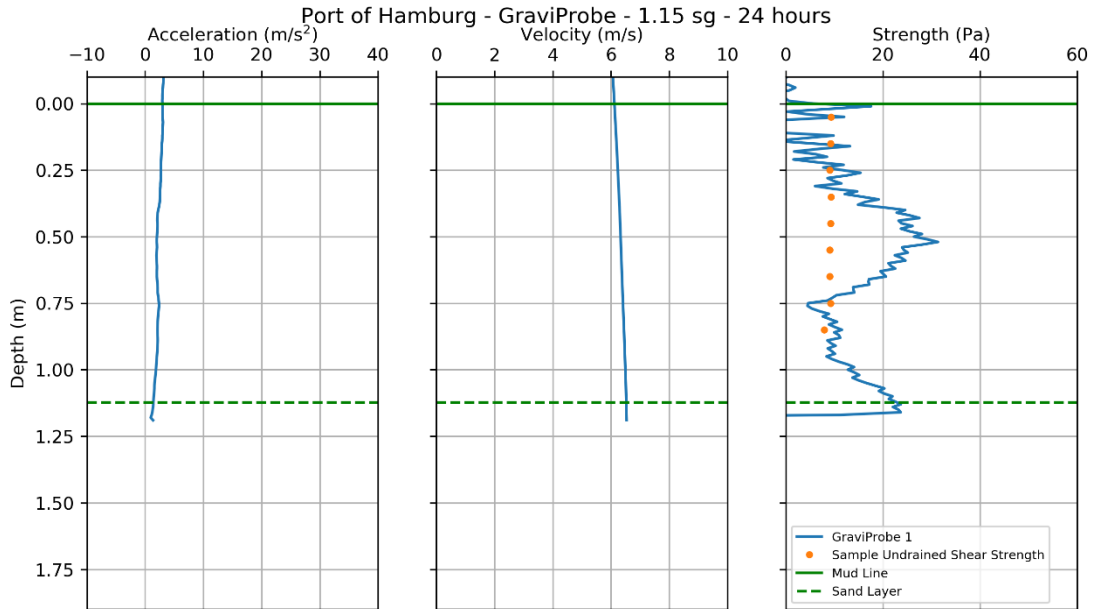


Figure 3-19: GraviProbe testing in PoH's mud with target density of $1.15 \text{ g}\cdot\text{cm}^{-3}$ and 24 hours of rest. Right panel shows GraviProbe measurements (blue line) and undrained shear strength (orange circles).

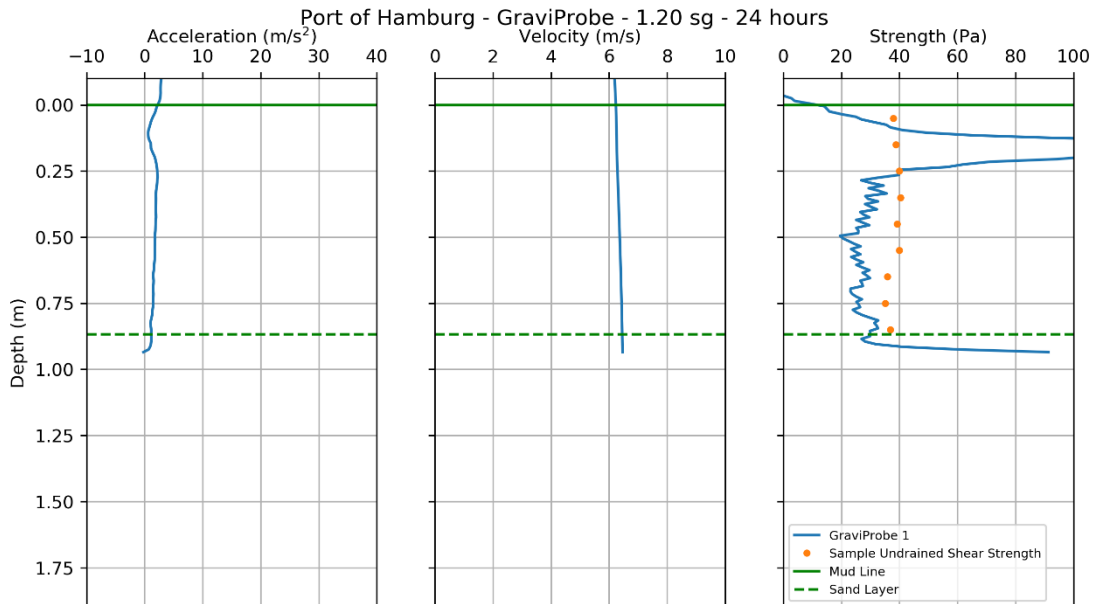


Figure 3-20: Port of Hamburg GraviProbe results, target density of $1.20 \text{ g}\cdot\text{cm}^{-3}$, after 24 hours of rest for the slurry. Right panel shows GraviProbe measurements (blue line) and undrained shear strength (orange circles).

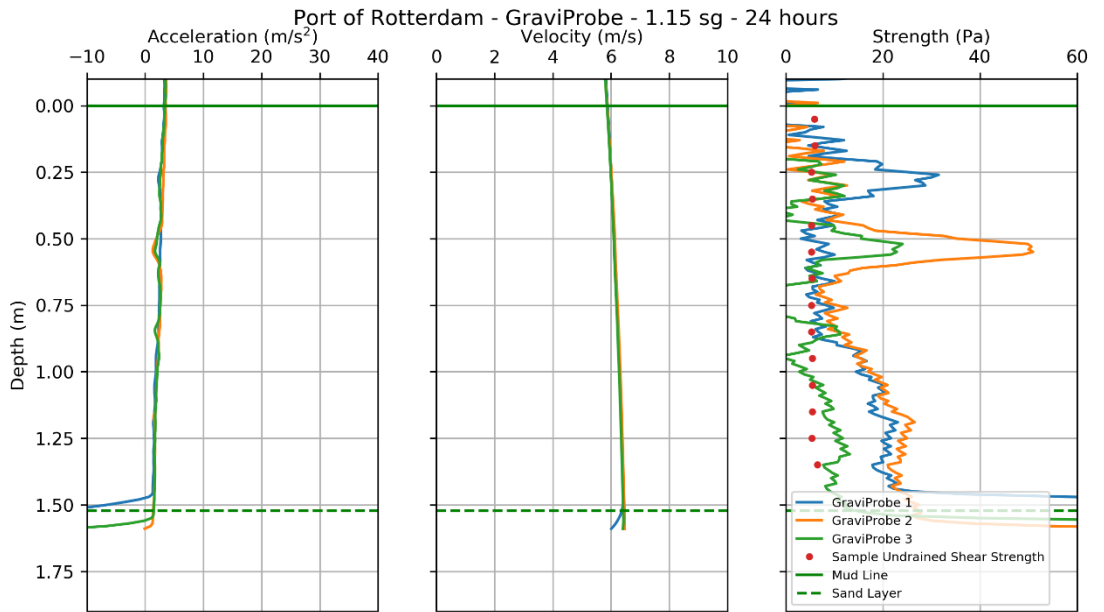


Figure 3-21: Port of Rotterdam GraviProbe results, target density of $1.15 \text{ g}\cdot\text{cm}^{-3}$, 24 hours of rest. Right panel shows GraviProbe measurements (blue line) and undrained shear strength (orange circles).

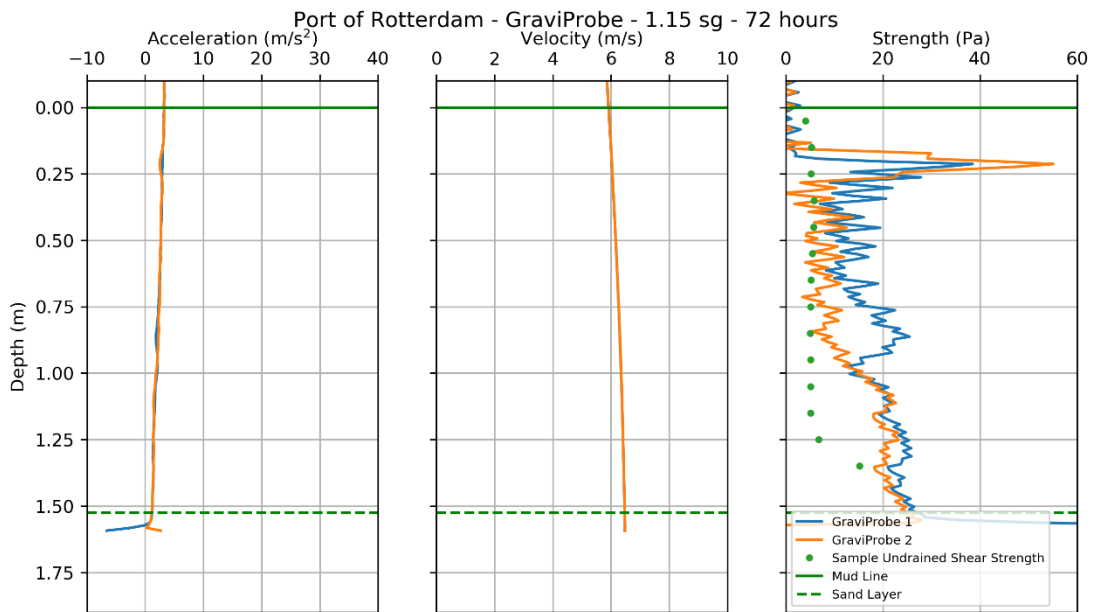


Figure 3-22: Port of Rotterdam GraviProbe results, target density of $1.15 \text{ g}\cdot\text{cm}^{-3}$, 72 hours of rest. Right panel shows GraviProbe measurements (blue line) and undrained shear strength (orange circles).

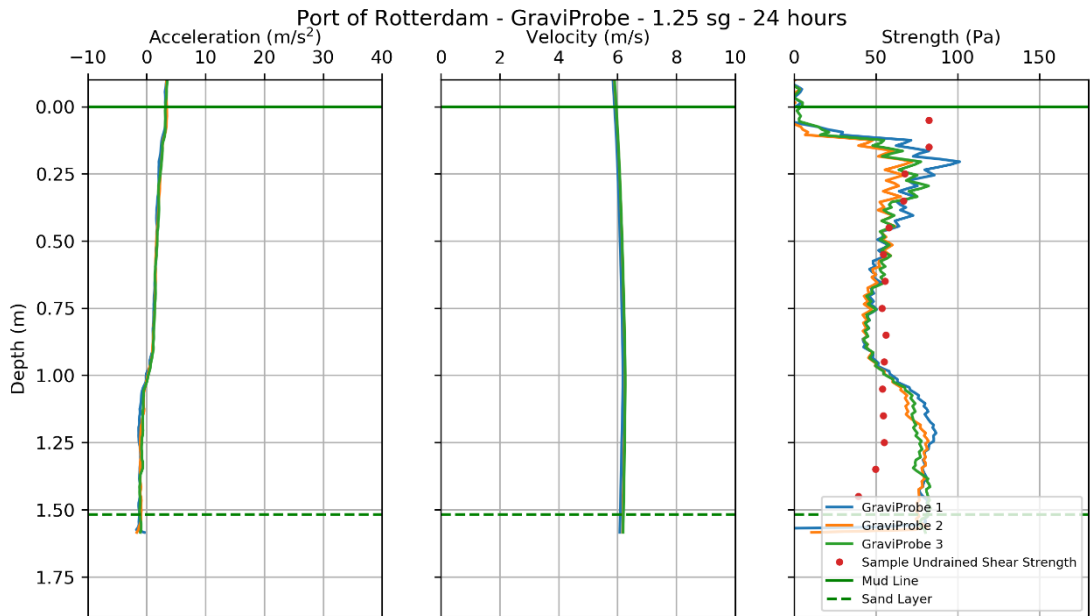


Figure 3-23: Port of Rotterdam GraviProbe results, target density of $1.25 \text{ g}\cdot\text{cm}^{-3}$, 24 hours of rest. Right panel shows GraviProbe measurements (blue line) and undrained shear strength (orange circles).

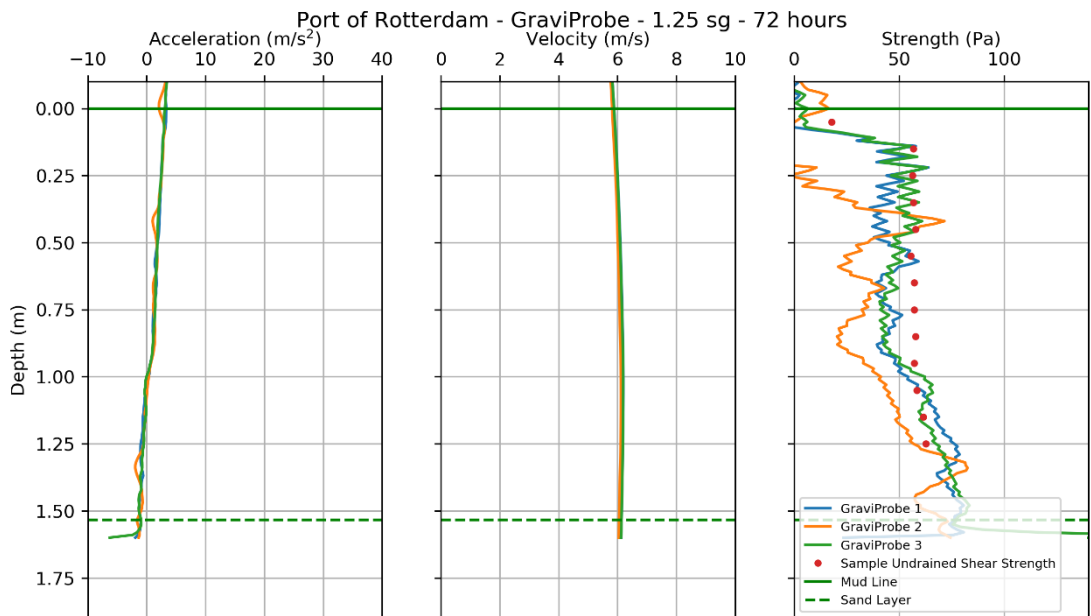


Figure 3-24: Port of Rotterdam GraviProbe results, target density of $1.25 \text{ g}\cdot\text{cm}^{-3}$, 72 hours of rest. Right panel shows GraviProbe measurements (blue line) and undrained shear strength (orange circles).

3.6.4 Summarized Results

A histogram was made to investigate the difference between the reference measurement and the probe measurement (Figure 3-25). Figure 3-25 shows the difference between undrained shear strength as measured by the probe, and the rheological procedure, expressed as an absolute value (left-hand side), and relative to the reference value (right-hand side). Values are average values over the subsample lengths. Values outside the histogram range as shown are collectively represented in an outlier bin. In order to eliminate the erratic values at the end of the penetration, and the stress build-up during the start of penetration of the mudline, the first and last two sub-samples have not been included in the histogram and the table.

In order to distinguish between specific tests, the data from the histograms has also been presented per test (Table 3.3 for undrained shear strength)

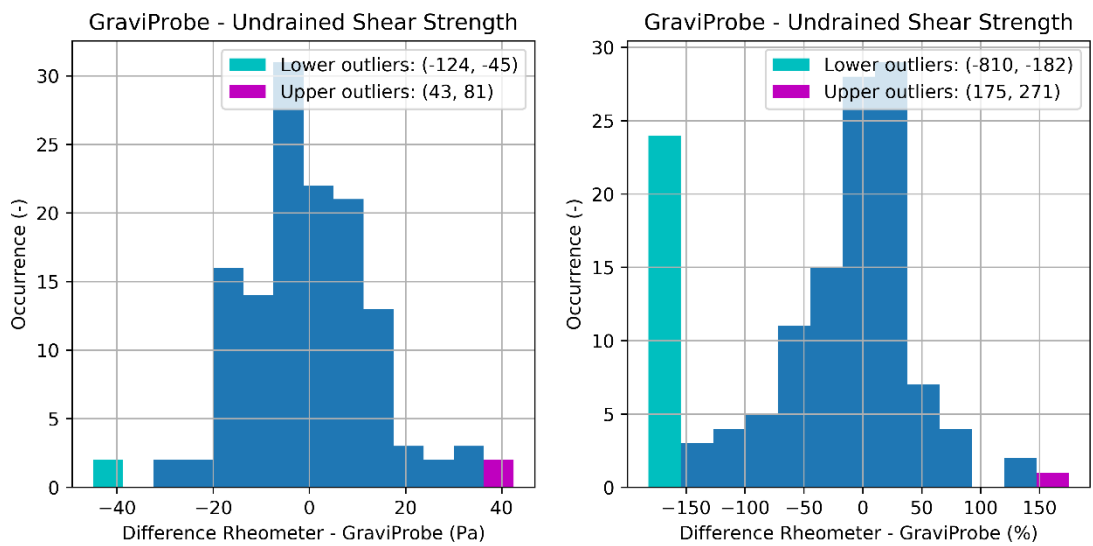


Figure 3-25: Distribution of difference between reference undrained shear strength and GraviProbe shear strength, expressed as absolute values (left-hand side) and relative (right-hand side).

Table 3.3- Summarized GraviProbe differences for undrained shear strength reference testing.

Port	Target Density γ ($\text{g}\cdot\text{cm}^{-3}$)	Rest Time (hours)	s_u^2 (Pa) ¹	Difference with GraviProbe (Pa) ¹			
Hamburg	1.15	24	9.2 ± 0.1	-7.8	± 6.9		
Hamburg	1.20	24	39.0 ± 1.5	-13.4	± 49.6		
Rotterdam	1.15	24	5.4 ± 0.2	-7.0	± 5.8		
Rotterdam	1.15	24	5.4 ± 0.2	-9.7	± 12.1		
Rotterdam	1.15	24	5.4 ± 0.2	0.1	± 7.5		
Rotterdam	1.15	72	5.3 ± 0.3	-10.6	± 5.7		
Rotterdam	1.15	72	5.3 ± 0.3	-6.6	± 5.6		
Rotterdam	1.25	24	59.5 ± 8.3	-4.0	± 13.3		
Rotterdam	1.25	24	59.5 ± 8.3	2.4	± 14.4		
Rotterdam	1.25	24	59.5 ± 8.3	-0.1	± 12.4		
Rotterdam	1.25	72	57.1 ± 0.8	9.3	± 6.2		
Rotterdam	1.25	72	57.1 ± 0.8	30.8	± 21.3		
Rotterdam	1.25	72	57.1 ± 0.8	6.1	± 6.0		

Note 1) The plus/minus values refer to one standard deviation.

Note 2) s_u refers to Undrained Shear Strength.

3.6.5 Parameter Plots

Figure 3-26 shows the GraviProbe shear strength versus the reference density and undrained shear strength. The data has been grouped based on location and density. This type of grouping was chosen because the variation in reference parameter per resting time and individual test is relatively small. The light-coloured symbols are the values for each sub sample, the darker coloured symbols are the median of each test type. The purpose of these figures is to visualize any relation, although no curves has been fitted through the data.

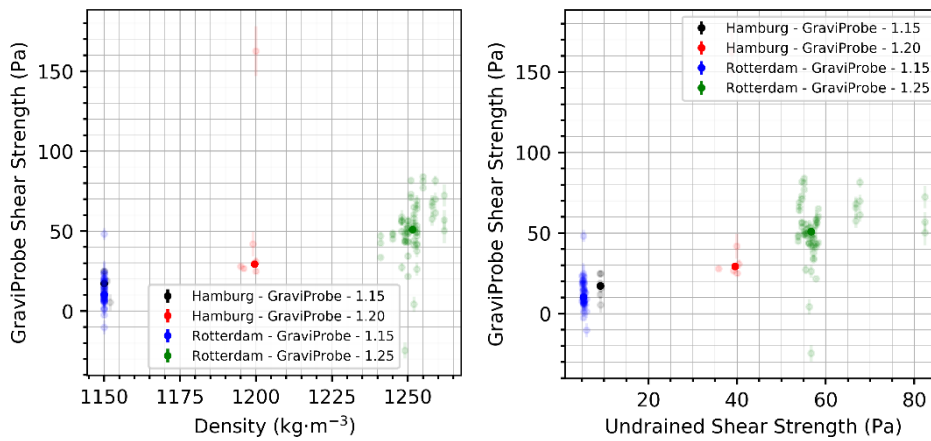


Figure 3-26: GraviProbe Shear strength values versus reference density and undrained shear strength.

3.6.6
3.6.7

RheoTune
Results versus Depth

RheoTune test results are shown in Figure 3-27 - Figure 3-32. These figures each consists of two subplots: on the left-hand side: the density versus depth and on the right-hand side: the yield stress versus depth. Both reference and probe measurements are shown, where available. Please note that, for optimal detail, that x-axis ranges may differ per plot. Other than the depth correction, the data is presented “as-is”, i.e. no further processing was performed other than converting the raw data to text files using the manufactures software.

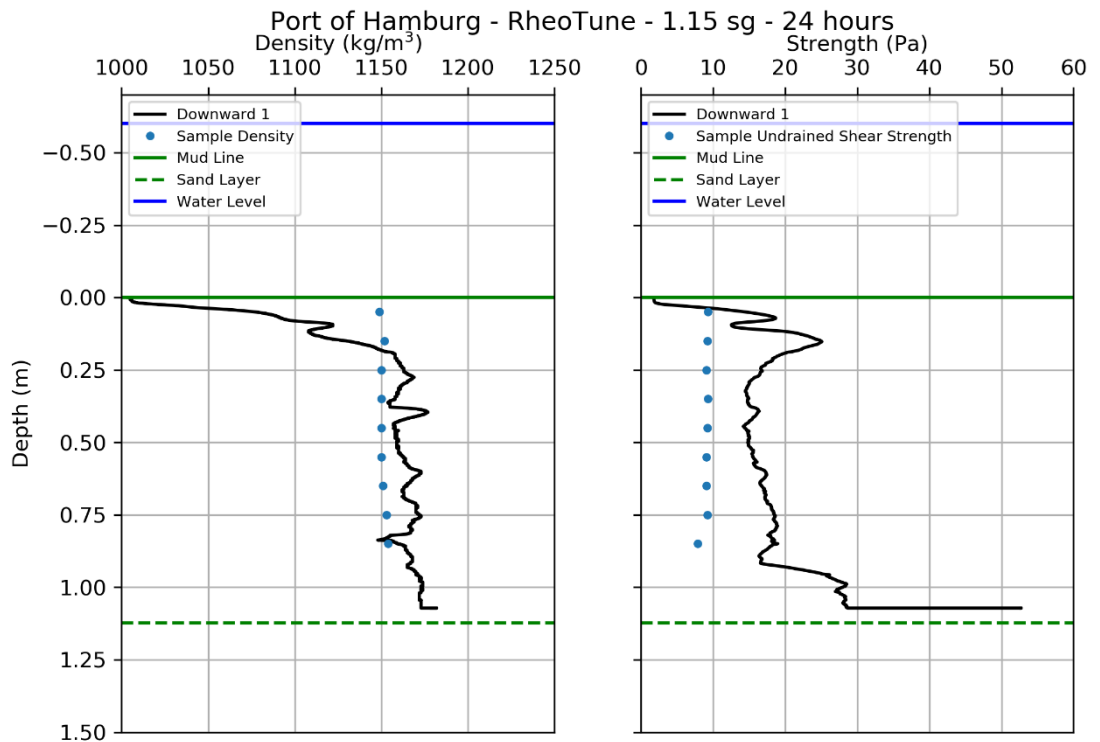


Figure 3-27: RheoTune testing in PoH's mud with target density of 1.15 g·cm⁻³ and 24 hours of rest. Left panel shows RheoTune's density measurements (solid black line) and density measured on core samples (blue circles). Right panel shows RheoTune's yield stress (black solid line) and undrained shear strength (blue circles).

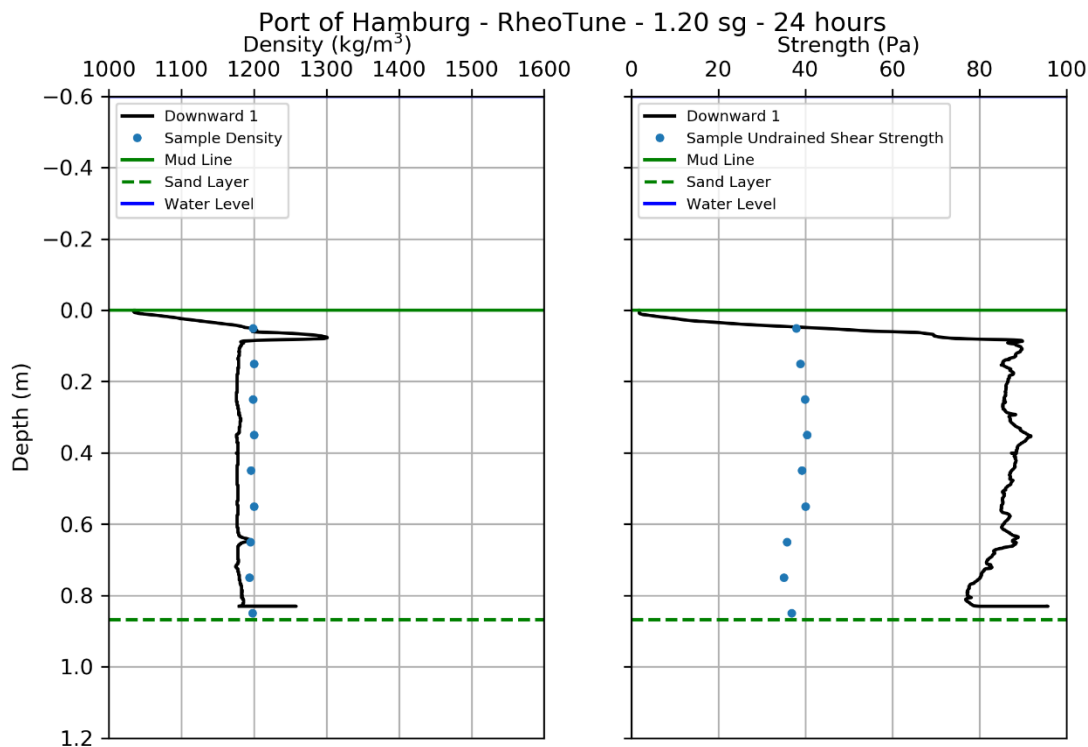


Figure 3-28: Port of Hamburg RheoTune results, target density of 1.20 g cm^{-3} , 24 hours of rest. Left panel shows RheoTune's density measurements (solid black line) and density measured on core samples (blue circles). Right panel shows RheoTune's yield stress (black solid line) and undrained shear strength (blue circles).

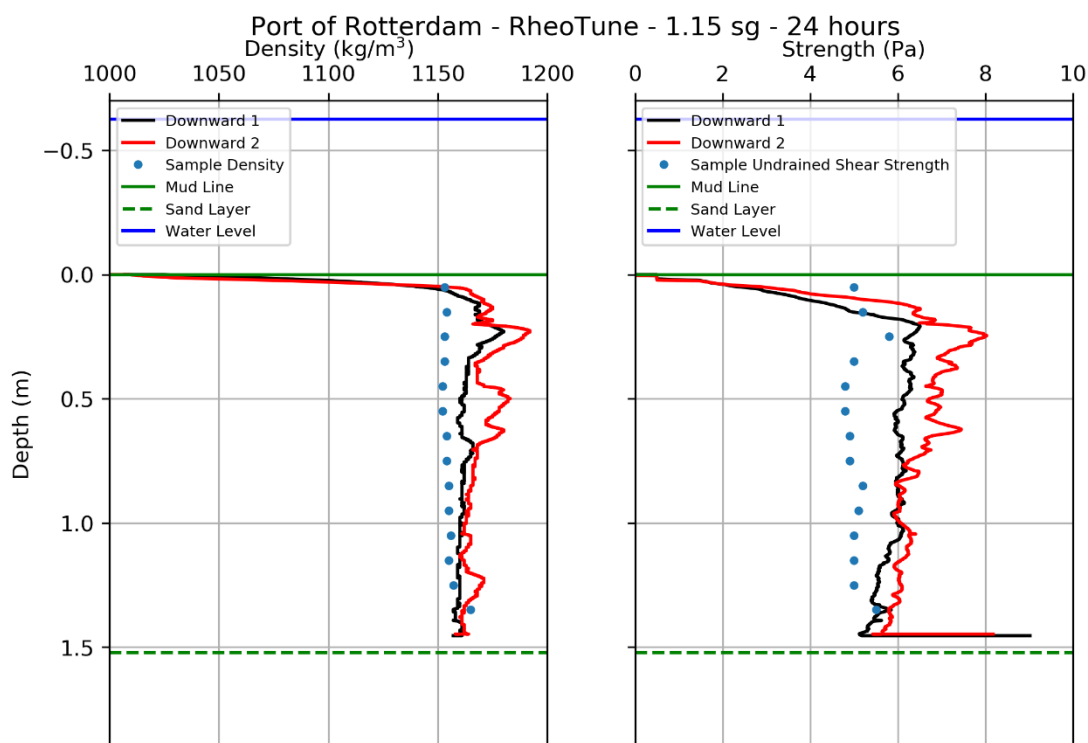


Figure 3-29: Port of Rotterdam RheoTune results, target density of 1.15 g cm^{-3} , 24 hours of rest. Left panel shows RheoTune's density measurements (solid black line) and density measured on core samples (blue circles). Right panel shows RheoTune's yield stress (black solid line) and undrained shear strength (blue circles).

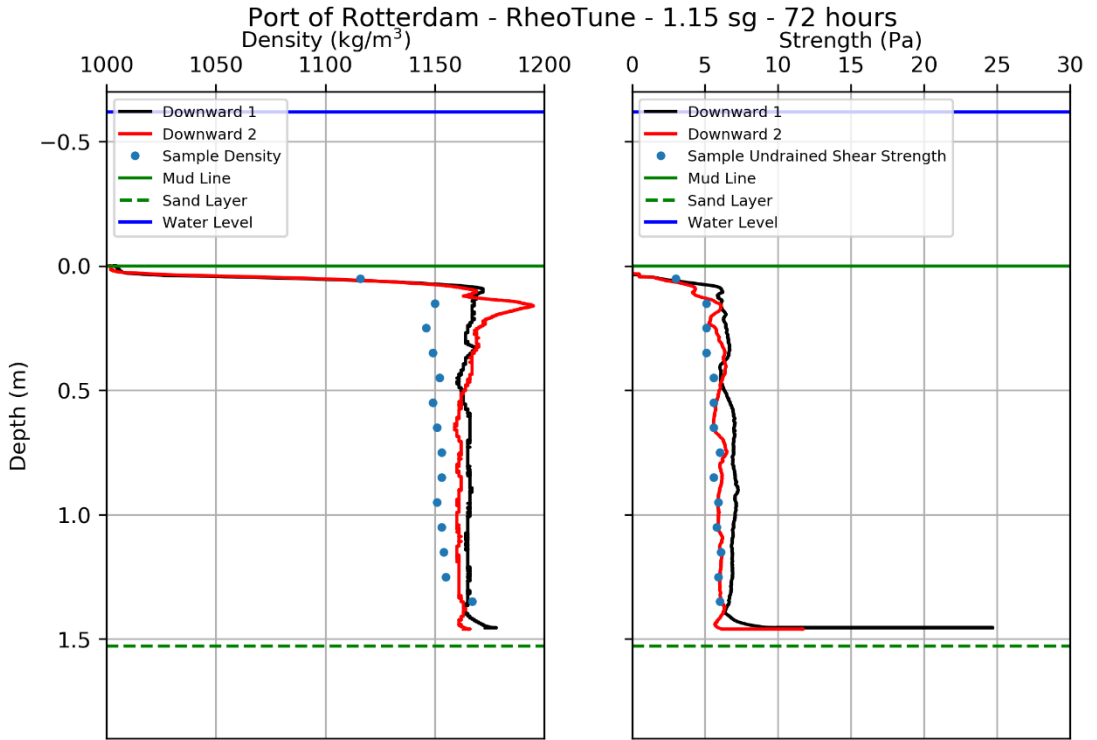


Figure 3-30: Port of Rotterdam RheoTune results, target density of $1.15 \text{ g}\cdot\text{cm}^{-3}$, 72 hours of rest. Left panel shows RheoTune's density measurements (solid black line) and density measured on core samples (blue circles). Right panel shows RheoTune's yield stress (black solid line) and undrained shear strength (blue circles).

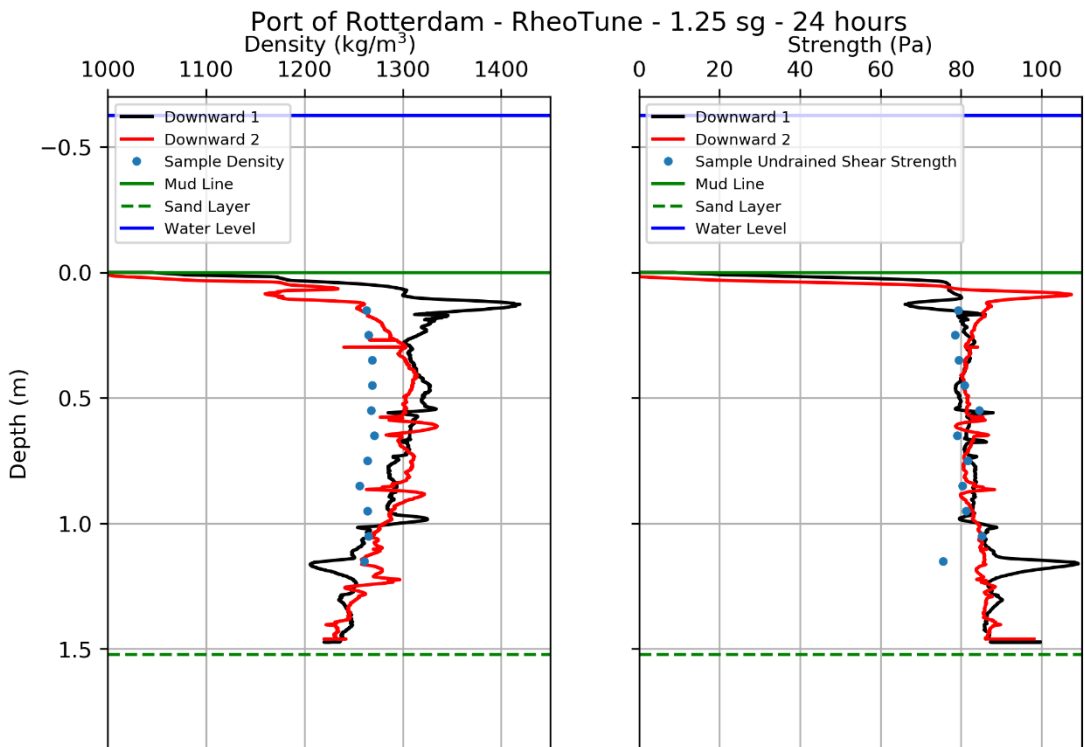


Figure 3-31: Port of Rotterdam RheoTune results, target density of $1.25 \text{ g}\cdot\text{cm}^{-3}$, 24 hours of rest. Left panel shows RheoTune's density measurements (solid black line) and density measured on core samples (blue circles). Right panel shows RheoTune's yield stress (black solid line) and undrained shear strength (blue circles).

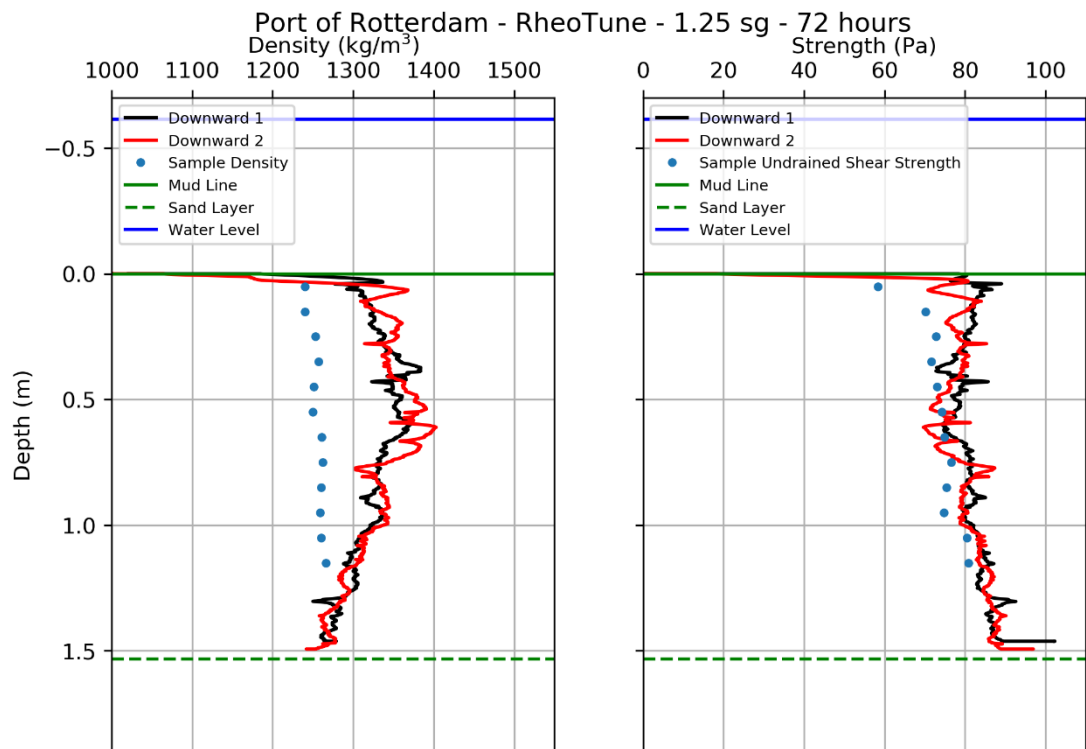


Figure 3-32: Port of Rotterdam RheoTune results, target density of $1.25 \text{ g}\cdot\text{cm}^{-3}$, 72 hours of rest. Left panel shows RheoTune's density measurements (solid black line) and density measured on core samples (blue circles). Right panel shows RheoTune's yield stress (black solid line) and undrained shear strength (blue circles).

3.6.8 Summarized Results

As for the GraviProbe, a histogram for Rheotune was made of the difference between the reference measurement, and the probe measurement, shown in Figure 3-33 and Figure 3-34, for yield stress and density, respectively.

Location-specific splits are shown in Table 3.4 - Table 3.5 for yield stress and density, respectively. Notable are the yield stresses for the Port of Hamburg. For these samples, the RheoTune significantly overestimates the yield stress. Also notable are the density measurements for the Port of Rotterdam for a density of $1.25 \text{ g}\cdot\text{cm}^{-3}$, with 72 hours of rest. Here the RheoTune overestimates the density with about $0.08 \text{ g}\cdot\text{cm}^{-3}$. It is unclear what is the cause, but it might be that material from the upper layer adheres to the tuning fork. As can be seen in Figure 3-32, the RheoTune output converges eventually to the reference density measurements.

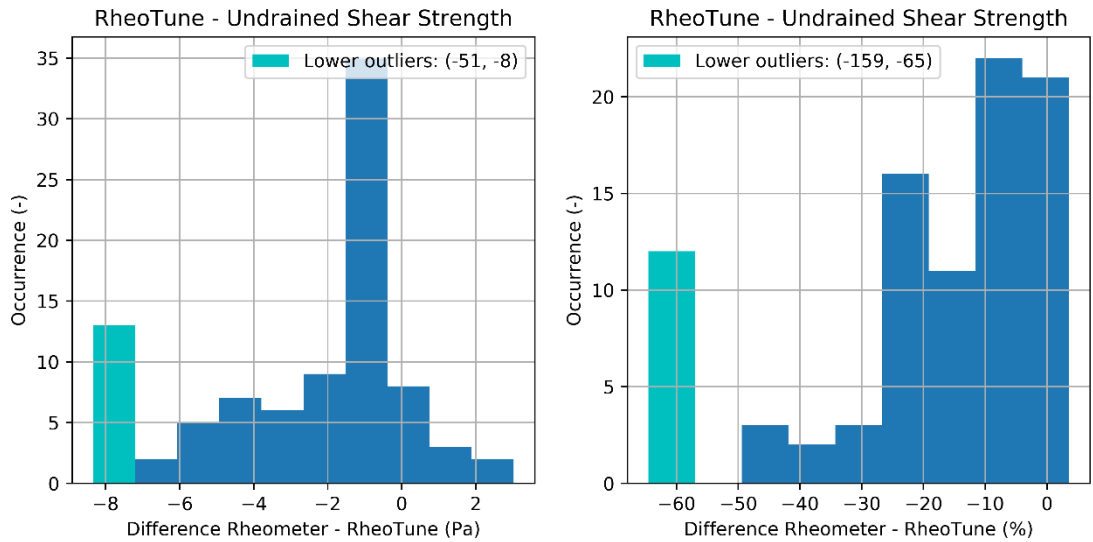


Figure 3-33: Distribution of difference between reference undrained shear strength and RheoTune yield stress, expressed as absolute values (left-hand side) and relative (right-hand side).

Table 3.4- Summarized RheoTune differences for yield stress reference testing.

Port	Target Density (g·cm ⁻³)	Rest (hours)	s _u ² (Pa) ¹	Difference with RheoTune (Pa) ¹
Hamburg	1.15	24	9.2 ± 0.1	-7.9 ± 3.1
Hamburg	1.20	24	39.0 ± 1.5	-48.1 ± 2.1
Rotterdam	1.15	24	5.1 ± 0.3	-0.9 ± 0.4
Rotterdam	1.15	24	5.1 ± 0.3	-1.5 ± 0.5
Rotterdam	1.15	72	5.6 ± 0.3	-1.1 ± 0.3
Rotterdam	1.15	72	5.6 ± 0.3	-0.4 ± 0.4
Rotterdam	1.25	24	80.7 ± 1.8	-1.2 ± 2.2
Rotterdam	1.25	24	80.7 ± 1.8	-1.4 ± 2.4
Rotterdam	1.25	72	73.7 ± 1.9	-5.8 ± 2.6
Rotterdam	1.25	72	73.7 ± 1.9	-4.2 ± 3.4

Note 1) The plus/minus values refer to one standard deviation.

Note 2) s_u refers to undrained shear strength.

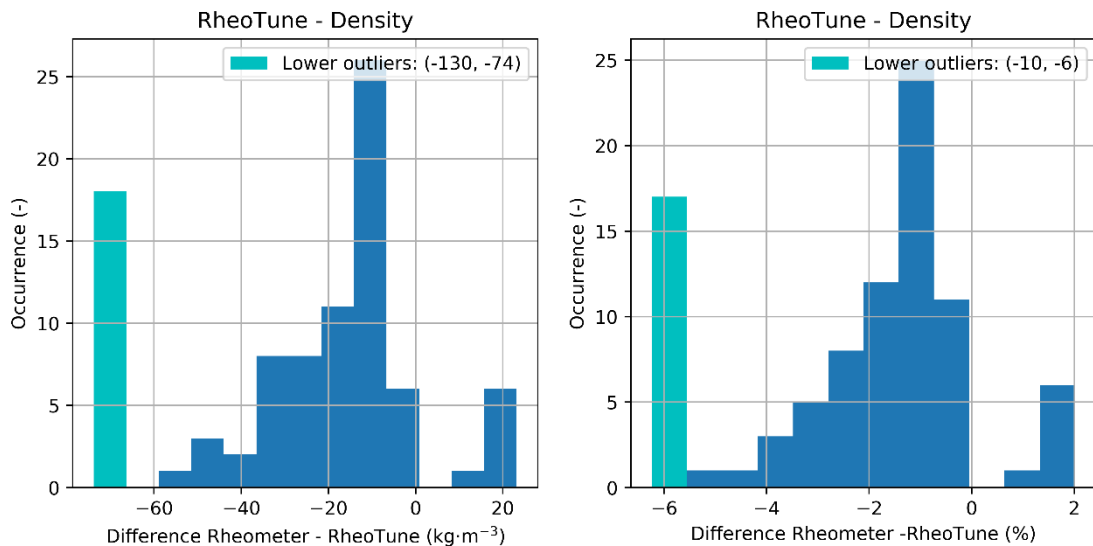


Figure 3-34: Distribution of difference between reference and RheoTune density, expressed as absolute values (left-hand side) and relative (right-hand side).

Table 3.5- Summarized RheoTune differences for density reference testing.

Port	Target Density (g·cm ⁻³)	Rest Time (hours)	Density (kg·m ⁻³) ¹	Difference with RheoTune (kg·m ⁻³) ¹
Hamburg	1.15	24	1150.5 ± 0.8	-5.2 ± 13.0
Hamburg	1.20	24	1198.3 ± 2.1	19.8 ± 3.6
Rotterdam	1.15	24	1153.9 ± 1.2	-9.8 ± 5.1
Rotterdam	1.15	24	1153.9 ± 1.2	-16.9 ± 8.5
Rotterdam	1.15	72	1151.0 ± 2.3	-14.2 ± 3.0
Rotterdam	1.15	72	1151.0 ± 2.3	-14.0 ± 8.5
Rotterdam	1.25	24	1265.8 ± 4.4	-39.8 ± 10.0
Rotterdam	1.25	24	1265.8 ± 4.4	-33.0 ± 7.3
Rotterdam	1.25	72	1254.8 ± 6.7	-86.7 ± 13.0
Rotterdam	1.25	72	1254.8 ± 6.7	-97.0 ± 19.2

Note 1) The plus/minus values refer to one standard deviation.

3.6.9 Parameter Plots

Figure 3-26 shows the RheoTune parameters versus the reference density and undrained shear strength. The data has been grouped according to location and density. This type of grouping was chosen because the variation in reference parameter per resting time and individual test is relatively small. The light-coloured symbols are the values for each sub sample, the darker coloured symbols are the median of each test type. The purpose of these figures is to visualize any relation, although no curves have been fitted through the data.

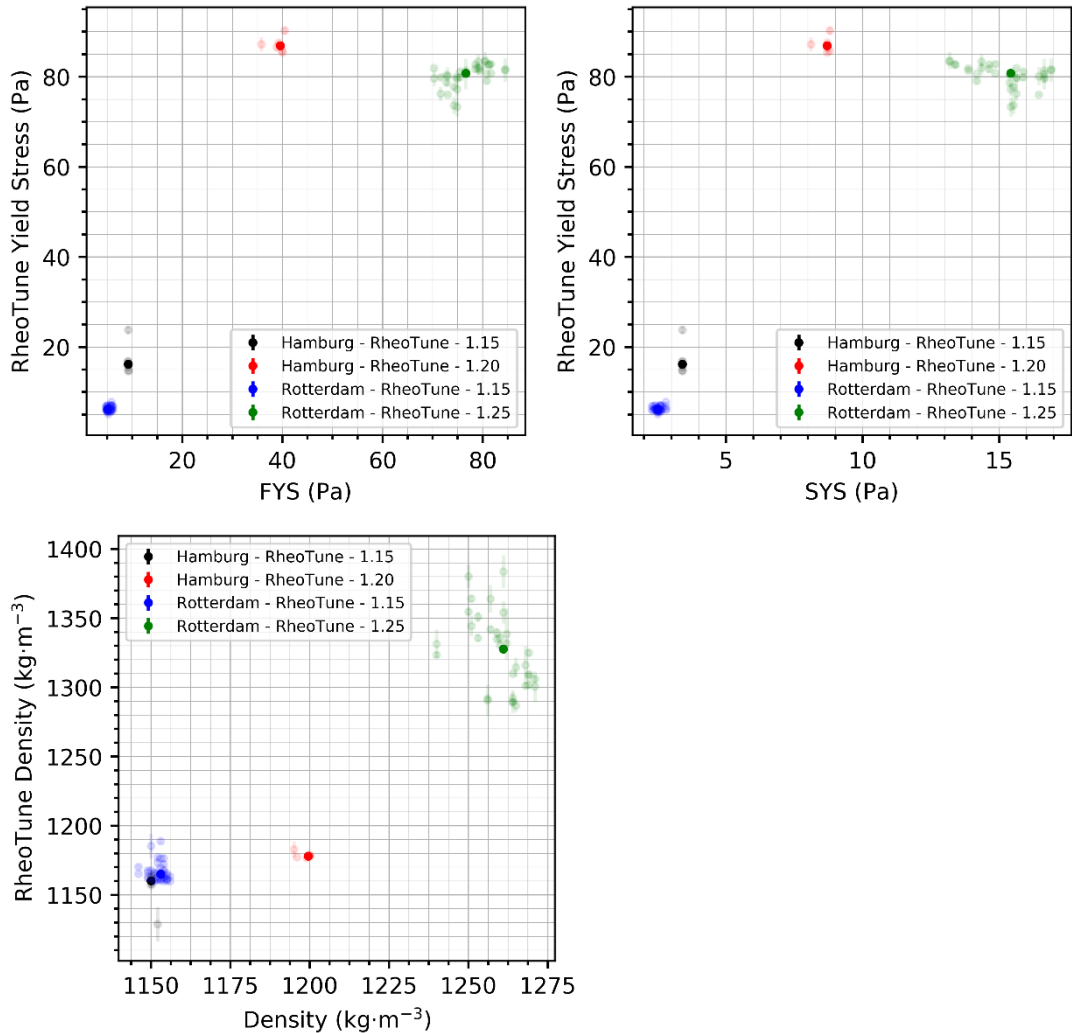


Figure 3-35: RheoTune parameter values versus reference FYS and SYS and density.

3.7 Comments on Test Results

Based on the results, the general conclusions are:

- The Rheotune gives reliable results for density and yield strength profiles for Port of Rotterdam mud in most cases. The accuracy of the density profiles (most values within 2%) is higher than the accuracy of the strength profiles (most values within 20%).
- The Graviprobe does not provide density profiles, only yield strength profiles. The accuracy of these strength profiles is generally a bit less (most values within 50%).

More detailed conclusions and discussion follow below.

RheoTune comments:

- It appears that, under the employed test conditions, despite following the correct calibration procedure, the RheoTune does not give correct depth. Clogging of the pressure sensor by mud seems the obvious reason, as trials in pure water did not show this behaviour. Pressure correction can be done in RheoEdit.
- Usually, there is a significant difference between upward and downward stroke. This is likely caused by material sticking in-between the tuning fork, resulting in erroneous measurements in the upward stroke.
- The yield stress measurements on the port of Hamburg mud deviate significantly more from the undrained shear strength reference measurements when compared to the results on the Port of Rotterdam mud. This indicates that a location-specific calibration may be required, depending on the mud composition.
- Density measurements on the Port of Rotterdam mud with $1.25 \text{ g}\cdot\text{cm}^{-3}$ density and 72 hours rest, deviate significantly more when compared to other tests on the Port of Rotterdam mud, although near the end of the stroke the two measurements show better agreement. Sediment from the top layer adhering to the tuning fork could be a possible cause.

Comments for GraviProbe tests:

- For the test on Port of Rotterdam mud, density of $1.25 \text{ g}\cdot\text{cm}^{-3}$, 24 hours of rest, the Beeker sampler was not available, therefore samples were taken with a syringe with a 1.5 m long tube connected to it. However, the measurement values derived from these samples are consistent with the other measurements.
- Port of Rotterdam mud, density of $1.15 \text{ g}\cdot\text{cm}^{-3}$, 72 hours rest, the second deployment was not processed by the software due to an unknown error.
- During processing the point of impact was manually selected. It may be difficult to select point of impact if the mudline depth is not accurately known (i.e. in the field, where mudline depth is the uncertainty). This may lead to added depth uncertainty in the measurement results.
- The sign of the deceleration upon impact in the sand layer is inconsistent; for some tests the probe appears to accelerate instead of stopping, as shown for example in Port of Rotterdam test, density of $1.15 \text{ g}\cdot\text{cm}^{-3}$, 24 hours rest. Although this does not affect measurements inside the mud layer directly, it does raise concern regarding robustness of the probe measurements in layered soils.
- Apart from accuracy, the trend with increasing depth indicated by the GraviProbe is not always consistent with the trend shown by the reference measurements. For example, for the Port of Rotterdam test, at density $1.25 \text{ g}\cdot\text{cm}^{-3}$, 24 hours rest, the reference measurements show a decreasing trend, while the GraviProbe shows an increasing trend.
- The density of the mud determines the buoyancy forces on the GraviProbe and does also influence the deceleration in the mud. It is unclear how this is handled in the GraviProbe software, where the density is no input.

Comments for the Beeker sampler:

- The recovery was typically less than the sample penetration. This may be the result of (a) compression (although unlikely due to incompressibility of the mud), (b) pushing the first section of sample out in front of sampler (under-sampling) or (c) loss of sample during retrieval. The exact reason is unclear, although under-sampling may be the most likely.

4 WP3: Far-field modelling tools

4.1 Introduction

Sediment dynamics and specifically, the siltation of mud, in the ports and access channels of the Port of Rotterdam is of great interest to both the Port Authorities and to Rijkswaterstaat. Both are responsible for the maintenance of the harbours and access channels. The amount of siltation determines the frequency and amount of maintenance dredging to maintain navigable depth. However, significant siltation can occur in a short time, even between field surveys, as a result of the transport and deposition of fluid mud layers. The mud supply towards the Maasvlakte harbours is thought to be mainly of marine origin, driven by near-bed landward transport. However, the mud supply towards some harbours further upstream such as Botlek, is thought to be mainly of fluvial origin. The estuarine turbidity maximum (ETM) plays a complex role in trapping fluvial sediments near the front of the salt wedge (de Nijs et al., 2010).

In addition to field surveys, numerical models can be an important tool for port maintenance. The simulation and determination of water levels, flow rates and salinity through models is already done in practice for the Rhine-Meuse estuary, but not yet for fine sediment dynamics. One of the reasons is that, in the past sediment models, especially fine cohesive sediment models were less developed and still very computationally expensive. Recently these limitations have been largely overcome, although cohesive sediment models remain complex and appropriate calibration data is often lacking.

Table 4.1 gives an overview of most relevant processes for mud transport and which are or aren't included in the models discussed in this chapter. There are three models, one is a hydrodynamic base model (D3D), another a mud transport model coupled off-line to the hydrodynamic model (WAQ) and another a mud transport mode fully integrated with the hydrodynamic model (D3D-SED).

Table 4.1 Overview of processes in applied hydrodynamic and sediment transport models

Process	D3D	WAQ	SED
Currents	X		
Waves	X		
Salinity	X		
sediment transport		X	X
settling		X	X
deposition		X	X
resuspension		X	X
sediment-induced buoyancy			X
Flocculation dynamics			
fluid mud rheology			
morphology			

Both sediment models include suspended sediment transport. The difference between the on- and off-line sediment transport model is that the first include the effect of suspended sediment on the fluid density. This is an essential feature for fluid mud transport, as fluid mud may not only be transported by drag forces of the tidal current, but also by pressure gradients induced by sediment-induced density gradients. Therefore, the off-line option is only suitable for low-concentrated suspended sediment transport (typically < 1 g/l), whereas the on-line option may also be suitable for fluid mud transport. The advantage of the off-line option is that it is computationally more efficient and allows the computation of many scenarios with many different sediment fractions.

However, sediment-induced buoyancy is not the only requirement to compute fluid mud transport. Another requirement is model resolution, both in vertical and horizontal direction. If present, fluid mud is confined near the bed with a strong concentration and density gradients at the interface. Also, in horizontal direction strong gradients may exist, notably if fluid mud is locally generated by water injection dredging. Hence the need for near-field models such as discussed in Chapter 5. In the present chapter we discuss the far-field transport, requiring less horizontal resolution. Vertical resolution remains an issue, which is addressed with a sensitivity analysis.

At high fluid-mud concentration, not only the buoyancy effect is relevant, but also the effect on viscosity and yield stress. This rheological behaviour may reduce fluid mud transport, as a higher viscosity or even a yield stress implies more resistance to flow. This effect is not included in the present models, so computed dispersion is representative for fluid mud with low density and gives an upper limit for transport. Fluid mud with a high density may remain more confined and disperse less.

Two more processes are excluded, i.e. flocculation dynamics and morphology. The effect of flocculation itself is included via the settling velocity, which for the various fractions is set at a value representative for the state of flocculation as observed in the Rotterdam harbour area for average conditions. However, the dynamics of flocculation, i.e. the growth and break-up of flocs is not included. Such dynamics are most relevant in the near-field where conditions quickly change, but the near-field is excluded from this chapter. In the far-field, the use of fixed values for settling velocity representative for average conditions implies that mud transport in non-average conditions is less accurately modelled.

Finally, some remarks on morphology. Although this can be easily included in the coupled model, bed level changes during the simulation period (days to weeks) are very small compared to water depth. Hence there is hardly any effect of these bed level changes on the hydrodynamics and this effect has therefore been neglected.

4.1.1 Objective of the modelling work in PRISMA

Within PRISMA 1 the main objectives of the modelling work were to:

- Use the sediment transport model developed in a TKI and Port of Rotterdam funded project (Cronin *et al.*, 2019) to simulate where high density plumes from WID would disperse and deposit, both locally within the harbour and over a wider area.
- To assess model performance of high-density sediment transport.
- To determine return flows of the WID plume.
- To test the implementation of sediment pits.
- To assess WID for different hydrodynamic conditions i.e. under what tidal conditions does the sediment leave the system or remain within the system i.e. what is more efficient.

Given the objectives outlined above, the modelling work will contribute insights into WID plume behaviour that will improve efficiency in operations and potentially reduce return flow. Plume behaviour may be both active (driven by its buoyancy, also called density current) and passive (advection and dispersion by ambient currents and particle settling). In this chapter we consider both types of plumes, as the fluid mud properties from the near-field model that is used as input for the far-field model is still at a density that sediment-induced buoyancy should be considered. However, because of sedimentation and mixing with ambient the plume concentration decreased until it becomes a passive plume that gradually dispersed further by ambient currents.

4.1.2 Background of the existing models

In the 2018-2019 HBR TKI project, a first step was made towards the development of a high-resolution fine sediment/mud transport model of the Maasmond and port basins. The OSR-model (Operationeel Stromingsmodel Rotterdam) was used as the basis for setting up a 3D model for mud dynamics. The OSR model from the Port of Rotterdam (PoR) is used for calculating flow velocities and salinity concentrations for operational use in the Rhine Meuse Delta and runs with the SIMONA software¹. The model system consists of two model components:

- 1 The 2DH model (OSR-Harbour), which covers the full Rhine Meuse Delta and a large part of the ocean (see Figure 4-1, dark blue grid);
- 2 The 3D model (OSR-NSC), which covers a smaller domain (see Figure 4-1, light blue grid).

To save computational time, the OSR-Harbour model is used to generate the boundary conditions for the OSR-NSC model, with which more detailed 3D flow computations can be carried out. There are two versions of the NSC-model, a model with a coarse schematization for fast computations (NSC-coarse, with grid resolution identical to the Harbour model) and a model with a finer schematization for more detailed computations (NSC-fine, with grid resolution 3x as fine with the Harbour model). Further details about the models can be found in Kranenburg (2015a, 2015b) and Kranenburg and Schreuder (2015).

¹ Release Notes Major Release SIMONA 2012 and Release Notes Major Release SIMONA 2014; <http://www.helpdeskwater.nl/onderwerpen/applicaties-modellen/>



Figure 4-1 Overview of the domains from the OSR model. In dark blue the large domain (Harbour model) and in light blue the smaller domain (NSC).

4.1.3 Development of TKI HBR model

In order to calculate the mud dynamics in the harbour area of the Rhine Meuse Delta, a chain of models was necessary to capture the essential features of sediment dynamics over both shorter (tidal) and longer (monthly) time periods. The model chain was setup in three interconnected parts as visualized in the flow chart below in Figure 4-2.

The OSR-NSC (coarse) model was converted from SIMONA to Delft3D and hydrodynamic conditions, including wave effects were calculated for a full month. This hydrodynamic model was used as (offline) input to a Delft3D-WAQ model. More details can be found in Cronin et al., (2019).

A Delft3D-WAQ model is suitable for computing long term sediment dynamics and therefore allows the simulated sediment distribution in the water column and in the bed to reach a dynamic equilibrium. This is necessary when first spinning up a model from an empty bed. Sediment bed concentrations require a longer spin-up time than in the water column and so reaching this equilibrium with a fully coupled Delft3D sediment model was too computationally expensive in this case. However, Delft3D-WAQ does not include sediment-induced density effects, nor does it update the bed as a result of morphological changes and is therefore not suitable for modelling fluid mud dynamics. Instead, the WAQ model was valuable to more efficiently generate initial conditions for the Delft3D model, for sediment concentrations in the water column and in the bed for the simulation period with and without the effects of dredging.

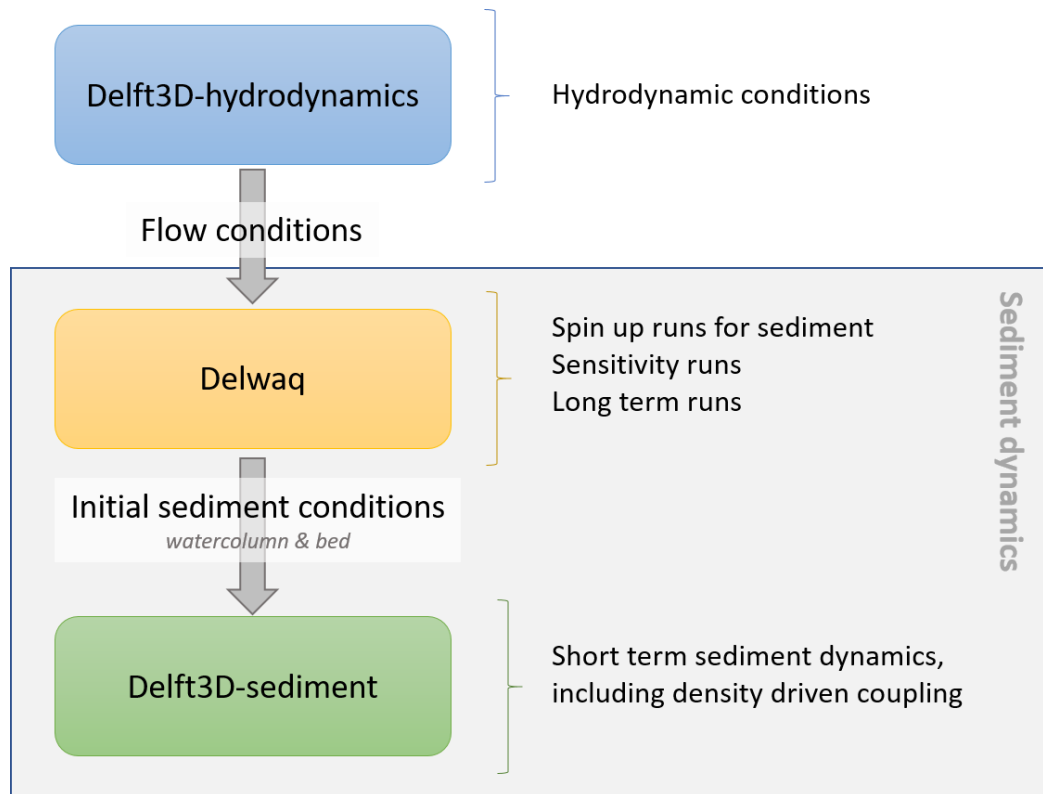


Figure 4-2 Model structure for computing mud dynamics.

A sensitivity study was also performed of the critical parameter influencing fine sediment transport in and around the harbour basins in the Port of Rotterdam for the simulation period. These parameters included the settling velocity of the fine sediment fractions (including primary particles, micro- and macro-flocs), the efficiency at which sediment can be deposited to the bed, the dominance of different processes in the water column and on the bed and the impact of dredging and dumping. For more detail on the results of these sensitivity tests see Cronin *et al.*, (2019).

Very little calibration data was available to find the optimum set of parameters. The Delft3D-WAQ model could only be qualitatively compared with previous studies and the annual dredge volumes that end up in the Verdiepte Loswal disposal location from different harbour basins, which gives an indication if the amount being dredged, and therefore sedimentation rates is captured. The modelled surface and near-bed suspended sediment concentrations are in the right order of magnitude when comparing to previous studies. The estimated total amount of dredged material being relocated to the Verdiepte Loswal (3 megatons per year) is overestimated in the model although this value is based on an extrapolation of model results for the month of May when calmer conditions results in greater sedimentation and so this annual assumption is probably overestimated. See Section 4.2 for a comparison between observed and computed dredging volumes per harbour area.

The Delft3D-FLOW model was rerun with the sediment module activated. To prevent a long spin up time, the model uses the sediment concentrations in both the water column and the bed from the Delft3D-WAQ spin-up runs described above. Settings and results were compared with the Delft3D-WAQ model. In general, the suspended sediment concentrations predicted by the Delft3D-FLOW model are lower than in the Delft3D-WAQ model. Test simulations were also performed with and without density coupling, however as concentrations in the water column were low, the effect of density coupling was not apparent. Based on a comparison between model scenarios with and without sediment-induced density

effects, it appears that under typical conditions natural fluid mud formation is limited. This conclusion still needs confirmation from field observations such as presented in Chapter 2, as limitations in model resolution and numerical accuracy may have suppressed fluid mud formation in the model.

In a scenario in which a local fluid mud layer (e.g. as created by water injection dredging) is imposed to the model as initial condition, a fast gravity-driven spreading of this layer was computed. Fluid mud propagated in both landward and seaward direction as a gravity-driven flow and as a result became thinner. Spreading continued by tidal advection and dispersion by vertical mixing. The fluid mud layer did not persist more than a tidal cycle (12.5h). Further investigations on the sensitivity of model resolution, numerical accuracy and assumed rheological properties of the fluid mud layer were recommended. In the next section this is further discussed based on additional WID scenarios with different locations, production rate and duration and phasing with respect to the tide.

4.2 Model set-up

4.2.1.1 Delft3D model

The Delft3D sed-online model used in this project was based on the model set up and settings from the Delft3D sed-online model in the previous HBR TKI project as described in Section 4.1 (Cronin et al., 2019), run for the same period in May 2016.

No additional calibration of settings was performed with respect to sediment transport parameters with Delft3D-WAQ as no additional field data were available since the initial set-up and calibration. However, a more comprehensive assessment of the model settings was done by comparison with weekly dredge volumes (converted to kton) from the Port of Rotterdam. The amount of sedimentation in the specific dredge areas as shown in Figure 4-3 was extracted from the Delft3D model. With this additional breakdown it is easier to see in which areas the model captures sedimentation rates well and where not. For example, dredge volumes are slightly underestimated in Maasvlakte 1 and underestimated further upstream in Botlek (Table 4-1).

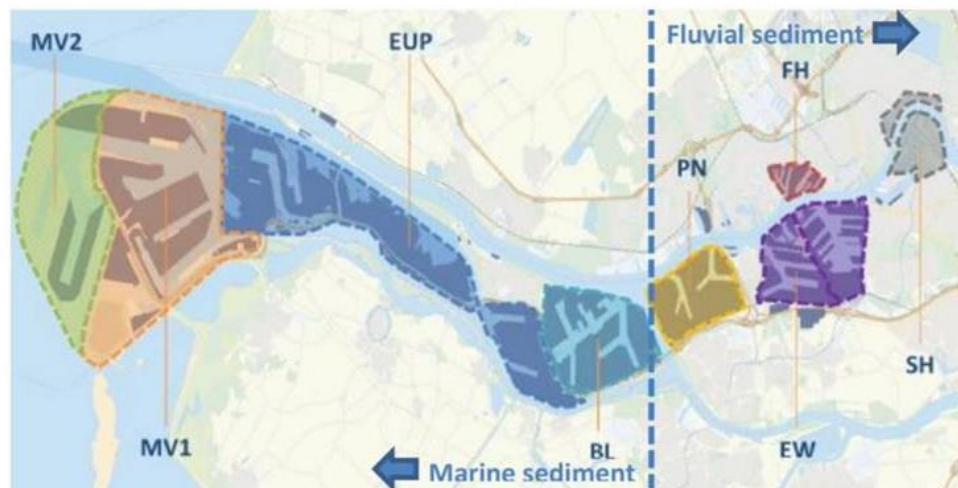


Figure 4-3 Map of the port basins from Kirichek et al., 2018: Maasvlakte II (MV2), Maasvlakte I (MV1), Europoort (EUP), Botlek (BL), Pernis (PN), Eem-Waalhaven (EW), Fruithavens (FH) and Stadhavens (SH).

Table 4-1 Simulated (Delft3D) compared to estimated dredge volumes per harbour area Basin Name	Dredged in reality (kton)	Dredged in the model (kton)	Difference (kton) Minus indicates model overestimation
Maasvlakte 2	0	0.45	-0.45
Maasvlakte 1	112	85	27
Europoort	25	5	20
Botlek	64	17	47
Pernis	34	5	29
Eem-Waalhaven	25	8	17
Stadhavens	0.3	1	-0.7

This shows that with the current model settings, sedimentation rates are suitable for continuation of this study on far-field sediment dispersion, particularly in the area around Maasvlakte 1 where the water injection pilots are to take place. Further east towards Botlek sedimentation is underestimated so this should be taken into account for any studies there.

4.2.2 Water Injection Dredging Investigations

4.2.2.1 Set-up

The general model setup is described in Section 4.1 and further details can be found in Cronin et al., (2019). In this section we describe how water injection dredging (WID) was implemented in the far-field model and how the generated sediment plume dispersed. The model period of the HBR TKI model (Cronin et al., 2019) is extended by 1 week to ensure that the model runs for a sufficient time once the WID has completed. The total simulation period is now 15 days from 01-05-2016 until 15-05-2016.

As described in Section 1.2, in reality WID is carried out by fluidizing the fine sediment bed and creating a gravity current that is transported as a dynamic plume. When the density of the plume is low enough that particles are transported in suspension due to advection and dispersion processes a far-field model such as Delft3D can be used to determine where the plume settles and the resulting sediment footprint. Typical dredging scenarios, such as dredging with a hopper dredger are implemented in Delft3D by removal of mass from the sediment bed and relocation of the sediment to another part of the model domain. WID however involves injecting water into the bed to create an in-situ fluid mud layer. This fluidization process is not a feature of Delft3D and so the creation of a fluid mud layer needs to be mimicked in the model through other methods. The sections below describe numerical experiments to test the best approach for mimicking WID in Delft3D.

4.2.2.2 Implementation of WID in the Delft3D model

In order to explore the best way of simulating water injection dredging in the model, a step-wise approach was used.

For the first model experiments, the initial SSC expected in a plume resulting from WID was prescribed as a sediment patch, based on observations of settling-consolidation at and near the sediment trap after a WID pilot. Density coupling was activated in the model. Therefore, the high concentration of suspended sediment resulting from the WID plume caused sediment-induced density effects. This approach was used for initial testing of the plume behaviour, to see how modelled plume behaved in comparison to what was observed in the pilots, as well

as to check the limits in model settings. This was particularly important to assess the model limits with respect to sediment concentrations and the transition between turbulent and laminar flow (which may occur in fluid mud with a high density because of increased viscosity or yield stress not included in the model).

Using the effective Reynolds number generated by the hydrodynamic model, an analysis was undertaken to determine at which sediment concentrations the density current remains turbulent (Appendix C). Using the sediment concentrations prescribed with an initial patch of sediment the active sediment plume was estimated to be below or near the turbulent to laminar transition. Although the standard Delft3D code used here is not suitable to model laminar mud flows (rheology not included), first analyses to test behaviour with an initial sediment patch are described briefly below.

In the second approach sediment release is based on the actual production rate of the WID vessel and so contains detail on the position and timing of fluid mud generation. The analysis with the effective Reynolds numbers indicated that the density current would remain turbulent (see Appendix C1). As this was the method implemented for further tests, only results using this method are described in Chapter 5.

Initial sediment patch

As a first test on how accurately WID could be simulated in the model, the simulations were initialized with a localised patch of very high SSC values in the near bed layers to represent the fluid mud formation that occurs as a result of WID in Calandkanaal (Figure 4-4).

- Kirichek and Rutgers, (2020) investigated the fluidization of mud during the WID pilot in the Calandkanaal in the autumn of 2018. It was observed that two weeks after the WID pilot a layer of two meters of (fluid) mud had developed within the sediment trap with average density of 1150 to 1200 kg/m³. The observed density of 1200 kg/m³ translates to an initial concentration of ~100 kg/m³ for each of the three sediment fractions in the model. In (initial) experimental runs the grid cells of near bed layers (up to a height of ~2m) within the bounds of the WID area were initialized with an SSC of ~300 kg/m³. These simulations showed an unrealistically fast spreading during the first hours. The plume had spread up to 10 km for the WID area with concentration above 10 kg/m³. The rapid spreading is caused by a density gradient and the absence of rheological processes in Delft3D, because at high concentrations the WID fluid mud will have substantially higher viscosity than water and may also have a yield stress which will influence dispersion.
- Henceforth, we initialized the sediment patch with initial concentrations of 37.5, 75 and 150 kg/m³ corresponding to a density of ~1048, 1070 and 1116 kg/m³ respectively. With these initial concentrations, it was certain that the sediment plume could be modelled as turbulent flow. Applying these initial concentrations, a total sediment load of 65, 81 and 125 kTon is released in the model. This is substantially lower than with SSC of 300 kg/m³, but would reflect 36, 45 and 69 hours of WID using a production rate of 500 kg/s. Although the WID plume is represented by a lower initial SSC, initial plume spreading still remained unrealistic, compared to what was observed during the WID pilots.

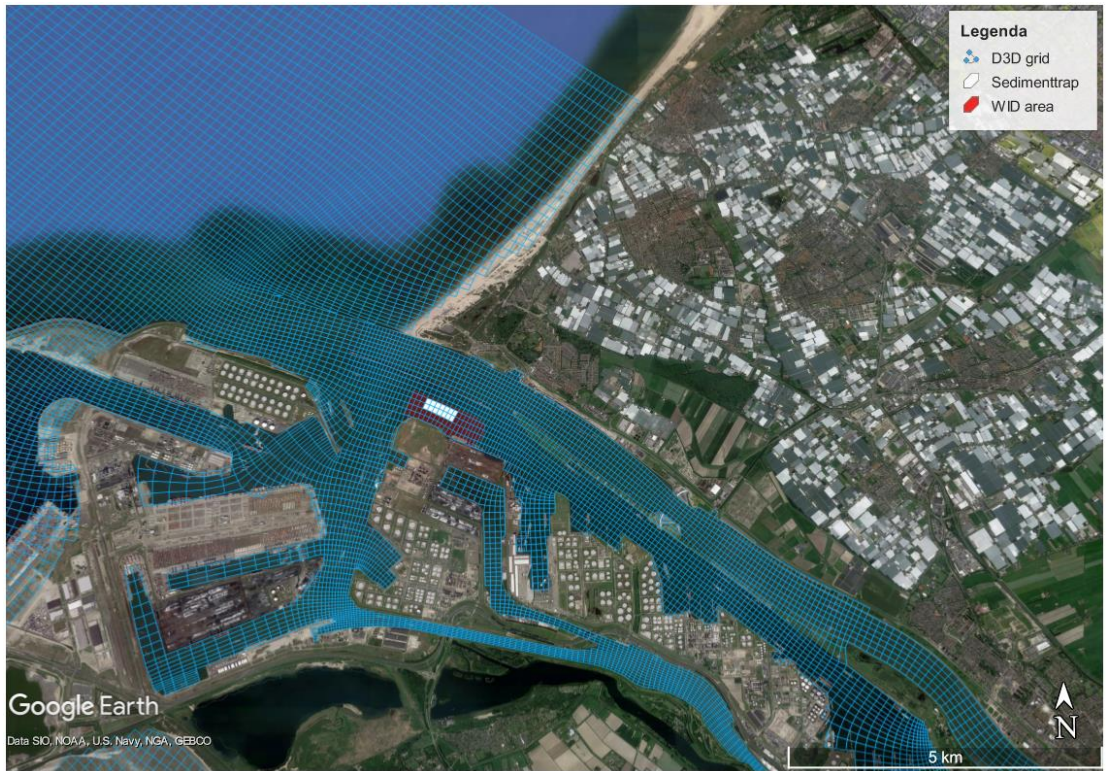


Figure 4-4 WID area (red) and sediment trap (white).

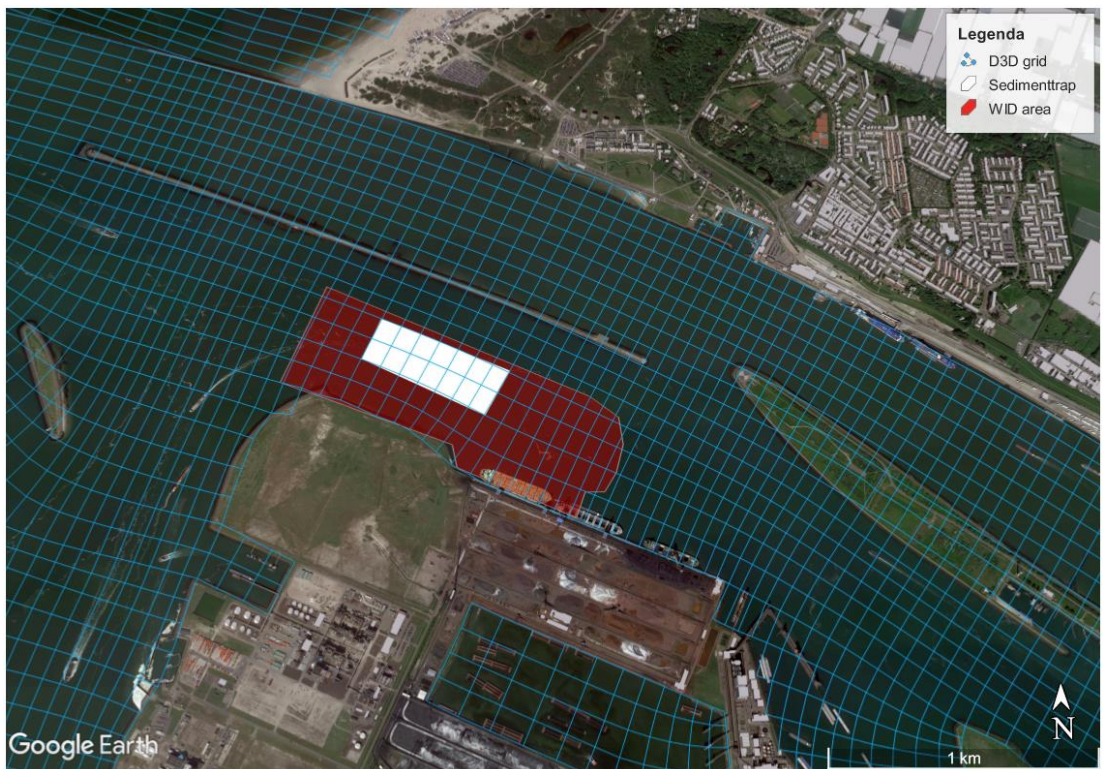


Figure 4-5 WID area (red) and sediment trap (white).

Sediment discharges

An alternative method is to gradually release sediment throughout the simulation period. This has the advantage that sediment is not released at once. Furthermore, it enables a more realistic link to be made with a WID campaign and to directly relate sediment release to the production rate of the WID vessel.

Sediment was released over a period of 7 days within the WID area (see Figure 4-4). The WID area has been divided in seven sub areas (see Figure 4-7). For each day sediment is released between 9:00 AM and 17:00 PM, representing a full work day in one of these sub areas. Release of sediment is implemented in the model as a discharge, for which a discharge (m^3/s) and a concentration (kg/m^3) must be described. The values for discharge, sediment concentration and plume height in the water column were determined in the near-field modelling carried out in Work Package 4 (WP4) as described in Chapter 5. This information was then fed into the far-field model. Observations also indicated that height of a sediment plume after several tracks of the WID vessel over the same line is between 2 – 3m. Hence, we divided the discharge between the lower two sigma layers to have an approximate initial plume height of 2m. The prescribed sediment concentration represents the amount of sediment that is being stirred up by the WID vessels. Literature indicates that the production rate of WID vessels vary between 200 – 800 kg/s. It was chosen not to prescribe a momentum flux as initial experiments showed that the model is capable of reproducing density driven flow.

4.2.2.3 Implementation of sediment trap

The sediment trap is implemented by deepening the bathymetry of the model at the location of the trap. In reality, the depth of the trap is -1 – -1.3m relative to the channel bed. However, the sigma-layers are known to have a smoothing effect when it comes to depth representation. Therefore, we exaggerated the depth of the trap in the model by lowering the model bed by 2m. The actual area of the sediment trap is 600x120m but in the model has been slightly adapted in order to cover 2 grid cells in width. This resolution is only sufficient for modelling far-field spreading, for the near field a local more refined model is used (see Chapter 5).

4.2.3 Scenarios

To test the representation of WID in the model two numerical experiments were set-up.

- The first experiment is focussed on investigating the moment of sediment release with respect to the tidal phasing. This is done in order to assess the impact tidal phasing has on the plume dispersion and sediment deposition into the trap. These simulations are short in duration (3 days) and so only reflect initial deposition patterns.
- The second experiment explores plume spreading and sedimentation patterns over a full week of WID. This is in order to understand the cumulative impacts of continuous WID over several days. The simulation period was three weeks long, so that the impact of WID could also be investigated during the two weeks after WID had stopped.

4.2.3.1 Type 1: Simulating single HW or LW release

This experiment is setup to explore the effect of the tidal phasing on the (initial) plume spreading.

Two scenarios were investigated, namely: one in which sediment is released between HW – HW+8h and a second scenario in which sediment is released between LW – LW+8 (flood) (Figure 4-6).

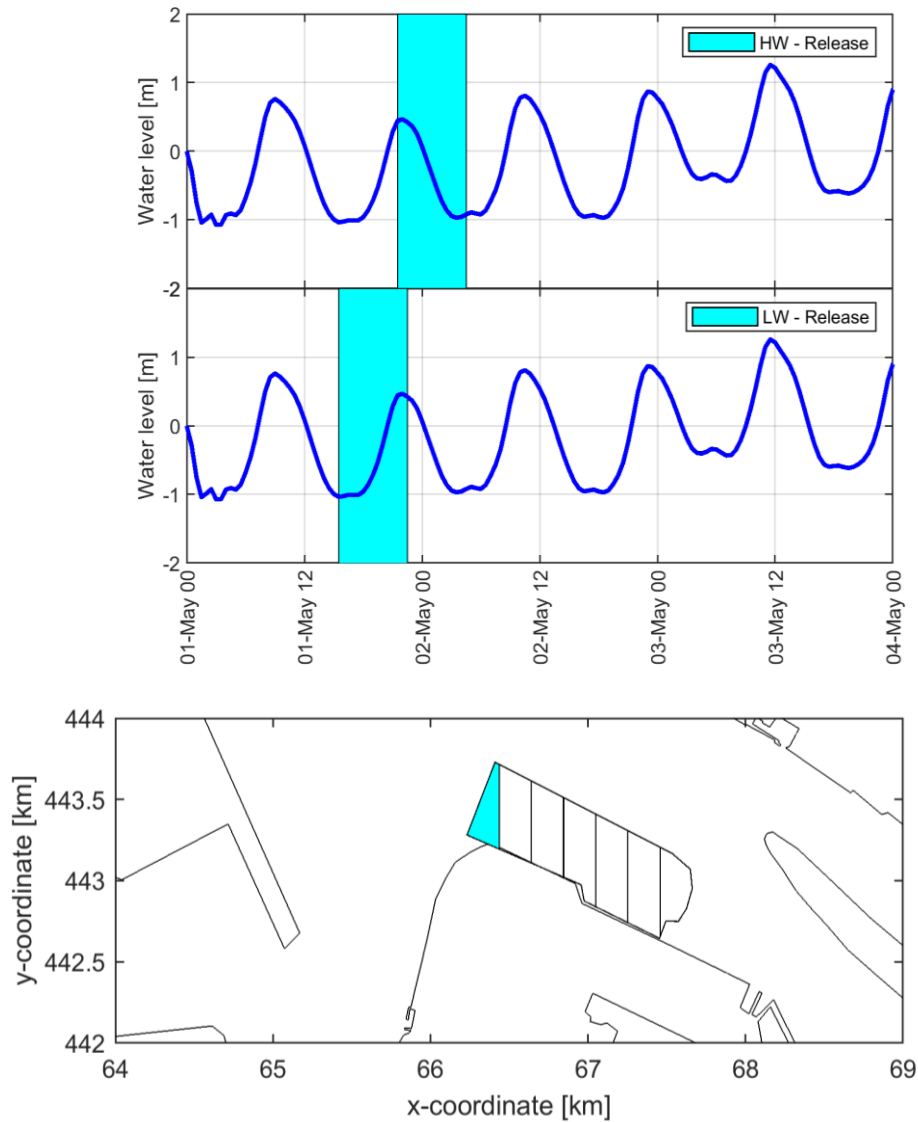


Figure 4-6 Water levels near the sediment trap. Cyan boxes indicate the period in which WID is simulated for the HW and LW release experiment

Both experiments represent one single day of WID (8h). For both experiments, sediment release is implemented in the first WID sub area of Calandkanaal (CK), see Figure 42 above. This sub area covers six grid cells, which implies that sediment is released in 12 cells. Release of sediment is equally divided over the grid cells for the period of release. As a result, sediment is released for a period of circa 1.2h. For both scenarios a production rate of 500 kg/s is assumed. Therefore, over a period of 8 hours, 14.4 kTon of sediment is released in the model. It should be noted that in reality this sediment would be stirred up from the bed, whereas in the model it is implemented as a discharge of additional sediment into the system.

4.2.3.2 Type 2: Week of water injection dredging

The main goal of this experiment is to investigate the plume spreading, sedimentation and return flow for and after one week of WID. This experiment differs from the previous experiment since the sediment plume, erosion and sedimentation pattern are affected by the cumulative effect of multiple days of WID. In addition, the phasing of the tide changes in respect to the moment of release throughout the week. On the first day the WID release starts (9:00 AM) at HW and at the last day LW. Sediment is released between 9:00 AM and 17:00 PM, representing

a full work day, in one of these sub areas. For this numerical experiment three scenarios are evaluated with different production rates between 200 and 800 kg/s (Table 4-2).

Table 4-2 Overview of the production rate and total released sediment per scenario.

Scenario:	WID production flux [kg/s]	Total WID input [kTon]
1	500	120
2	200	48
3	800	192

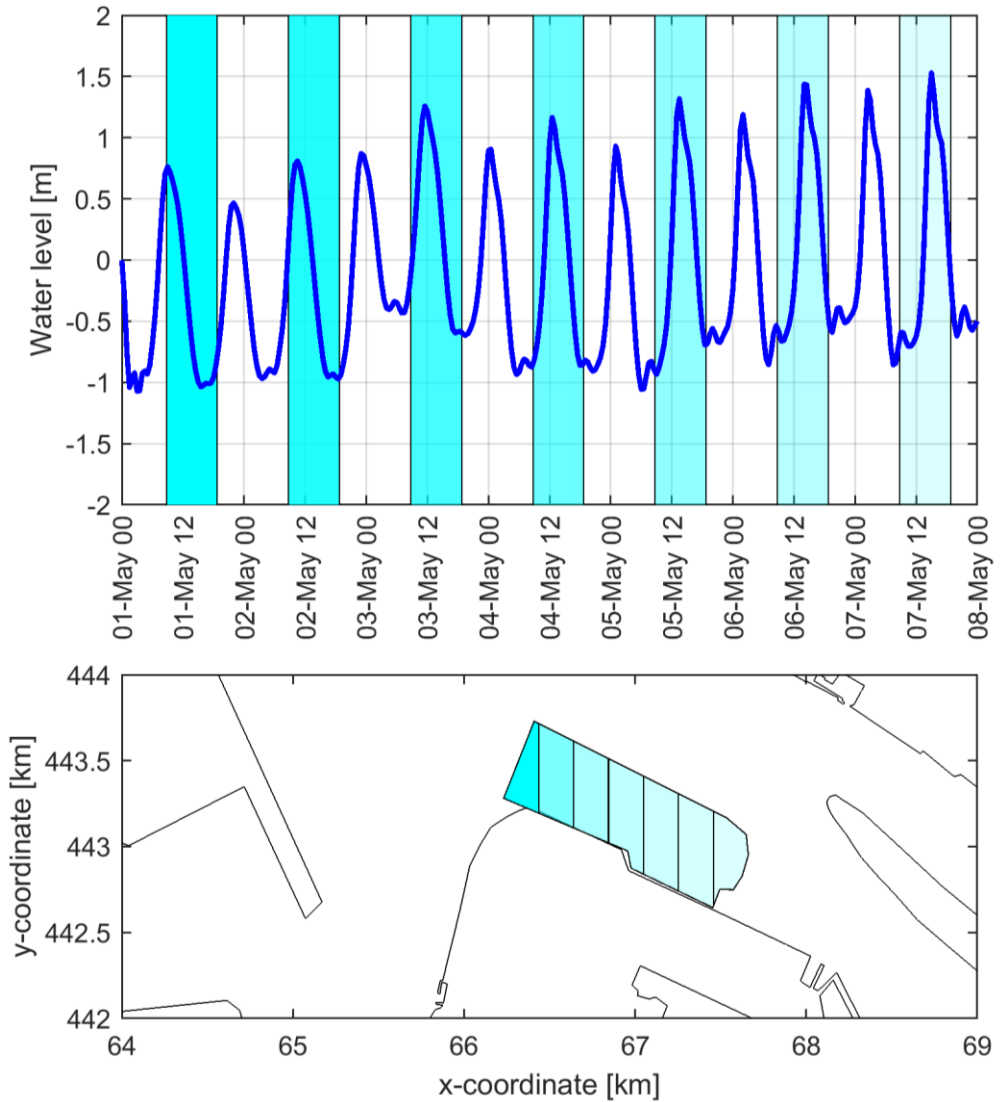


Figure 4-7 **Top**) Water level variations near the sediment trap. The blue boxes indicate the WID period and correspond to a sub area where WID is applied. **Bottom**) Overview of the WID sub areas.

4.3 Insights gained from model results

4.3.1 Hydrodynamics near the WID area.

The following section provides a brief introduction to the hydrodynamic conditions near the WID area, such as the residual currents, bed shear stresses and vertical mixing. This is done to understand the transport mechanisms around the WID area and subsequent dispersion of the sediment plume.

- Figure 4-8 and Figure 4-9 below shows the residual flow vectors near the surface and bottom respectively, overlain on the tide averaged bed shear stresses. The direction and magnitude of the residual vectors slightly deviated between individual tidal cycles, but the overall patterns remained the same. The magnitude of the residual velocities near the bottom are small compared to the surface and are often not oriented in the same direction because of salinity stratification. In the Nieuwe Waterweg, there is a strong eastward (flood) directed near bed residual current. This explains why the sediment import from sea is so high. At the surface a strong seaward westward (ebb) directed residual surface current occurs.
- At Beerkanaal, the surface velocities are predominantly directed west, except for the northern reach. Here the residual velocities are directed more more to the north. Near bed velocities are weak and more variable with no clear overall direction.
- For the Calandkanaal, the surface residual velocities are flood directed, but the near-bed residual velocities are more complex: at the entrance they are directed east, whereas at the back they are directed west, resulting in a convergence zone in Calandkanaal.
- The tide averaged bed shear stresses are low in the Beerkanaal and Calandkanaal compared to the Nieuwe Waterweg. Less sedimentation will occur in areas of higher bed shear stresses.
- Figure 4-10 shows the mean vertical eddy diffusivity for the water column averaged over a tidal cycle. The vertical eddy diffusivity results from the hydrodynamics simulations and drives mixing of (suspended) sediment in the vertical. Examining where the eddy diffusivity is high helps to identify locations where suspended sediment is mixed vertically in the water column. Potential areas with significant vertical mixing are the Nieuwe Waterweg and the area west of the sediment trap, at the junction with Beerkanaal.

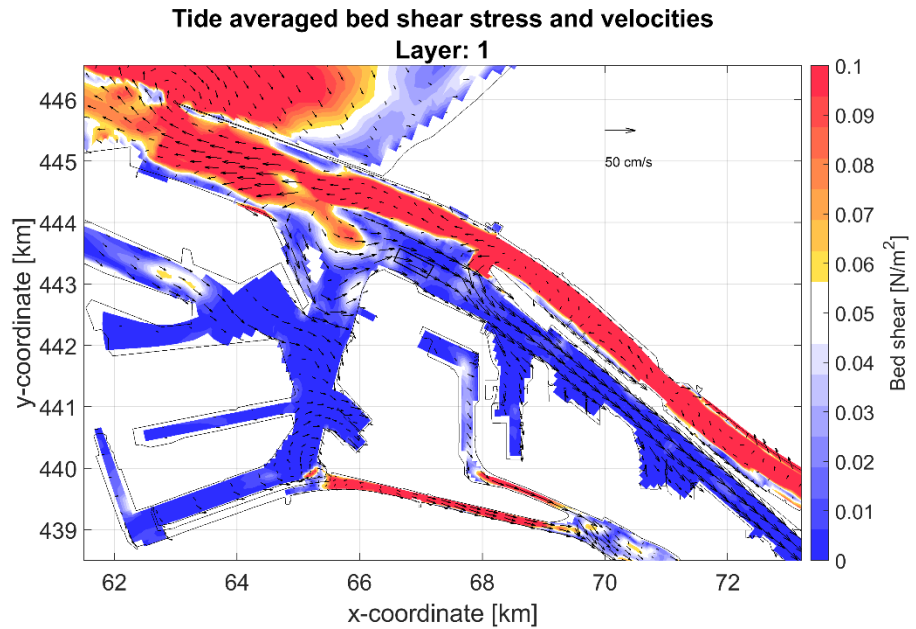


Figure 4-8 Residual flow vectors for layer 1 (surface) and the tide averaged bed shear stress is indicated by the colour gradient, both have been calculated for a single tidal cycle

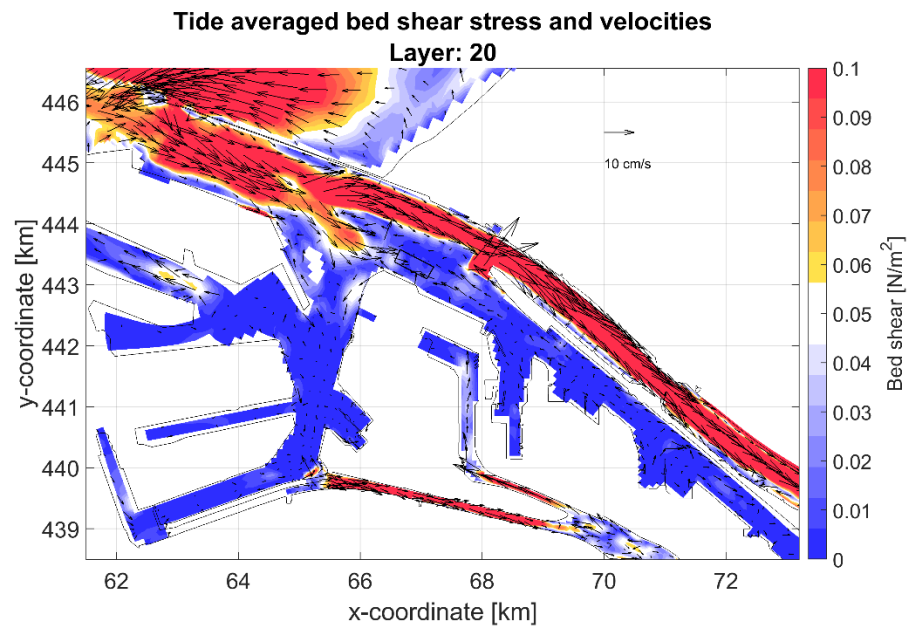


Figure 4-9 Residual flow vectors for layer 20 (near bottom) and the tide averaged bed shear stress is indicated by the colour gradient, both have been calculated for a single tidal cycle .

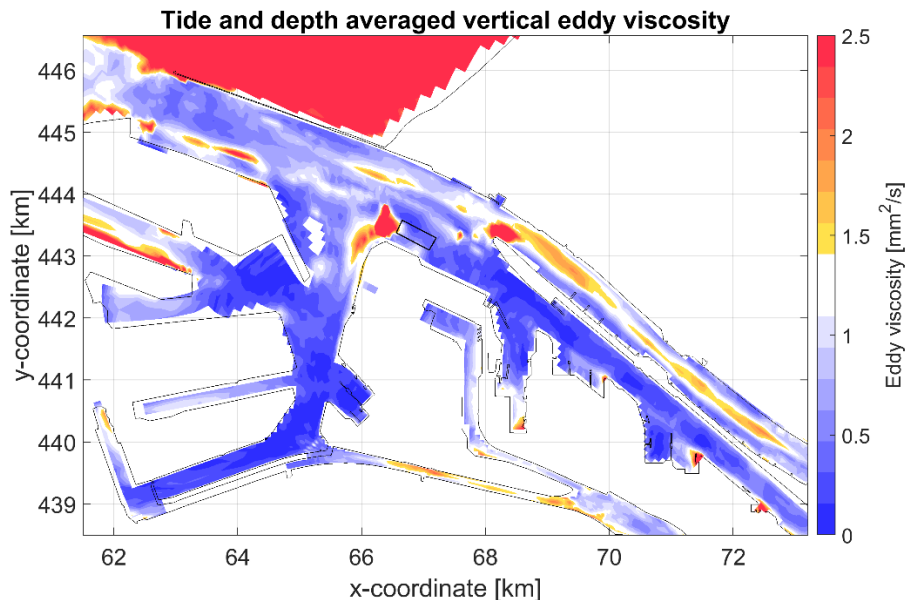


Figure 4-10 Vertical eddy viscosity averaged over one tidal cycle and over the water column.

4.3.2 WID plume dispersion

4.3.2.1 Influence of HW or LW release on the sediment plume

Figure 4-11 and Figure 4-12 show the initial horizontal near bed plume dispersion for the numerical experiment of either generating the plume at HW or LW. In addition, mid column horizontal plume dispersions are shown in Appendix C in Figure C2 and Figure C3. The individual panels show the sediment plume at distinct moment in time after the start of WID. Note, for both figures a production rate of 500 kg/s is assumed and WID last for eight hours. The used production rate represents the average or most likely value based on literature.

Both simulations show a spreading of the plume consistent with that observed during the WID pilots, with spreading of the plume limited to ~ 0.4 km relative to the location of release. Over several hours, the sediment plume is maintained due to a constant supply of WID sediment to simulate a full day of dredging. The result is a sediment plume that progressively built up throughout the day, which provides a realistic estimate of typical WID operations.

The plume initially disperses differently when comparing the HW and LW release. From Figure 4-11 it is observed that the plume (predominantly) disperses in seaward direction with the outgoing tide. After approximately six hours, the flow reverses and the plume is transported in a landward direction. The LW release plume (see Figure 4-12) initially disperses in a similar way compared to the HW release experiment. However, between four and eight hours a landward dispersion is observed. After the flow reversal, the plume starts to disperse in the seaward direction. However, a continuation of the landward spreading is observed in the Calandkanaal. Overall, in both experiments, the near bed plume has spread approximately 0.25 km in up- and/or downstream direction. Mid column plume dispersion (Appendix B) shows a more noticeable difference between two releases. In the HW release experiment the plume becomes visible half way through the column after two hours and is subsequently advected in a seaward direction. For the LW release experiment the plume only reaches mid-way the water column after four hours and is advected seawards during the end of the simulation. This indicates that mixing in the vertical mainly occurs during flood.

Production rate: 500 [kg/s], TIM for layer 20

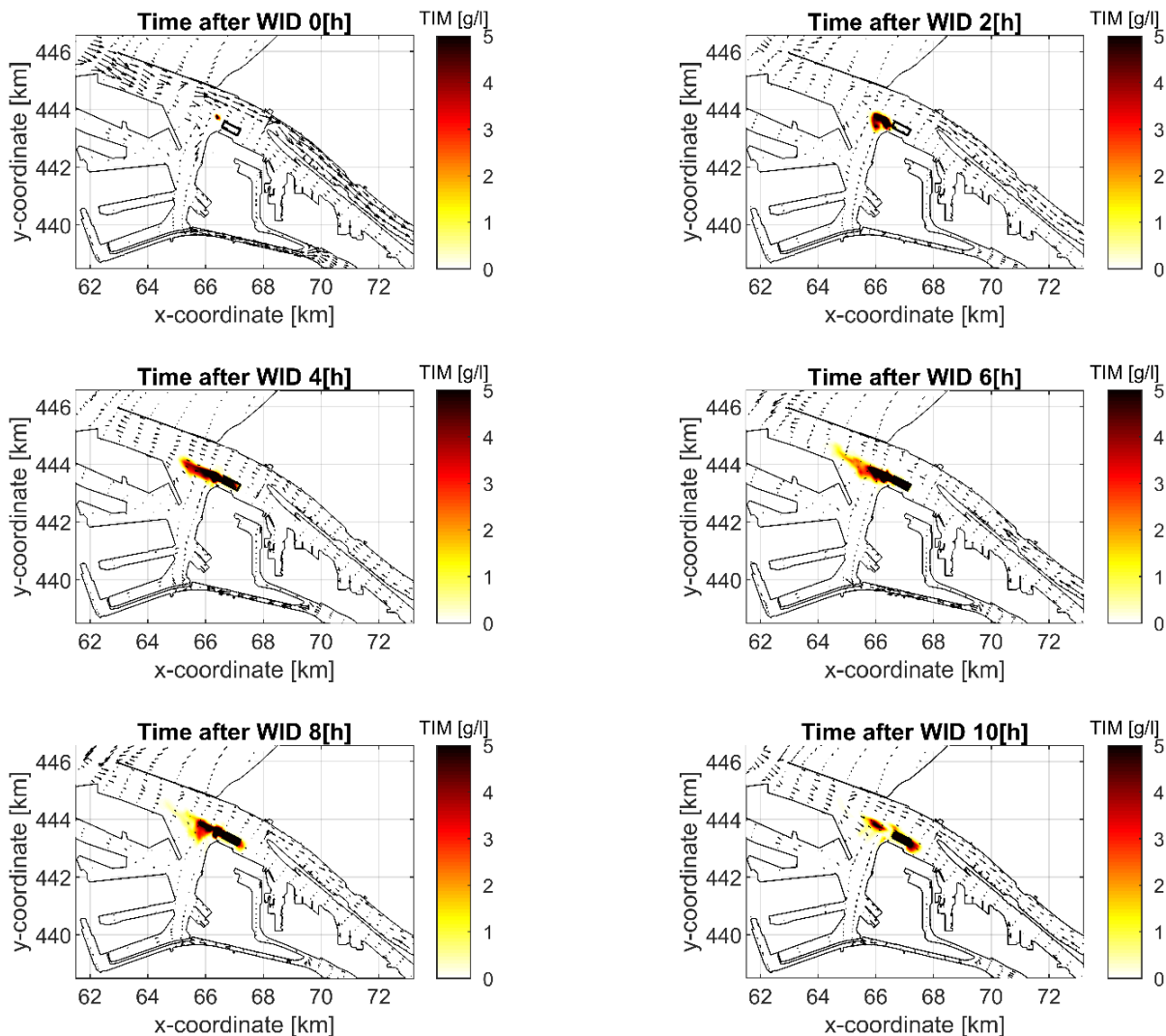


Figure 4-11 Horizontal near bed plume spreading (layer 20), WID release just before HW with a production rate of 500 kg/s. The arrows in the background indicate the direction and magnitude of the horizontal near bed velocity component. The colourbar represents Total Inorganic Matter (TIM) in g/l.

Production rate: 500 [kg/s], TIM for layer 20

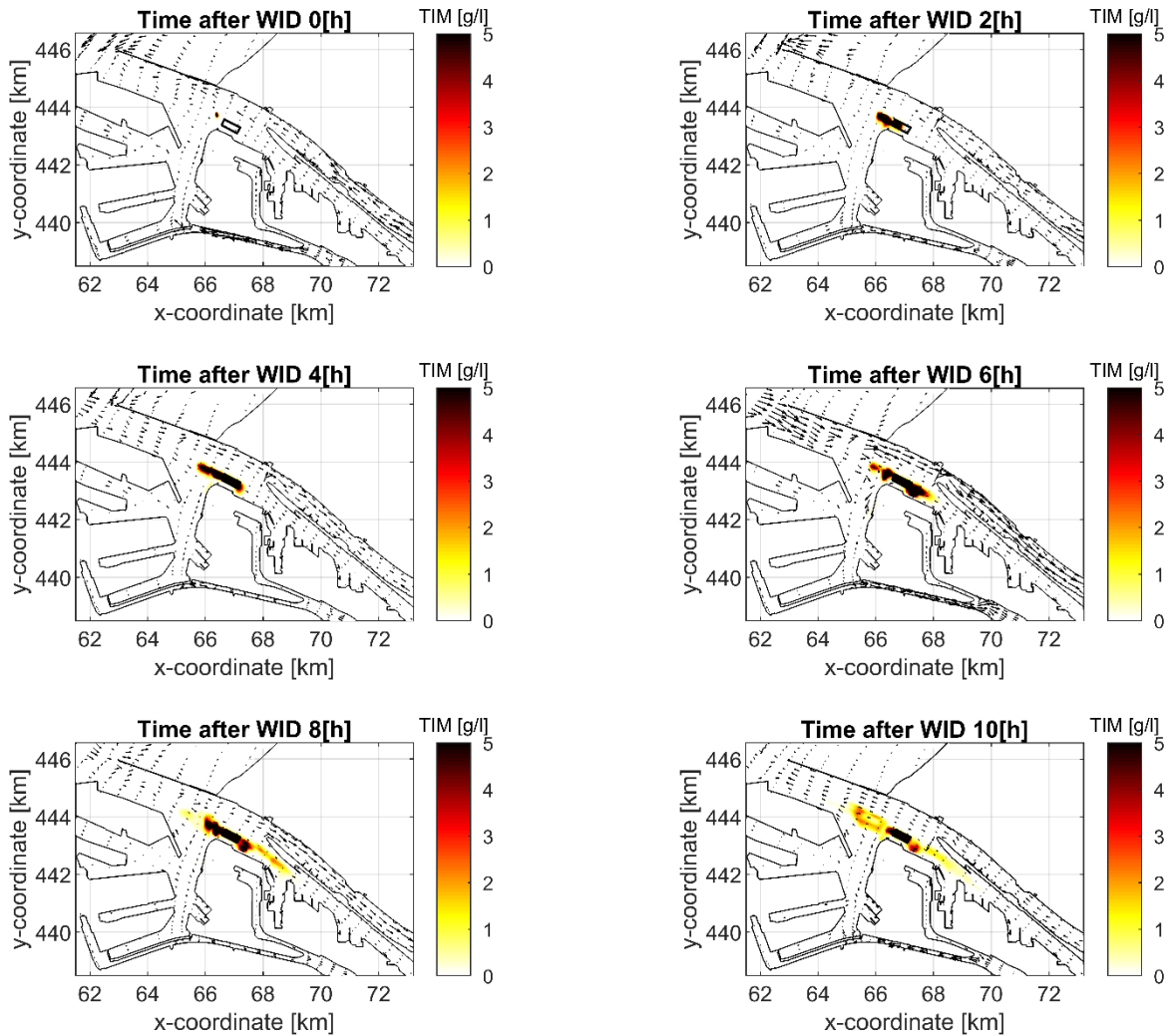


Figure 4-12 Horizontal near bed plume spreading (layer 20), WID release just before LW with a production rate of 500 kg/s. The arrows in the background indicate the direction and magnitude of the horizontal near bed velocity component. The colourbar represents Total Inorganic Matter (TIM) in g/l

4.3.2.2 Influence of HW or LW release on the sediment footprint

The paragraph above describes the moment of WID in respect to the tidal phasing influences the (initial) spreading of sediment plume. Here is shown the impact this has on where the WID sediment plume deposits (sediment footprint). The total sediment deposition is shown, as well as the partitioning between the upper unconsolidated bed layer (fluff layer) and the deeper bed layer (buffer layer). The impact of particle size on deposition patterns is also shown. It should be considered that these numerical experiments were short in duration (3 days) and therefore the sediment footprint is representative of initial settling.

Figure 4-13 and Figure 4-14 show where the WID sediment have deposited three days after the end of WID for release at HW or LW. For both scenarios, the highest values are observed in and near the sediment trap. Figure C8 and Figure C9 in Appendix C show the sediment footprint for the individual fractions. Most of the coarser sediment has deposited in the trap and west of the sediment trap for both runs. However, for the finest fraction some small differences between the HW and LW release experiment are visible. In the LW experiment the sediment footprint is more east oriented of the sediment trap.

Table 4.3 presents a summary of the total amount of WID sediments deposited in the upper bed (fluff) layer, the deeper bed (buffer) layer and in the sediment trap (fluff + buffer layers combined) after 3 days.

Here we make the distinction between the bed layers because most of the sediments released during WID are stored in the upper bed (fluff) layer and are thus easily resuspended and will do so if bed shear stresses exceed the critical shear stress for erosion of the bed. Looking at the different sediment fractions, a slightly larger fraction of the coarsest sediment fraction has deposited and is stored in bed. Comparing the HW and LW release experiment, a near equal amount of sediment is stored in the bed and deposition is independent of the moment of release. However, relatively more sediment is trapped by the sediment trap in the LW release compared to the HW release experiment. Higher trapping efficiency (being the ratio between mass of sediment in the trap at the end of the simulation compared to the total sediment mass release due to WID) in the LW release experiment is, most likely, due to the initial movement of the plume towards the trap. In both experiments the efficiency of the trap is roughly between 22 and 25%. This value may increase over time as sediment that is still in suspension or resuspended from the upper bed layers is pushing back and forth around the area of the trap.

Table 4-3 Total mass of WID sediment stored in the upper and deeper bed layers and located in the sediment trap (total bed) at the end of the short simulation. In total approximately 16.2 kTon of WID sediment is released in the simulation, therefore ~95% of the sediments end up back in the bed.

Layer:	Experiment	Fraction 1 [kTon]	Fraction 2 [kTon]	Fraction 3 [kTon]	Total [kTon]
Upper (Fluff) bed layer	HW release	5.28	5.28	4.85	15.41
	LW release	5.25	5.26	4.93	15.44
Deeper bed (Buffer) layer	HW release	0.12	0.11	0.08	0.32
	LW release	0.15	0.14	0.11	0.39
Total Bed	HW release	5.4	5.39	4.93	15.73
Total Bed	LW release	5.4	5.37	5.04	15.83
Sediment Trap (total)	HW release	1.83	1.23	0.49	3.55 (22%)
	LW release	2.21	1.38	0.55	4.14 (25%)

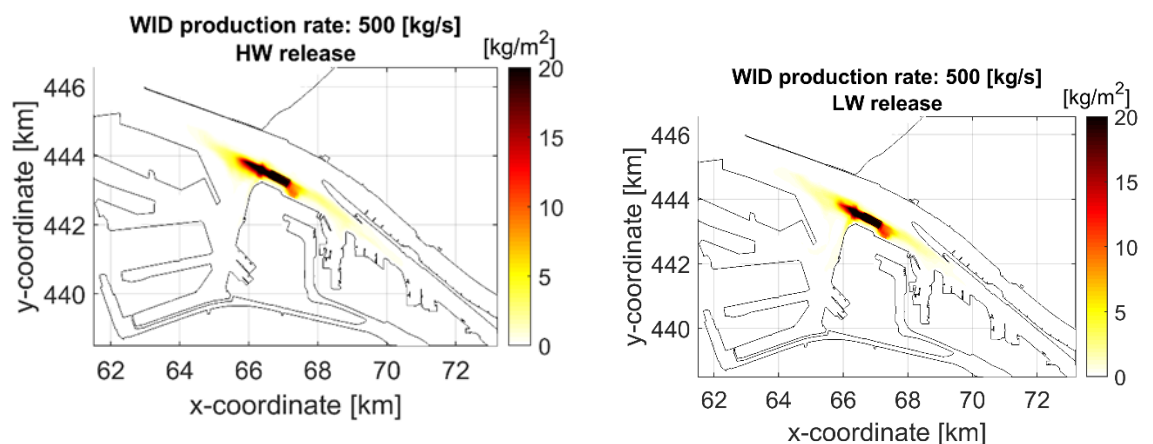


Figure 4-13 Sediment depositional footprint as a result of starting WID at HW versus starting at LW

4.3.2.3 Influence of a week of water injection modelling on sediment plume dispersion

Figure 4-14 and Figure 4-15 show the near bed sediment concentrations at 18:00 PM and 9:00 AM from Day 2 until Day 7 of week of WID dredging. These moments correspond to start and end of the WID activities at each day. In addition, Figure 4-16 shows the total amount of released WID sediment, total amount of suspended sediment and the amount of deposition throughout the first week of the simulation period for the different production rates.

During the day, when WID would occur in reality, sediment is released in the model, mimicking fluidization of the mud layer, and as expected the suspended sediment concentrations (SSCs) increase both over time and spatially. The highest sediment concentrations are observed at the end of the “working” day. The higher the sediment concentration, the less sediment remains in suspension. At the end of the WID day (17:00 PM), no more sediment is added to the model and the SSCs drop rapidly. The next morning, by the time dredging is due to start again, most of the previously disturbed sediments have deposited and/or dispersed in the water column. This implies that the cumulation of several consecutive days of WID has limited impact on the SSC in the plume and therefore it’s spreading, although there may be resuspension of material from the upper bed layer during this time on a lower order of magnitude than the WID plume.

The horizontal plume dispersion shows a similar spreading for all the three runs with different production rates (note colour bars are scaled proportional to the production rate). This indicates that the spreading of the plume is to an extent independent of the production rate. However, there are differences in the SSCs. Most notable is that the plume from the simulations with a higher production rate (800 kg/s) shows the least dispersion and the simulation with the lowest production rate (200 kg/s) is relatively more dispersed. **The less buoyant fluid mud layer generated by the lower production rate is more easily dispersed and mixed by turbulence.**

During the WID week, it is observed that the plume disperses in an opposite direction at the beginning and end of the week. At the end of Day 2 and Day 3, highest concentrations are observed west of the sediment trap, indicating a westward plume dispersion. At the end of Day 4 until Day 7, highest concentrations occur east of the sediment trap. **The directional shift of the sediment plume dispersion can (partly) be explained from how WID is implemented.** During the first days the tide is falling, and the current is directed seawards. Later in the week the tidal phasing has shifted, and the current is mainly directed landwards, also see Figure 4-7. In addition, throughout the week the location where sediment is released moves eastwards of the WID area.

Production rate 500 [kg/s], TIM for layer 20

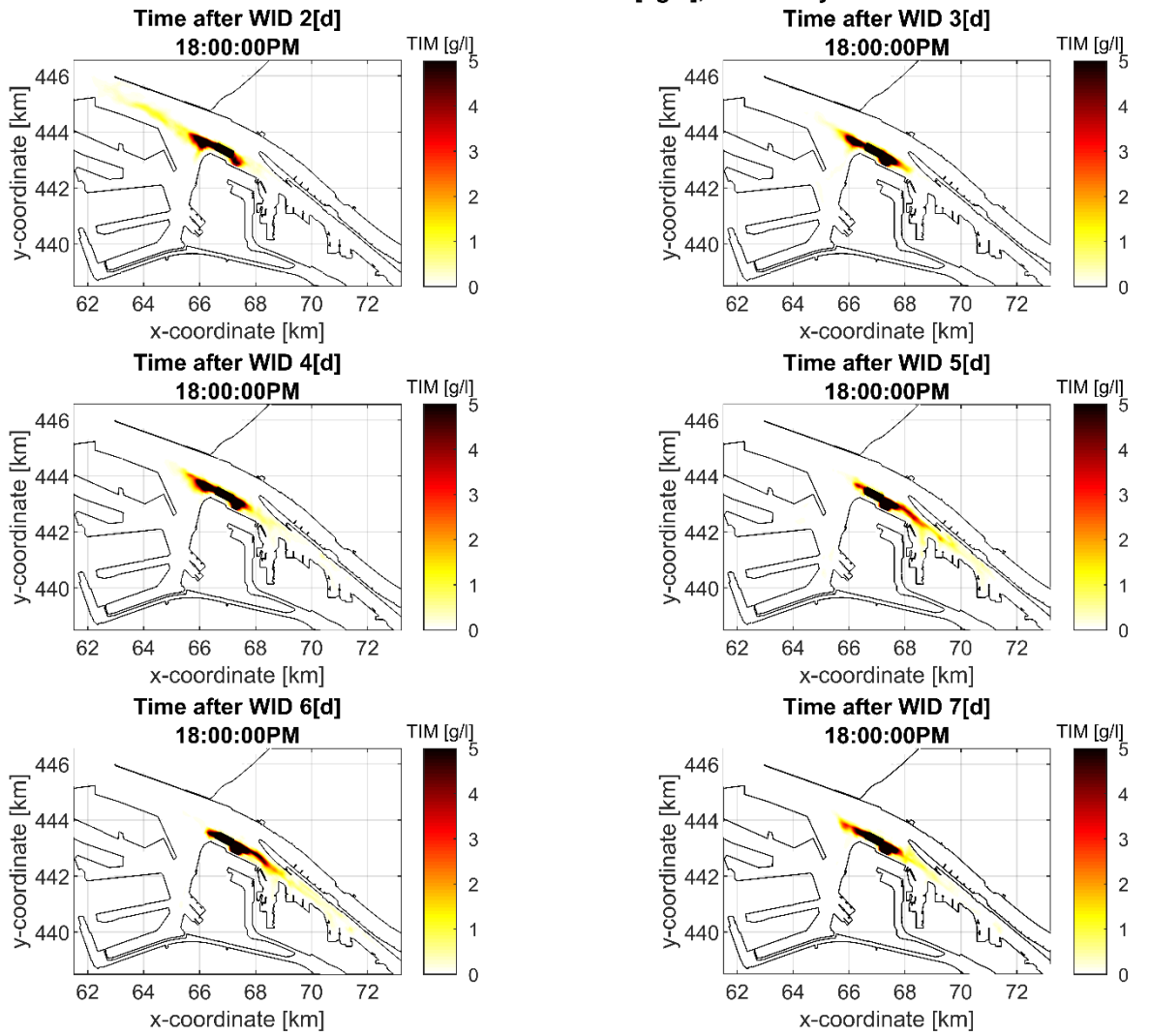


Figure 4-14 Horizontal near bed plume spreading. Panels show the TIM model evaluated at 18:00 PM (end of WID) for day 2 – 7 of WID period.

Production rate 500 [kg/s], TIM for layer 20

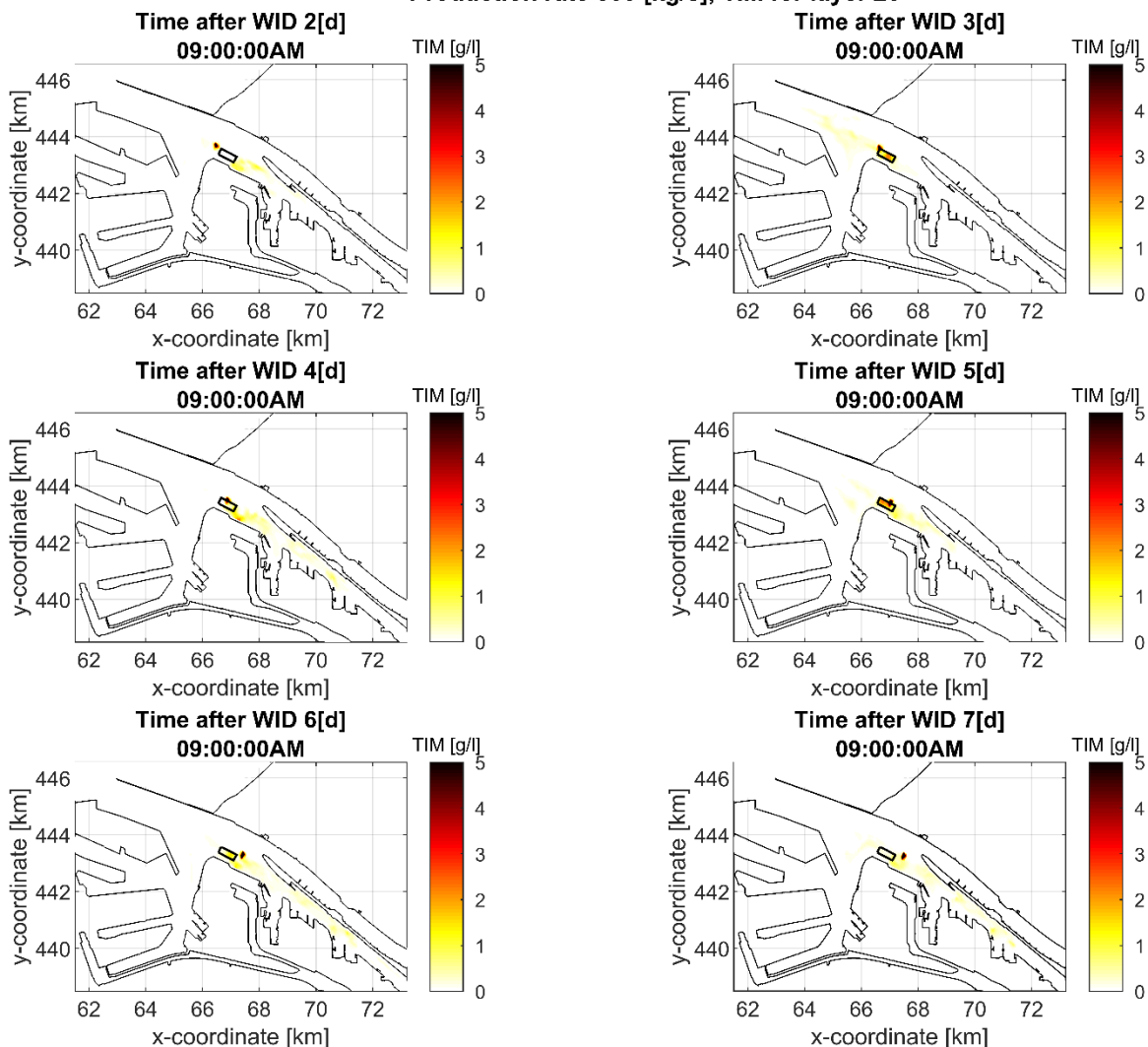


Figure 4-15 Horizontal near bed plume spreading. Panels show the TIM model evaluated at 09:00 AM (start of WID) for day 2 – 7 of WID period.

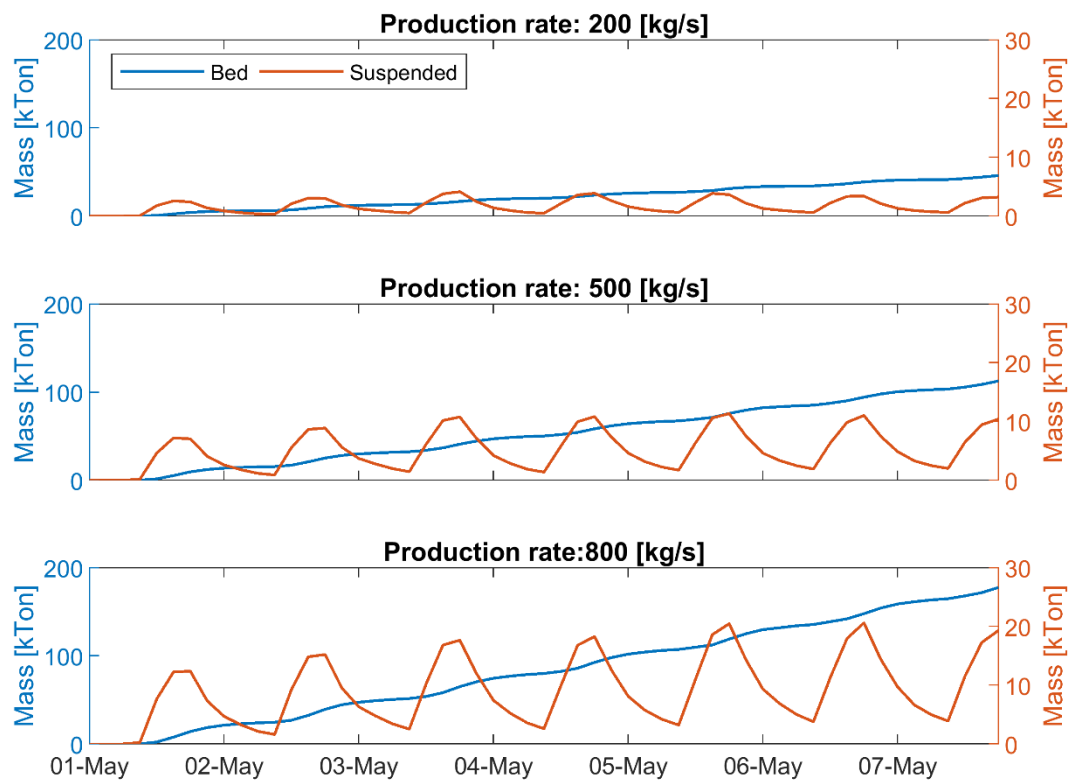


Figure 4-16 Overview of the total amount of WID sediment that is released, in suspension and stored in the bed (fluff + buffer) of the entire model domain.

4.3.2.4 Influence of a week of water injection modelling on the sediment footprint

The sediment footprint after a week of WID is shown at two distinct scales (Figure 4-17). An upper scale of 50 kg/m² is applied to indicate where most of the sediment has deposited. The lower scale of 1 kg/m² is used to visualize where resuspension of WID sediment could occur between the end of the WID activities and the end of the model simulation, as most of the sediment remains in the upper unconsolidated (fluff) layer during the simulation.

The right of Figure 4-17 shows that most WID sediment is trapped and stored in the bed of the sediment trap, showing that the trap works efficiently in the model. Furthermore, a large amount has deposited directly east of the trap, which is deeper than the surrounding area, with exception of the sediment trap which is deepened artificially. Hence this area acts as a natural sediment trap. The majority of the WID sediment is initially stored in the upper unconsolidated (fluff) layer but over time will move to deeper layers, if not resuspended. Resuspension from the sediment trap is less likely to occur due to the low bed shear stresses.

The contours of the sedimentation pattern are comparable for both the fluff and buffer layer between the different production rate simulations. This observation is in line with the horizontal and vertical plume dispersion resulting from different production rates. For all three production rates tested, the majority of the sediment has deposited within the vicinity of the WID area (Calandkanaal and Beneluxhaven). However, it is visible that a large portion of the WID sediment has been transported in upstream direction. In contrast, seaward transport is limited and the amount of sediment that is being transported out towards the North Sea is in the order of a few percent.

Table 4-4 presents a summary of the WID sediments stored in the fluff, buffer layer, total bed (fluff and buffer) and sediment trap (fluff + buffer) at the end of the three-week simulation. Most of the sediments (~71%) are stored in the fluff layer compared to the buffer layer (~29%). This implies that the majority of the WID sediments are still easily resuspended. As the simulation period is relatively short, the distribution of WID sediments in the bed layers will change further over time, as a result of resuspension or further burial and compaction.

The trapping efficiency between the production runs differ, with trapping efficiency being the ratio between mass of sediment in the trap at the end of the simulation compared to the total sediment mass release due to WID. For the lowest production rate simulation (200 kg/s) the trapping efficiency is 29%, whereas for the largest production rate of 800 kg/s it is 21%. This means slightly more of the sediment released in the lower production rate generated plume ends up in the trap. However, the total mass trapped increases with a higher production rate.

This implies that with higher production rates the trap becomes relatively less efficient, at least under the conditions in the existing model. However, there are a few things to consider when interpreting these results. Although the area of the trap in the Calandkanaal is not as fast moving as locations in the Nieuwe Waterweg, it is still more dynamic than the harbours. In addition, the sediment trap is located within the WID area, so WID that occurs to the east of the trap may not be transported back towards the trap given the current dynamics in that location. In a quieter harbour area, results may show more trapping (relative and absolute) for higher production rates if the plume motion is dominated by density driven flow rather than advection and dispersion as can be the case at the Calandkanaal location.

Regarding different sediment fractions, as expected finer sediment are more dispersive and so less settles in the trap. For all three production rate simulations, ~50% of the sediment trapped in the trap consisted of the coarse fraction (2 mm/s) and only ~14% consisted of the fines fraction (0.5 mm/s). Figure in Appendix C show the sediment footprint for the individual fractions (simulation with a production rate of 500 kg/s). Most of the coarse sediment has deposited near the WID area. This is contrast to finest fraction, which is more dispersive and larger portion has deposited upstream of the Calandkanaal, Beerkanaal and Maasvlakte. Note that the figures show only the sediment released during WID and the colour bar is scaled proportionally to the production rate. As stated earlier, the longer-term transport of freshly deposited WID sediments is not taken into account here due to the length of the simulations.

Table 4-4 Total mass of WID sediment stored in the fluff and buffer layer and located in the sediment trap.

Layer:	Production rate [kg/s]	Fraction 1 [kTon]	Fraction 2 [kTon]	Fraction 3 [kTon]	Total [kTon]
Fluff	200	11.69	11.68	11.48	34.85 (71%)
	500	29.19	29.22	28.69	87.10 (71%)
	800	46.72	46.82	45.79	139.33 (71%)
Buffer	200	4.78	4.74	4.60	14.12 (29%)
	500	11.90	11.81	11.46	35.17 (29%)
	800	19.01	18.87	18.24	56.12 (29%)
Bed (Fluff + Buffer)	200	16,47	16,42	16,08	48,97
	500	41,09	41,03	40,15	122,27
	800	65,73	65,69	64,03	195,45
Trap	200	6.81	4.97	2.40	14.18 (29%)
	500	17.11	10.12	4.29	31.51 (26%)
	800	23.56	12.59	5.18	41.32 (21%)

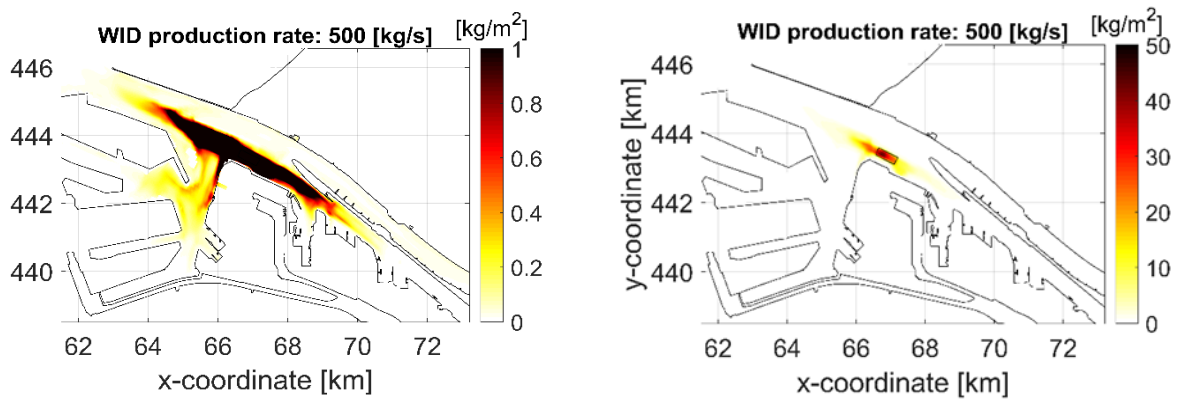


Figure 4-17 Mass of WID sediment deposited in the bed at the end of the simulation, assuming a production rate of 500 kg/s. The right and left figure show the same model output but differ in the used scale of the colour bar

4.3.3 Mixing over the vertical

4.3.3.1 Influence of HW or LW release on vertical mixing of the plume

Dispersion of the plume in the vertical seems to be limited. This because the plume is only visible near the bottom (on a linear scale). This limited vertical mixing can be explained from the tidally averaged vertical eddy viscosity values (see Figure 4-10), which is generally low near the WID area. An exception is a small area west of the WID area where the tide averaged eddy viscosity values are higher ($2.5 \text{ m}^2/\text{s}$). This location, approximately between A-A' 2000 and 3000m (Figure 4-18) corresponds to the location where vertical mixing is observed in Figure 4-19 and Figure 4-20. Both figures, show that after the WID starts a layer with a thickness of 1-3 m develops with an SSC above 1 kg/m^3 after which the plume starts to spread mainly in the horizontal direction. In addition, Richardson numbers² above unity are observed at the location of the sediment plume. This implied that buoyancy is dominant and there is insufficient shear/turbulence to mix the plume throughout the water column.

The horizontal spreading is caused by the ambient flow conditions and gravitational spreading of the fluid mud layer. The occurrence of gravitational spreading is to be expected from the Richardson number, but is also visible from the arrow indication the flow parallel to the cross-sectional transect. The effect of the ambient flow and the phasing of the tide is clearly visible after comparing in Figure 4-19 and Figure 4-20. From Figure 4-19 (HW release experiment) it is visible that the sediment plume moves seawards in the first six hours. Hereafter, the flow reverses and the sediment plume is pushed landward.

² The Richardson number is expressed by the ratio between the buoyancy and the flow shear term ($Ri = \frac{\text{Buoyancy term}}{\text{Flow shear term}}$) and indicates whether buoyancy is capable of suppressing shear which homogenise the fluid. A Richardson number above unity indicates buoyancy is dominant to shear.

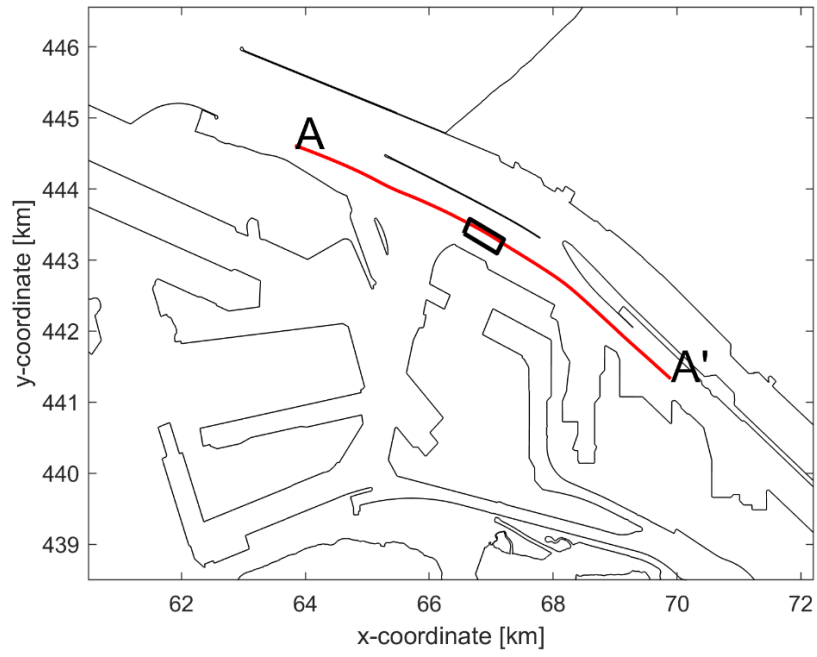


Figure 4-18 Location cross-sectional transect used to display the vertical plume spreading.

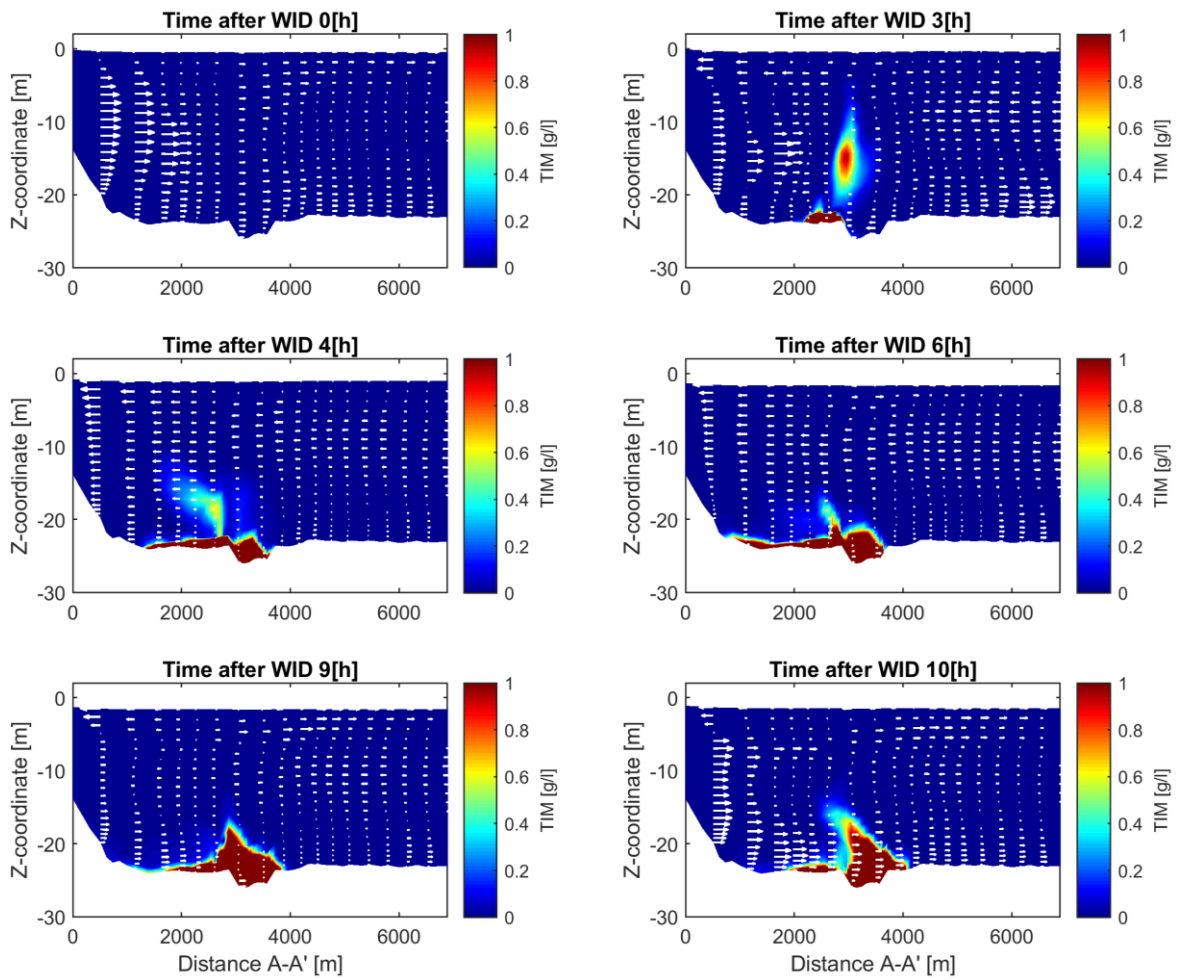


Figure 4-19 Vertical plume dispersion for the HW release experiment.

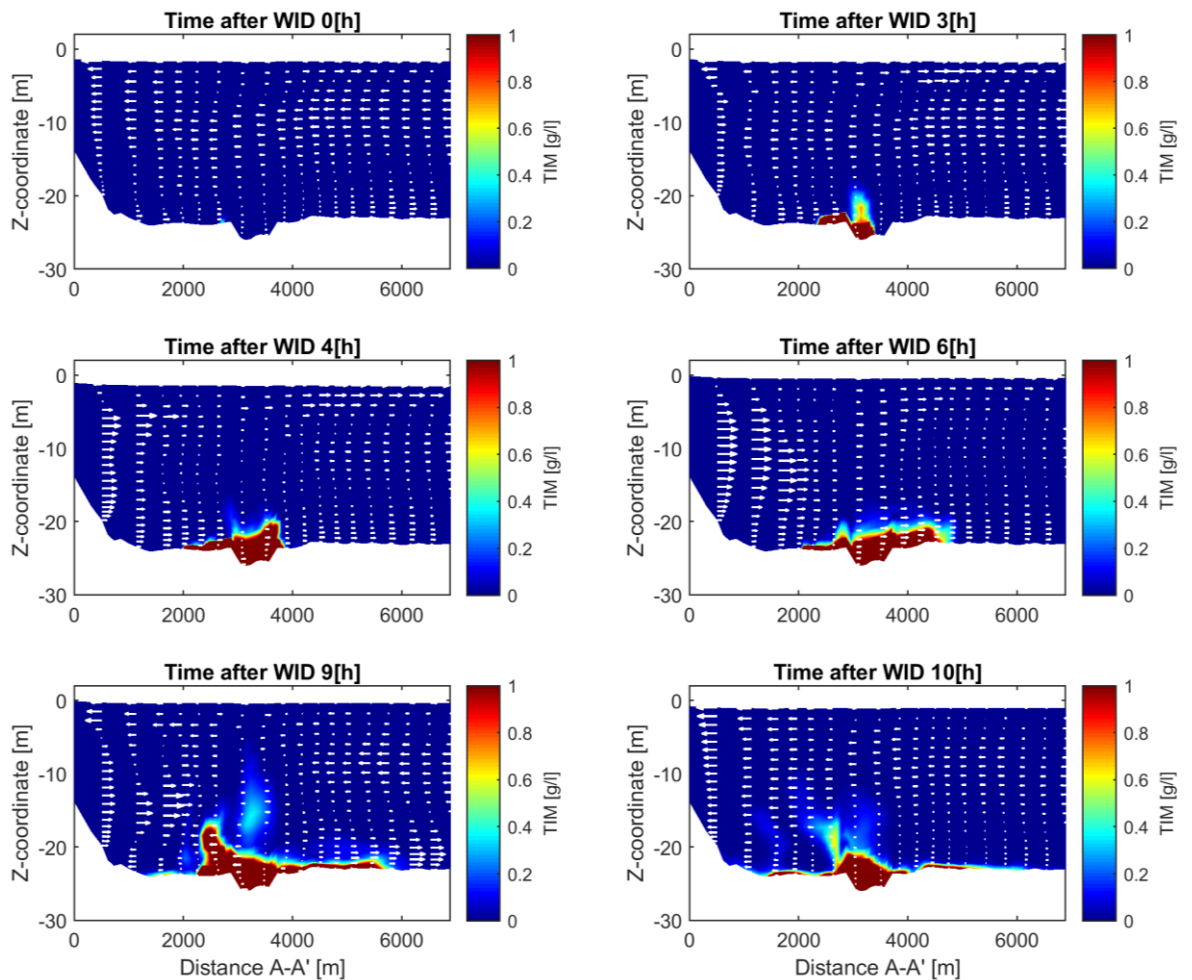


Figure 4-20 Vertical plume dispersion for the LW release experiment.

4.3.3.2 Influence of a week of water injection modelling on vertical mixing of the plume

Vertical mixing at the end of each WID day during the week of WID activities in the model is shown below in Figure 4-21. Variations in the vertical over a tidal cycle appear greater than the variations between days under similar conditions. The sediment plume is often centred around the trap and sometimes skewed more to the east. The plume remains in the near bed layers throughout the week.

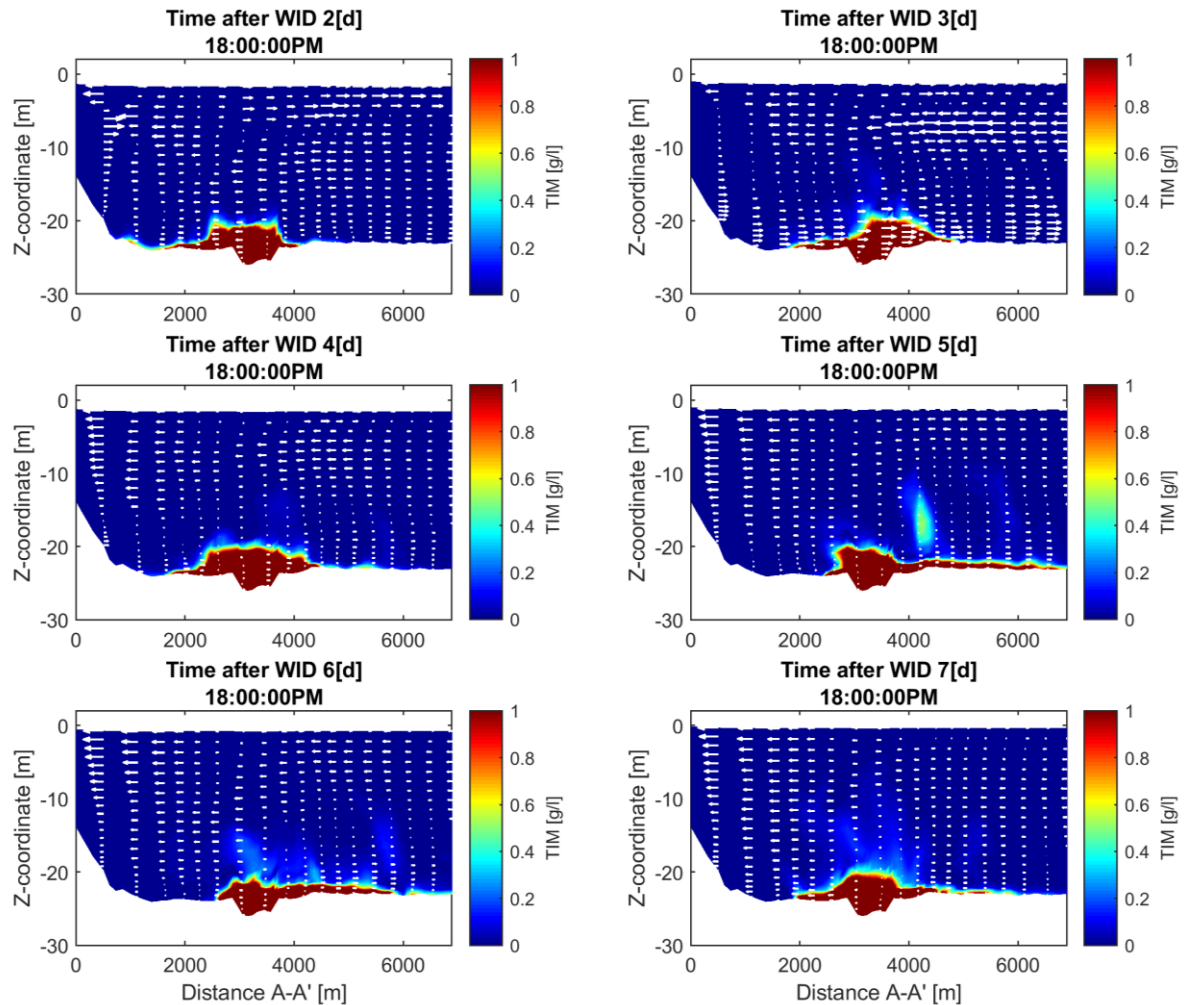


Figure 4-21 Vertical plume dispersion at the end of each day of the WID week, assuming a production rate of 500 kg/s.

4.3.4 Fate of the WID sediment and return flows

For all three numerical experiments, more than half of the released WID sediment returned within two weeks to one of the dredge areas (Figure 4-22) maintained by the port. This sediment return flow is stronger with a lower production rate. Namely, in total 72% of released sediment returned to the dredge areas in Figure 4-22 with a production rate of 200 kg/s and for the simulation with 800 kg/s production rate ~66% returned.

Figure 4-22 provides a spatial overview of the amount of sediment returning the individual dredge areas. Most of the sediment, approximately between 35 and 48%, deposit in the dredge area ABO in which the sediment trap is located. The dredge areas ABN and ABP located east of ABO store most of the remaining sediment. Only a small percentage (less than 5%) deposits in the Beerkanaal and Maasvlakte. Figure 4.24 compares sedimentation in individual dredge areas of the different simulations. In line with the previous results, relatively more sediment is trapped in ABO (location sediment trap) with a lower production rate. In the neighbouring dredge areas sedimentation increases for higher production rates.

indicates that less sediment has returned to the dredge areas than was fluidized during WID with a production rate higher than 200 kg/s. A higher production rate results in more sediment removal, a relatively less efficient sediment trap but relatively less sediment stored in the dredge areas.

As mentioned at the start of this section, 60-70% of the WID sediments has settled around the dredge areas of the Calandkanaal two weeks after WID has stopped. On the larger scale, Figure 4-24 shows where the rest of the WID sediment ends up, relative to the amount released during the different production scenarios. What this shows is that 90% overall ends up in the Calandkanaal area, and particularly for the higher production scenario several percent (~5.5%) flows into Maasvlakte 1. A small percentage ends up in Europort and less still out to the North Sea. Only a tiny percentage remains in suspension (green band in Figure 4-24). After such a short period, most of the sediment that has settled to the bed will be available for resuspension if shear stresses due to currents, waves, or possibly also ship induced bed shear stresses (not in the model) exceed the critical shear stress for resuspension of this freshly deposited sediment layer.

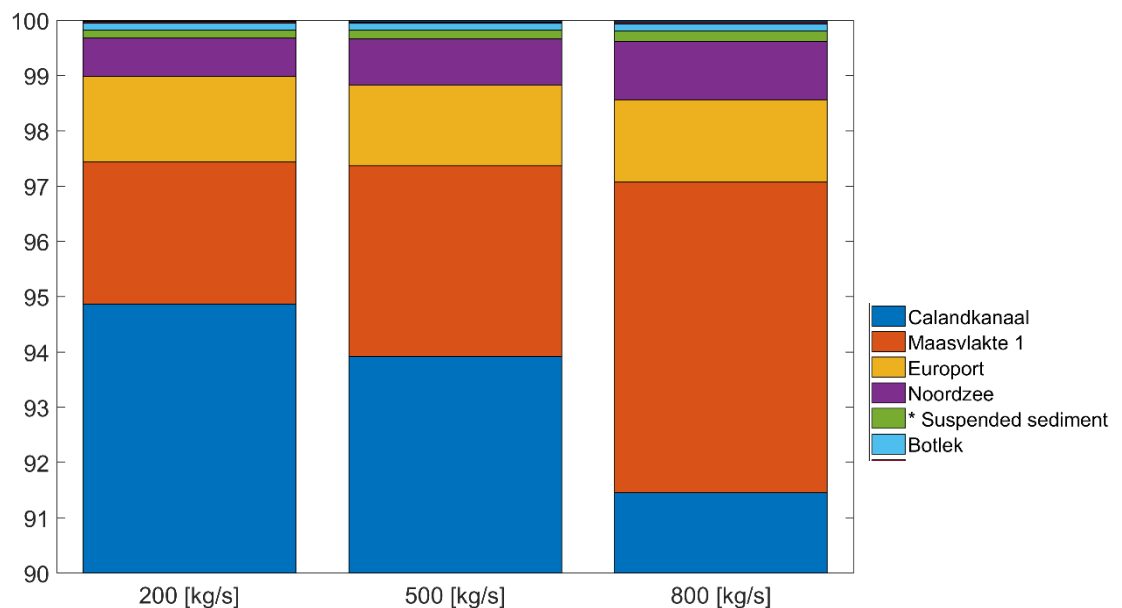


Figure 4-24 Total sedimentation (background and WID sediment) and sedimentation of WID sediment (WID) per dredge area, expressed in mass (kTon) and as a % of total amount of released WID sediment.

4.3.5 Recommendations from WP3

- The goal of this study was to simulate both how the sediment plume disperses both locally within the harbour and over a wider area. In the ideal situation, the computational grid would be fine enough that it captures the dynamics on both scales. However, the finer the computational grid the longer the simulation time. Therefore, the grid resolution applied here is a trade of between computational time and resolution. This, however, implies that the sediment pit is only captured by 14 grid cells and some local flow, settling and resuspension patterns cannot be resolved. In future steps it is recommended to improve the grid resolution of areas under investigation.
- During WID mud is fluidized and removed from the bed. In the modelling experiments described in this chapter, sediment from the modelled bed layer is not brought in suspension but rather sediment is added to the model as a discharge. It

is recommended to implement simultaneous removal from the bed and release over the water column.

- In the current version of this model, rheology is not implemented. Rheological properties become important at the turbulent to laminar transition and affect the spreading of the sediment plume. Without considering rheological processes a high-density plume can spread without any constraints. Whether the sediment plume behaves as a turbulent or laminar flow mainly depends on the density of the plume and the velocity at which the plume spreads. Although analyses as part of this work indicated that the plume likely remains turbulent for all simulations in which sediment discharges had been implemented, it is recommended to further advance the implementation of rheology in the model so that higher-density plumes can be investigated.
- Finally, the ambient hydrodynamic conditions under which WID is tested in the model is limited now to a rather quiet period, a specific location and simulation duration is also limited to a few weeks. It is recommended to a) assess the difference in results for a quieter harbour area where the impact of density driven flow may be more dominant; b) test under stormier or higher discharge conditions and c) look at the longer-term resuspension and distribution of the WID sediment footprint.

5 WP 4: near field modelling tools

5.1 Introduction

Within work package 4 of PRISMA the near field behaviour of WID density currents is investigated. In the near field the WID fluidized slurry layer really behaves as a density current and is called as such in this report and in the far field modelling it is called plume. Two different model tools have been applied: a rapid assessment Lagrangian 1DV model and a 3D multiphase CFD model. 3D CFD can be applied in complex situations where the simplifications of the 1DV model hinder its application.

This chapter starts with a WID characterization based on observations during the monitoring campaigns in the Port of Rotterdam and on literature, leading to a working definition of the WID near field zone. Next section continues with the application of the 1DV model for PRISMA WP4. A brief description of the model is given, it is validated by experimental data and it is applied for a parameter study. Subsequent section provides the application of the 3D CFD model for PRISMA WP4, starting with a brief description of the model, followed by validation with experimental data and application for the real 3D area of the Calandkanaal in the Port of Rotterdam. A direct comparison between the 1DV model and the 3D CFD model is provided and a link between the findings of WP4 and WP3 is established. This part ends with the conclusions of WP4.

5.1.1 WID characteristics

Purpose of WID is to generate a fluidized sediment density current by injecting high volumes of water with low pressure and then let nature do the work by moving the sediment under the influence of gravity. A WID often works by making multiple trails at the same stretch. In this manner the density current is growing every trail. This is an important characteristic of WID operations. When judging measurements or doing near field simulations, it is important to consider how many WID trails have been made and how much time this required.

WID observations during field trials in the Calandkanaal area of the Port of Rotterdam show:

- 2m layer thickness with density $\sim 1130 \text{ kg/m}^3$ (SSC (suspended sediment concentration) $\sim 170 \text{ kg/m}^3$). It is unknown how many trails the WID unit had done already, but probably several.
- 0.5-1m layer thickness with smallest density in the order of $\sim 1100 \text{ kg/m}^3$ (SSC $\sim 115 \text{ kg/m}^3$) for a single WID trail.
- 3.4-4m layer thickness after 6 hours working on just 2 lines in the sediment trap
- A WID dredge moves $\sim 0.4\text{-}0.6 \text{ m/s}$; it typically works along lines of $\sim 100\text{-}400\text{m}$ long; it typically works $\sim 1\text{-}4$ times on the same track and then moves on to a next track; it works 8 hours a day.
- Please note that for different parts of the PoR these WID characteristics may be different due to different sediment characteristics and ambient conditions.

Regarding WID production, there are two numbers which one might call WID production. The first number is the amount of sediment being stirred up by a WID vessel. The second number is the amount of sediment being stirred up by WID *and* leaving the (harbour) area. The second number can be considered as an *effective* WID production. Within PRISMA production according to the first definition is required as input to the models. In PRISMA the effectiveness of WID will be studied by determining how much of the WID density current will leave the maintenance area and where it will deposit.

The following literature sources provide insight in WID characteristics and productions.

- Water Injection Dredging paper of Van Rijn (<https://www.leovanrijn-sediment.com/papers/Waterinjectiondredging.pdf>) assumes the following:
 - Production WID is 30-250 kg/s (according to first definition, production as in stirring sediment up).
 - Layer thickness 0.5-1m
 - Excess density 25-50 kg/m³
 - $U = 0.25-0.5$ m/s (densimetric $Fr \sim 0.9$)
 - Van Rijn assumes a boom width of 10m (N.B. the boom width of JETSED WID unit working in Port of Rotterdam is 13.8m)
- Pianc Report 120 Injection Dredging (Pianc 2013)
 - Production rates for several projects are provided in a table. The definition of production is not mentioned, but probably effective production is meant.
 - Silt/clay 500-2800 m³/h → order of 70-400 kg/s assuming in-situ density 1.4 t/m³ (excess density ~525 kg/m³)
 - Sand and sand/silt 140-800 m³/h → order of 50-320 kg/s assuming in-situ density 1.9 t/m³ (excess density ~1430 kg/m³)
 - If indeed effective production is meant, then the stirring up WID production is a factor higher. Assuming a factor 2 the WID stirring up production mentioned in Pianc (2013) becomes of the order of ~100-800 kg/s.
 - Indicative sketch of WID density current shows a density of 1025-1100 kg/m³ (excess density 40-115 kg/m³)
 - Example shown of measured WID density current ~3.5m high; 0.4 m/s max velocity; ~0.2 m/s avg velocity (density not given).

These two literature sources combined give a bandwidth of ~30-800 kg/s for WID production defined as stirring sediment up. For fine sediment ~200-800 kg/s seem to be realistic WID production values.

Wrapping up, based on field campaign observations and literature values, WID near field characteristics in PoR circumstances round the Calandkanaal are given by:

- An expected WID production of ~200-800 kg/s of fine sediments (production defined as stirring sediment up).
- A WID works along lines of several hundred meters long and for multiple times in a row.
- After several trails a WID density current is expected to have a height of 2-4m with densities in the order of ~1050-1130 kg/m³ (SSC ~30-170 kg/m³) and maximum velocities in the order of ~0.4-1 m/s.

5.1.2 Working definition of 'near field' within PRISMA

In WP4 the near field behavior of a WID density current is considered. But what is the 'near field' for a WID density current. Where does 'near field' end and 'far field' begin and where does 'near field' begin? To begin with the latter, the WID jets themselves and the interaction of the jets and the sediment from the bed is not considered in the near field modelling for PRISMA. Instead, a sediment and momentum source caused by the WID jets is applied as inflow boundary condition in the near field modelling.

Normally, for other dredge plumes the transition from near field to far field is defined at the location where plume behavior goes from dynamic to passive. In a dynamic plume internal momentum, density differences and local turbulent mixing for instance by the interaction with dredging equipment itself are important. In the traditional definition, a far field plume behaves passively, e.g. internal momentum and density differences have diluted so far that they get negligible. Transport and mixing of a passive far field plume are governed by ambient (tidal) currents and settling of the sediment particles. Deposition on the bed and re-suspension by waves and currents are also important processes in the far field.

For WID density currents things are a bit more complicated because in the far field density differences still play a role and strictly speaking a WID density current always is dynamic, also in the far field. But, as a working definition within PRISMA, the transition from near field to far field for a WID density current is defined at a location far enough that individual trails of the WID dredger have no influence anymore and its behaviour can be captured on the coarser far field model grid (including density driven flow). In practice that will define the far field as the zone starting a few hundred meters from the WID dredger.

5.2 1DV modelling of WID

5.2.1 Brief description 1DV model

The Lagrangian 1-Dimensional vertical (1DV) model is a rapid assessment tool which models the density current generated by a WID vessel. The 1DV point model is based upon the Delft3D-Flow model, by stripping all the horizontal gradients, except for the horizontal pressure gradient. Normally, the 1DV model is used to simulate vertical processes at a fixed location in space. However, for WID applications, we use the 1DV model to follow a density current through space, i.e. we apply a Lagrangian approach.

An example of how the Lagrangian 1DV approach can be applied is shown in Figure 5-1. A slurry density current is generated by a WID vessel, and this slurry will start to move in an opposite direction to the direction of the ship (the latter is indicated with U_{ship}). For our modelling approach, we start the computation at $x=0$. At this location, the initial conditions for the 1DV model are applied. The model domain then moves along the x -coordinate, and follows the development of the slurry in space. It keeps track of the amount of sediment that is deposited along the pathway of the slurry, and calculates how fast the slurry travels along the seabed.

The Lagrangian 1DV approach can be applied for slurries that move in only 1 direction, i.e. along a line. Lateral spreading cannot be modelled in this approach. The model includes the option to model the development of a slurry along a slope. This is important, as most WID-induced slurries will move over a sloping bed, and can be seen as a gravity-driven flow. Hence, we can use the 1DV model to estimate where the WID-induced slurry will deposit. Additionally, we can calculate the amount of sediment that is mixed into the overlying water from the WID-induced slurry, resulting in turbidity higher up in the water column. It can deal with fluidized sandy and / or muddy sediment layers. Details on the 1DV WID model can be found in Hendriks et al. (2019).

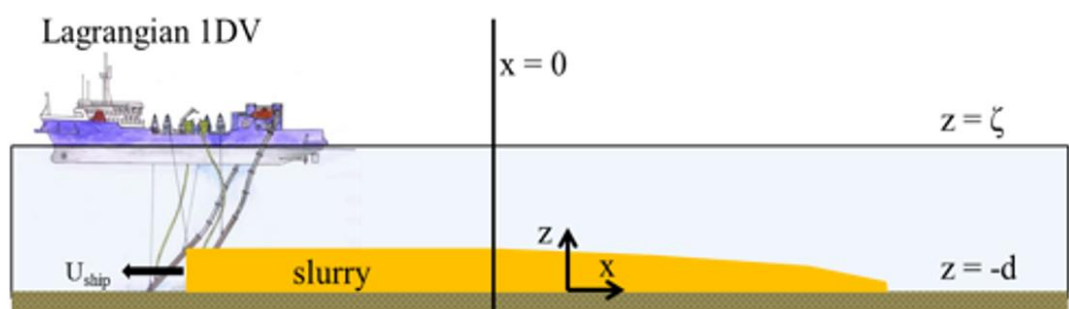


Figure 5-1 Conceptual sketch of a fluidized sediment layer

5.2.2 Application of 1DV model for a turbidity current on an erodible bed (experiment of Parker et al. 1987)

The 1DV model is applied for an experiment of Parker et al. (1987) consisting of a turbidity current on an erodible bed. The validation of the 1DV model is repeated from Hendriks et al. (2019), for more details of this experimental case and other validation cases for density currents see the original report of Hendriks et al. (2019).

Parker et al. (1987) conducted 24 experimental runs to investigate the behaviour of turbidity currents laden with non-cohesive silt (silica flour). In these experiments the turbidity currents moved down a slope, where the bed was covered with similar silt. The motion of the head was not studied; measurements were concentrated on the continuous part of the current that was essentially constant in time but developing in space. Only internal supercritical currents were studied. The currents were free to erode sediment from, and deposit sediment on the bed. Vertical profiles of velocity and sediment concentration were measured downstream of the sediment inlet. These measurements allow for the development of approximate similarity relations, and comparison with numerical models.

Parker et al. (1987) measured profiles of concentration and velocity along the slope of their flume. Profiles were measured at three locations, at 1.5, 4.5 and 8.5 meters downstream of the flume inlet. For these three locations, we compare the velocity and concentration profiles computed by the 1DV model with data of one representative experimental run. Results are shown in Figure 5-2 and Figure 5-3. The 1DV settings are compared with experimental settings in Table 5.1. Values for z_0 (bed roughness) and \bar{U} (depth-averaged velocity) were not given by Parker et al. (1987) but have been calculated, see Hendriks et al. (2019) for details. Other settings were chosen such that they agree with the experimental settings.

Table 5.1 Experimental settings of experiment 13 as presented by Parker et al (1987), compared with Lagrangian 1DV settings.

Parameter	Parker et al. (1987)	Lagrangian 1DV setting
Slope	0.05	0.05
Average fluidized layer velocity (U_0)	0.27 m/s	0.27 m/s
Inlet height (h_0)	0.08 m	0.08 m
Water discharge through inlet (Q_{w0})	15 l/s	not specified
Sediment discharge through inlet (Q_{s0})	164.6 g/s	not specified
Volumetric sediment concentration at inlet (C_0)	$4.1 \cdot 10^{-3}$ [-]	not specified
Sediment density	2650 kg/m ³	2650 kg/m ³
Average fluidized layer sediment concentration (Q_{s0}/Q_{w0})	10.9 g/l	10.9 g/l
d_{50} of sediment	30 μ m	30 μ m
d_{90} of sediment (estimated from PSD curve)	50 μ m	50 μ m
z_0 (calculated)	not specified	$5 \cdot 10^{-6}$ m
\bar{U} (calculated)	not specified	0.025 m/s
initial velocity profile	not specified	double logarithmic profile
initial concentration profile	not specified	step function (i.e. constant)

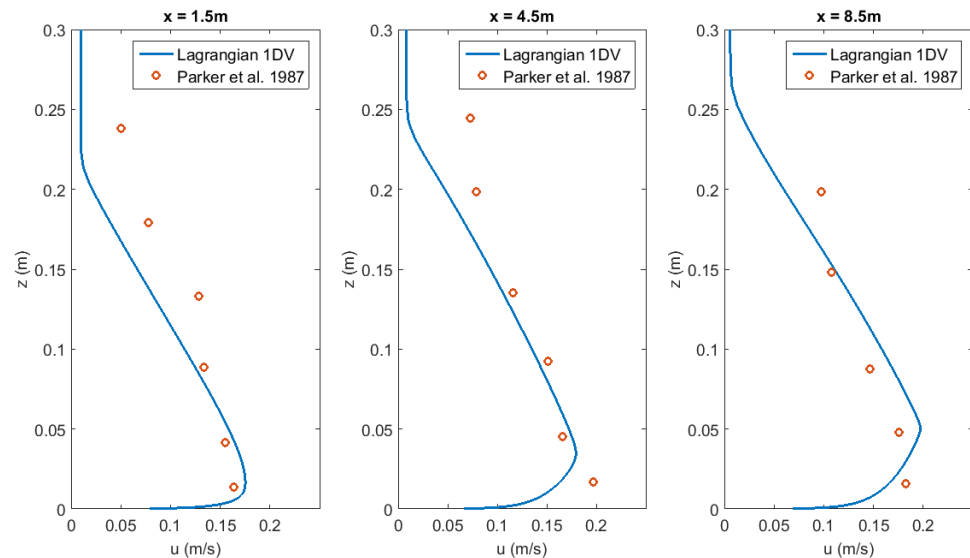


Figure 5-2 Velocity profiles computed using the Lagrangian 1DV model compared to the measurements of Parker et al. (1987).

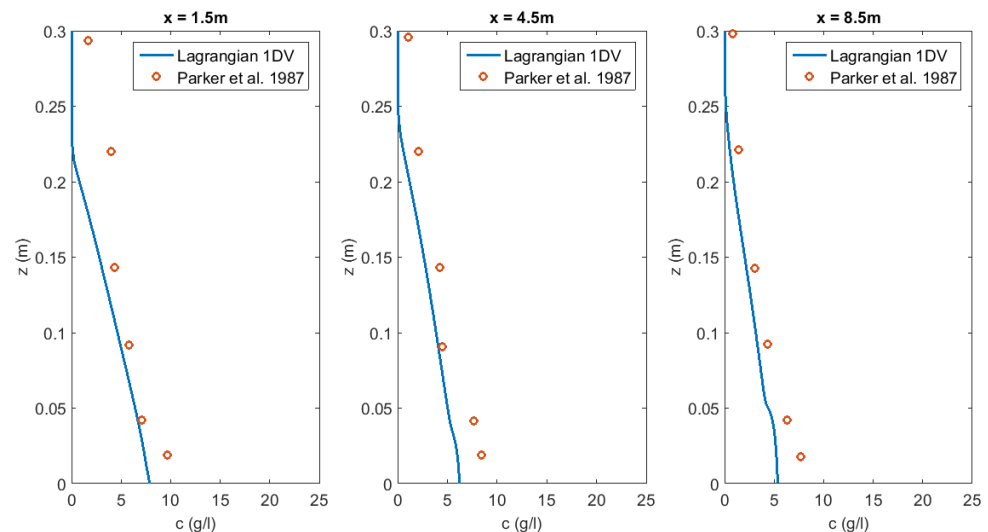


Figure 5-3 Concentration profiles computed using the Lagrangian 1DV model compared to the measurements of Parker et al. (1987).

The Lagrangian 1DV model shows a good agreement with the data of Parker et al (1987). Within the turbidity current, from 0 to 0.2m above the bed, the velocity is computed accurately. Above the turbidity current, the velocity is slightly underestimated by the model. The computed concentration profiles show a similar trend to the measured concentrations.

For the boundary at the bed, we have chosen the Zyserman and Fredsoe (1994) reference concentration. This reference concentration is imposed on the lowest grid cell, based on the value of the Shields parameter. At locations $x = 4.5$ m and $x = 8.5$ m, we observe that this reference concentration influences the concentrations above, as there is a small inflection at 0.025 m and 0.05m above the bed, respectively. While this boundary condition may be valid for modelling turbidity currents, it should not be used for calculating the sedimentation footprint of a fluidized layer, as a sediment concentration is imposed instantaneously on the lowest grid cell.

Other options would be to specify that no sediment is eroded from the bed or to use a pickup function. If the fluidized layer flow is mainly depositional, which is the case for fluidized layers generated by dredging, a 'no-erosion' formulation will suffice. We advise to use this boundary condition when modelling fluidized layer flow using the Lagrangian 1DV model.

5.2.3 Input parameter study

The 1DV model requires several inputs in order to determine where the slurry will deposit. The inputs are the initial conditions of the slurry (height, concentration, velocity), the properties of the mud, the slope along the path of the slurry and ambient hydrodynamics (e.g., average flow velocity, amount of turbulent mixing). An extensive explanation and description of the settings can be found in the 1DV user guide (Hendriks et al. 2018).

The 1DV model is used for a parameter study consisting of thousands of simulations. Some WID input variables are known, but others have a range of possible values for the Port of Rotterdam situation. The parameter study is performed to find the most likely near field WID density current characteristics given the uncertainty in some input parameters and to find the most important input parameters for the resulting near field WID sedimentation.

Table 5.2 presents the deterministic inputs, comprising measured values in the field campaign and default/standard values chosen by the user. Table 5.3 instead gives a representative value and a band of variation for each uncertain input variable. The input values are chosen in line with the WID characteristics described in Section 5.1.1. An exception is the gelling concentration used as input in the model $c_{gel}=500-1700 \text{ kg/m}^3$. This input value is larger than the measured WID maximum concentration of $\sim 170 \text{ kg/m}^3$. This is because rheology and consolidation are not included in the model. In the model sedimentation of sediment out of the WID density current follows purely from deposition out of the water column. When in the lowest grid cell $c > c_{gel}$ deposition stops in the model, but in reality consolidation starts at this moment and in this manner sediment is removed from the WID density current. That is the reason for using large values for c_{gel} as model input to make sure deposition in the model still occurs for the situation that the concentration in the lowest grid cell gets above the physical gelling concentration.

The combinations of inputs used in the analyses may give supercritical starting conditions or an ambient flow velocity that is faster as the initial velocity of the fluidized layer, therefore those combinations are adjusted such that they always satisfy the conditions $U_{ambient} < U_{fluidized\ layer}$ and $Fr < 1$. This is required because the 1DV model cannot deal with strongly non-stationary flows which occur in the transition from supercritical starting conditions to subcritical flow which would happen in nature at some distance from the source.

Table 5.2 Deterministic input variables 1DV model

Input type	Description	Unit	Value
Model parameters	Water depth	[m]	25
	Time step	[s]	0.5
	number of top layers KMAXT	[-]	100
Mud properties	sediment type (SAND / MUD)	[-]	MUD
	density of sediment particles	[kg/m ³]	2650
	erosion type	[-]	Erooff (no erosion, only deposition)
	prandtl-schmidt number	[-]	0.7 (default value)
	Richardson-Zaki exponent	[-]	4 (default value)
Initial Conditions	Profile type for initial velocity	[-]	hybrid

Table 5.3 Uncertain inputs variables 1DV model

	Description	Unit	Reference value	Lowest : Upper values
Model parameters	depth-averaged velocity (\bar{U})	[m/s]	0.2	0 : 0.5
	fall velocity of single floc	[m/s]	1.0e-3	0.5e-3 : 1e-2
	Structural dry density / gelling concentration (c _{gel}) *	[kg/m ³]	600	500 : 1700
Initial conditions	fluidized layer height (h _{fl}) [m]	[m]	2	1 : 3
	Average fluidized layer velocity (literature values)	[m/s]	0.7	0.1 : 1.65 m/s
	slurry concentration (c _{fl})	[kg/m ³]	170	40: 170 **
	Profile type for initial concentration		Block	
Bathymetry	Bed slope		0 (flat bed)	0 : 1:100

* This is the concentration at which the volume concentration of suspended particles becomes equal to 1 and hindered settling gives zero settling velocity

** Density 1050-1130 kg/m³ (excess density 41-171 kg/m³).

5.2.4 Results 1DV parameter study

A Saltelli sampler (a Monte Carlo method) is used to generate 16000 samples (random combinations of input) for the 1DV model based on the input parameters in Table 5.2 and Table 5.3. After running the 1DV model for all the samples the results are analysed. In the analysis of the results only 4990 of the samples are considered because of a memory limitation. Tests with analysis of 2000, 3000, 4000 samples gave similar results indicating that using 4990 of the 16000 samples is sufficient for representative results. Some individual 1DV WID results are described and compared with a 3D CFD model in Section 5.4. This section continues with the results of the parameter study.

The simulated most likely velocity of the WID fluidized layer (concentration averaged velocity) is shown in Figure 5-4. After 1000m distance from the WID the 1-sigma bandwidth of the WID fluidized layer velocity is 0.1-1.4 m/s with a mean value of ~0.7 m/s which similar to the mean input velocity at x=0. The extra driving force caused by the density difference and bed slope leads to an overall increase in WID fluidized layer velocity up to x~250m and further from the WID dredge the fluidized layer starts to decelerate as sediment is depositing out of the density current (leading to a reduction in driving force) and because of bed friction.

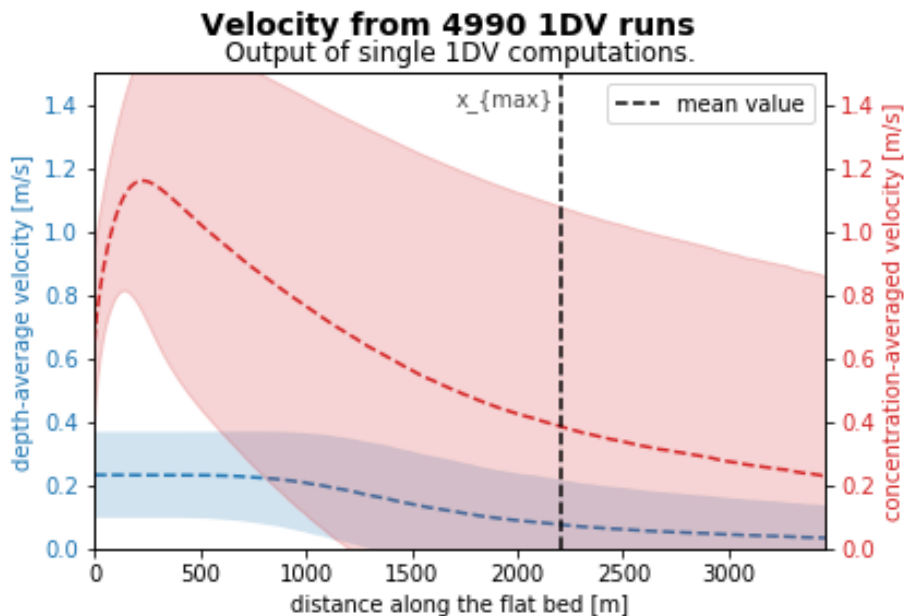


Figure 5-4 Mean and 1-sigma bandwidth velocity from 4990 samples. The depth averaged velocity is the average velocity in the whole vertical and the concentration averaged velocity is the average velocity of the fluidized layer

The most likely sedimentation of a WID working along a 250m long line following from the 4990 1DV runs is shown in Figure 5-4.

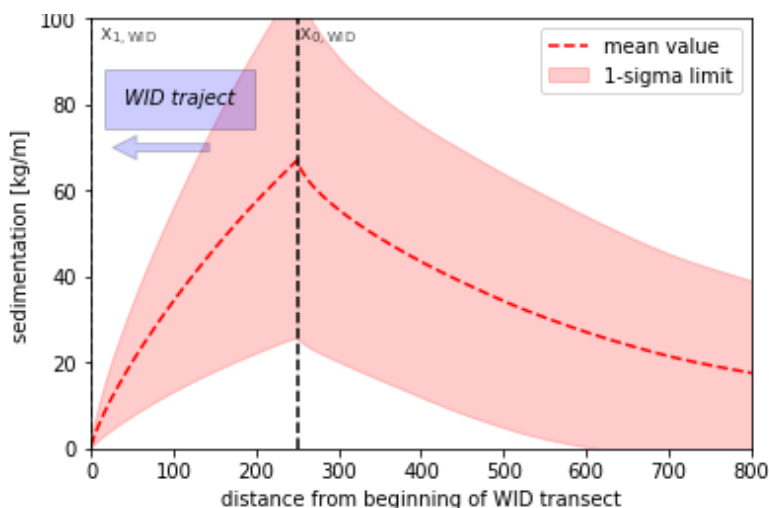


Figure 5-5 Mean and 1-sigma bandwidth of the sedimentation based on 4990 samples.

A Sobol sensitivity analysis is performed to find the most important input parameters for the resulting simulated WID sedimentation distance. The first order and total Sobol's indices are given in Figure 5-6 and Figure 5-7. The first order and total Sobol index give respectively the direct contribution to the output variance (SED max) from individual input factors and the overall contribution from an input factor considering its direct effect and its interactions with all the other factors. It shows that the parameters c_{fl} , ini_layer_height , bathymetry bed slope (see Table 5.3 for an explanation of these parameters) have a strong influence on the sedimentation distance together with c_{gel} and $fall_velocity$. This first group of parameters (c_{fl} , ini_layer_height , bathymetry) being important indicates that a WID fluidized layer has a density driven character. The bathymetry bed slope input dictates the extra gravity pull and

c_{fl} and ini_layer_height govern the amount of potential energy of the density current and for that reason are in the denominator of the densimetric Froude number which consists of the ratio of the square root of kinetic energy and potential energy ($Fr = \frac{u}{\sqrt{g c_{fl} H_{fl}}}$). The second group of parameters (c_{gel} and $fall_velocity$) govern the speed of the settling of sediment out the fluidized layer and therefore are important for the sedimentation distance. The ambient velocity and $ini_layer_velocity$ are less important for the sedimentation distance.

This analysis shows that the initial layer height of the fluidized layer and initial concentration together with the bed slope and mud properties are important for the WID density current behaviour. The right application of a WID dredge can lead to optimal initial layer height and initial concentration. Furthermore, WID can only be carried out under the right bed slope conditions. Mud properties like the gelling concentration and the settling velocity are important properties to consider when applying WID.

Sensitivity index - sobol method - sedimentation distance - 30 % sample size

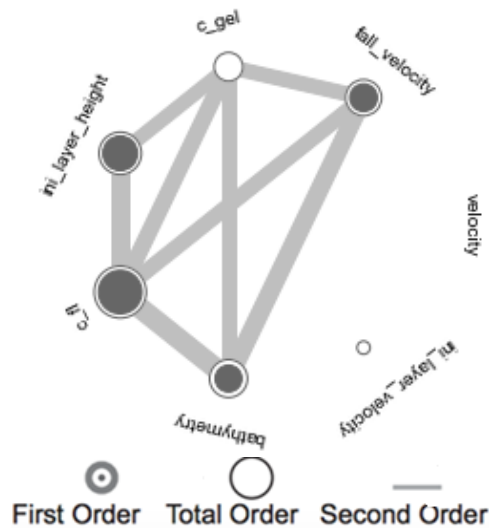


Figure 5-6 First, total and second order Sobol's indices

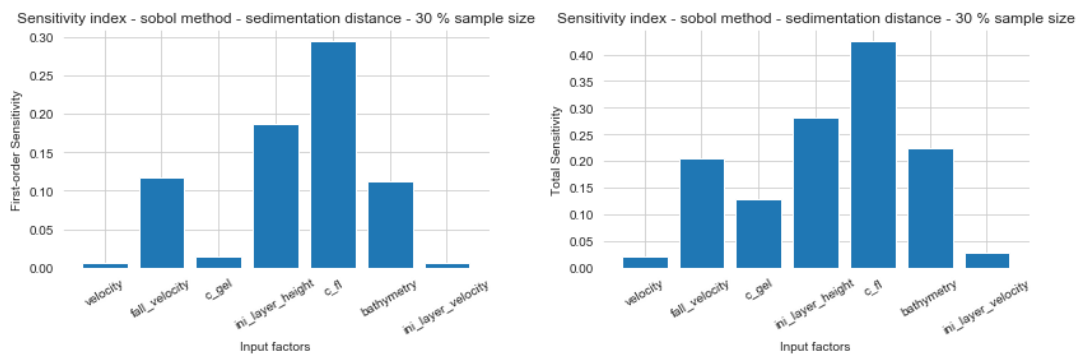


Figure 5-7 First order Sobol's indices (left) and total order Sobol's indices (right)

5.2.5 Conclusions 1DV

The Lagrangian 1DV model can be used as a rapid assessment tool for WID density currents. A parameter study for near field WID simulations has been carried out with the 1DV model. It provides a simulated characteristic WID density current velocity of ~0.7 m/s at 1000m distance from the WID dredger – similar to the applied mean input WID density current velocity at $x=0$. For the sedimentation distance the parameter study shows that initial layer height of the fluidized layer, the initial concentration together with the bed slope and

mud properties are the most important parameters being varied. The ambient velocity and the initial velocity of the fluidized layer are less important.

5.3 3D CFD modelling of WID

5.3.1 Brief description 3D CFD model TUDflow3d

TUDflow3d is an open source 3D multiphase, variable density CFD model (<https://github.com/openearth/tudflow3d>) and has originally been developed for accurate near field simulations of TSHD (Trailing Suction Hopper Dredger) overflow plumes on real scale. It has also been used for WID (Water Injection Dredging) density currents, MFE (Mass Flow Excavation) plumes, deep sea mining tailing plumes and salinity driven density flows. TUDflow3d has been validated for a wide range of flows where turbulence and/or density differences and/or interaction with objects are important. TUDflow3d can deal with sediment bed update (morphological change: erosion and sedimentation) within reasonable run times (hours-days).

In summary, TUDflow3d has the following characteristics:

- 3D multiphase, variable density, non-hydrostatic CFD solver;
- Fast, multiprocessor simulations on clusters via MPI;
- Less generic, but much faster than more generic CFD codes like Fluent and OpenFOAM;
- Open-source and easily adaptable for new features;
- Multi fraction sediment via the mixture approach (1-100 particle classes);
- Cohesive and/or non-cohesive sediment;
- Poly-disperse hindered settling and flocculation taken into account;
- Bed update (eroding and/or accreting bed);
- Real bathymetry from monitoring can be used in CFD model;
- Bathymetry and objects are simulated by an immersed boundary method;
- Several LES or RANS turbulence models.

Details on the numerics of TUDflow3d can be found in Appendix D and in De Wit (2015).

5.3.2 Application of TUDflow3d for a turbidity current on an erodible bed (experiment of Parker et al. 1987)

The 3D CFD model TUDflow3d is also applied for an experiment of Parker et al. (1987) consisting of a turbidity current on an erodible bed. An instantaneous snapshot of the modelled density current for experiment 13 (Parker et al. 1987) employing the Large Eddy Simulation (LES) turbulence model is shown in Figure 5-8. This is the same experiment as used for validating the 1DV model. The density current moves down the bed-slope and the bed consists of erodible fine sand. The individual turbulent eddies and whirls resolved on the grid in LES are clearly visible. When LES simulation is too expensive, it is also possible to carry out a RANS (Reynolds Averaged Navier Stokes) simulation in TUDflow3d. When a RANS turbulence model is employed the individual turbulent eddies are not resolved and the average turbulent flow is modelled.

Comparisons of simulated time averaged velocity and SSC profiles with measured ones is given in Figure 5-9. Different turbulence models are being compared: LES and RANS Realizable K-Epsilon. The vertical SSC profile and layer thickness of the density current is captured very well in the CFD LES model and the velocity profile is captured reasonably well with a small overprediction of the near bed velocity. The RANS Realizable K-Epsilon model is less accurate, but the RANS Realizable K-Epsilon model with a reduced near bed viscosity exactly giving the right amount of bed shear stress is almost as good as the LES result.

RANS Realizable K-Epsilon is computationally faster as LES because of the finer grid employed in LES runs.

For more details of this experimental case and other validation cases for density currents please see Appendix D. The conclusion is that TUDflow3d can accurately simulate density currents including erosion and sedimentation of the sediment and therefore is a suitable tool for simulating WID density currents.

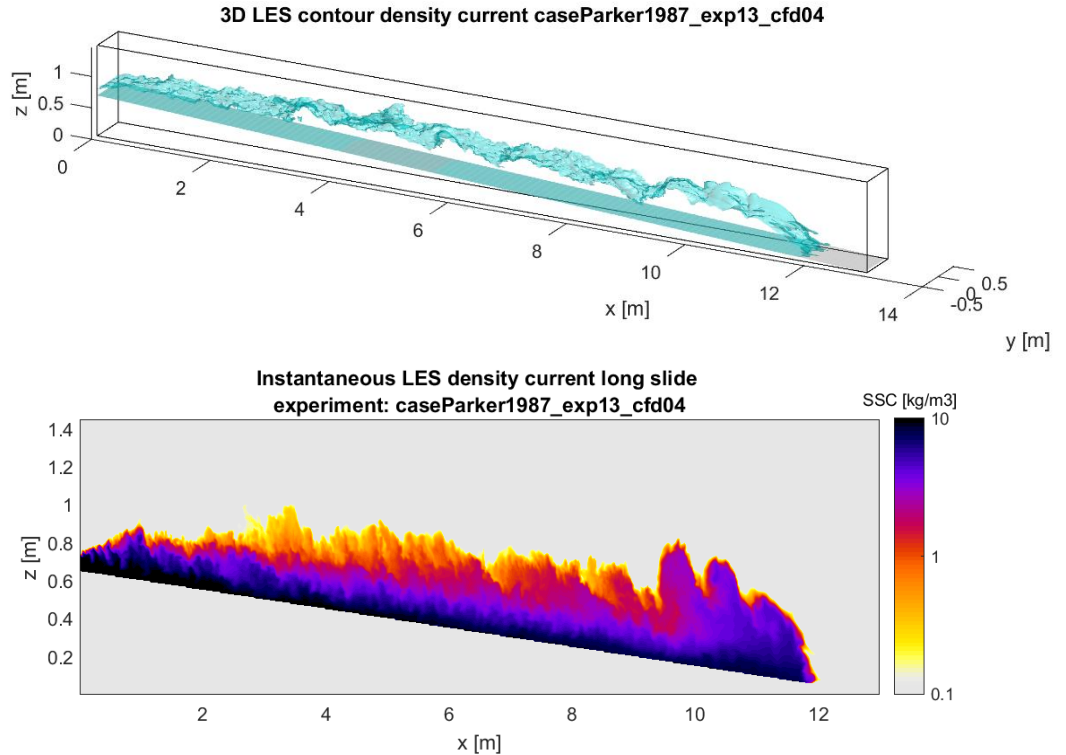


Figure 5-8 Instantaneous LES snapshot of 3D contour (top) of turbidity current and SSC at 2Dv slice through centre of turbidity current (bottom) for experiment 13 Parker et al. 1987

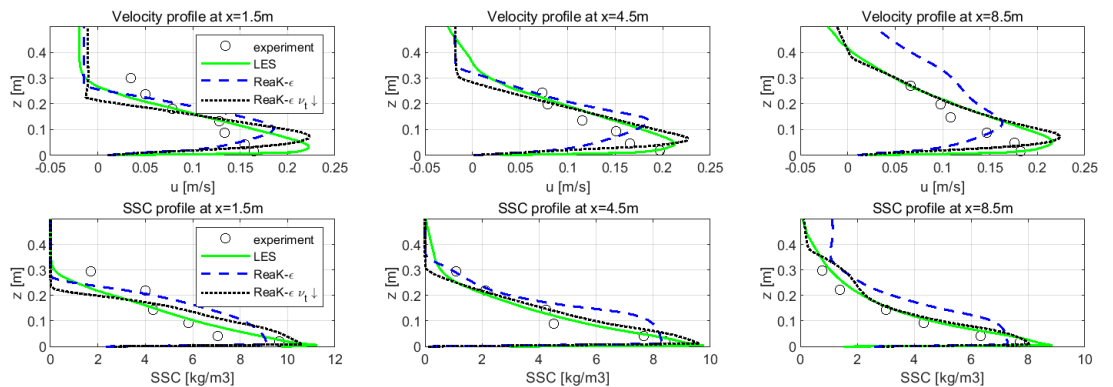


Figure 5-9 Comparison modelled time averaged velocity and SSC profiles with 3 different turbulence settings (LES; Realizable K-Epsilon and Realizable K-Epsilon with reduced near bed viscosity) and measurements for experiment 13 Parker et al. 1987

5.3.3 3D CFD of WID in real Port of Rotterdam bathymetry

TUDflow3d is applied for 3D CFD modelling WID in a real 3D environment in the Calandkanaal of the Port of Rotterdam. The measured multibeam bathymetry is used as input in the CFD model. The WID is modelled with a moving near bed suspended sediment source of 800 kg/s over a boom width of 13.8m with a flow discharge of 3.6 m³/s. The WID moves with a speed of 0.5 m/s and takes 600s to finish the 300m long track. While working the WID moves from East to West along the track and in between the WID moves back with a speed of 1.5 m/s without production. The applied CFD grid size is $\Delta x; \Delta y; \Delta z = 1\text{m}; 1\text{m}; 0.2\text{m}$ around the WID track with $\Delta x, \Delta y$ smoothly growing at larger distances. The LES turbulence approach is used. For the mud a floc settling velocity of 1 mm/s is applied with $c_{\text{gel}} = 600 \text{ kg/m}^3$ used in the hindered settling formulation. Non-Newtonian rheology is not included in the CFD model, but this improvement is foreseen in a next phase of Prisma as rheology may have some influence on the WID density current.

Figure 5-10 and Figure 5-11 show the 3D CFD result for a WID working along a 300m long line at the northern edge of the Calandkanaal. Figure 5-12 and Figure 5-13 show the result for a WID working along a 300m long line a little south of the middle of the Calandkanaal. At the moment of these density current images the WID has finished the 6th time along the track. Under influence of gravity the WID density current flows down the sloping bathymetry perpendicular to the line of working towards the deeper parts in the neighbourhood, which have been created as a sedimentation trap. For the WID action along the northern line these deeper parts are the dark blue spots in Figure 5-10 located just north of the middle of the Calandkanaal. For the WID action along the southern line the WID density current flows slowly towards the dark blue spot in Figure 5-12 round $x_{\text{RD}} = 6.65 \times 10^4$; $y_{\text{RD}} = 4.434 \times 10^5 \text{m}$. The bathymetry shows multiple little deeper ridges, perhaps from previous hopper dredging, and in the CFD model the WID density current follows those little ridges – just as is observed in reality.

These simulations show that TUDflow3d can be used for near field WID simulations in a real 3D environment using real bathymetry data. Comparison with WID lab experimental data and field WID data would be necessary to quantitate how accurate the near field WID simulations are for these conditions. It may be possible that in the CFD model the WID density current spreads more in lateral direction as in reality a WID density current can behave like a non-Newtonian fluid, see for example Figure 2.6 which indicates an expected yield stress of 5-10 Pa for 1170 kg/m³ WID fluid mud. Non-Newtonian flow is not included in the CFD model, but this improvement is foreseen in a next step.

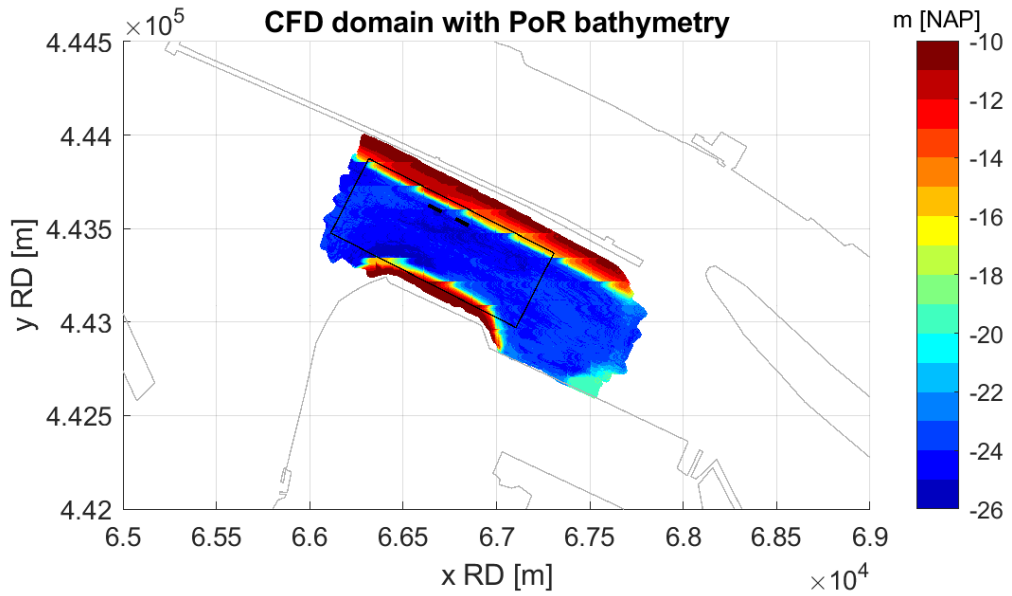


Figure 5-10 CFD modelling WID Calandkanaal along line A. Bathymetry indicated in colours, outline of the CFD model domain indicated with a black line and the WID line indicated with black dashed line.

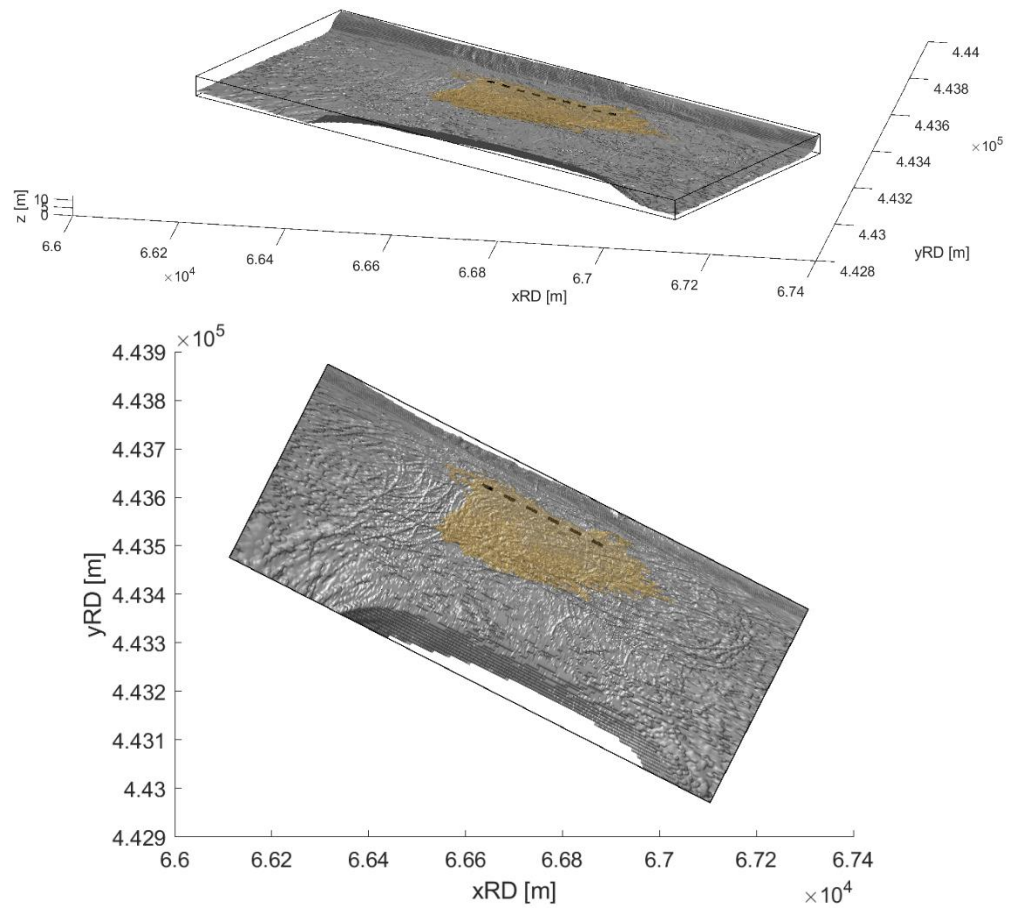


Figure 5-11 Impression of the modelled 3D WID density current Calandkanaal created along line A. 3D image (top) and top view (bottom) shows the location and extent of the density current in brown and the bathymetry in grey.

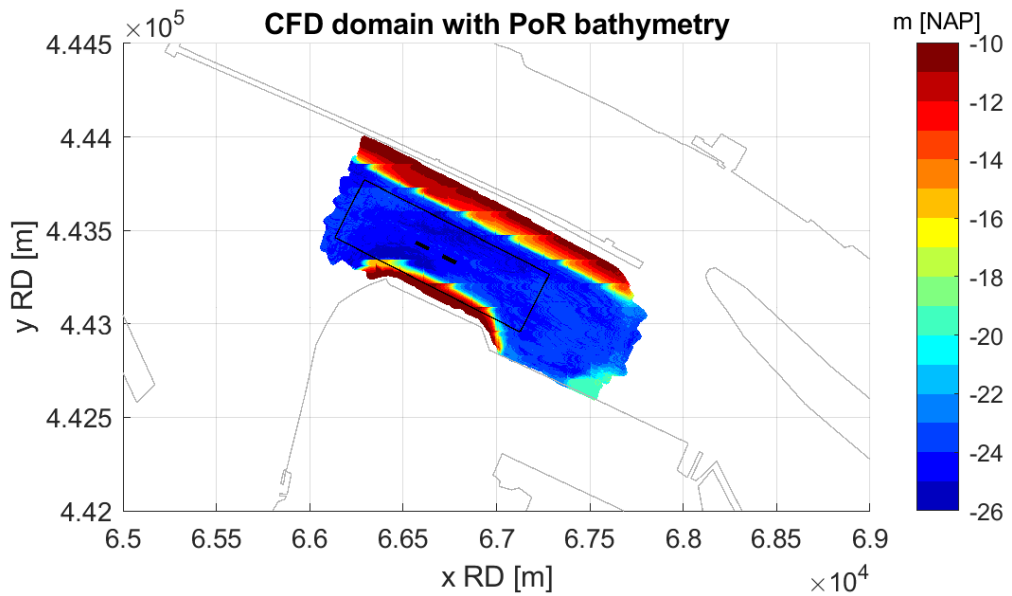


Figure 5-12 CFD modelling WID Calandkanaal along line B. Bathymetry indicated in colours, outline of the CFD model domain indicated with a black line and the WID line indicated with black dashed line.

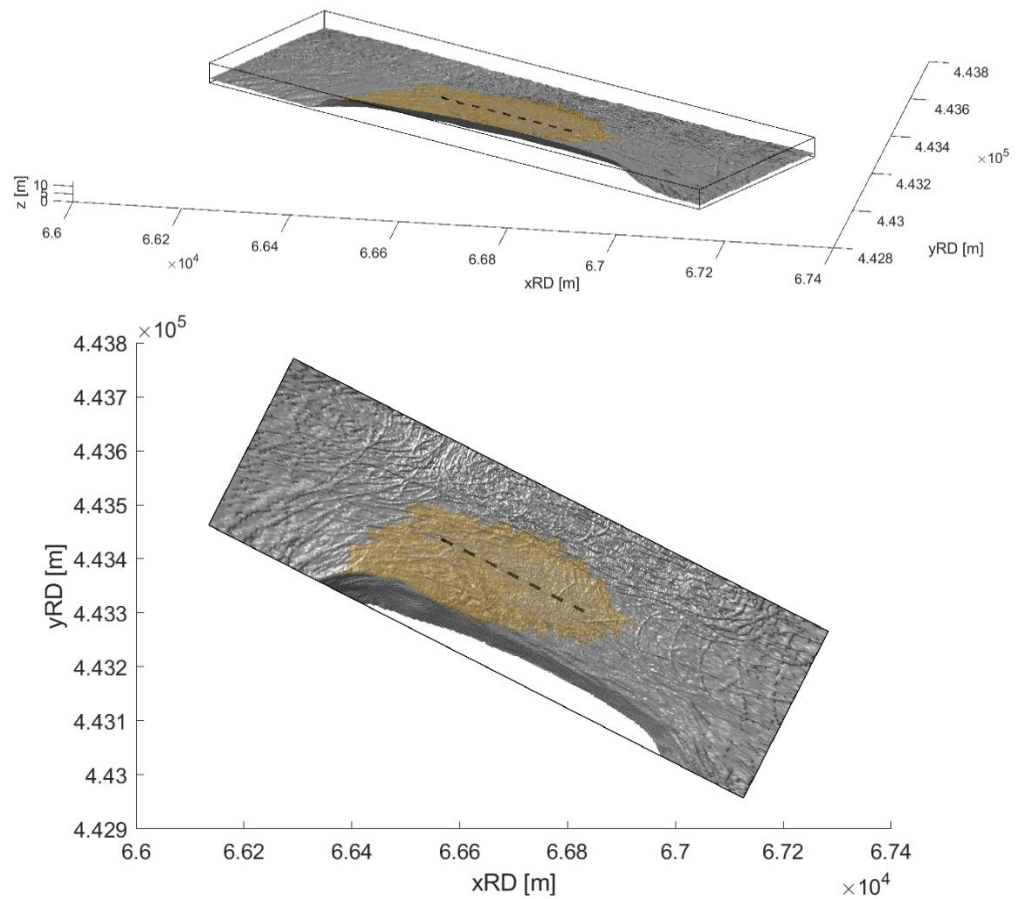


Figure 5-13 Impression of the modelled 3D WID density current Calandkanaal created along line B. 3D image (top) and top view (bottom) shows the location and extent of the density current in brown and the bathymetry in grey.

5.3.4 Conclusions 3D CFD modelling of WID

The 3D CFD model TUDflow3d is a suitable tool for near field simulations of a WID density current. It can handle fine near field grids and real bathymetry as initial bed. Turbulence is captured by the accurate LES approach or by a K-Epsilon RANS model. The feedback from sediment concentration in the WID density current to fluid density and resulting pull from gravity is incorporated. Sedimentation on the bed; erosion from the bed; hindered settling and multi-fraction sediment are included. Non-Newtonian rheology is not included in the CFD model, but this improvement is foreseen in a next step. The model can be applied for real 3D areas including bathymetric steering and lateral spreading perpendicular to the line of working of a WID.

5.4 Comparison CFD and 1Dv model

5.4.1 Introduction

For three cases a direct comparison between the CFD model and 1DV model for WID near field application is made:

- a) Reference WID input in Table 5.3;
- b) Reference WID input with a slurry concentration of 40 kg/m³ instead of 170 kg/m³;
- c) Reference WID input with a 1:100 bed slope instead of a flat bed.

The reference WID input consists of an initial layer thickness of the fluidized layer of 2m; a slurry concentration of 170 kg/m³ (block profile) with 0.7 m/s as velocity of the fluidized layer; a depth averaged velocity of 0.2 m/s; gelling concentration of 600 kg/m³; settling velocity of 1 mm/s and a flat bed.

Because the 1DV model cannot handle lateral spreading, for this comparison the lateral spreading is switched off in the CFD model by using a limited width of the computational domain and free slip lateral boundaries. The CFD model is used with the LES approach to capture turbulence as well as with the Realizable K-Epsilon RANS model. 1DV employs a standard K-Epsilon RANS model.

5.4.2 Results of the comparison

The comparison for reference input case a) is shown in Figure 5-14. The vertical velocity and concentration profiles are rather similar for the two transects (x=100 and x=500m) closer to the WID source and start to deviate more for x=1000 and x=1500m. The vertical height of the WID density current is very similar in both models, but the velocities inside the WID density current are a bit lower in the 1DV model and the upper edge of the WID density current is sharper in the 1DV model. The deposition flux of sediment from the WID density current towards the bed is similar in both models. The sediment flux per unit width in the WID density current ($S = \int uc dz$) starts exactly similar at x=0, because this is governed by the same starting input of the WID density current, but begins to deviate between 1DV and CFD for x>0. In equilibrium state (no buildup of sediment in the water column) the sediment flux in the WID density current only gets lower via the deposition flux and the following relation holds $S = S(x = 0) - \int Depo(x) dx$. The CFD model shows a sediment flux which is almost in equilibrium state (a longer CFD simulation period would have resulted exactly in the equilibrium state), but although the deposition in the 1DV model is similar to the deposition in the CFD model, the 1DV model shows a sediment flux which is different from the CFD model flux and from the expected equilibrium flux. This is a consequence of the fact that the Lagrangian 1DV model conserves mass in the water column and not sediment flux.

Figure 5-15 shows the comparison for an initial slurry concentration of 40 kg/m³ instead of 170 kg/m³. Again, the vertical profiles are rather similar at x=100 and x=500m and start to deviate for x=1000 and x=1500m. At x=1500m the WID density current is depleted of

sediment in the 1DV model, but in the CFD model there still is a considerable amount of sediment (~30% from initial sediment flux) available. Also for this case the deposition flux of the 1DV model and the CFD model are very similar up to $x=1200\text{m}$, but the resulting sediment flux in the water column is very different. The CFD model follows the equilibrium state of sediment flux nicely where the 1DV model sediment flux is considerably lower, leading to a too fast depletion of sediment.

For the case with a 1:100 bed slope in Figure 5-16 the 1DV model overpredicts the velocity and concentration compared to the CFD model. The sediment flux in the 1DV model even increases considerably, this is not possible without bed erosion and it is a consequence of the fact that the Lagrangian 1DV model conserves mass in the water column and not sediment flux. The deposition flux starts accurately at $x=0$, but then decreases to zero because of the very high near bed shear stresses caused by the simulated large velocity in the WID density current for this case.

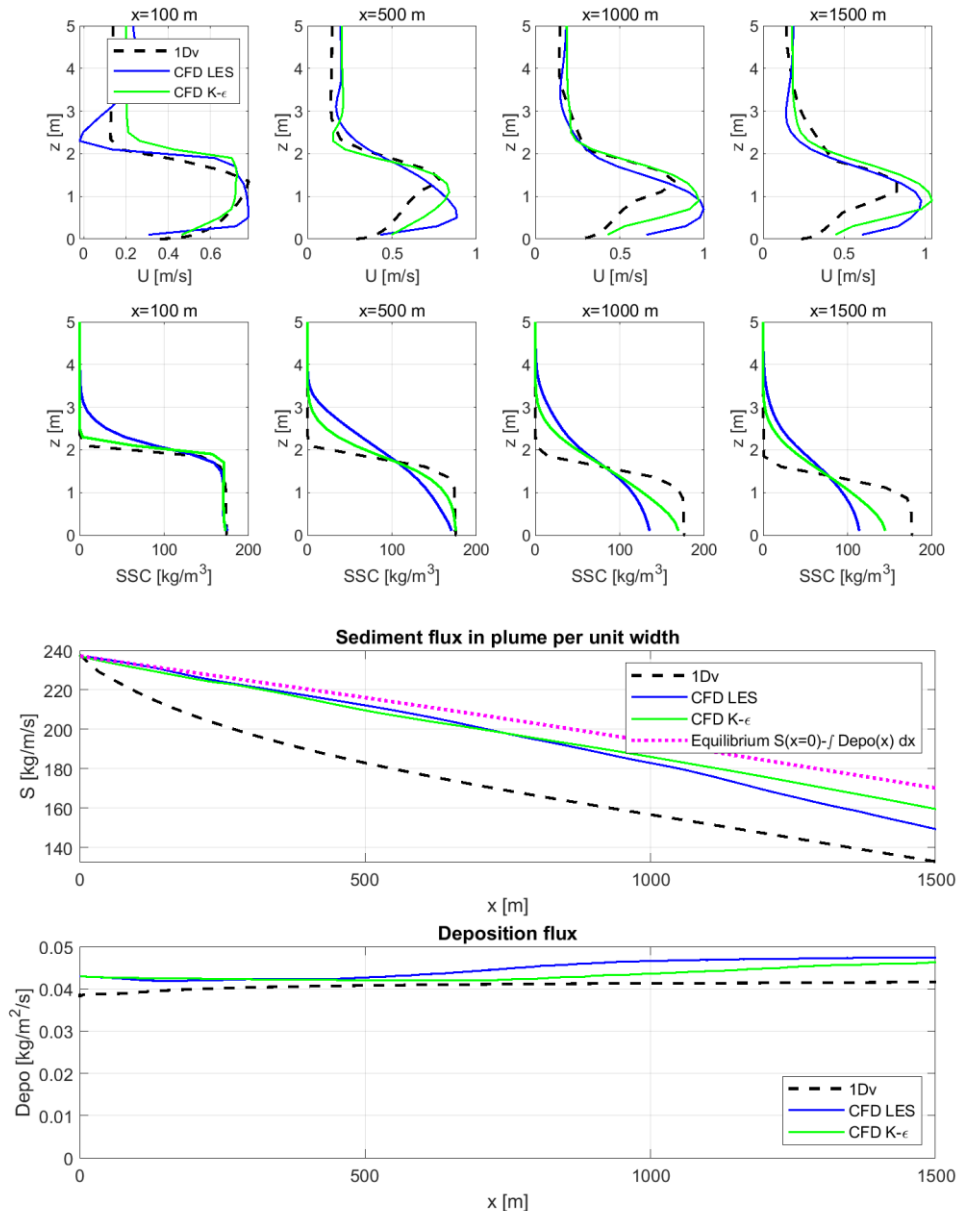


Figure 5-14 Comparison 1Dv with CFD for reference 1Dv WID simulation

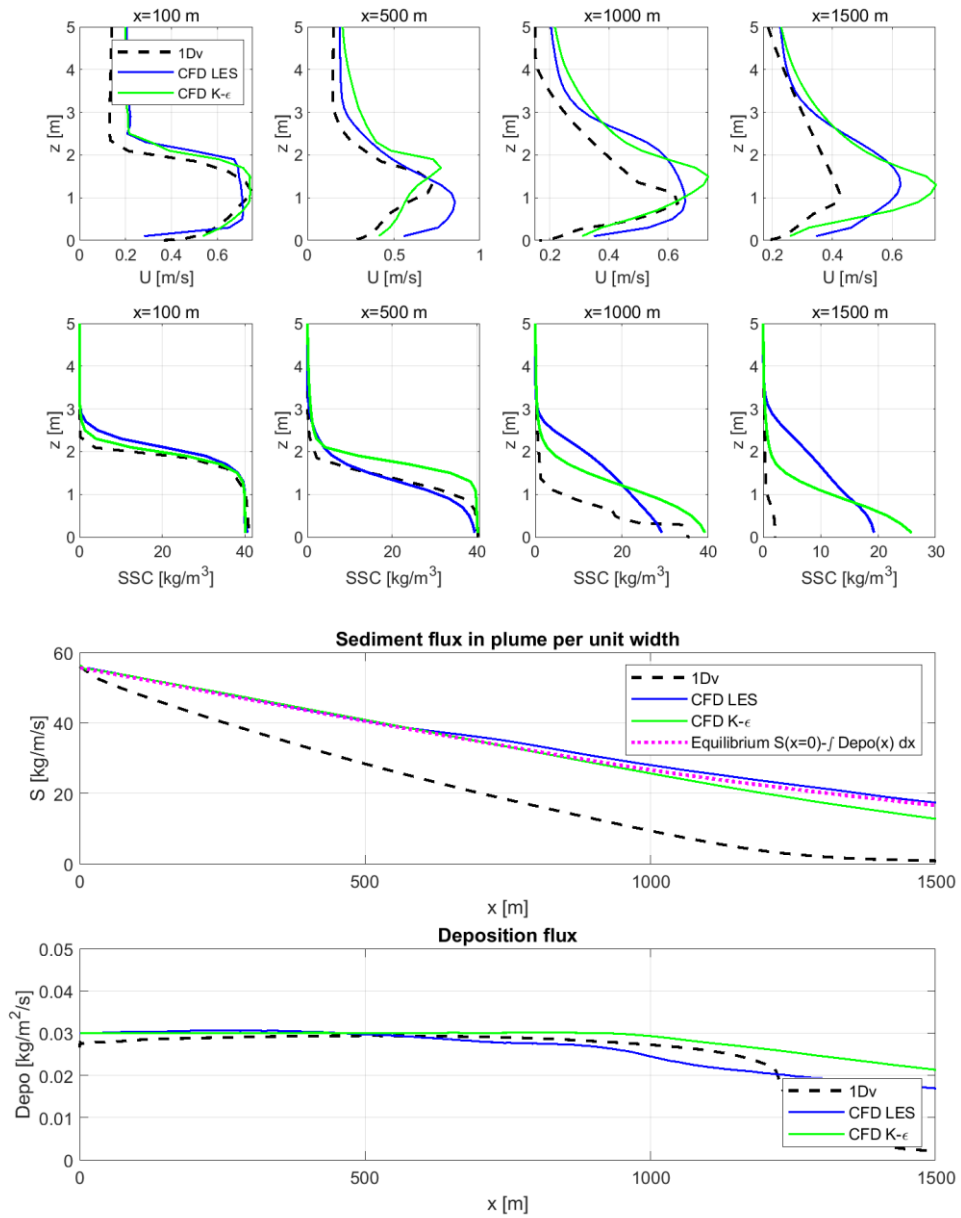


Figure 5-15 Comparison 1Dv with CFD for 1Dv WID simulation with 40 kg/m³ initial slurry concentration

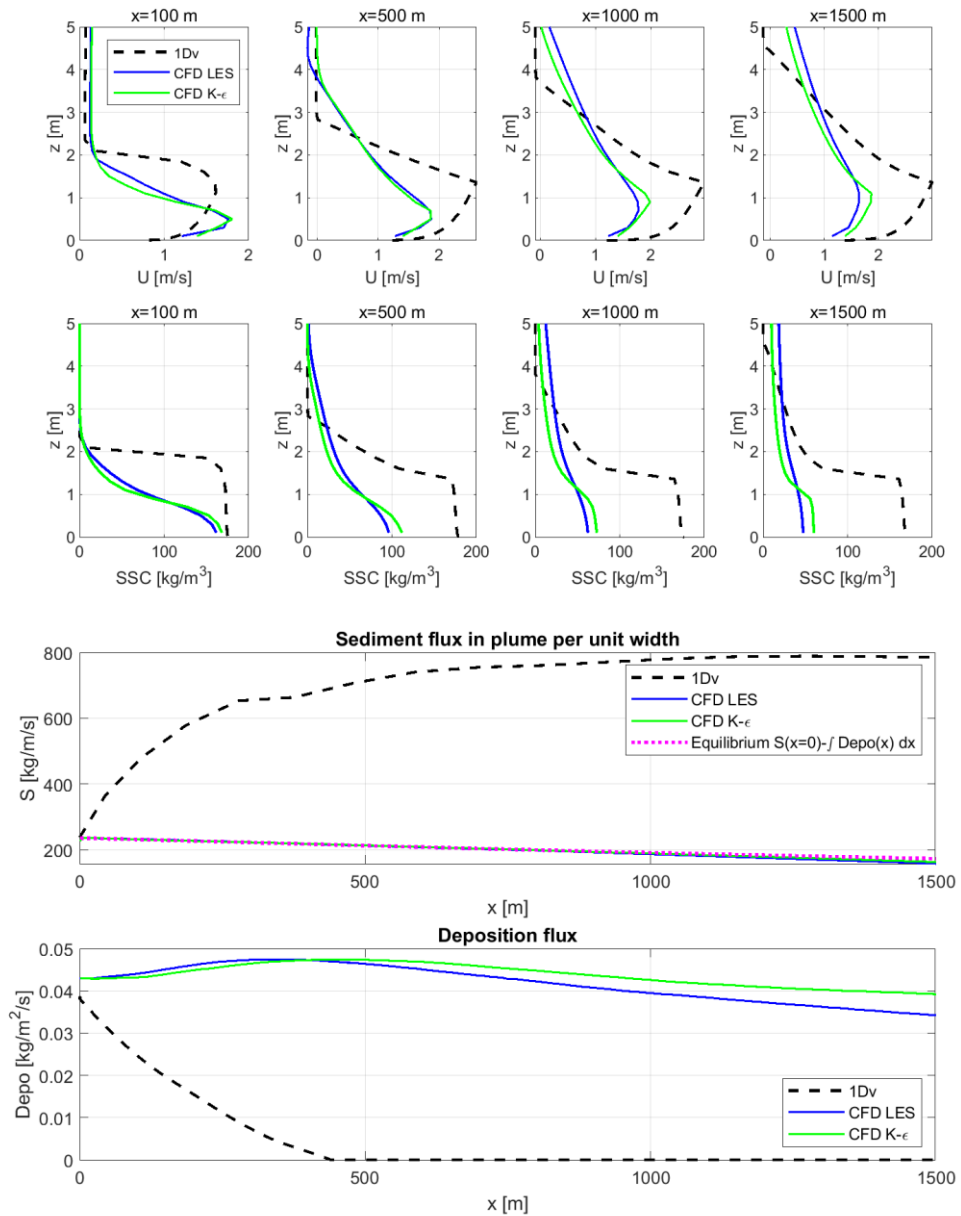


Figure 5-16 Comparison 1Dv with CFD for 1Dv WID simulation with 1:100 bed slope

5.4.3 Conclusion

The Lagrangian 1DV model has been developed as a rapid assessment tool which models the slurry generated by a WID vessel. It has some assumptions which need to be considered when using the model and interpreting its results. Most obvious assumption is neglecting lateral spreading in the 1DV model. For cases where lateral spreading is dominant it cannot be applied. The comparison between the 1DV model and a 3D CFD model with lateral spreading switched off carried out in this section highlighted the limitation of another assumption in the 1DV model, namely the conservation of mass in the water column instead of conservation of sediment flux in the water column. This is not a huge problem for moderate, slowly changing conditions, but can impact the results for different conditions.

The first two cases in this comparison, without bed slope, showed that for $x < 1000\text{m}$ from the WID the simulated deposition flux in 1DV agrees well with the CFD modelled deposition flux and also the vertical velocity and concentration profiles are not too far off. At larger distances

the deviations between 1DV and CFD start to grow. For the third test case with a steep bed slope of 1:100 results from the 1DV model were very different from the 3D CFD model.

5.5 Linking PRISMA WP3 and WP4

WP3 of PRISMA deals with far field WID plume dispersion and where the sediment will flow and deposit on the scale of several kilometers and WP4 deals with the near field density current behaviour. In a far field model interaction with ambient (tidal) currents, deposition on the bed, density influences are taken into account and the resulting WID plume velocities including topographic and bathymetric steering come out of the far field model albeit on the coarse resolution inherent to far field modelling.

The far field model does not incorporate near field physics and requires input on the WID density current characteristics at the end of near field. Therefore, the characteristic WID density current layer thickness and WID production found in WP4 will be used as input in the far field model. The initial velocity of the WID density current at the end of near field will be neglected as input because it is rather small (~0.4-1 m/s) and under influence of the initial density difference a velocity will be calculated by the far field model itself. Also, the amount of deposition in the near field is limited (after 500m distance ~10% has deposited in the simulated base case) and will be neglected. The complete WID production can be prescribed as suspended sediment flux in the far field model without prescribing extra sediment in the bed. The far field model itself can then determine where and how much sediment will deposit from the WID plume. Deposition processes are implemented adequately in the far field model.

Within PRISMA we defined the start of far field a few hundred meters from the WID dredger at the location far enough that individual trails of the WID dredger have no influence anymore and its behaviour can be captured on the coarser far field model grid (including density driven flow). Typical WID density current characteristics for the Calandkanaal area of the Port of Rotterdam consist of a density current height of 2-4m, densities in the order of ~1050-1130 kg/m³ (excess density ~30-170 kg/m³) and an estimated fine sediment flux of ~200-800 kg/s. This can be used as far field input over a zone of a few hundred meters from the WID dredger.

5.6 Conclusions of WP4

In WP4 the near field behaviour of WID density currents has been studied. Purpose of WID is to generate a fluidized soil density current by injecting high volumes of water with low pressure and then let nature do the work by moving the sediment under the influence of gravity. A WID often works by doing multiple trails at the same stretch. In this manner the density current is growing every trail.

As a working definition within PRISMA, the transition from near field to far field for a WID density current is defined at a location far enough that individual trails of the WID dredger have no influence anymore and its behaviour can be captured on the coarser far field model grid (including density driven flow). In practice that will define the far field as the zone starting a few hundred meters from the WID dredger.

Two different models have been applied for the near field WID behaviour and both models have been validated with experimental density current data.

- The Lagrangian 1DV model as a rapid assessment tool
- 3D multiphase CFD model TUDflow3d

The 3D multiphase CFD model has been applied for simulating WID in the Calandkanaal in the Port of Rotterdam using real 3D bathymetric data. Turbulence is captured by the accurate LES approach. The feedback from sediment concentration in the WID density current to fluid density and resulting pull from gravity is incorporated. Sedimentation on the bed; erosion from the bed; hindered settling and multi-fraction sediment are included. The model can be applied for real 3D areas including bathymetric steering and lateral spreading perpendicular to the line of working of a WID.

The 1DV model cannot handle lateral spreading and can only be used for cases with moderate conditions where the assumptions of the 1DV model hold. A benefit of the 1DV model is its very limited computational time. Comparison between the 1DV model and the 3D CFD model with lateral spreading switched off showed that for two cases without bed slope 1DV results and 3D CFD results are rather close for $x < 1000\text{m}$ from the WID and start to deviate more for $x > 1000\text{m}$. For a test case with a steep bed slope of 1:100 results from the 1DV model were very different from the 3D CFD model. The 1DV model has been used for a parameter study of thousands of simulations investigating the most likely WID density current characteristics and the most important input parameters. For the sedimentation distance the parameter study shows that initial layer height of the fluidized layer, the initial concentration together with the bed slope and mud properties are the most important parameters being varied. The ambient velocity and the initial velocity of the fluidized layer are less important for the initial flow development of the sediment layer fluidized by a WID.

In the near field zone of a few hundred meters round a WID dredge a WID density current in the Calandkanaal area of the Port of Rotterdam can be characterised by the following: it consist of a density current height of 2-4m, velocities in the order of $\sim 0.4\text{-}1\text{ m/s}$, densities of $\sim 1050\text{-}1130\text{ kg/m}^3$ (excess density $\sim 30\text{-}170\text{ kg/m}^3$) and an estimated fine sediment flux of $\sim 200\text{-}800\text{ kg/s}$.

6 Conclusions

The main objective of the project was to improve the understanding of fine sediment transport and sedimentation in the Port of Rotterdam and to deliver tools which can be utilized for successful employment, quantitative assessment and generic improvement of WID actions and sediment trapping. The developed knowledge can be further used for optimizing in-situ pilots at the Port of Rotterdam. Particularly, new knowledge, methods, tools and experience were gained on the following:

- Generated system knowledge: spatial and temporal variability of mud;
- Reliability of measuring devices: Graviprobe and Rheotune;
- Improved flow model (Delft3D);
- New sediment dynamics model (Delft3D);
- Near field behavior of WID density current models (the Lagrangian 1DV model as a rapid assessment tool and 3D multiphase CFD model TUDflow3d).

A series of four monitoring campaigns conducted in 2019/2020 helped to identify natural accumulation of fluid mud deposits in the Port of Rotterdam. The results of all monitoring campaigns showed that fluid mud layers are detected mainly in proximity to the coastal area, near the quay walls and in sediment traps. Based on the obtained system knowledge, new strategies for integrating WID into port maintenance can be developed:

- First, WID can be performed during the ebb tide in port locations in proximity to the coastal area. The hydrodynamic model can be used for predicting the tidal window for conducting WID.
- Second, WID can be performed near the quay walls combining WID with the knowledge of natural currents and the nautical bottom approach.
- Finally, sediment traps can potentially trap fluid mud. Thus, a number of sediment traps can be used for collecting WID-fluidized mud from the quay walls areas and the waterways. Newly-developed tools (the sediment dynamics model, the Lagrangian 1DV model as a rapid assessment tool and 3D multiphase CFD model TUDflow3d) can be used for designing sediment traps in the port and testing efficient WID scenarios in designated port areas.

Yield stress measurements of the in-situ devices Rheotune and Graviprobe were compared to yield stress values measured independently with MARS Haake rheometer tests on mud from the Port of Rotterdam and the Port of Hamburg. It was found out that both instruments can provide reliable indication of fluid mud layer thickness. The reliability of measured yield stress and density profiles by Rheotune and Graviprobe (yield stress only) depends on the availability of a reliable calibration database and turbulence correction, respectively. For Port of Rotterdam mud, Rheotune provides reliable data, the accuracy for density is within 2% and for strength within 20% most of the time, respectively. Without further corrections, the accuracy of Graviprobe strength profiles is a somewhat less (within 50% most of the time). Currently, there is no available monitoring tool that can be used for measuring rheological properties of fluid mud layers in a non-intrusive way. Furthermore, it is challenging to detect the spatial and temporal variability of fluid mud layer thickness and rheological properties. Thus, new tools should become available for practical application.

The developed modeling tools allowed to simulate sediment plume dispersion locally within the WID area and on the scale of the entire port. However, the finer the computational grid the longer the simulation time. Therefore, in future steps it is recommended to improve the grid resolution of areas under investigation. Furthermore, it is recommended to implement rheology because rheological properties become important at the turbulent to laminar transition and

affect the spreading of the sediment density current. Finally, the transport and deposition of fluid mud layers generated by WID have been evaluated with the modeling tools for a limited range of conditions and locations, i.e. a quiet period, a specific location (the Calandkanaal) and a period of few weeks. It is recommended to assess the difference in results for a quieter port area where the impact of density driven flow may be more dominant, test under stormier or higher discharge conditions and look at the longer-term resuspension and distribution of the WID sediment footprint.

The near field behaviour of WID density currents has been studied by two different models (the Lagrangian 1DV model as a rapid assessment tool and 3D multiphase CFD model TUDflow3d), which have been applied for the near field WID behaviour and validated with experimental density current data.

The 3D multiphase CFD model has been applied for simulating WID in the Calandkanaal in the Port of Rotterdam using real 3D bathymetric data. Sedimentation on the bed; erosion from the bed; hindered settling and multi-fraction sediment are included. The model can be applied for real 3D areas including bathymetric steering and lateral spreading perpendicular to the line of working of a WID.

Although the 1DV model cannot handle lateral spreading and can only be used for cases with slowly varying conditions where the assumptions of the 1DV model hold, an advantage of the 1DV model is its very limited computational time. Comparison between the 1DV model and the 3D CFD model with lateral spreading switched off showed that for two cases without bed slope 1DV results and 3D CFD results are rather close to each other for $x < 1000\text{m}$ from the WID and start to deviate more for $x > 1000\text{m}$. For a test case with a steep bed slope of 1:100 results from the 1DV model were very different from the 3D CFD model. The 1DV model has been used for a parameter study of thousands of simulations investigating the most likely WID density current characteristics and the most important input parameters. For the sedimentation distance the parameter study shows that initial layer height of the fluidized layer, the initial concentration together with the bed slope and mud properties are the most sensitive parameters. The ambient velocity and the initial velocity of the fluidized layer are less important for the initial flow development of the sediment layer fluidized by WID.

Overall, the tools for generating new knowledge, testing and piloting WID are now available. The developed tools can be used for predicting suspended sediment deposition and fluid mud dynamics within the entire port area and locally. The efficiency of various mitigation measures can be estimated by using the developed models. For instance, sediment trap locations and geometry can be chosen based on the models output such as bottom shear stresses, turbulence and siltation rates. Furthermore, WID actions can be designed for port areas, where WID can be conducted. Different WID strategies can be tested based on the WID area, type of sediment and hydrodynamic conditions. In this way the fate of WID-generated fluid mud can be studied and it can be quantified how much flows into the sediment trap, flows back to dredging areas (and will thus need to be dredged again if the fluid mud consolidates) or will leave the port area. This is essential input for optimization of WID strategies. Finally, in-situ monitoring tools can be applied for measuring density and yield stress of mud for applying the nautical bottom approach. The in-situ measurements can be combined with model predictions for planning dredging campaigns and WID actions.

References

Allwright D. 2002. The vibrating tuning fork fluid density tool. Study Group Report, Smith Institute, London.

Anton Paar. 2020a. <https://wiki.anton-paar.com/en/density-and-density-measurement/>, last accessed 10 February 2020.

Anton Paar. 2020b. <https://www.anton-paar.com/corp-en/products/details/dma-35/>, last accessed 10 February 2020.

Beeker AER. 1989. Nieuwe Waterbodemonsteker en de Kwaliteitsbeoordeling van Bodemonsters, H₂O (22), 1989, nr. 9.

Bezuijen A, den Hamer DA, Vincke L, Geirnaert K. 2018. Free Fall Cone Tests in Kaolin Clay. In Proceedings of the International Conference on Physical Modelling in Geotechnics, London, UK, 17–20 July 2018. Taylor & Francis Group, London, pp. 285–291

Boot M. 2000. *Near-field dispersal of overflow loss of hopper dredgers* (in Dutch). Master's thesis, TU Delft. Civil Engineering.

Cronin K, Huismans Y and van Kessel T. 2019. Local mud dynamics and sedimentation around the Maasmond. Final report. Deltares, 11202804-000-ZKS-0003

de Wit L. 2019. 3D CFD modelling of hopper sedimentation, *CEDA Dredging Days 2019*

de Wit L. 2015. 3D CFD modelling of overflow dredging plumes. *Ph.D. Thesis*, Delft University of Technology, Delft.

de Wit L and Van Rhee C. 2014a. Testing an Improved Artificial Viscosity Advection Scheme to Minimise Wiggles in Large Eddy Simulation of Buoyant Jet in Crossflow. *Flow, Turbulence and Combustion*, 92 (3)

de Wit L, Talmon AM and van Rhee C. 2014b, 3D CFD simulations of trailing suction hopper dredger plume mixing: a parameter study of near field conditions influencing the suspended sediment source flux, *Marine Pollution Bulletin*

Diaferia G, Kruiver PP and Vermaas T. 2013. Validation study of SILAS. Final report. Deltares, 1207624-000-BGS-0006.

dotOcean. 2020. GraviProbe 2.0 Datasheet Version GP-R02, obtained through <https://www.dotocean.eu/products/sediment-profilers/graviprobe/>, last accessed 10 February 2020.

Fonseca DL, Marroig PC, Carneiro JC, Gallo MN and Vinzon SB. 2019. Assessing rheological properties of fluid mud samples through tuning fork data, *Ocean Dynamics* 69: 51-57.

Gordon RB. 1974. Dispersion of dredge spoil dumped in near-shore waters. *Estuarine and Coastal Marine Science*, 2(4):349-58. [https://doi.org/10.1016/0302-3524\(74\)90004-8](https://doi.org/10.1016/0302-3524(74)90004-8)

Groposo V, Mosquera RL, Pedocchi F, Vinzón SB and Gallo M. 2015. Mud Density Propection Using a Tuning Fork, *J. Waterway, Port, Coastal, Ocean Eng.*, 2015, 141(5): 04014047.

Hallworth MA, Hogg AJ and Huppert HE. 1998. Effects of external flow on compositional and particle gravity currents. *Journal of Fluid Mechanics* 359(1), 109–142.

Harrison W and Wass ML. 1965. Frequencies of infaunal invertebrates related to water content of Chesapeake Bay sediments. *Southeastern Geology*, 6(4):177-86.

Hendrix E and Schuurman F. 2017. Modellingern alternatieve loswal locaties, Final report, Deltares, 1230860-000.

Hendriks EL, Sittoni L, van Kessel T and Winterwerp H. 2019. Development of a numerical rapid assessment tool to simulate fate and environmental impact of fluidized sediment layers, Deltares report 11203293-000-ZKS-0002 v1.2.

Inglis C and Allen F. 1957. The regimen of the Thames estuary as affected by currents, salinities, and river flow. *Proceedings of the Institution of Civil Engineers*, 7(4):827-68. <https://doi.org/10.1680/iicep.1957.2705>

Kirichek A. 2016. Rheological characteristics of fluid mud for ports and waterways. Internal report, the Port of Rotterdam.

Kirichek A, Rutgers R, Wensveen M and Van Hassent. 2017. Sediment management in the Port of Rotterdam. In: *Proceedings of the 10th Rostocker Baggergutseminar*; 11-12 September 2017; Rostock.

Kirichek A, Chassagne C, Winterwerp H and Vellinga T. 2018. How navigable are fluid mud layers? *Terra et Aqua*, 151:6-18.

Kirichek A and Rutgers R. 2020. Monitoring of settling and consolidation of mud after water injection dredging in the Calandkanaal. *Terra et Aqua*, 160:16-26

Kirichek A, Shakeel A and Chassagne C. 2020. Using in situ density and strength measurements for sediment maintenance in ports and waterways. *J. Soils Sediments*, 2546–2552. DOI: 10.1007/s11368-020-02581-8.

Kranenburg WM. 2015a. Evaluatie van Het OSR-Model Voor Zoutindringing in de Rijn-Maasmonding (I) - Onderdeel KPP B&O Waterkwaliteitsmodelschematisaties 2014. 209459–000. Delft: Deltares.

Kranenburg WM. 2015b. Evaluatie van Het OSR-Model Voor Zoutindringing in de Rijn-Maasmonding (II) - Onderdeel KPP B&O Waterkwaliteitsmodelschematisaties 2015.1220070-000-ZKS-0009. Delft: Deltares.

Kranenburg WM and Schreuder R. 2015. OSR-Simulaties Voor Zoutindringing in de Rijn-Maasmonding Zomer 2003 - Onderdeel KPP Waterkwaliteitsmodelschematisaties 2015.1220070–000. Delft: Deltares.

Masson E, Harrington J, Widjeveld A, Groot H, Lord R, Debuigne T, Wensveen M, Hamilton A, Benzerzour M, O'Connor M and Lemiere B. 2019. SURICATES: demonstration through pilots of sediment reuse for coastal defence or climate change mitigation, in proceedings of 10th International Conference on the Remediation and Management of Contaminated Sediments, Battelle Sediments Conference, New Orleans, the USA.

McAnally WH, Friedrichs C, Hamilton D, Hayter E, Shrestha P, Rodriguez H, Sheremet A, Teeter A. 2007. Management of fluid mud in estuaries, bays, and lakes. I: Present state of understanding on character and behavior. *J Hydraulic Eng* 133:9-22

Manninen M, Taivassalo V and Kallio S. 1996. On the Mixture Model for Multiphase Flow VTT Publications 288. *Technical Research Center of Finland*.

Mehta AJ. 2013. An introduction to hydraulics of fine sediment transport: World Scientific Publishing Company.

de Nijs M, Winterwerp JC and Pietrzak JD. 2010. The Effects of the Internal Flow Structure on SPM Entrapment in the Rotterdam Waterway. *Journal of Physical Oceanography*, 40 (11):2357–2380, ISSN 0022-3670. doi: 10.1175/2010jpo4233.1.

Stema Systems. 2017. RheoTune Datasheet, obtained through <https://stema-systems.nl/equipment/rheotune-densitune-dredging-equipment-insitu-measurements/>, last accessed 10 February 2020.

Parker WR and Sills GC. 1990. Observation of Corer Penetration and Sample Entry During Gravity Coring. In E.A. Hailwood et al. (eds.). *Marine Geological and Surveying Sampling*: pp 101-107. Dordrecht, the Netherlands: Kluwer Academic Publishers.

Parker G, Garcia M, Fukushima Y and Yu W. 1987. Experiments on turbidity currents over an erodible bed, *Journal of Hydraulic Research*, 25:1, 123-147, DOI:10.1080/00221688709499292

Pedocchi F, Groppo V, Mosquera R, Gallo M and Vinzon S. 2015. Measuring mud properties with a tuning-forks device, in: Toorman EA et al. (Ed.) INTERCOH2015: 13th International Conference on Cohesive Sediment Transport Processes. Leuven, Belgium, 7-11 September 2015. VLIZ Special Publication, 74: pp. 198-199.

PIANC. 2013. Injection Dredging, Report 120, PIANC, Brussels.

PIANC. 2014. Harbour Approach Channels - Design Guidelines, Report 121, PIANC, Brussels.

Radermacher M, de Wit L, Winterwerp JC and Uijttewaal WSJ. 2016. Efficiency of hanging silt screens in crossflow. *Journal of Waterway, Port, Coastal and Ocean Engineering*, 142 (1).

Ross MA and Mehta AJ. 1989. On the Mechanics of Lutoclines and Fluid Mud. *Journal of Coastal Research*, 51-62.

Shakeel A, Kirichek A and Chassagne C. 2019. Rheological Analysis of Mud from Port of Hamburg, Germany. In *Journal of Soils and Sediments*, 10 September 2019, <https://doi.org/10.1007/s11368-019-02448-7>.

Skinner LC and McCave IN. 2003. Analysis and Modelling of Gravity- and Piston Coring Based on Soil Mechanics. *Marine Geology* 199(1):181-204

Smolar J, Maček M and Petkovšek A. 2017. Rheological properties of marine sediments determined by using two coaxial cylinder rheometers. In Proceedings of the 19th International Conference on Soil Mechanics and Geotechnical Engineering, Seoul 2017, pp: 517-520.

van Rijn L. 1984., Sediment pick-up functions, *Journal of Hydraulic Engineering*, 110(10).

van Rijn L, Water Injection Dredging <https://www.leovanrijn-sediment.com/papers/Waterinjectiondredging.pdf>

Wegener SB and Kalumba D. 2016. Discrete Element Analysis of Granular Soil Recovery in a Vibrocore. In *Proceedings of the first Southern Africa Geotechnical Conference*, 169-175

Whitehouse R, Soulsby R, Roberts W, Mitchener H. 2000. *Dynamics of Estuarine Muds: A Manual for Practical Applications*: Thomas Telford.

Wikipedia. 2020. Drag Coefficient, website https://en.wikipedia.org/wiki/Drag_coefficient, last accessed 21 April 2020.

Winterwerp J. 2002. Near-Field Behavior of Dredging Spill in Shallow Water. *Journal of Waterway, Port, Coastal, and Ocean Engineering* 128(2), 96–98.

Wurpts R and Torn P. 2005. 15 Years' Experience with Fluid Mud: Definition of the Nautical Bottom with Rheological Parameters, *Terra et Aqua*, 99:22-32

A In-situ and lab measurements

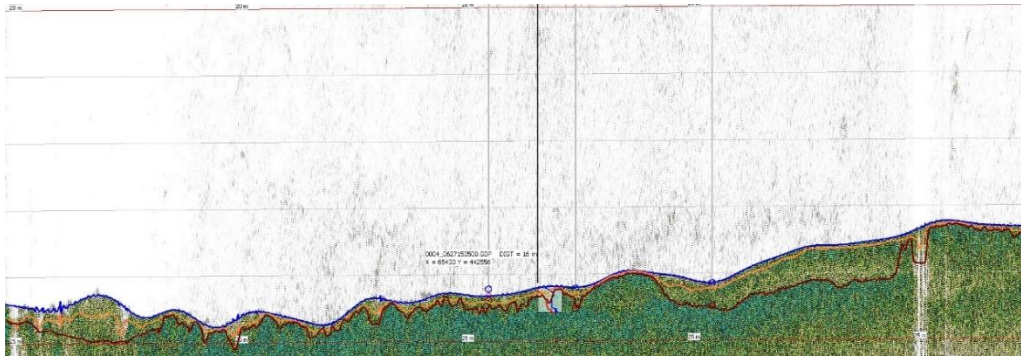


Figure A1. Fluid mud detection at the Beerkanaal on 27-06-2019: line 1. Blue level – water-mud interface, red level – sharp density contrast in seismic data, orange level – 100 Pa (Bingham yield stress) level. Blue and red vertical lines show density and Bingham yield stress profiles, respectively.

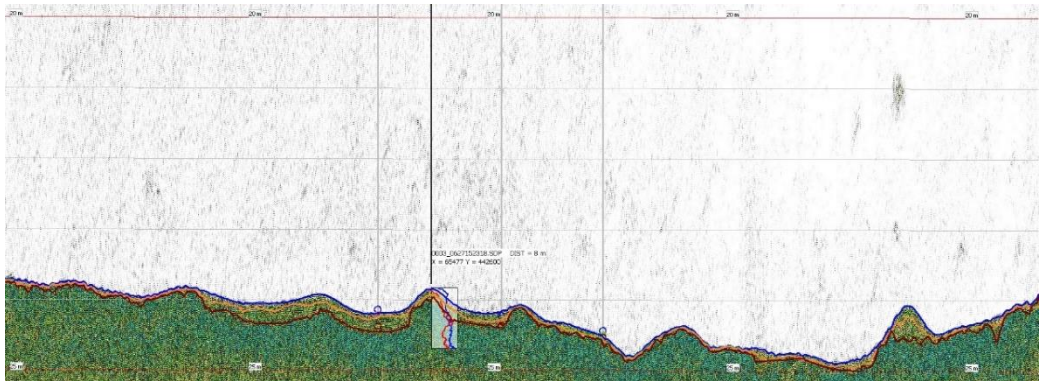


Figure A2. Fluid mud detection at the Beerkanaal on 27-06-2019: line 2. Blue level – water-mud interface, red level – sharp density contrast in seismic data, orange level – 100 Pa (Bingham yield stress) level. Blue and red vertical lines show density and Bingham yield stress profiles, respectively.

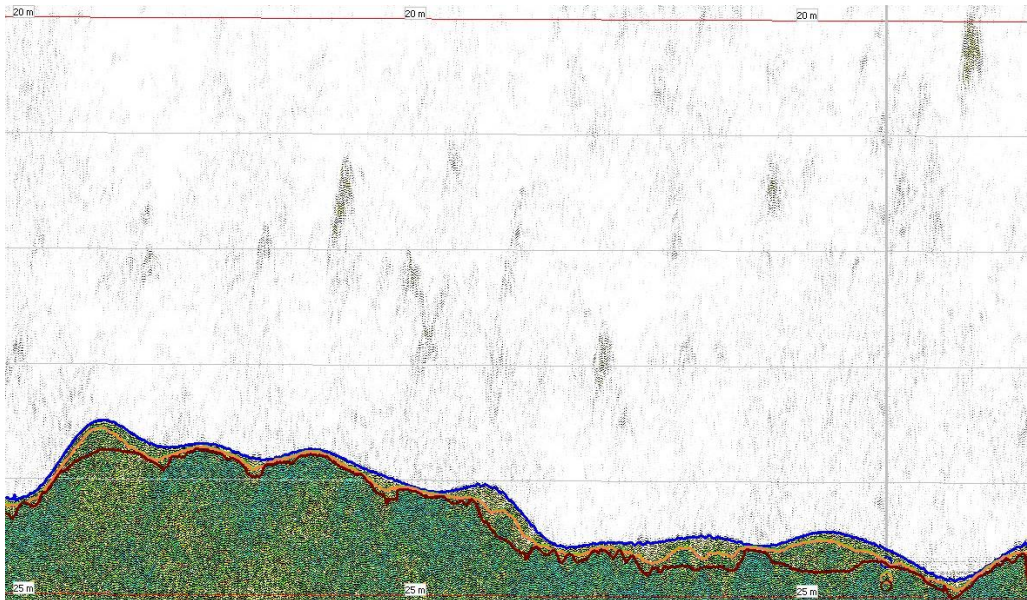


Figure A3. Fluid mud detection at the Beerkanaal on 27-06-2019: line 3. Blue level – water-mud interface, red level – sharp density contrast in seismic data, orange level – 100 Pa (Bingham yield stress) level.

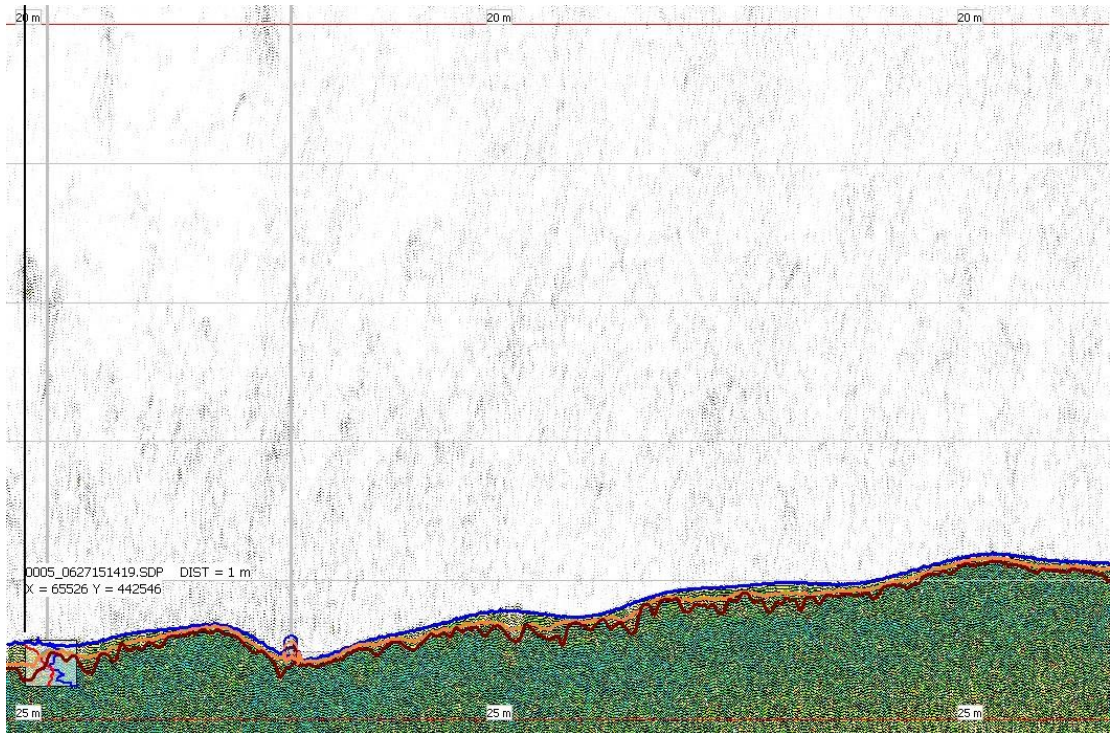


Figure A4. Fluid mud detection at the Beerkanaal on 27-06-2019: line 3 (continued). Blue level – water-mud interface, red level – sharp density contrast in seismic data, orange level – 100 Pa (Bingham yield stress) level. Blue and red vertical lines show density and Bingham yield stress profiles, respectively.

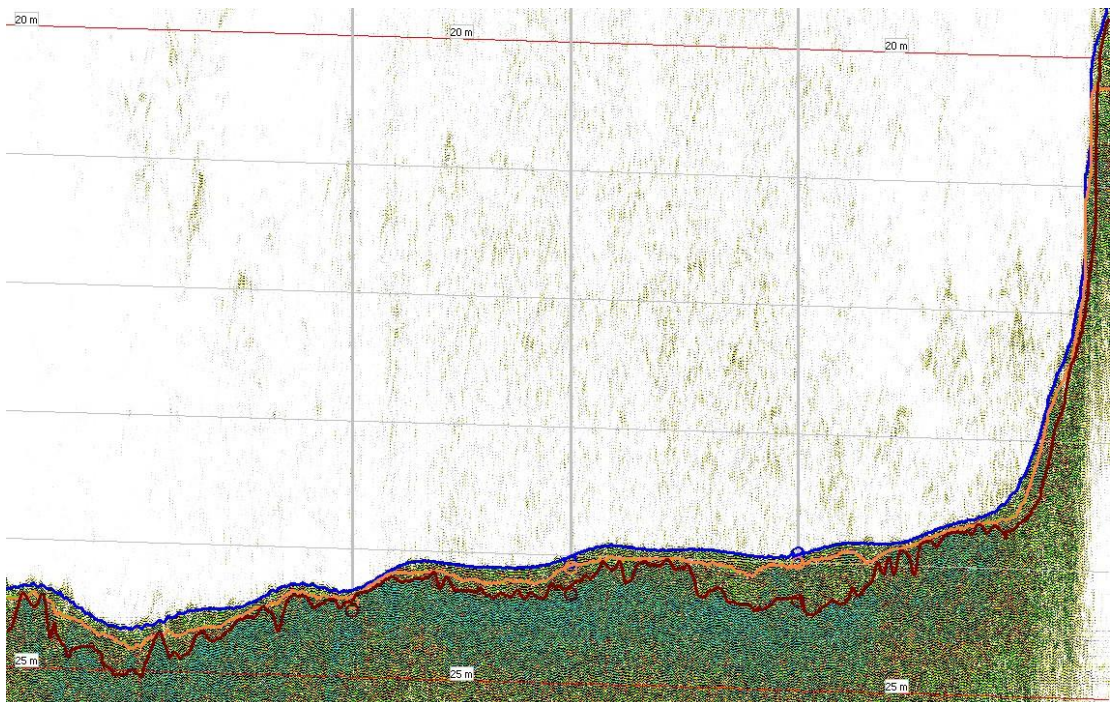


Figure A5. Fluid mud detection at the Beerkanaal on 27-06-2019: crossline 1. Blue level – water-mud interface, red level – sharp density contrast in seismic data, orange level – 100 Pa (Bingham yield stress) level.

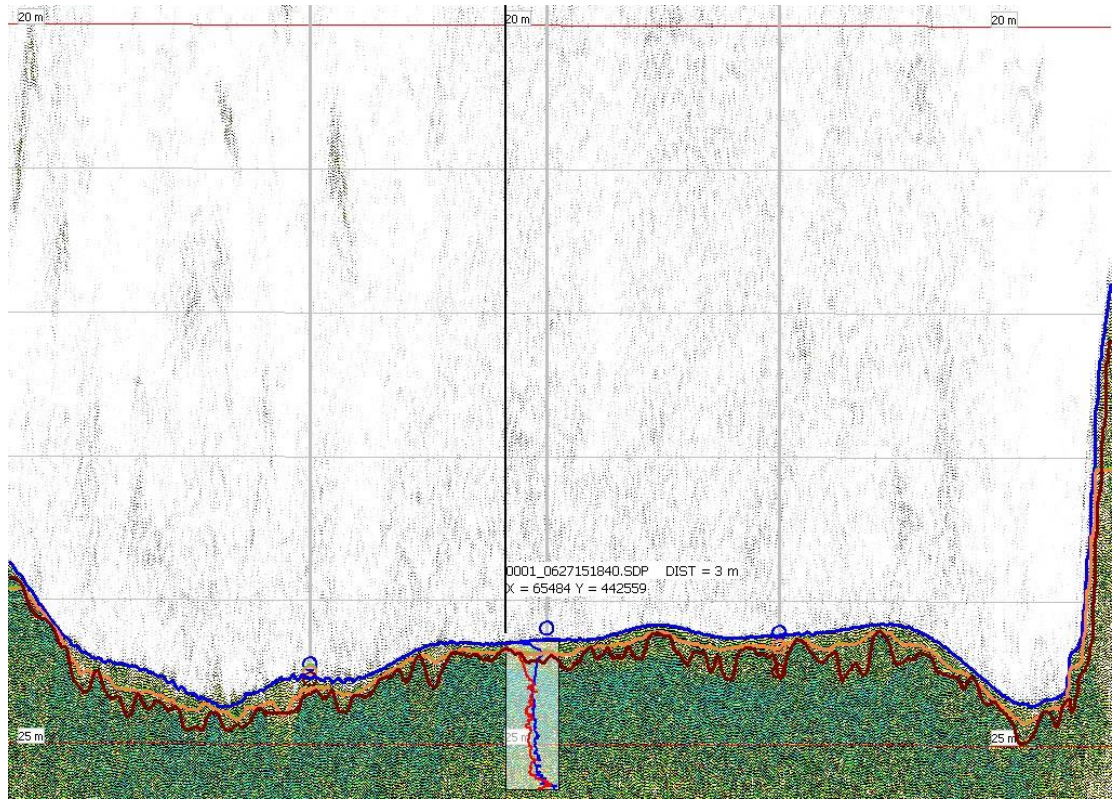


Figure A6. Fluid mud detection at the Beerkanaal on 27-06-2019: crossline 2. Blue level – water-mud interface, red level – sharp density contrast in seismic data, orange level – 100 Pa (Bingham yield stress) level. Blue and red vertical lines show density and Bingham yield stress profiles, respectively.

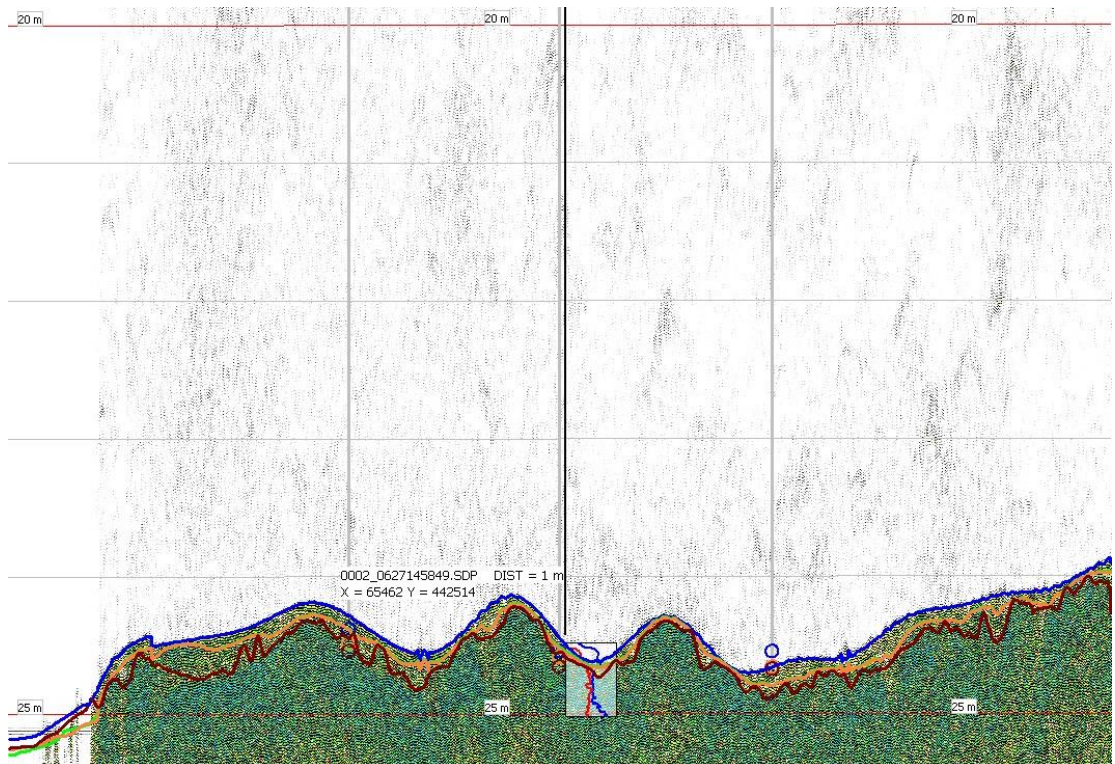


Figure A7. Fluid mud detection at the Beerkanaal on 27-06-2019: crossline 3. Blue level – water-mud interface, red level – sharp density contrast in seismic data, orange level – 100 Pa (Bingham yield stress) level. Blue and red vertical lines show density and Bingham yield stress profiles, respectively.

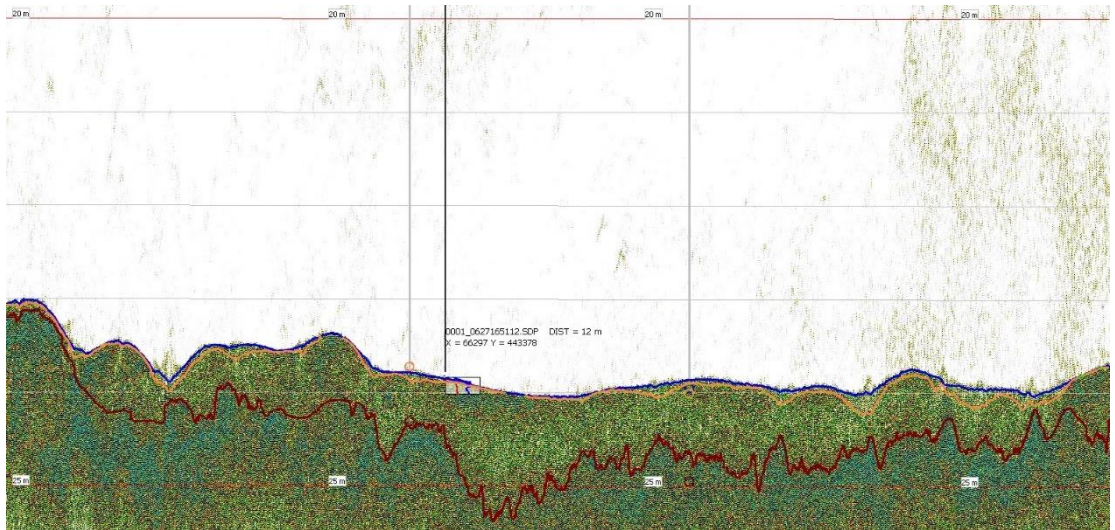


Figure A8. Fluid mud detection at the Calandkanaal on 27-06-2019: line 1. Blue level – water-mud interface, red level – sharp density contrast in seismic data, orange level – 100 Pa (Bingham yield stress) level. Blue and red vertical lines show density and Bingham yield stress profiles, respectively.

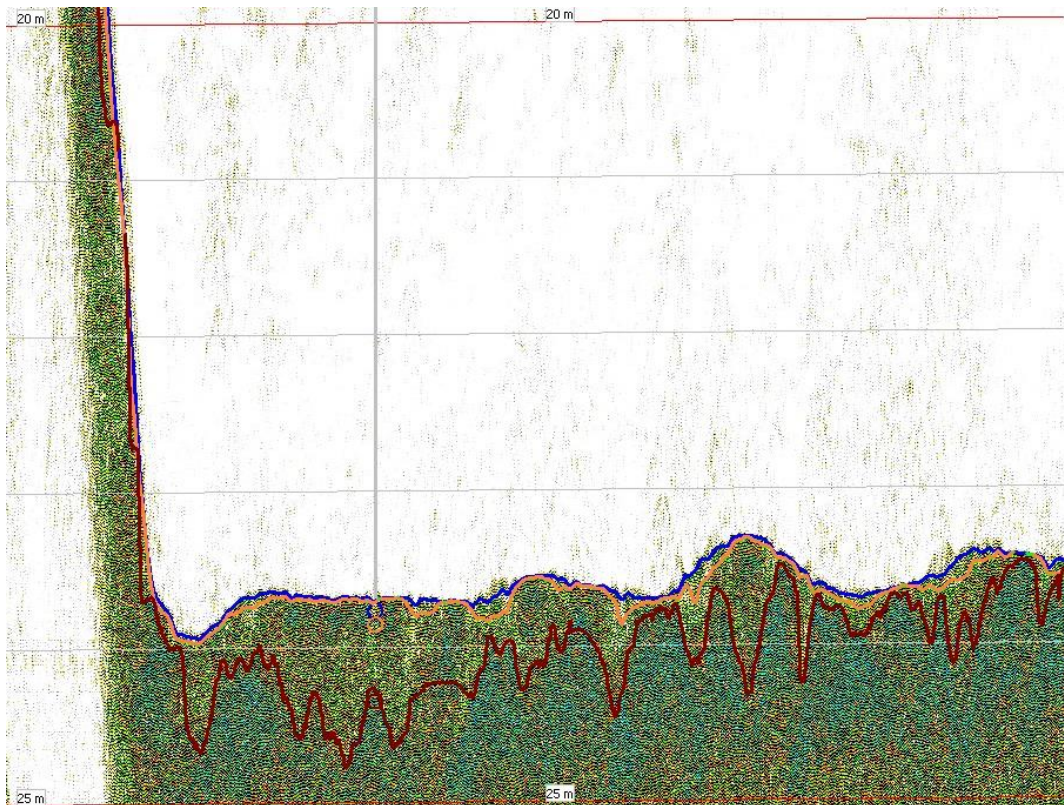


Figure A9. Fluid mud detection at the Calandkanaal on 27-06-2019: line 2. Blue level – water-mud interface, red level – sharp density contrast in seismic data, orange level – 100 Pa (Bingham yield stress) level.

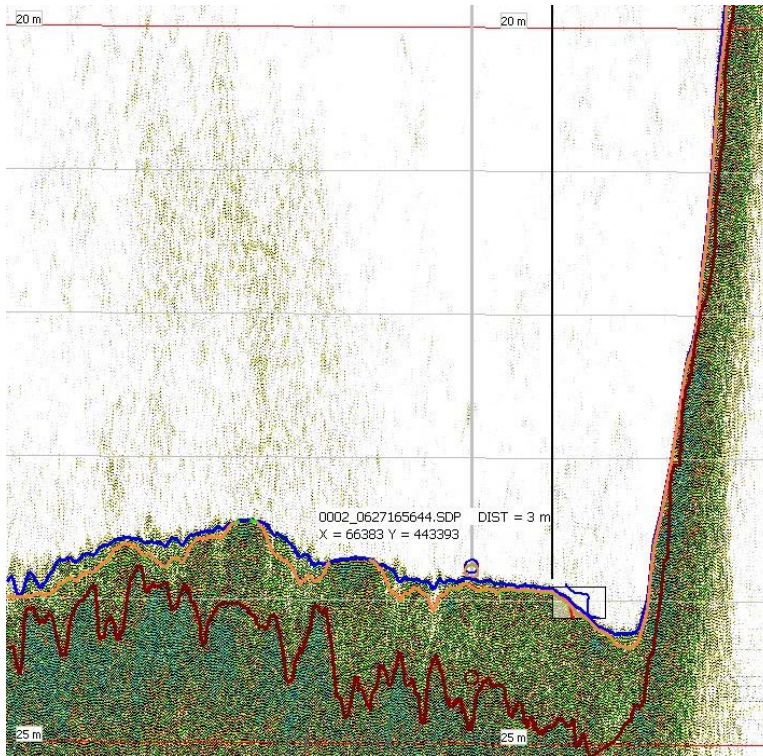


Figure A10. Fluid mud detection at the Calandkanaal on 27-06-2019: crossline 1. Blue level – water-mud interface, red level – sharp density contrast in seismic data, orange level – 100 Pa (Bingham yield stress) level.

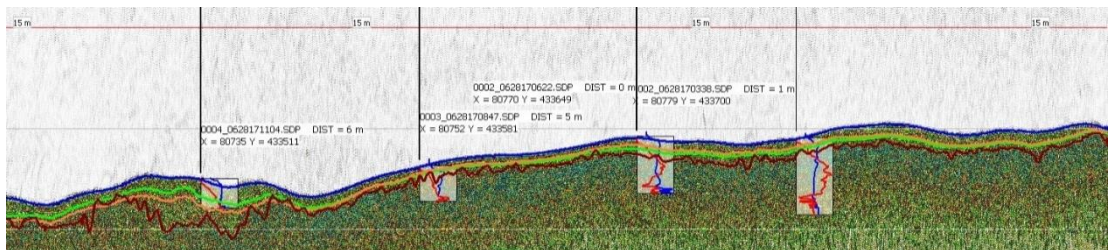


Figure A11. Fluid mud detection at the 3e Petroleumhaven on 28-06-2019: line 1. Blue level – water-mud interface, red level – sharp density contrast in seismic data, orange level – 1.2 kg/l (density) level, green level – 100 Pa (Bingham yield stress) level. Blue and red vertical lines show density and Bingham yield stress profiles, respectively.

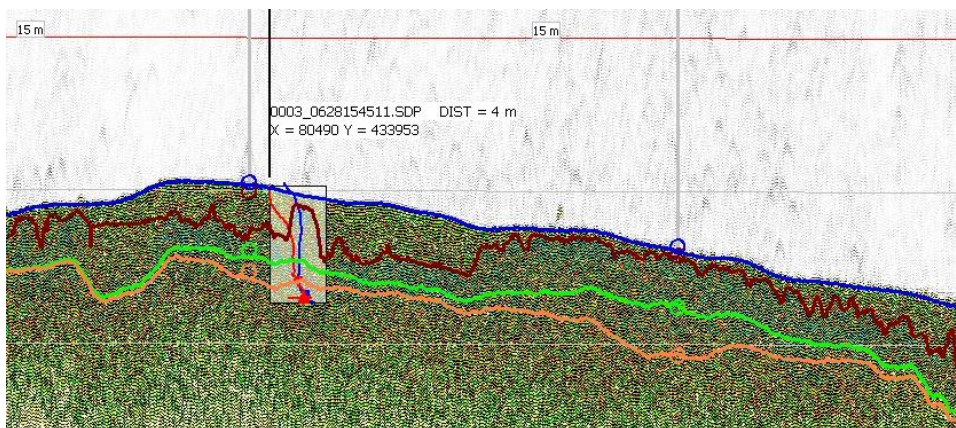


Figure A12. Fluid mud detection at Botlek on 28-06-2019: line 1. Blue level – water-mud interface, red level – sharp density contrast in seismic data, orange level – 1.2 kg/l (density) level, green level – 100 Pa (Bingham yield stress) level. Blue and red vertical lines show density and Bingham yield stress profiles, respectively.

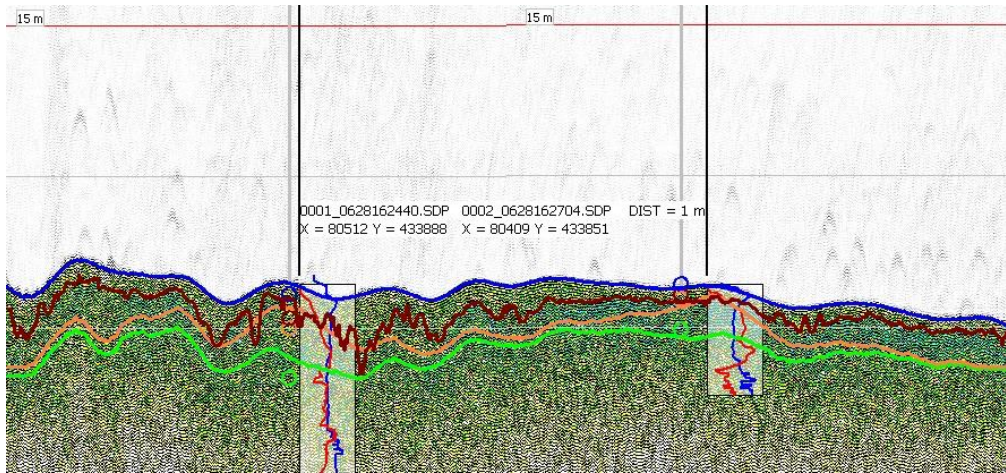


Figure A13. Fluid mud detection at Botlek on 28-06-2019: line 2. Blue level – water-mud interface, red level – sharp density contrast in seismic data, orange level – 1.2 kg/l (density) level, green level – 100 Pa (Bingham yield stress) level. Blue and red vertical lines show density and Bingham yield stress profiles, respectively.

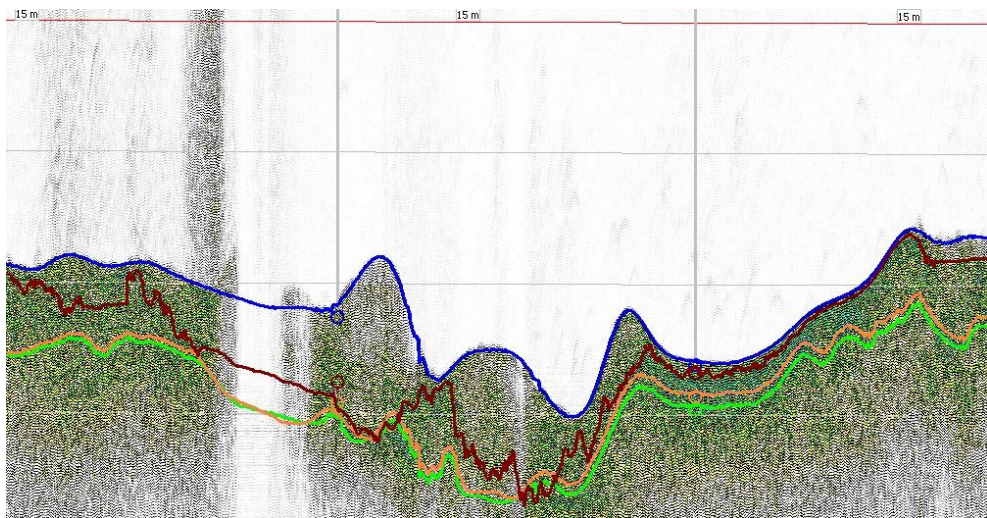


Figure A14. Fluid mud detection at Botlek on 28-06-2019: line 3. Blue level – water-mud interface, red level – sharp density contrast in seismic data, orange level – 1.2 kg/l (density) level, green level – 100 Pa (Bingham yield stress) level. Blue and red vertical lines show density and Bingham yield stress profiles, respectively.

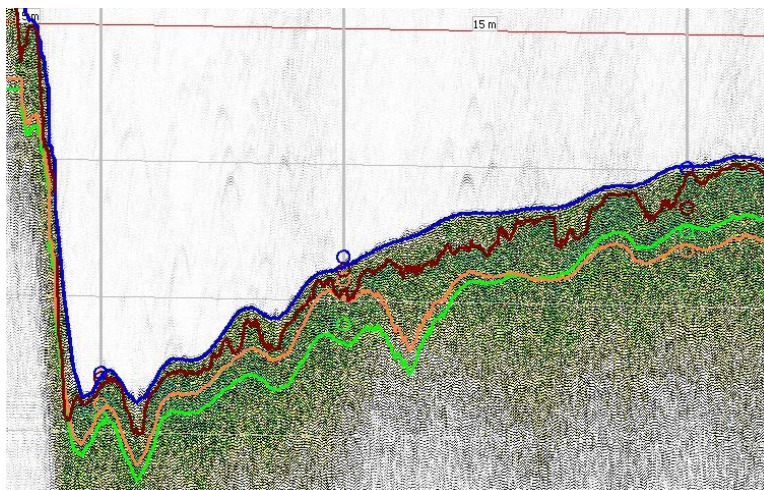


Figure A15. Fluid mud detection at Botlek on 28-06-2019: crossline 1. Blue level – water-mud interface, red level – sharp density contrast in seismic data, orange level – 1.2 kg/l (density) level, green level – 100 Pa (Bingham yield stress) level.. Blue and red vertical lines show density and Bingham yield stress profiles, respectively.

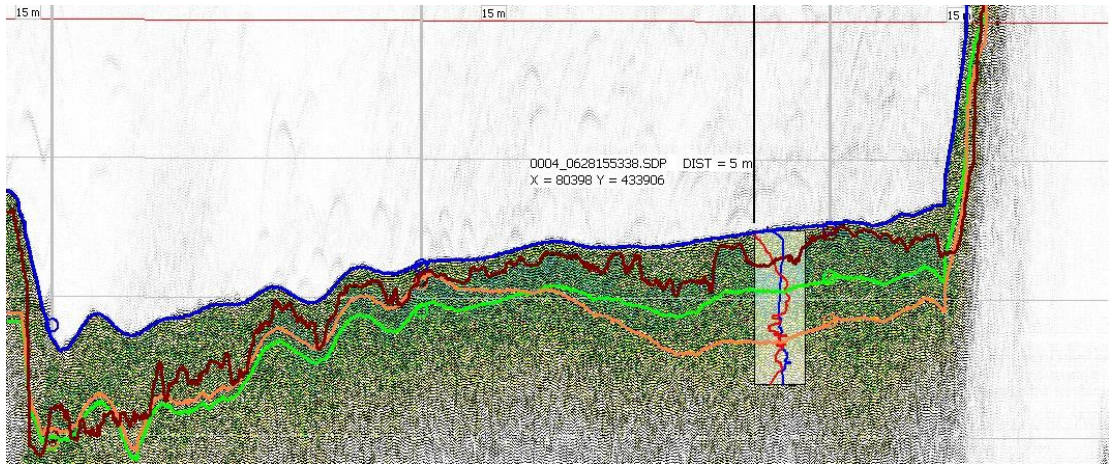


Figure A16. Fluid mud detection at Botlek on 28-06-2019: crossline 2. Blue level – water-mud interface, red level – sharp density contrast in seismic data, orange level – 1.2 kg/l (density) level, green level – 100 Pa (Bingham yield stress) level. Blue and red vertical lines show density and Bingham yield stress profiles, respectively.

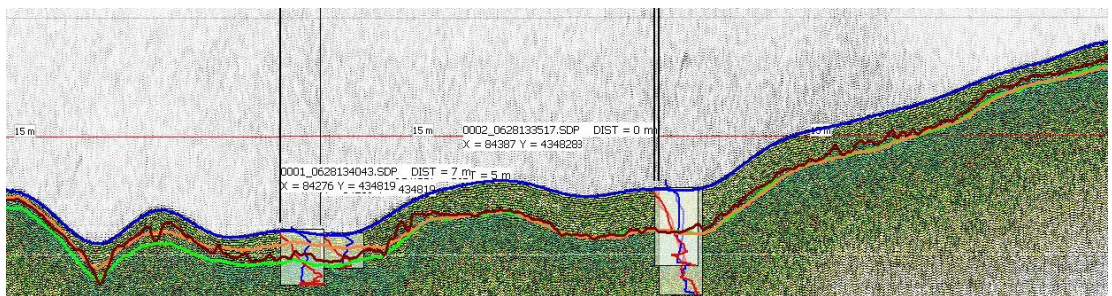


Figure A17. Fluid mud detection at KTM kade on 28-06-2019: line 1. Blue level – water-mud interface, red level – sharp density contrast in seismic data, orange level – 1.2 kg/l (density) level, green level – 100 Pa (Bingham yield stress) level. Blue and red vertical lines show density and Bingham yield stress profiles, respectively.

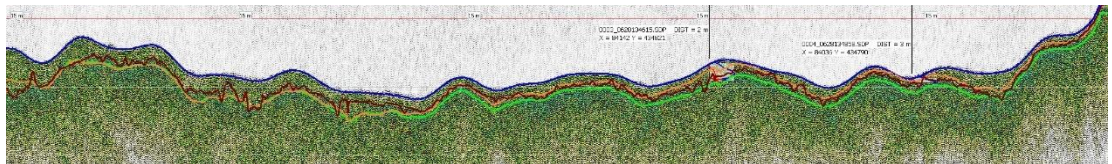


Figure A18. Fluid mud detection at KTM kade on 28-06-2019: line 2. Blue level – water-mud interface, red level – sharp density contrast in seismic data, orange level – 1.2 kg/l (density) level, green level – 100 Pa (Bingham yield stress) level. Blue and red vertical lines show density and Bingham yield stress profiles, respectively.

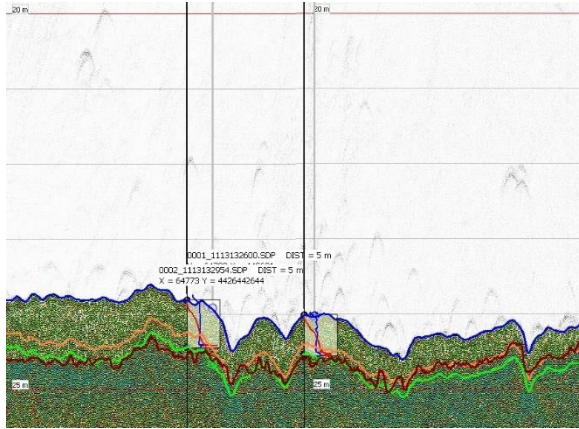


Figure A19. Fluid mud detection at the 8 Petroleumhaven on 13-11-2019: center. Blue level – water-mud interface, red level – sharp density contrast in seismic data, orange level – 1.2 kg/l (density) level, green level – 100 Pa (Bingham yield stress) level.

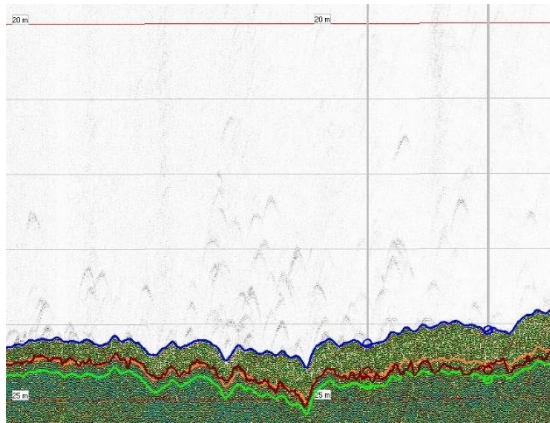


Figure A20. Fluid mud detection at the 8 Petroleumhaven on 13-11-2019: east. Blue level – water-mud interface, red level – sharp density contrast in seismic data, orange level – 1.2 kg/l (density) level, green level – 100 Pa (Bingham yield stress) level.

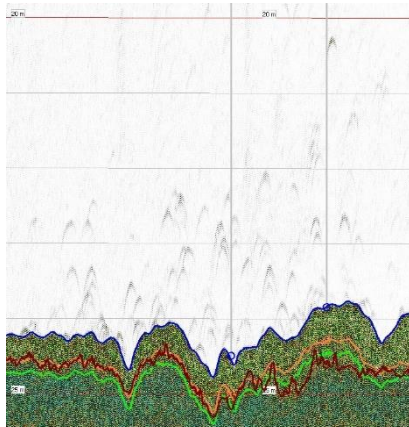


Figure A21. Fluid mud detection at the 8 Petroleumhaven on 13-11-2019: west. Blue level – water-mud interface, red level – sharp density contrast in seismic data, orange level – 1.2 kg/l (density) level, green level – 100 Pa (Bingham yield stress) level.

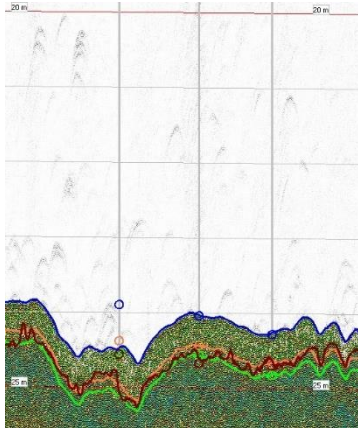


Figure A22. Fluid mud detection at the 8 Petroleumhaven on 13-11-2019: north. Blue level – water-mud interface, red level – sharp density contrast in seismic data, orange level – 1.2 kg/l (density) level, green level – 100 Pa (Bingham yield stress) level.

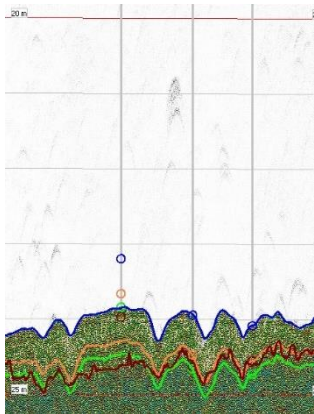


Figure A23. Fluid mud detection at the 8 Petroleumhaven on 13-11-2019: south. Blue level – water-mud interface, red level – sharp density contrast in seismic data, orange level – 1.2 kg/l (density) level, green level – 100 Pa (Bingham yield stress) level.

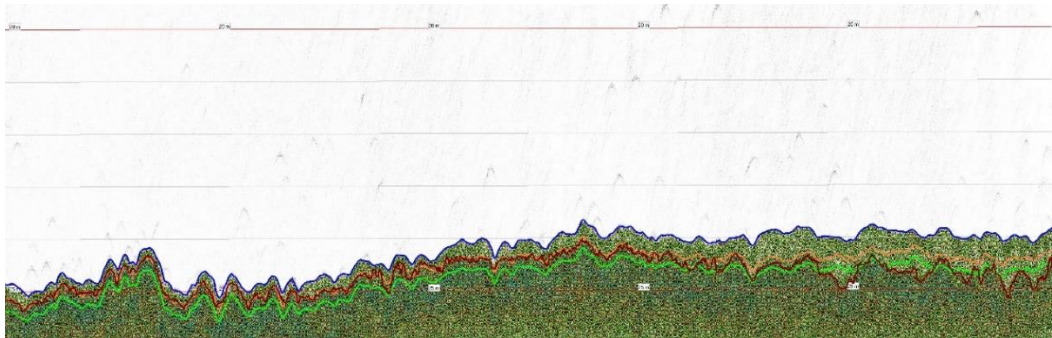


Figure A24. Fluid mud detection at the Calandkanaal on 13-11-2019: line 10. Blue level – water-mud interface, red level – sharp density contrast in seismic data, orange level – 1.2 kg/l (density) level, green level – 100 Pa (Bingham yield stress) level.

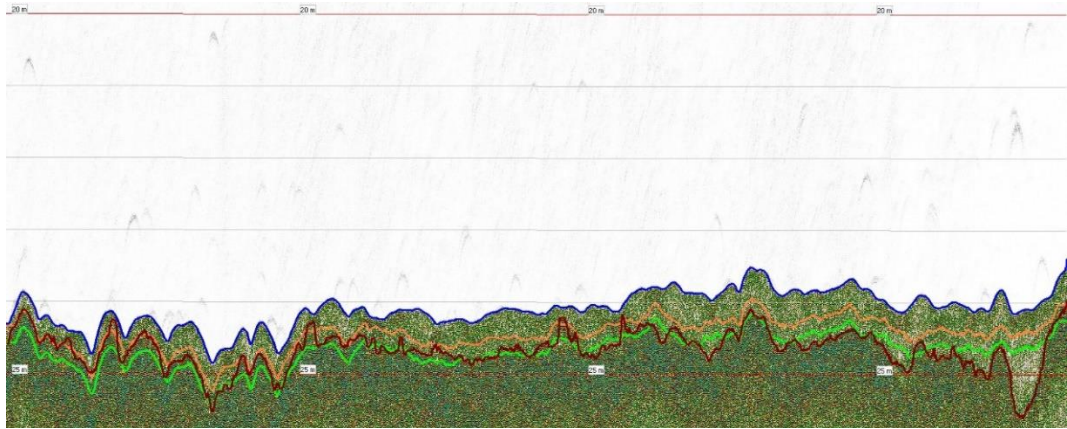


Figure A25. Fluid mud detection at the Calandkanaal on 13-11-2019: line 11. Blue level – water-mud interface, red level – sharp density contrast in seismic data, orange level – 1.2 kg/l (density) level, green level – 100 Pa (Bingham yield stress) level.

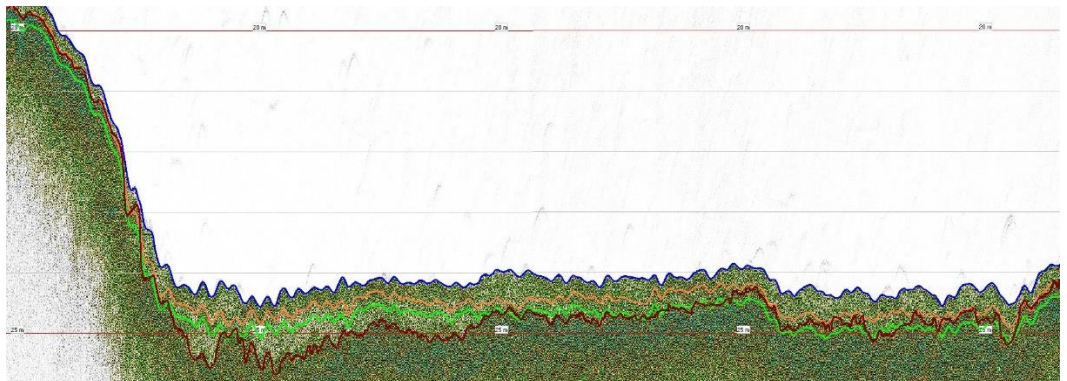


Figure A26. Fluid mud detection at the Calandkanaal on 13-11-2019: line 12. Blue level – water-mud interface, red level – sharp density contrast in seismic data, orange level – 1.2 kg/l (density) level, green level – 100 Pa (Bingham yield stress) level.

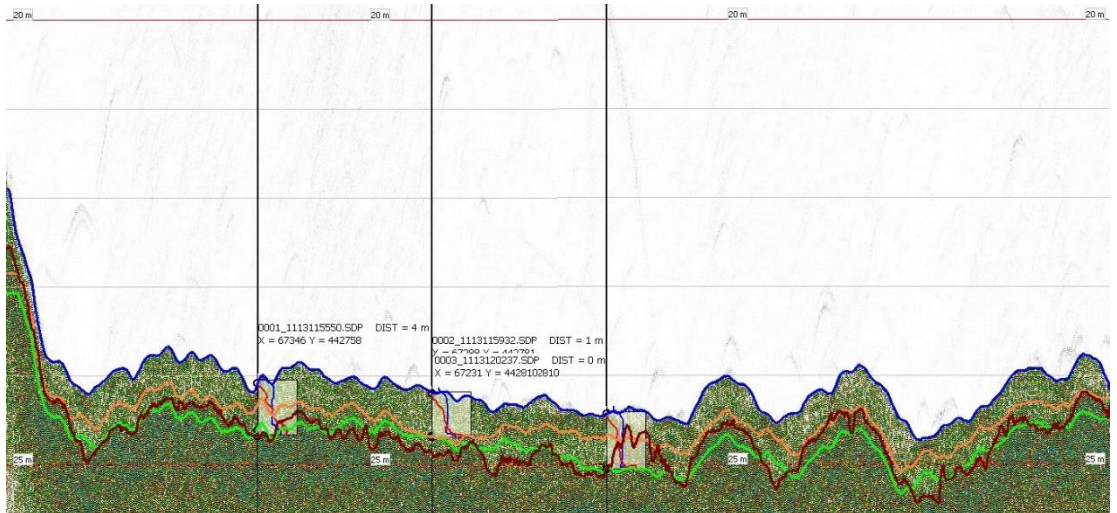


Figure A27. Fluid mud detection at the Calandkanaal on 13-11-2019: line 13. Blue level – water-mud interface, red level – sharp density contrast in seismic data, orange level – 1.2 kg/l (density) level, green level – 100 Pa (Bingham yield stress) level. Blue and red vertical lines show density and Bingham yield stress profiles, respectively.

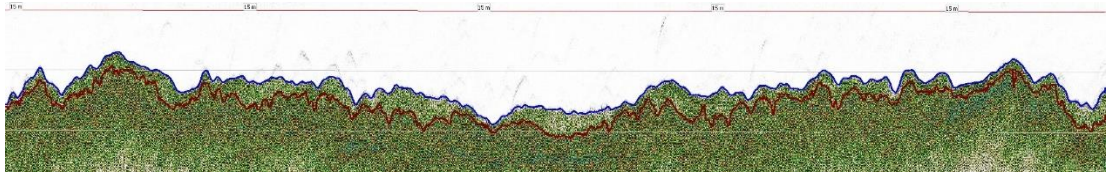


Figure A28. Fluid mud detection at the 3 Petroleumhaven on 13-11-2019: line 1. Blue level – water-mud interface, red level – sharp density contrast in seismic data, orange level – 100 Pa (Bingham yield stress) level.

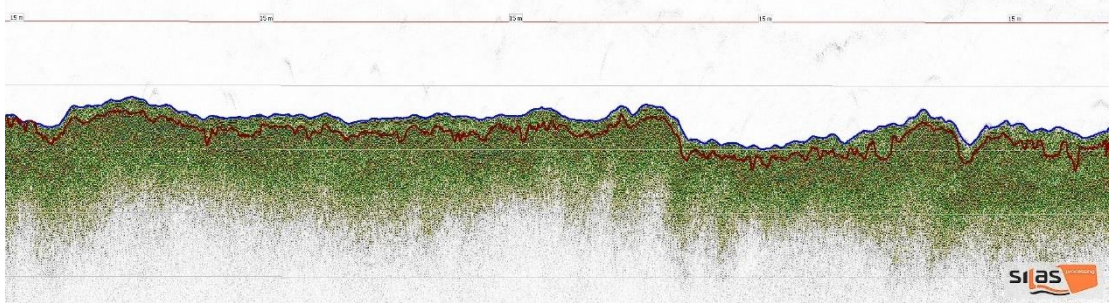


Figure A29. Fluid mud detection at the 3 Petroleumhaven on 13-11-2019: line 2. Blue level – water-mud interface, red level – sharp density contrast in seismic data, orange level – 100 Pa (Bingham yield stress) level.

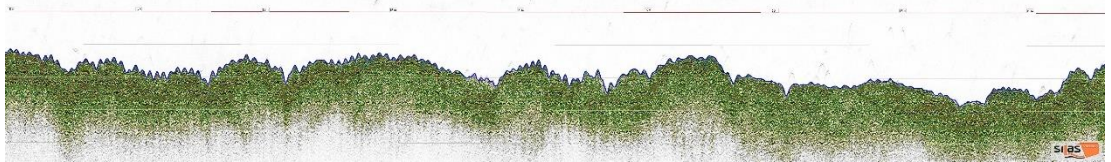


Figure A30. Fluid mud detection at Botlek on 13-11-2019: line 1.

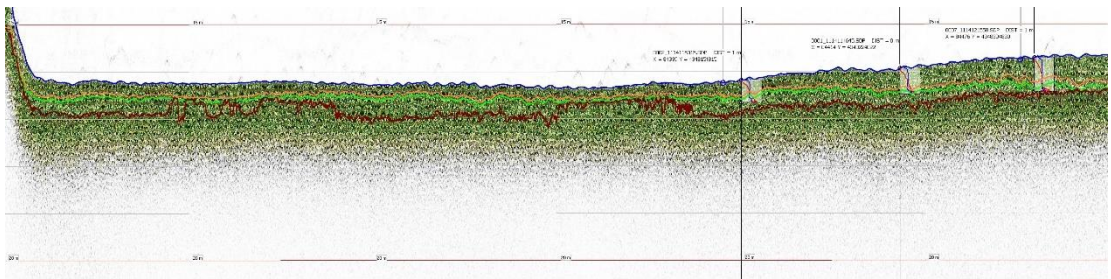


Figure A31. Fluid mud detection at KTM kade on 13-11-2019: line 1. Blue level – water-mud interface, red level – sharp density contrast in seismic data, orange level – 1.2 kg/l (density) level, green level – 100 Pa (Bingham yield stress) level.

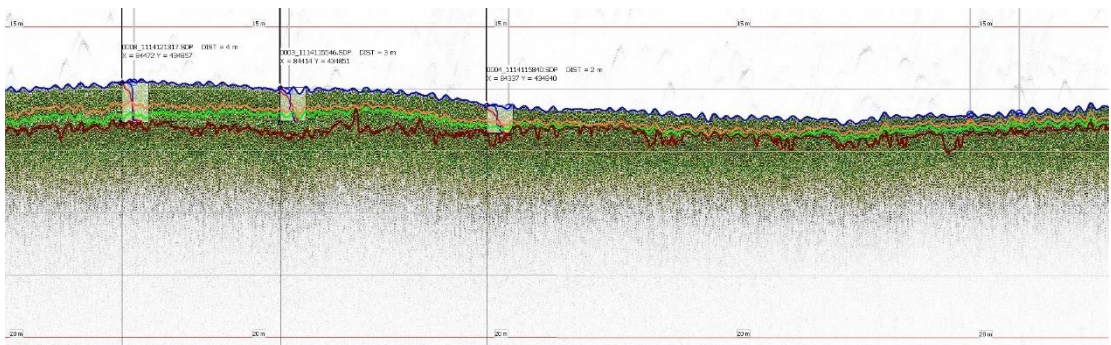


Figure A32. Fluid mud detection at KTM kade on 13-11-2019: line 2. Blue level – water-mud interface, red level – sharp density contrast in seismic data, orange level – 1.2 kg/l (density) level, green level – 100 Pa (Bingham yield stress) level. Blue and red vertical lines show density and Bingham yield stress profiles, respectively.

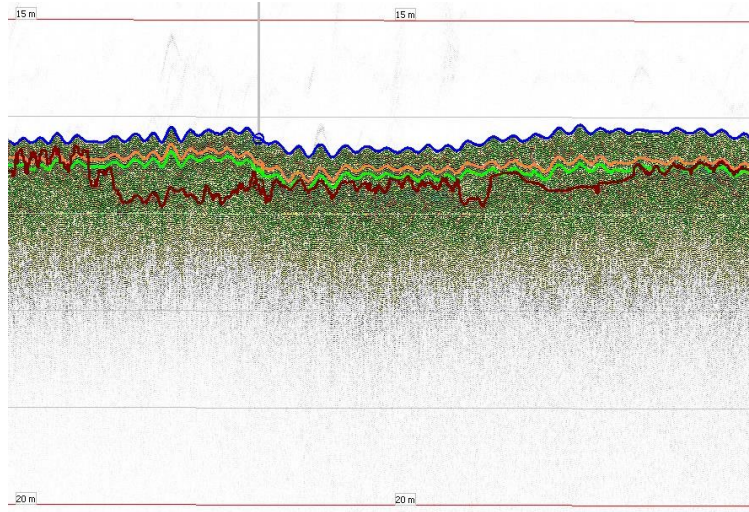


Figure A33. Fluid mud detection at KTM kade on 13-11-2019: line 2 (continued). Blue level – water-mud interface, red level – sharp density contrast in seismic data, orange level – 1.2 kg/l (density) level, green level – 100 Pa (Bingham yield stress) level.

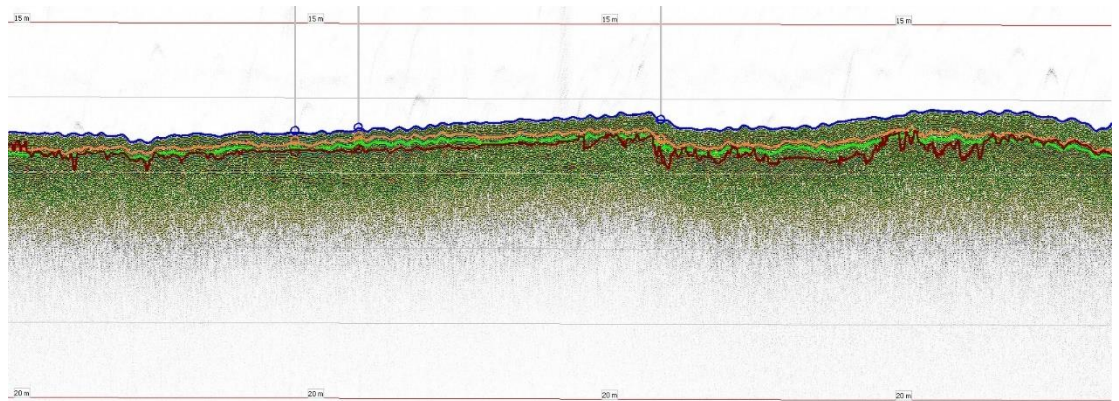


Figure A34. Fluid mud detection at KTM kade on 13-11-2019: line 2 (continued). Blue level – water-mud interface, red level – sharp density contrast in seismic data, orange level – 1.2 kg/l (density) level, green level – 100 Pa (Bingham yield stress) level.

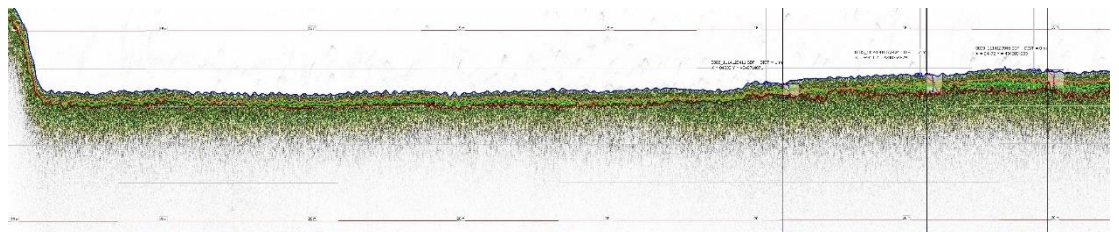


Figure A35. Fluid mud detection at KTM kade on 13-11-2019: line 3. Blue level – water-mud interface, red level – sharp density contrast in seismic data, orange level – 1.2 kg/l (density) level, green level – 100 Pa (Bingham yield stress) level. Blue and red vertical lines show density and Bingham yield stress profiles, respectively.

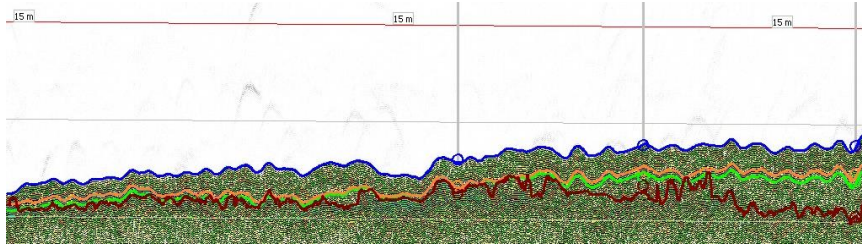


Figure A36. Fluid mud detection at KTM kade on 13-11-2019: line 4. Blue level – water-mud interface, red level – sharp density contrast in seismic data, orange level – 1.2 kg/l (density) level, green level – 100 Pa (Bingham yield stress) level.

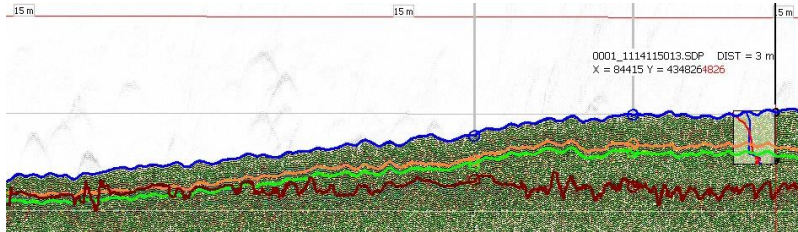


Figure A37. Fluid mud detection at KTM kade on 13-11-2019: line 5. Blue level – water-mud interface, red level – sharp density contrast in seismic data, orange level – 1.2 kg/l (density) level, green level – 100 Pa (Bingham yield stress) level.

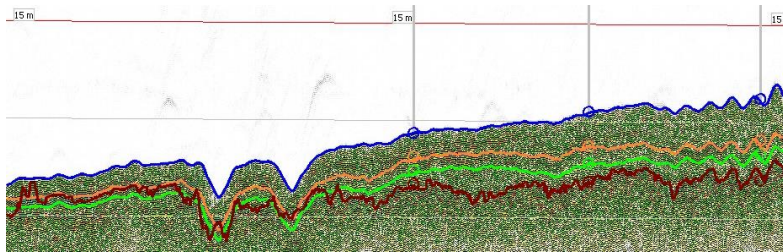


Figure A38. Fluid mud detection at KTM kade on 13-11-2019: line 6. Blue level – water-mud interface, red level – sharp density contrast in seismic data, orange level – 1.2 kg/l (density) level, green level – 100 Pa (Bingham yield stress) level.

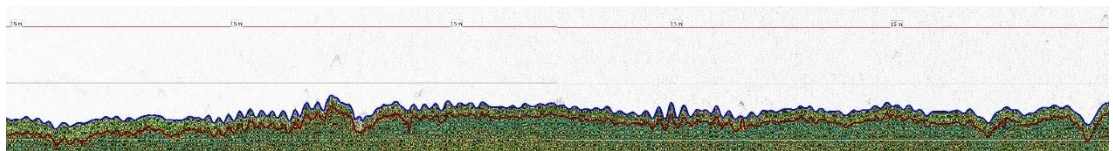


Figure A39. Fluid mud detection at the St. Laurens haven on 13-11-2019: line 1. Blue level – water-mud interface, red level – sharp density contrast in seismic data.

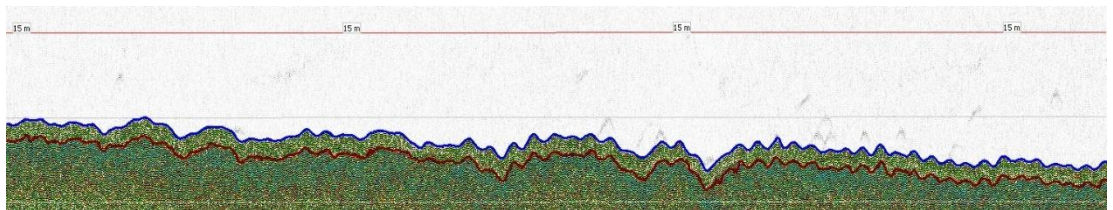


Figure A40. Fluid mud detection at the St. Laurens haven on 13-11-2019: line 2. Blue level – water-mud interface, red level – sharp density contrast in seismic data.

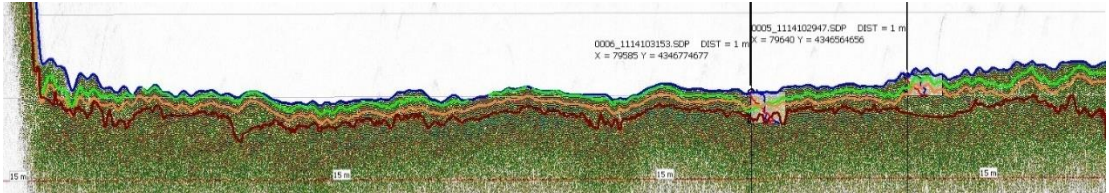


Figure A41. Fluid mud detection at Scheur kade on 13-11-2019: line 1. Blue level – water-mud interface, red level – sharp density contrast in seismic data, orange level – 1.2 kg/l (density) level, green level – 100 Pa (Bingham yield stress) level. Blue and red vertical lines show density and Bingham yield stress profiles, respectively.

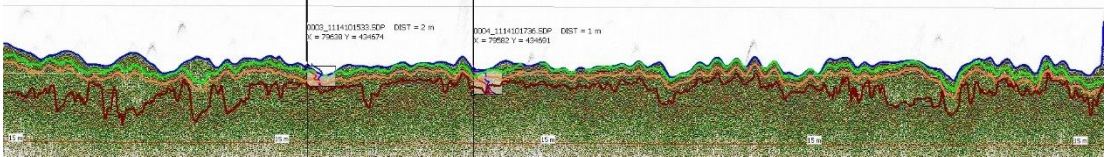


Figure A42. Fluid mud detection at Scheur kade on 13-11-2019: line 2. Blue level – water-mud interface, red level – sharp density contrast in seismic data, orange level – 1.2 kg/l (density) level, green level – 100 Pa (Bingham yield stress) level. Blue and red vertical lines show density and Bingham yield stress profiles, respectively.

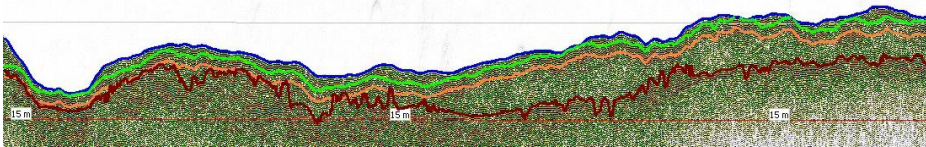


Figure A43. Fluid mud detection at Scheur kade on 13-11-2019: line 3. Blue level – water-mud interface, red level – sharp density contrast in seismic data, orange level – 1.2 kg/l (density) level, green level – 100 Pa (Bingham yield stress) level.

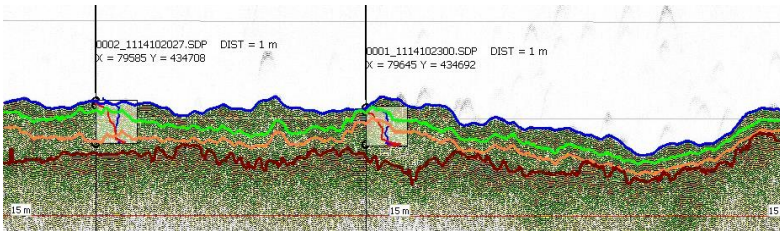


Figure A44. Fluid mud detection at Scheur kade on 13-11-2019: line 3 (continued). Blue level – water-mud interface, red level – sharp density contrast in seismic data, orange level – 1.2 kg/l (density) level, green level – 100 Pa (Bingham yield stress) level. Blue and red vertical lines show density and Bingham yield stress profiles, respectively.

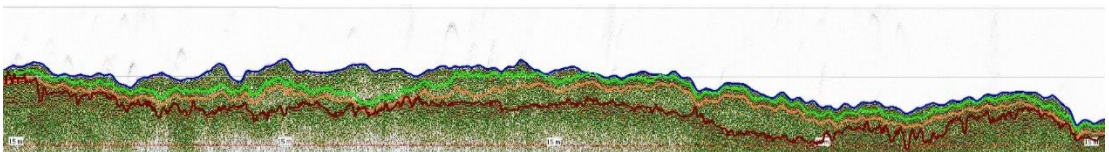


Figure A45. Fluid mud detection at Scheur kade on 13-11-2019: line 3 (continued). Blue level – water-mud interface, red level – sharp density contrast in seismic data, orange level – 1.2 kg/l (density) level, green level – 100 Pa (Bingham yield stress) level.

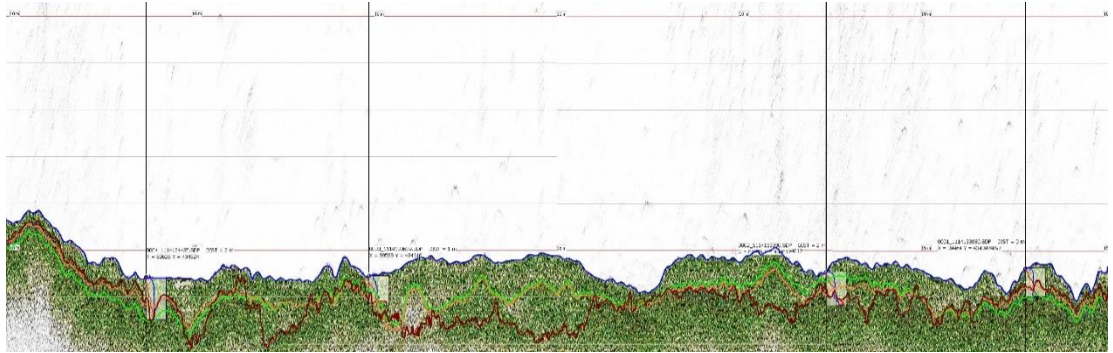


Figure A46. Fluid mud detection at the Waalhaven on 13-11-2019: line 1. Blue level – water-mud interface, red level – sharp density contrast in seismic data, orange level – 1.2 kg/l (density) level, green level – 100 Pa (Bingham yield stress) level. Blue and red vertical lines show density and Bingham yield stress profiles, respectively.

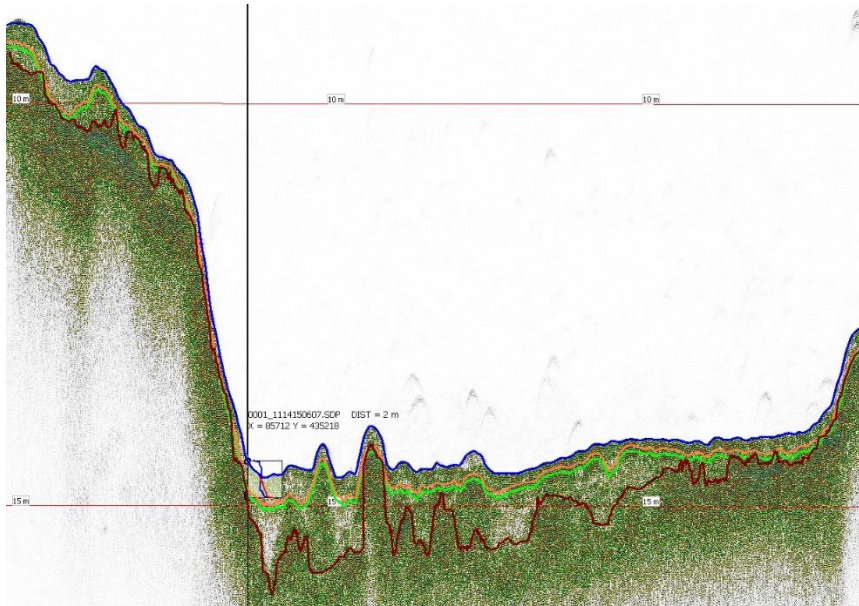


Figure A47. Fluid mud detection at the Wiltonhaven on 13-11-2019: line 1. Blue level – water-mud interface, red level – sharp density contrast in seismic data, orange level – 1.2 kg/l (density) level, green level – 100 Pa (Bingham yield stress) level. Blue and red vertical lines show density and Bingham yield stress profiles, respectively.

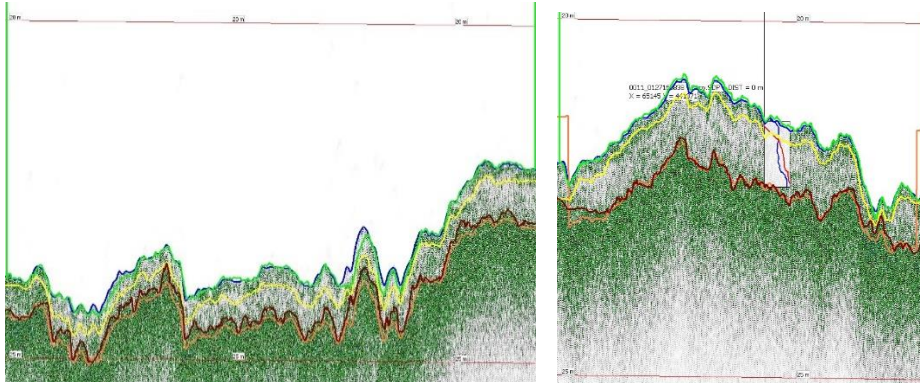


Figure A51. Fluid mud detection at the Beerkanaal on 27-01-2020: lines 1 (left) and 2 (right). Blue level – water-mud interface, red level – sharp density contrast in seismic data, green level – multibeam level, orange level – 100 Pa (Bingham yield stress) level, yellow level – 1.2 kg/l (density) level.

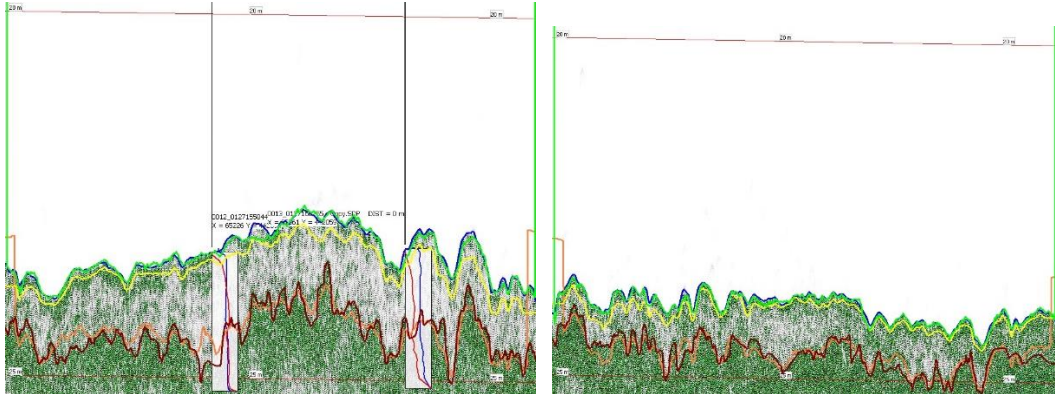


Figure A52. Fluid mud detection at the Beerkanaal on 27-01-2020: lines 3 (left) and 4 (right). Blue level – water-mud interface, red level – sharp density contrast in seismic data, green level – multibeam level, orange level – 100 Pa (Bingham yield stress) level, yellow level – 1.2 kg/l (density) level. Blue and red vertical lines show density and Bingham yield stress profiles, respectively.

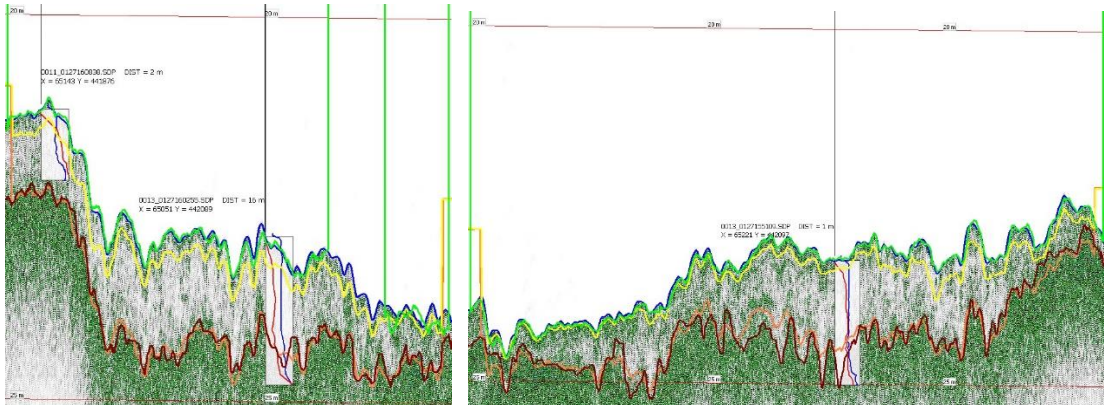


Figure A53. Fluid mud detection at the Beerkanaal on 27-01-2020: lines 5 (left) and 6 (right). Blue level – water-mud interface, red level – sharp density contrast in seismic data, green level – multibeam level, orange level – 100 Pa (Bingham yield stress) level, yellow level – 1.2 kg/l (density) level. Blue and red vertical lines show density and Bingham yield stress profiles, respectively.

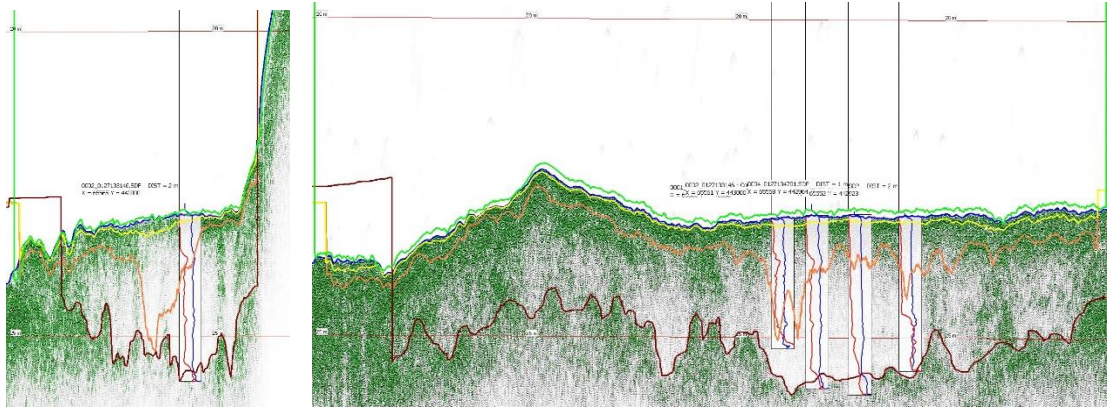


Figure A54. Fluid mud detection at Westbocht on 27-01-2020: lines beer2_0127125047 (left) and wk18_0127122021(right). Blue level – water-mud interface, red level – sharp density contrast in seismic data, green level – multibeam level, orange level – 100 Pa (Bingham yield stress) level, yellow level – 1.2 kg/l (density) level. Blue and red vertical lines show density and Bingham yield stress profiles, respectively.

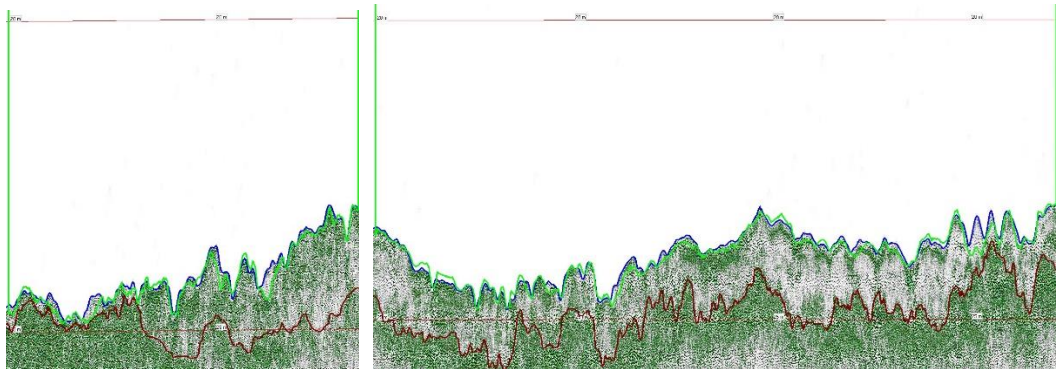


Figure A55. Fluid mud detection at the Calandkanaal on 27-01-2020: lines b kanaal 2_0127155559 (left) and b kanaal 2_0127160005 (right). Blue level – water-mud interface, red level – sharp density contrast in seismic data, green level – multibeam level.

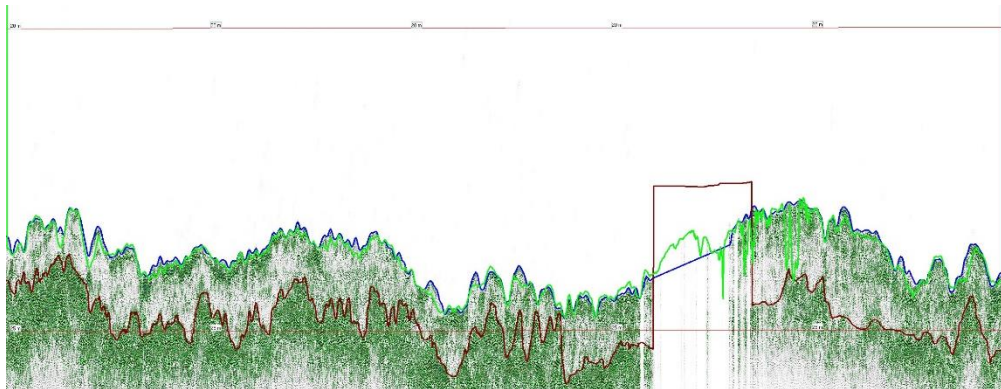


Figure A56. Fluid mud detection at the Calandkanaal on 27-01-2020: line wk18_0127115559. Blue level – water-mud interface, red level – sharp density contrast in seismic data, green level – multibeam level

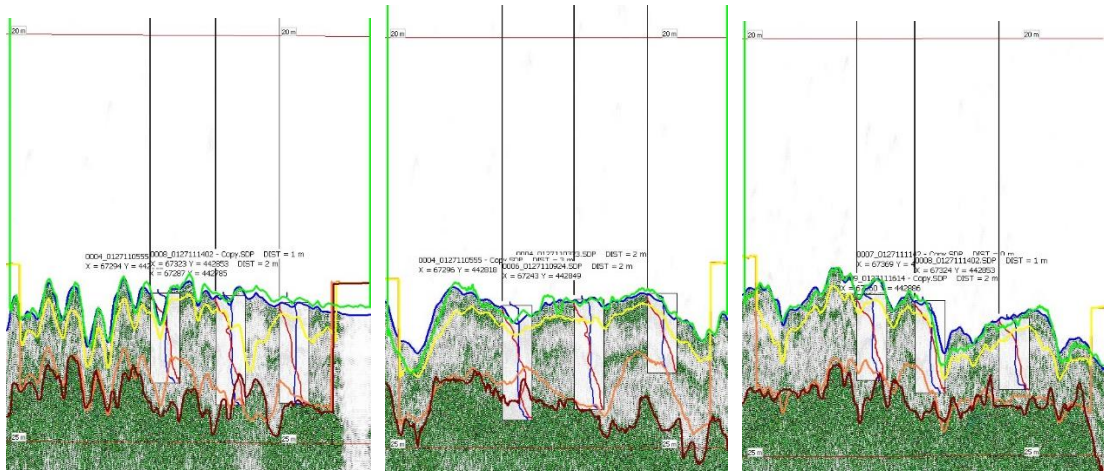


Figure A57. Fluid mud detection at the Calandkanaal on 27-01-2020: lines dwars midden (left), midden (center) and noord (right). Blue level – water-mud interface, red level – sharp density contrast in seismic data, green level – multibeam level, orange level – 100 Pa (Bingham yield stress) level, yellow level – 1.2 kg/l (density) level. Blue and red vertical lines show density and Bingham yield stress profiles, respectively.

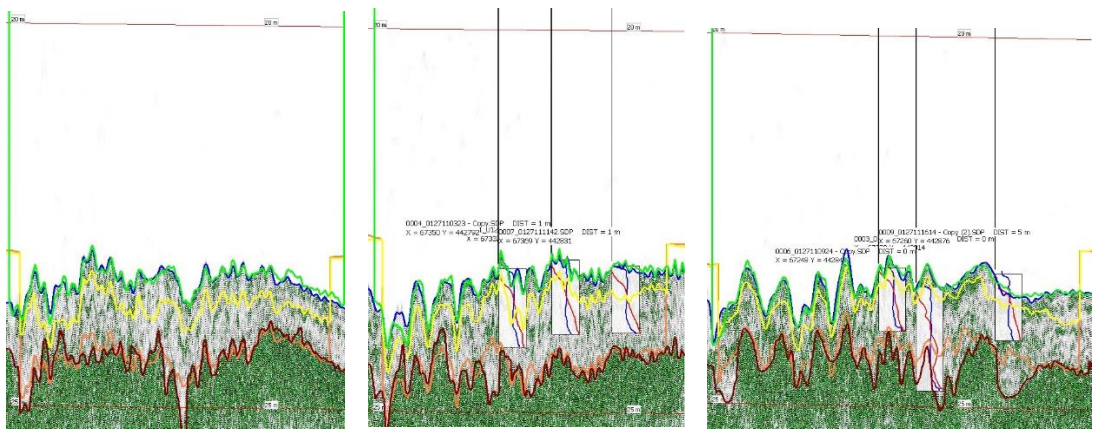


Figure A58. Fluid mud detection at the Calandkanaal on 27-01-2020: lines oost 2 (left), oost (center) and West (right). Blue level – water-mud interface, red level – sharp density contrast in seismic data, green level – multibeam level, orange level – 100 Pa (Bingham yield stress) level, yellow level – 1.2 kg/l (density) level. Blue and red vertical lines show density and Bingham yield stress profiles, respectively.

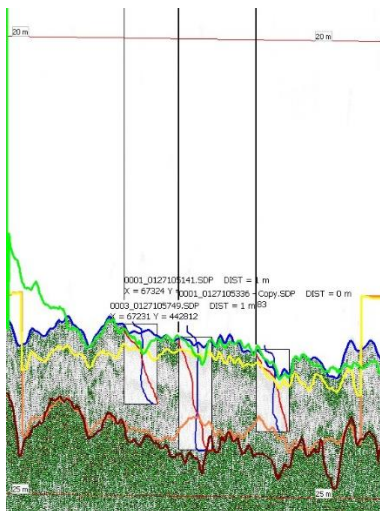


Figure A59. Fluid mud detection at the Calandkanaal on 27-01-2020: line zuid. Blue level – water-mud interface, red level – sharp density contrast in seismic data, green level – multibeam level, orange level – 100 Pa (Bingham yield stress) level, yellow level – 1.2 kg/l (density) level. Blue and red vertical lines show density and Bingham yield stress profiles, respectively.



Figure A60. Positioning of SILAS lines at the 3e Petroleumhaven, Botlek, Waalhaven, Wiltonhaven, Jobshaven, Scheur kade, KTM kade, Koole kade and the Schierhaven on 28-01-2020

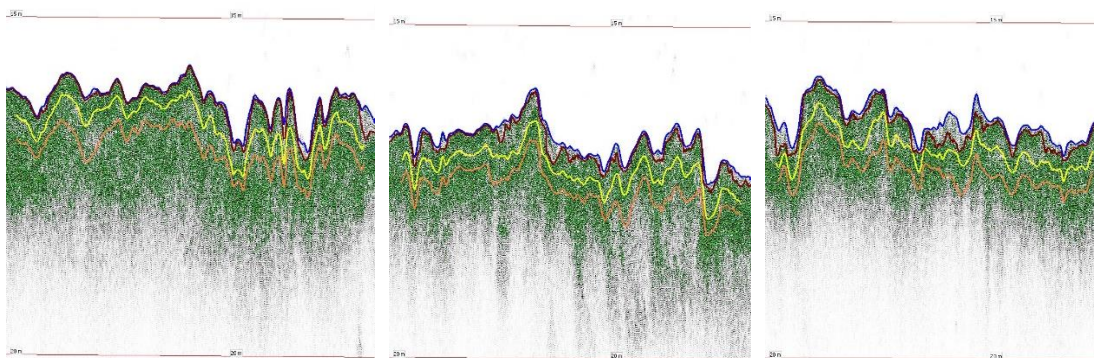


Figure A61. Fluid mud detection at the 3e Petroleumhaven on 28-01-2020: lines 1 (left), 01 (center) and 2 (right). Blue level – water-mud interface, red level – sharp density contrast in seismic data, green level – multibeam level, orange level – 100 Pa (Bingham yield stress) level, yellow level – 1.2 kg/l (density) level.

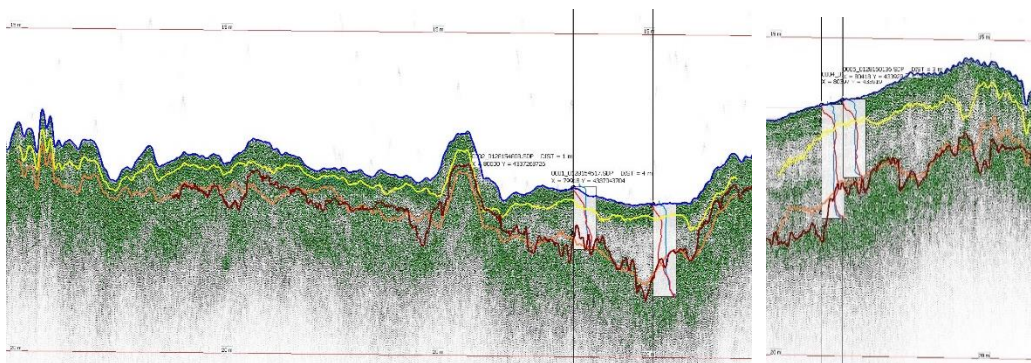


Figure A62. Fluid mud detection at Botlek on 28-01-2020: lines slibput (left) and 1 (right). Blue level – water-mud interface, red level – sharp density contrast in seismic data, green level – multibeam level, orange level – 100 Pa (Bingham yield stress) level, yellow level – 1.2 kg/l (density) level. Blue and red vertical lines show density and Bingham yield stress profiles, respectively.

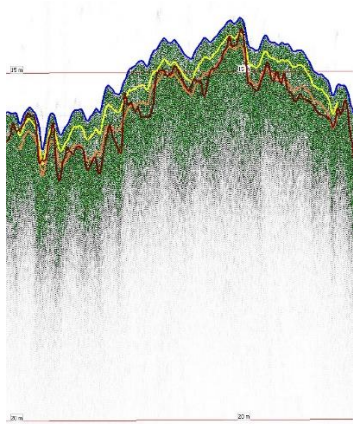


Figure A67. Fluid mud detection at Kole kade on 28-01-2020. Blue level – water-mud interface, red level – sharp density contrast in seismic data, green level – multibeam level, orange level – 100 Pa (Bingham yield stress) level, yellow level – 1.2 kg/l (density) level.

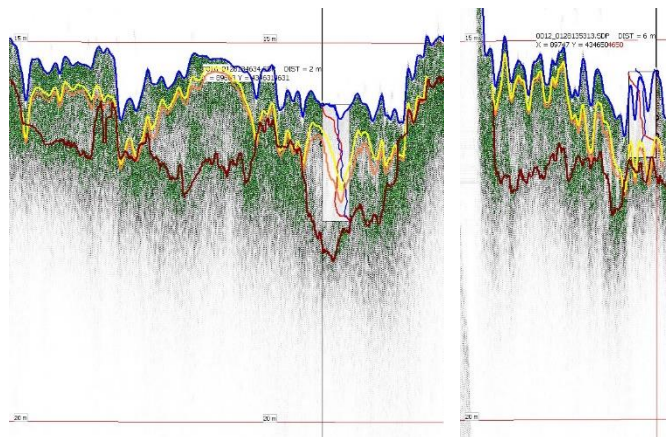


Figure A68. Fluid mud detection at the Waalhaven on 28-01-2020: line 1 (left) and cross line 1 (right). Blue level – water-mud interface, red level – sharp density contrast in seismic data, green level – multibeam level, orange level – 100 Pa (Bingham yield stress) level, yellow level – 1.2 kg/l (density) level. Blue and red vertical lines show density and Bingham yield stress profiles, respectively.

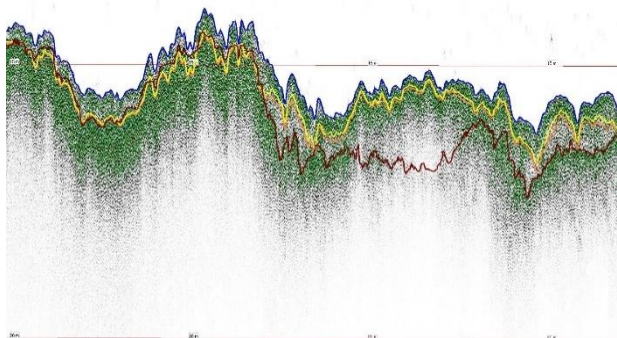


Figure A69. Fluid mud detection at the Waalhaven on 28-01-2020: line 2. Blue level – water-mud interface, red level – sharp density contrast in seismic data, green level – multibeam level, orange level – 100 Pa (Bingham yield stress) level, yellow level – 1.2 kg/l (density) level.

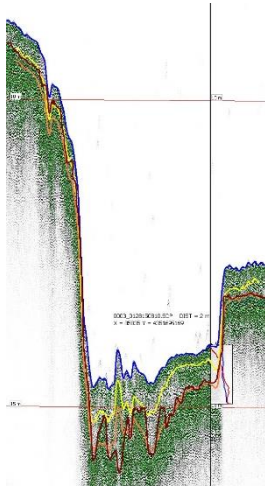


Figure A70. Fluid mud detection at the Wiltonhaven on 28-01-2020: line 1. Blue level – water-mud interface, red level – sharp density contrast in seismic data, green level – multibeam level, orange level – 100 Pa (Bingham yield stress) level, yellow level – 1.2 kg/l (density) level. Blue and red vertical lines show density and Bingham yield stress profiles, respectively.

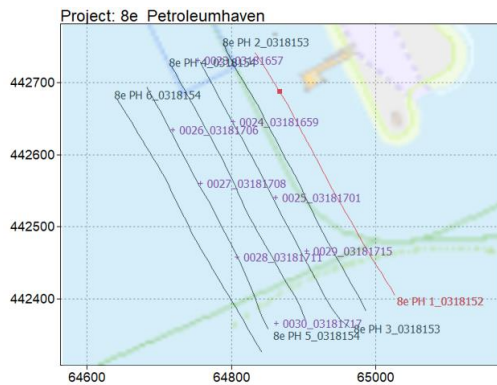


Figure A71. Positioning of SILAS lines at the 8e Petroleumhaven on 18-03-2020

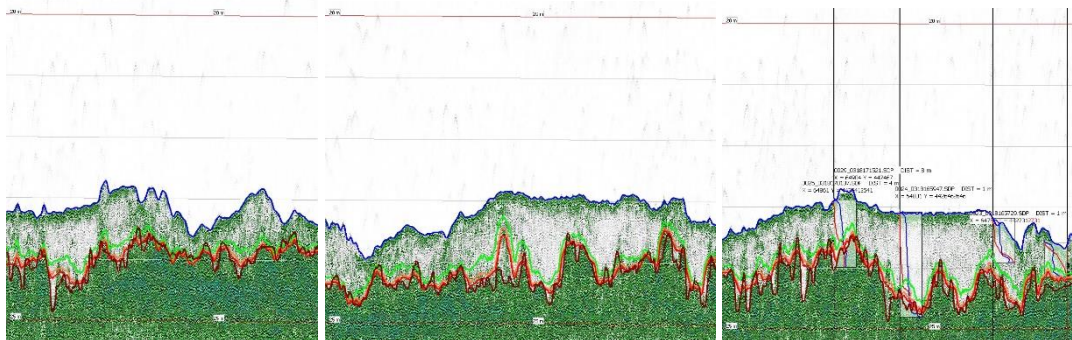


Figure A72. Fluid mud detection at the 8e Petroleumhaven on 18-03-2020: lines 8e PH 1_0318152900 (left), 8e PH 2_0318153229 (middle), 8e PH 3_0318153619 (right). Blue level – water-mud interface, dark red level – sharp density contrast in seismic data, green level – 50 Pa, orange level – 1.2 kg/l (density) level, bright red level – 100 Pa (Bingham yield stress) level. Blue and red vertical lines show density and Bingham yield stress profiles, respectively.

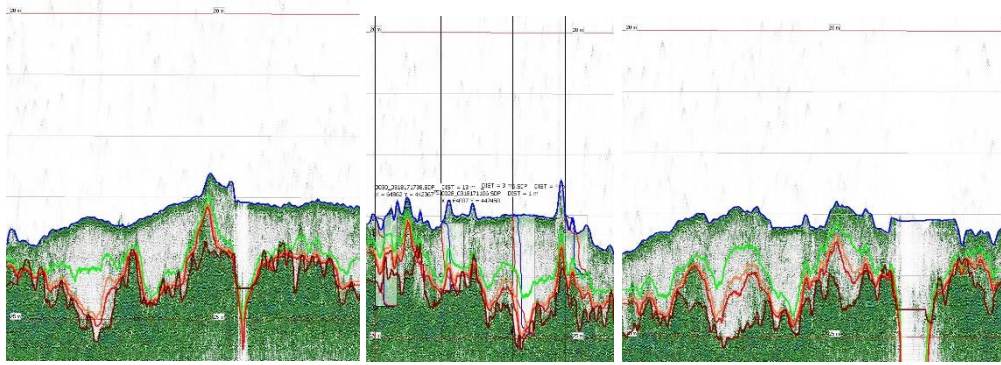


Figure A73. Fluid mud detection at the 8e Petroleumhaven on 18-03-2020: lines 8e PH 4_0318154017 (left), 8e PH 5_0318154353 (middle), 8e PH 6_0318154709 (right). Blue level – water-mud interface, dark red level – sharp density contrast in seismic data, green level – 50 Pa, orange level – 1.2 kg/l (density) level, bright red level – 100 Pa (Bingham yield stress) level. Blue and red vertical lines show density and Bingham yield stress profiles, respectively.

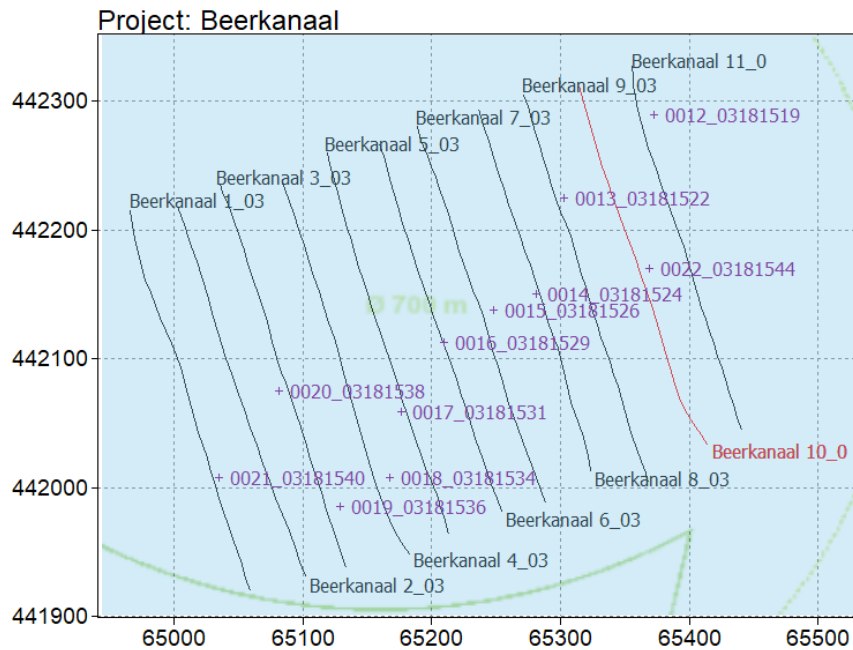


Figure A74. Positioning of SILAS lines at the Beerkanaal on 18-03-2020

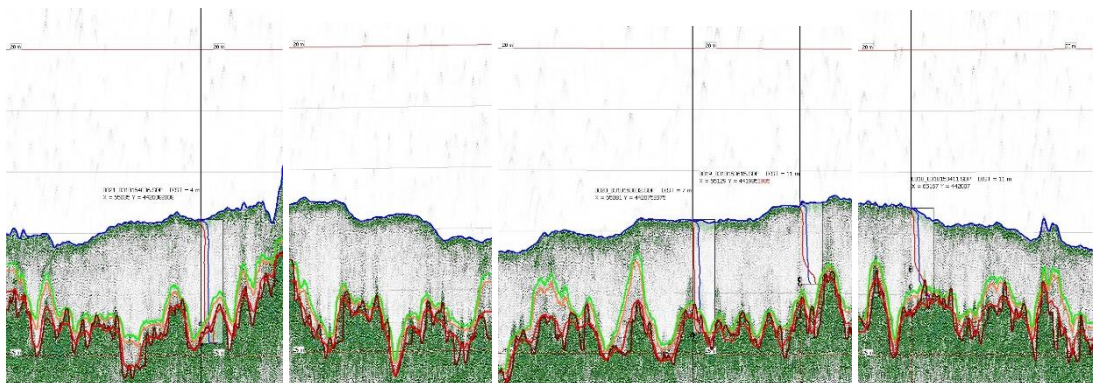


Figure A75. Fluid mud detection at the Beerkanaal on 18-03-2020: lines Beerkanaal 1_0318152328 (left), Beerkanaal 2_0318152036 (middle left), Beerkanaal 3_0318151643 (middle right), Beerkanaal 4_0318151340 (right). Blue level – water-mud interface, dark red level – sharp density contrast in seismic data, green level – 50 Pa, orange level – 1.2 kg/l (density) level, bright red level – 100 Pa (Bingham yield stress) level. Blue and red vertical lines show density and Bingham yield stress profiles, respectively.

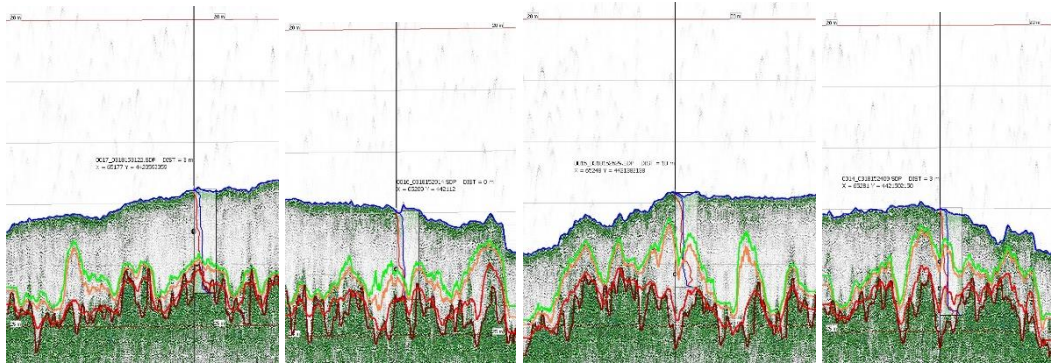


Figure A76. Fluid mud detection at the Beerkanaal on 18-03-2020: lines Beerkanaal 5_0318151042 (left), Beerkanaal 6_0318150733 (middle left), Beerkanaal 7_0318150422 (middle right), Beerkanaal 8_0318150129 (right). Blue level – water-mud interface, dark red level – sharp density contrast in seismic data, green level – 50 Pa, orange level – 1.2 kg/l (density) level, bright red level – 100 Pa (Bingham yield stress) level. Blue and red vertical lines show density and Bingham yield stress profiles, respectively

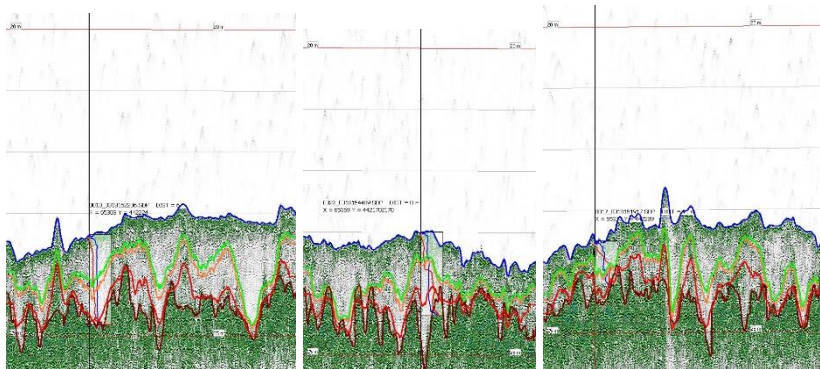


Figure A77. Fluid mud detection at the Beerkanaal on 18-03-2020: lines Beerkanaal 9_0318145824 (left), Beerkanaal 10_0318145521 (middle), Beerkanaal 11_0318145219 (right). Blue level – water-mud interface, dark red level – sharp density contrast in seismic data, green level – 50 Pa, orange level – 1.2 kg/l (density) level, bright red level – 100 Pa (Bingham yield stress) level. Blue and red vertical lines show density and Bingham yield stress profiles, respectively

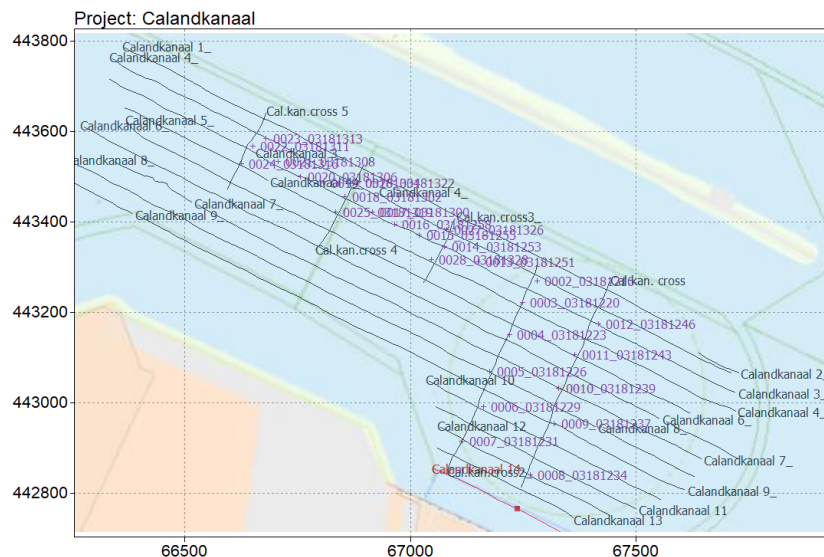


Figure A78. Positioning of SILAS lines at the Calandkanaal on 18-03-2020

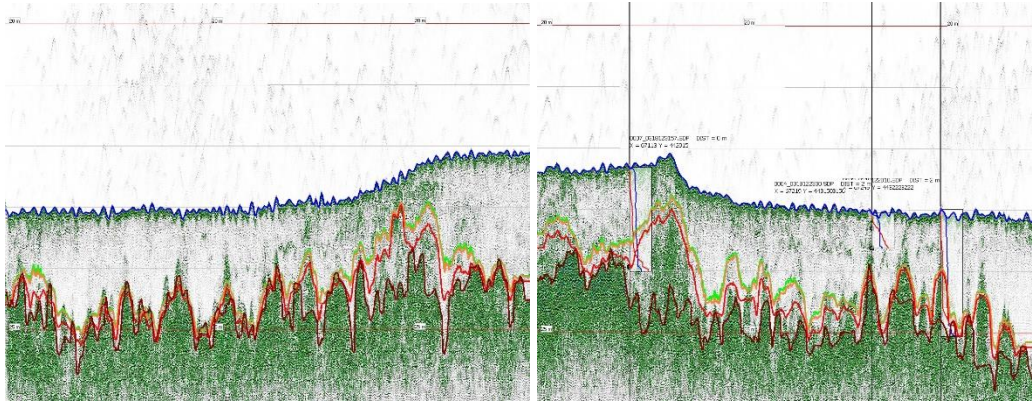


Figure A79. Fluid mud detection at the Calandkanaal on 18-03-2020: lines Cal.kan. cross 1_0318102257 (left), Cal.kan.cross 2_0318102905 (right). Blue level – water-mud interface, dark red level – sharp density contrast in seismic data, green level – 50 Pa, orange level – 1.2 kg/l (density) level, bright red level – 100 Pa (Bingham yield stress) level. Blue and red vertical lines show density and Bingham yield stress profiles, respectively

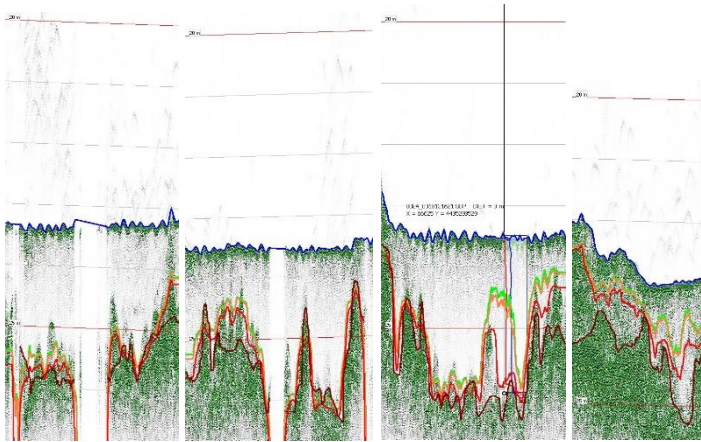


Figure A80. Fluid mud detection at the Calandkanaal on 18-03-2020: lines Cal.kan.cross 3_0318103517 (left), Cal.kan.cross 4_0318103914 (middle left), Cal.kan.cross 5_0318104317 (middle right), Calandkanaal 2_0318092929 (right). Blue level – water-mud interface, dark red level – sharp density contrast in seismic data, green level – 50 Pa, orange level – 1.2 kg/l (density) level, bright red level – 100 Pa (Bingham yield stress) level. Blue and red vertical lines show density and Bingham yield stress profiles, respectively

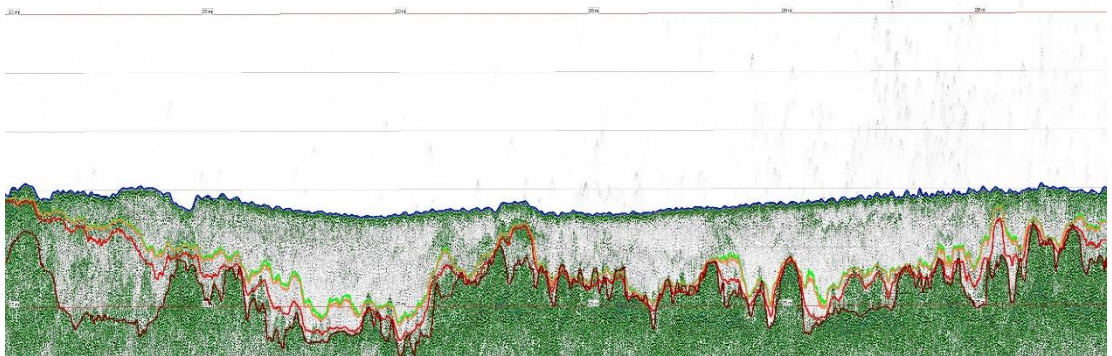


Figure A81. Fluid mud detection at the Calandkanaal on 18-03-2020: line Calandkanaal 1_0318091745. Blue level – water-mud interface, dark red level – sharp density contrast in seismic data, green level – 50 Pa, orange level – 1.2 kg/l (density) level, bright red level – 100 Pa (Bingham yield stress) level. Blue and red vertical lines show density and Bingham yield stress profiles, respectively

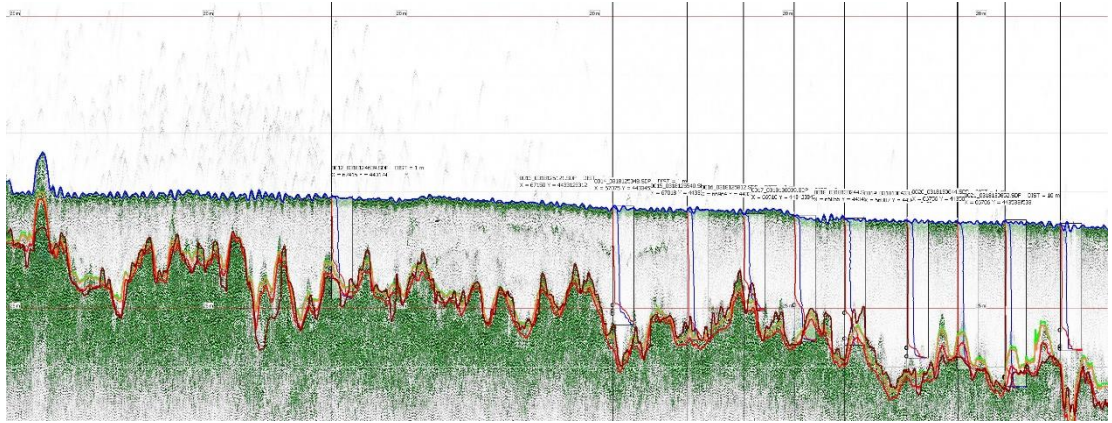


Figure A82. Fluid mud detection at the Calandkanaal on 18-03-2020: line Calandkanaal 3_0318085958. Blue level – water-mud interface, dark red level – sharp density contrast in seismic data, green level – 50 Pa, orange level – 1.2 kg/l (density) level, bright red level – 100 Pa (Bingham yield stress) level. Blue and red vertical lines show density and Bingham yield stress profiles, respectively

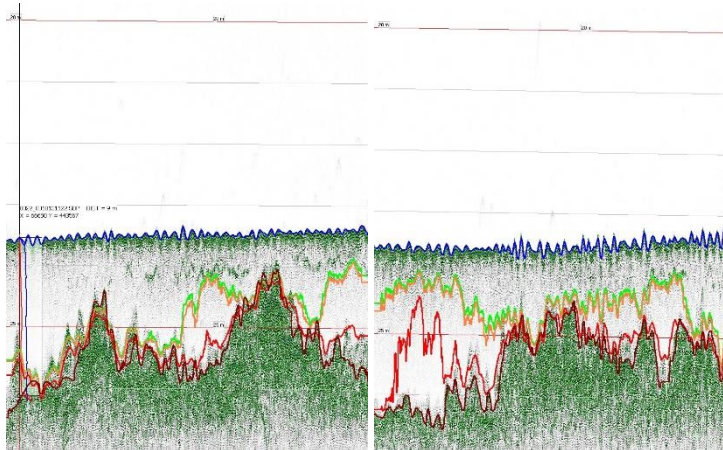


Figure A83. Fluid mud detection at the Calandkanaal on 18-03-2020: lines Calandkanaal 3_0318085958_1 (left) Calandkanaal 4_0318094952_1 (right). Blue level – water-mud interface, dark red level – sharp density contrast in seismic data, green level – 50 Pa, orange level – 1.2 kg/l (density) level, bright red level – 100 Pa (Bingham yield stress) level. Blue and red vertical lines show density and Bingham yield stress profiles, respectively

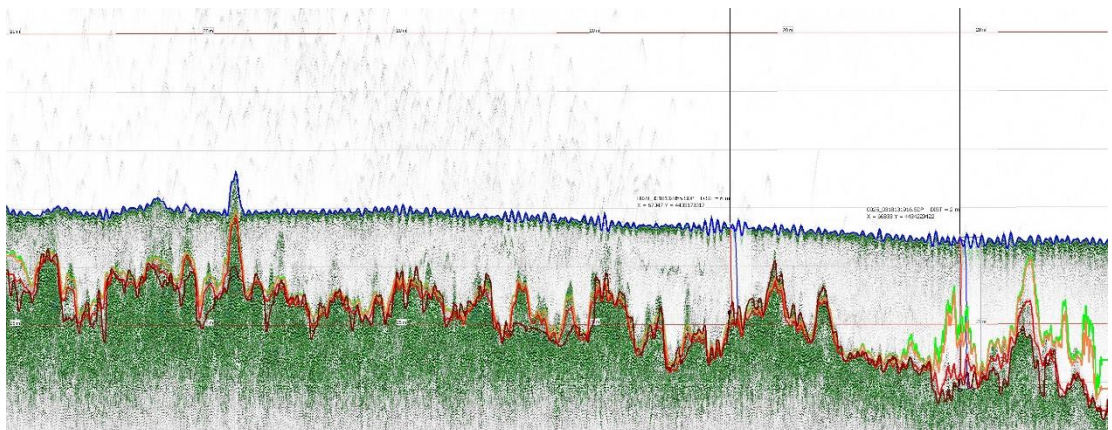


Figure A84. Fluid mud detection at the Calandkanaal on 18-03-2020: line Calandkanaal 4_0318094952. Blue level – water-mud interface, dark red level – sharp density contrast in seismic data, green level – 50 Pa, orange level – 1.2 kg/l (density) level, bright red level – 100 Pa (Bingham yield stress) level. Blue and red vertical lines show density and Bingham yield stress profiles, respectively

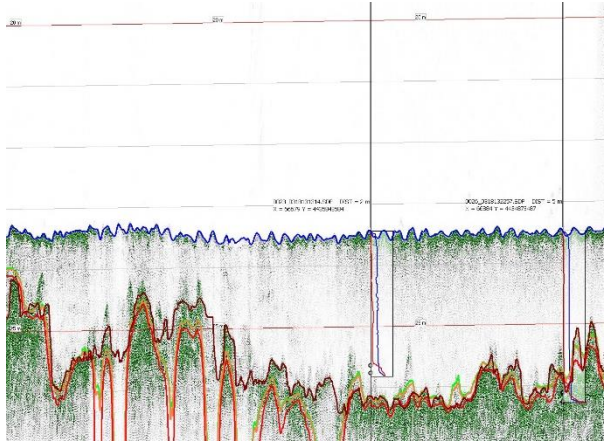


Figure A85. Fluid mud detection at the Calandkanaal on 18-03-2020: line Calandkanaal 4_0318100459. Blue level – water-mud interface, dark red level – sharp density contrast in seismic data, green level – 50 Pa, orange level – 1.2 kg/l (density) level, bright red level – 100 Pa (Bingham yield stress) level. Blue and red vertical lines show density and Bingham yield stress profiles, respectively

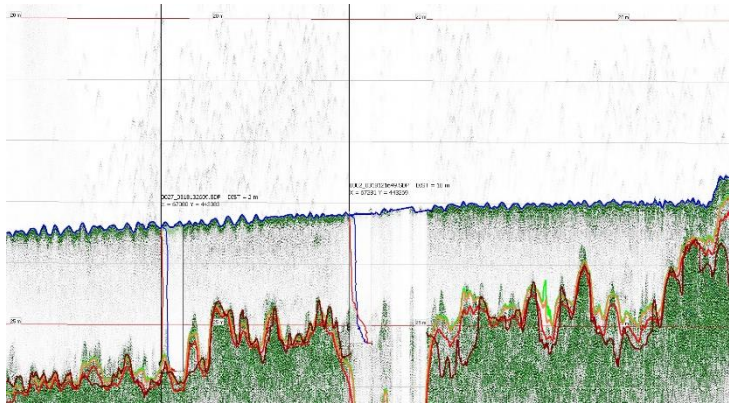


Figure A86. Fluid mud detection at the Calandkanaal on 18-03-2020: line Calandkanaal 4_0318101247. Blue level – water-mud interface, dark red level – sharp density contrast in seismic data, green level – 50 Pa, orange level – 1.2 kg/l (density) level, bright red level – 100 Pa (Bingham yield stress) level. Blue and red vertical lines show density and Bingham yield stress profiles, respectively

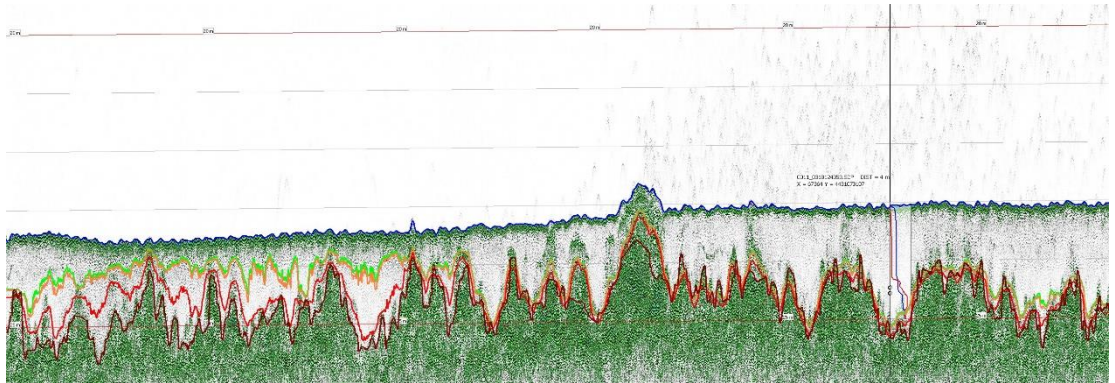


Figure A87. Fluid mud detection at the Calandkanaal on 18-03-2020: line Calandkanaal 5_0318093828. Blue level – water-mud interface, dark red level – sharp density contrast in seismic data, green level – 50 Pa, orange level – 1.2 kg/l (density) level, bright red level – 100 Pa (Bingham yield stress) level. Blue and red vertical lines show density and Bingham yield stress profiles, respectively

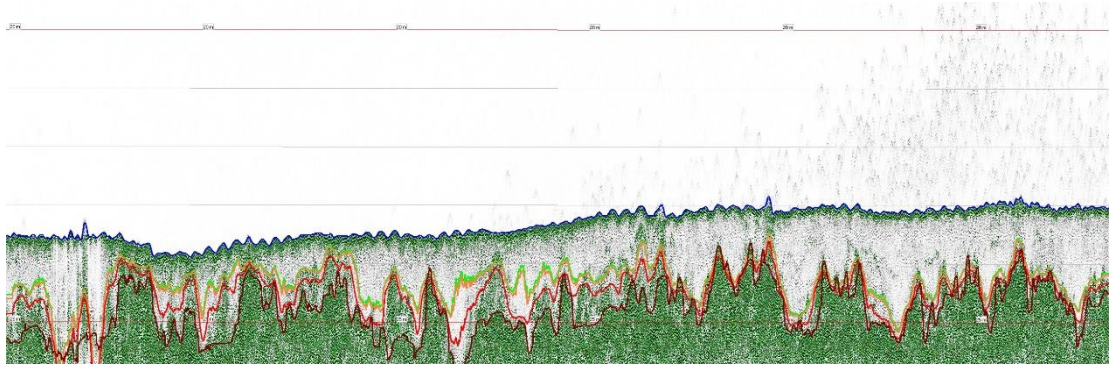


Figure A88. Fluid mud detection at the Calandkanaal on 18-03-2020: line Calandkanaal 6_0318084240. Blue level – water-mud interface, dark red level – sharp density contrast in seismic data, green level – 50 Pa, orange level – 1.2 kg/l (density) level, bright red level – 100 Pa (Bingham yield stress) level. Blue and red vertical lines show density and Bingham yield stress profiles, respectively

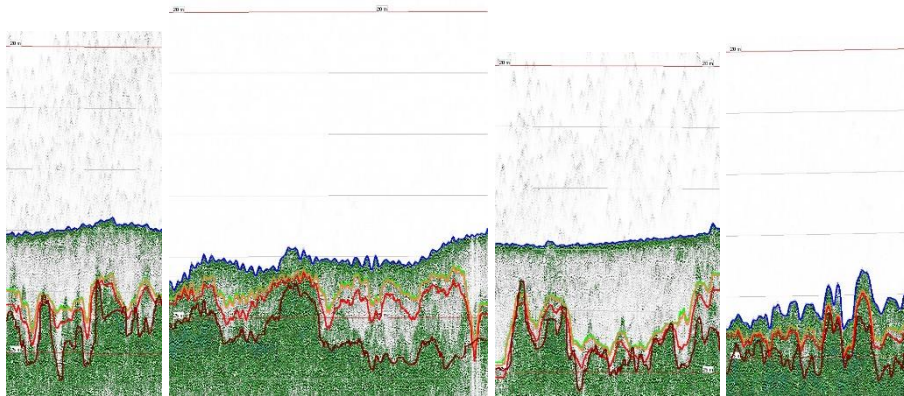


Figure A89. Fluid mud detection at the Calandkanaal on 18-03-2020: lines Calandkanaal 6_0318084240_1 (left), Calandkanaal 7_0318082830_1 (middle left), Calandkanaal 8_0318081543_1 (middle right), Calandkanaal 9_0318075930_1 (right). Blue level – water-mud interface, dark red level – sharp density contrast in seismic data, green level – 50 Pa, orange level – 1.2 kg/l (density) level, bright red level – 100 Pa (Bingham yield stress) level. Blue and red vertical lines show density and Bingham yield stress profiles, respectively

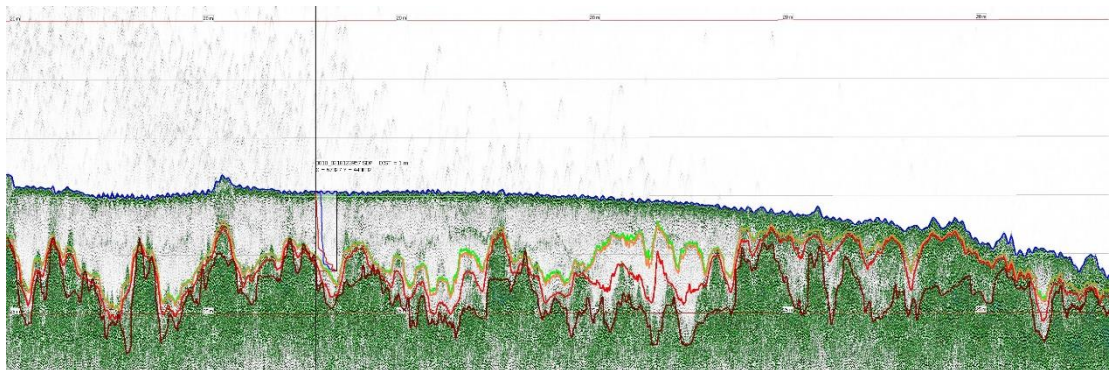


Figure A90. Fluid mud detection at the Calandkanaal on 18-03-2020: line Calandkanaal 7_0318082830. Blue level – water-mud interface, dark red level – sharp density contrast in seismic data, green level – 50 Pa, orange level – 1.2 kg/l (density) level, bright red level – 100 Pa (Bingham yield stress) level. Blue and red vertical lines show density and Bingham yield stress profiles, respectively

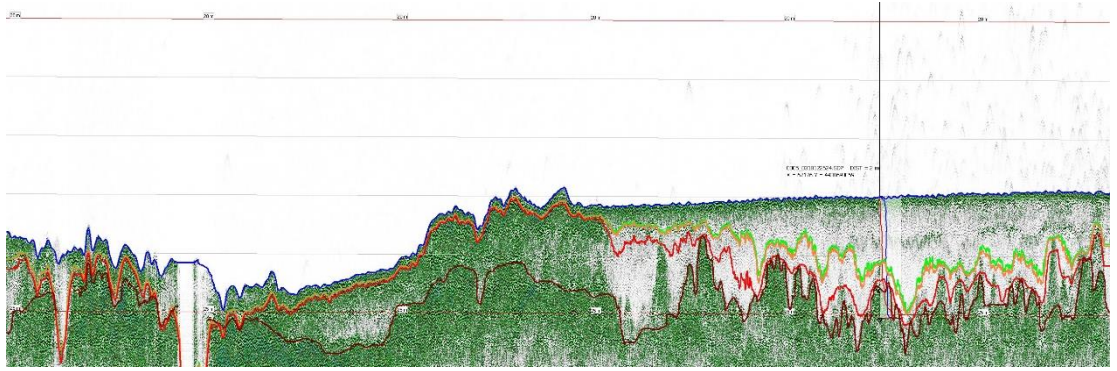


Figure A91. Fluid mud detection at the Calandkanaal on 18-03-2020: line Calandkanaal 8_0318081543. Blue level – water-mud interface, dark red level – sharp density contrast in seismic data, green level – 50 Pa, orange level – 1.2 kg/l (density) level, bright red level – 100 Pa (Bingham yield stress) level. Blue and red vertical lines show density and Bingham yield stress profiles, respectively

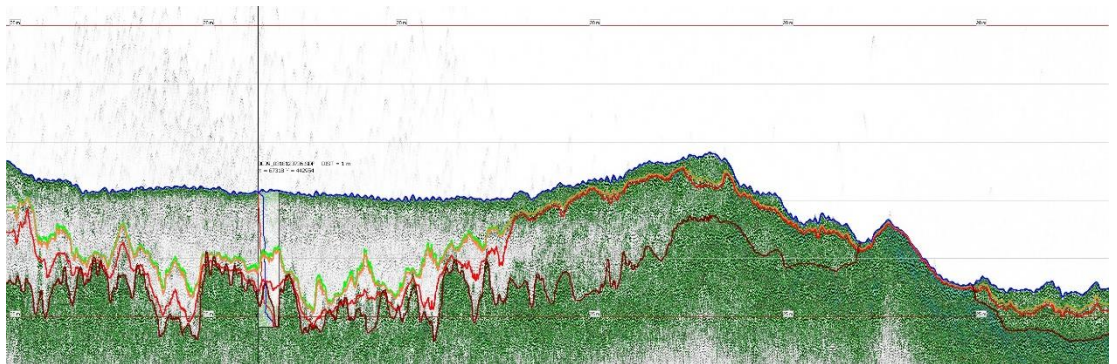


Figure A92. Fluid mud detection at the Calandkanaal on 18-03-2020: line Calandkanaal 9_0318075930. Blue level – water-mud interface, dark red level – sharp density contrast in seismic data, green level – 50 Pa, orange level – 1.2 kg/l (density) level, bright red level – 100 Pa (Bingham yield stress) level. Blue and red vertical lines show density and Bingham yield stress profiles, respectively

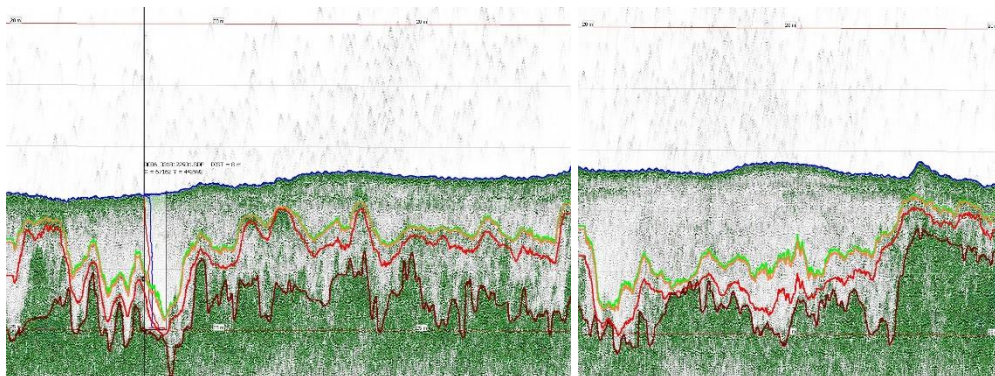


Figure A93. Fluid mud detection at the Calandkanaal on 18-03-2020: lines Calandkanaal 10_0318075318 (left), Calandkanaal 11_0318074842 (right). Blue level – water-mud interface, dark red level – sharp density contrast in seismic data, green level – 50 Pa, orange level – 1.2 kg/l (density) level, bright red level – 100 Pa (Bingham yield stress) level. Blue and red vertical lines show density and Bingham yield stress profiles, respectively

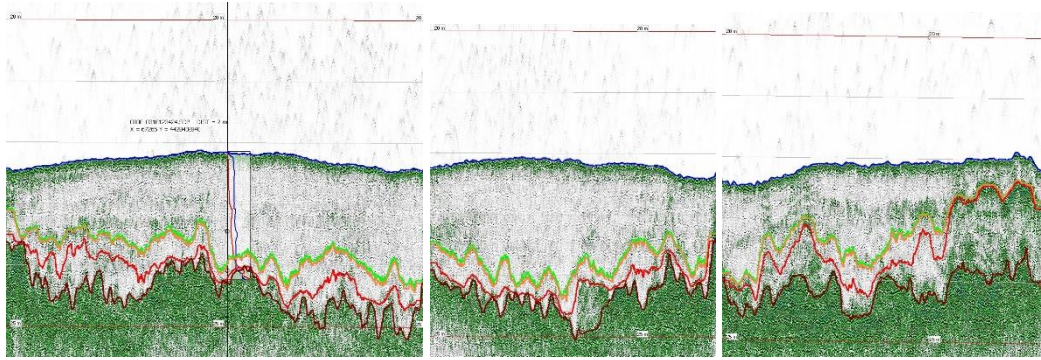


Figure A94. Fluid mud detection at the Calandkanaal on 18-03-2020: lines Calandkanaal 12_0318074328 (left), Calandkanaal 13_0318073940 (middle), Calandkanaal 14_0318073552 (right). Blue level – water-mud interface, dark red level – sharp density contrast in seismic data, green level – 50 Pa, orange level – 1.2 kg/l (density) level, bright red level – 100 Pa (Bingham yield stress) level. Blue and red vertical lines show density and Bingham yield stress profiles, respectively

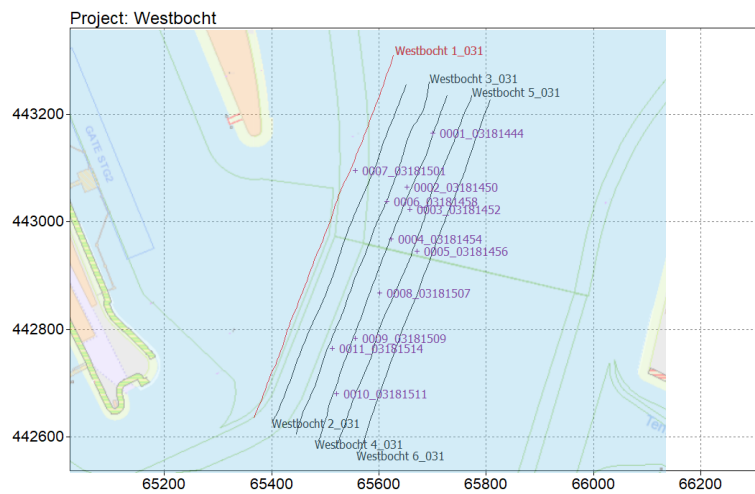


Figure A95. Positioning of SILAS lines at the Westbocht on 18-03-2020

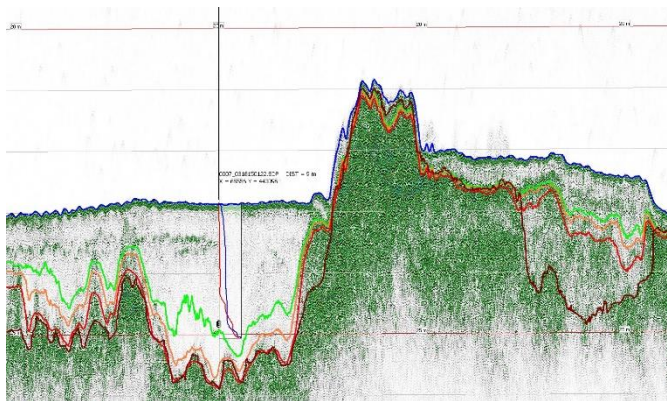


Figure A96. Fluid mud detection at the Westbocht on 18-03-2020: line Westbocht 1_0318124823. Blue level – water-mud interface, dark red level – sharp density contrast in seismic data, green level – 50 Pa, orange level – 1.2 kg/l (density) level, bright red level – 100 Pa (Bingham yield stress) level.

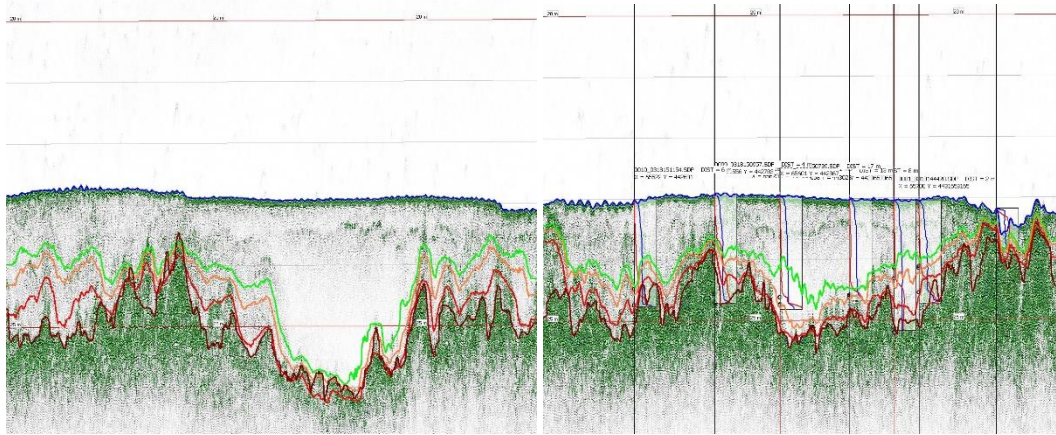


Figure A97. Fluid mud detection at the Westbocht on 18-03-2020: lines Westbocht 2_0318125513 (left), Westbocht 4_0318130752 (right). Blue level – water-mud interface, dark red level – sharp density contrast in seismic data, green level – 50 Pa, orange level – 1.2 kg/l (density) level, bright red level – 100 Pa (Bingham yield stress) level. Blue and red vertical lines show density and Bingham yield stress profiles, respectively

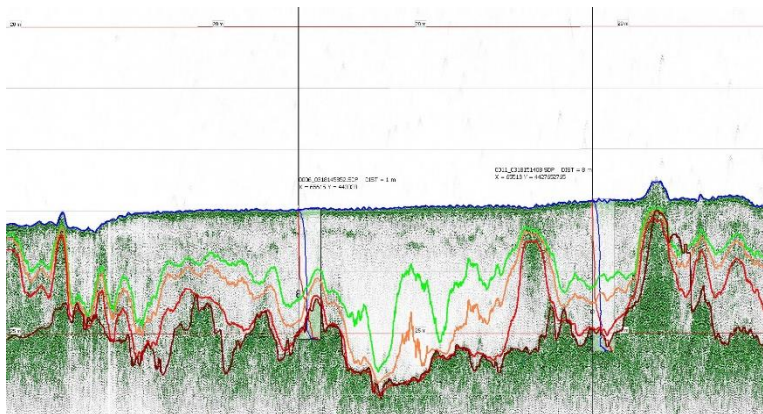


Figure A98. Fluid mud detection at the Westbocht on 18-03-2020: line Westbocht 3_0318130047. Blue level – water-mud interface, dark red level – sharp density contrast in seismic data, green level – 50 Pa, orange level – 1.2 kg/l (density) level, bright red level – 100 Pa (Bingham yield stress) level. Blue and red vertical lines show density and Bingham yield stress profiles, respectively

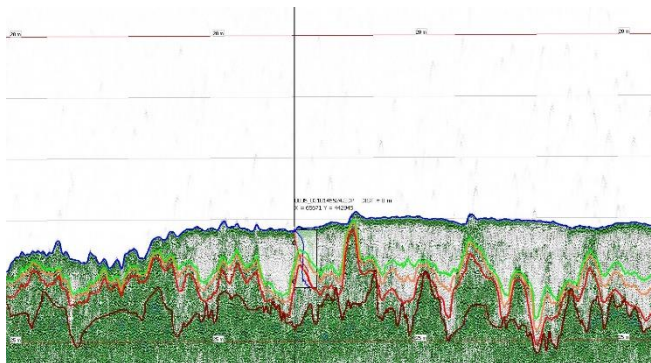


Figure A99. Fluid mud detection at the Westbocht on 18-03-2020: line Westbocht 5_0318131323. Blue level – water-mud interface, dark red level – sharp density contrast in seismic data, green level – 50 Pa, orange level – 1.2 kg/l (density) level, bright red level – 100 Pa (Bingham yield stress) level. Blue and red vertical lines show density and Bingham yield stress profiles, respectively

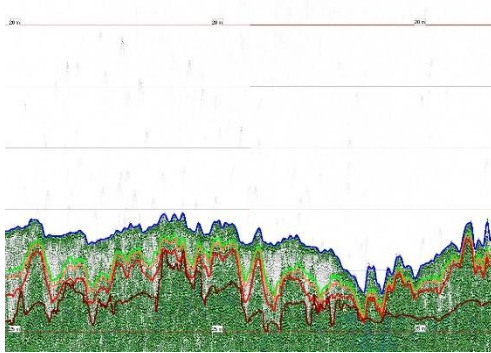


Figure A100. Fluid mud detection at the Westbocht on 18-03-2020: line Westbocht 6_0318131924. Blue level – water-mud interface, dark red level – sharp density contrast in seismic data, green level – 50 Pa, orange level – 1.2 kg/l (density) level, bright red level – 100 Pa (Bingham yield stress) level.

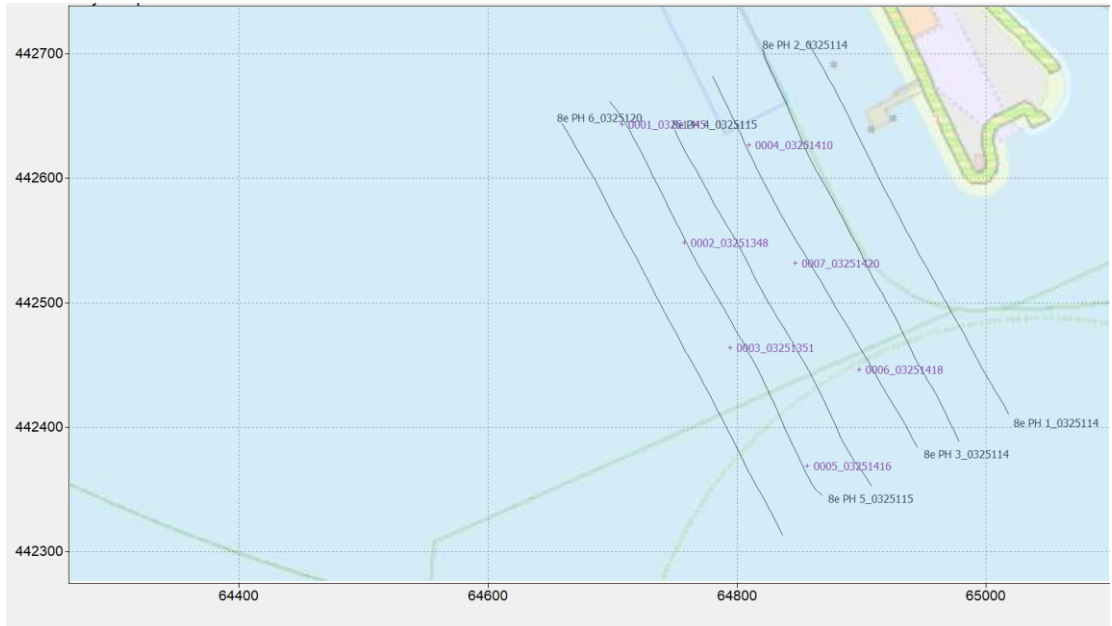


Figure A101. Positioning of SILAS lines at the 8e Petroleumhaven on 25-03-2020

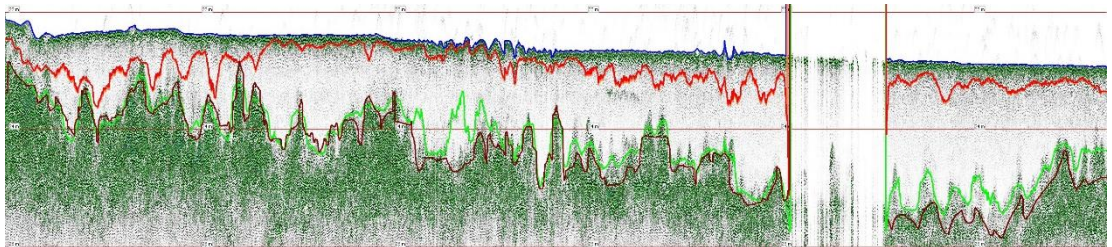


Figure A102. Fluid mud detection at the 8e Petroleumhaven on 25-03-2020: line 8e PH 1_0325083402. Blue level – water-mud interface, dark red level – sharp density contrast in seismic data, green level – 1.2 kg/l (density), bright red level – 1.17 kg/l (density) level.

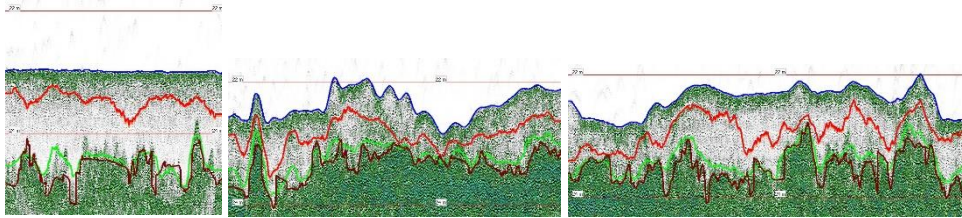


Figure A103. Fluid mud detection at the 8e Petroleumhaven on 25-03-2020: lines 8e PH 1_0325083402_1 (left), 8e PH 1_0325114149 (middle), 8e PH 2_0325114512 (right). Blue level – water-mud interface, dark red level – sharp density contrast in seismic data, green level – 1.2 kg/l (density), bright red level – 1.17 kg/l (density) level.

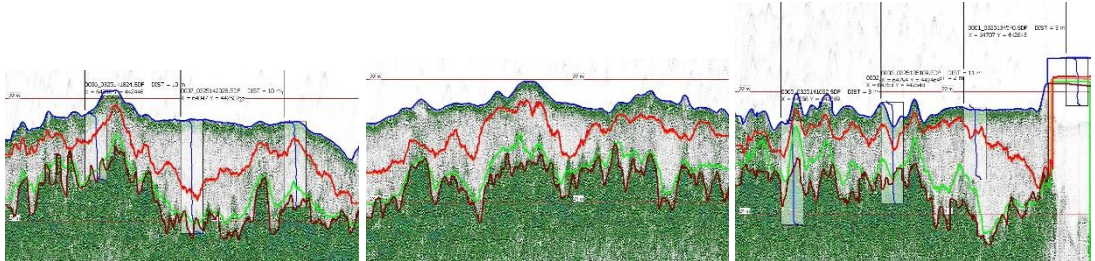


Figure A104. Fluid mud detection at the 8e Petroleumhaven on 25-03-2020: lines 8e PH 3_0325114900 (left), 8e PH 4_0325115308 (middle), 8e PH 5_0325115643 (right). Blue level – water-mud interface, dark red level – sharp density contrast in seismic data, green level – 1.2 kg/l (density), bright red level – 1.17 kg/l (density) level. Blue vertical lines show density profiles

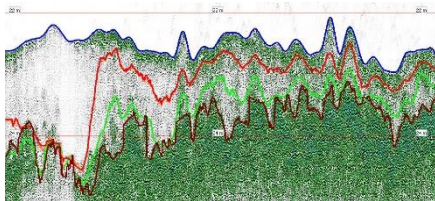


Figure A105. Fluid mud detection at the 8e Petroleumhaven on 25-03-2020: line 8e PH 6_0325120254. Blue level – water-mud interface, dark red level – sharp density contrast in seismic data, green level – 1.2 kg/l (density), bright red level – 1.17 kg/l (density) level. Blue vertical line shows density profiles

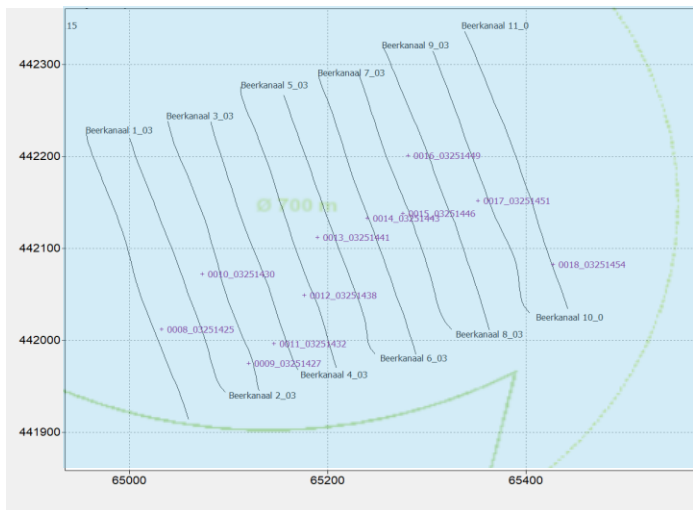


Figure A106. Positioning of SILAS lines at the Beerkanaal on 25-03-2020

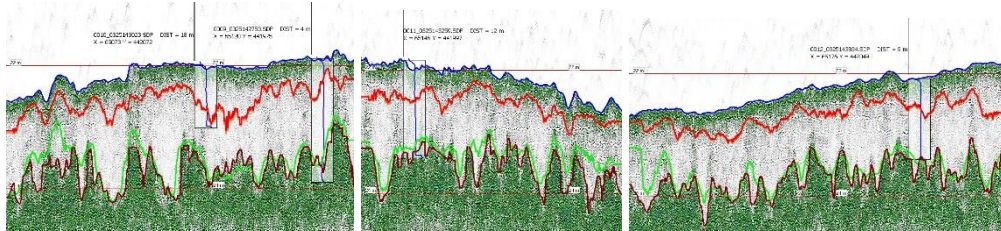


Figure A107. Fluid mud detection at the Beerkanaal on 25-03-2020: lines Beerkanaal 1_0325113513 (left), Beerkanaal 2_0325113142 (middle), Beerkanaal 3_0325112749 (right). Blue level – water-mud interface, dark red level – sharp density contrast in seismic data, green level – 1.2 kg/l (density), bright red level – 1.17 kg/l (density) level. Blue vertical line shows density profiles

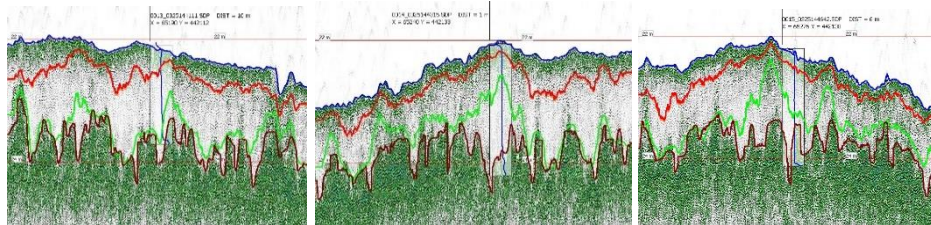


Figure A108. Fluid mud detection at the Beerkanaal on 25-03-2020: lines Beerkanaal 4_0325112459 (left), Beerkanaal 5_0325112121 (middle), Beerkanaal 6_0325111818 (right). Blue level – water-mud interface, dark red level – sharp density contrast in seismic data, green level – 1.2 kg/l (density), bright red level – 1.17 kg/l (density) level. Blue vertical line shows density profiles

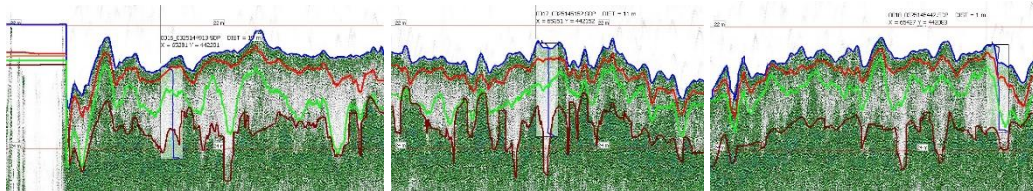


Figure A109. Fluid mud detection at the Beerkanaal on 25-03-2020: lines Beerkanaal 7_0325111513 (left), Beerkanaal 8_0325111204 (middle), Beerkanaal 9_0325110833 (right). Blue level – water-mud interface, dark red level – sharp density contrast in seismic data, green level – 1.2 kg/l (density), bright red level – 1.17 kg/l (density) level. Blue vertical line shows density profiles

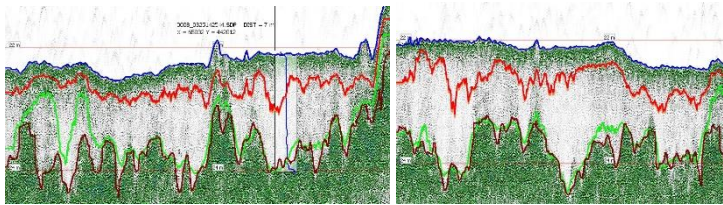


Figure A110. Fluid mud detection at the Beerkanaal on 25-03-2020: lines Beerkanaal 10_0325110404 (left), Beerkanaal 11_0325110051 (right). Blue level – water-mud interface, dark red level – sharp density contrast in seismic data, green level – 1.2 kg/l (density), bright red level – 1.17 kg/l (density) level. Blue vertical line shows density profiles



Figure A111. Positioning of SILAS lines at the Westbocht on 25-03-2020

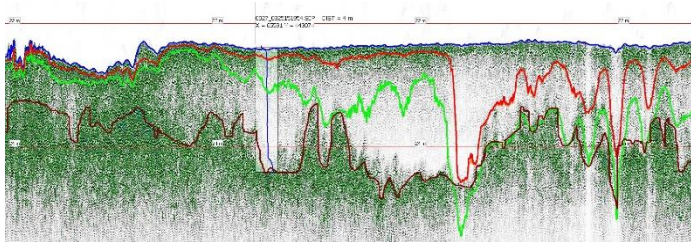


Figure A112. Fluid mud detection at the Westbocht on 25-03-2020: line Westbocht 1_0325095217. Blue level – water-mud interface, dark red level – sharp density contrast in seismic data, green level – 1.2 kg/l (density), bright red level – 1.17 kg/l (density) level.

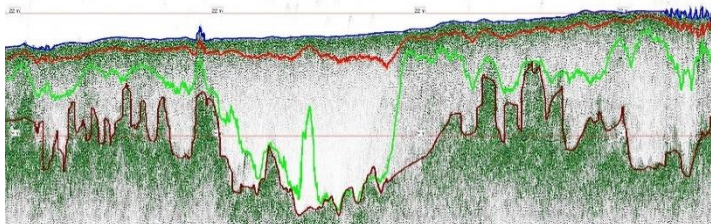


Figure A113. Fluid mud detection at the Westbocht on 25-03-2020: line Westbocht 2_0325102011. Blue level – water-mud interface, dark red level – sharp density contrast in seismic data, green level – 1.2 kg/l (density), bright red level – 1.17 kg/l (density) level.

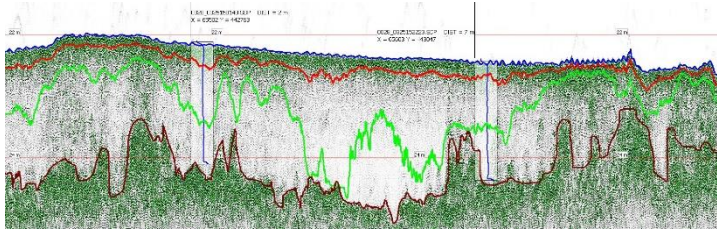


Figure A114. Fluid mud detection at the Westbocht on 25-03-2020: line Westbocht 3_0325102639. Blue level – water-mud interface, dark red level – sharp density contrast in seismic data, green level – 1.2 kg/l (density), bright red level – 1.17 kg/l (density) level. Blue vertical line shows density profiles

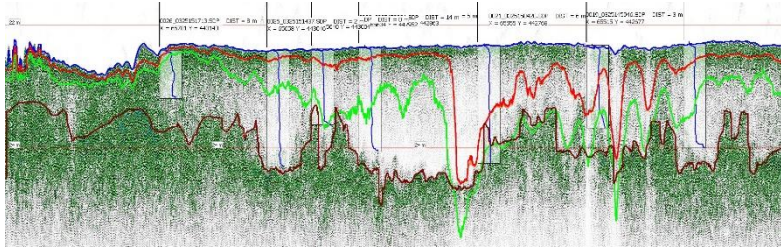


Figure A115. Fluid mud detection at the Westbocht on 25-03-2020: line Westbocht 4_0325103744. Blue level – water-mud interface, dark red level – sharp density contrast in seismic data, green level – 1.2 kg/l (density), bright red level – 1.17 kg/l (density) level. Blue vertical line shows density profiles

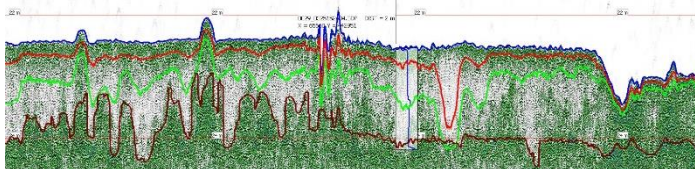


Figure A116. Fluid mud detection at the Westbocht on 25-03-2020: line Westbocht 5_0325105006. Blue level – water-mud interface, dark red level – sharp density contrast in seismic data, green level – 1.2 kg/l (density), bright red level – 1.17 kg/l (density) level. Blue vertical line shows density profiles

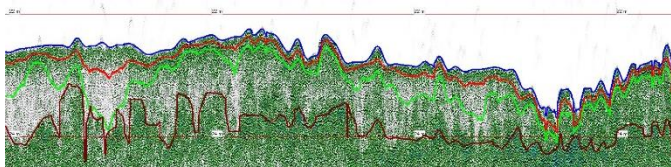


Figure A117. Fluid mud detection at the Westbocht on 25-03-2020: line Westbocht 6_0325101339. Blue level – water-mud interface, dark red level – sharp density contrast in seismic data, green level – 1.2 kg/l (density), bright red level – 1.17 kg/l (density) level. Blue vertical line shows density profiles

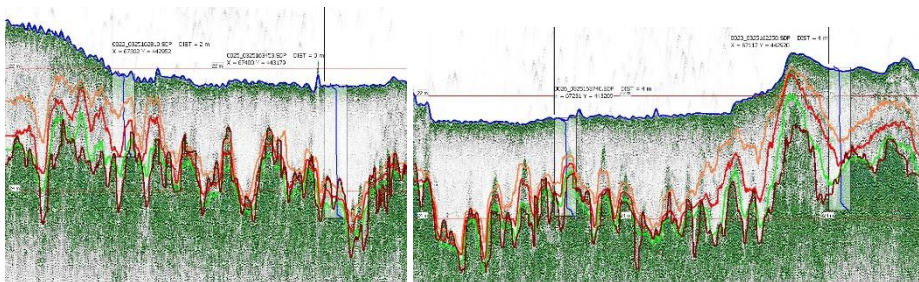


Figure A118. Fluid mud detection at the Calandkanaal on 25-03-2020: lines Cal.kan. cross 1_0325092226 (left), Cal.kan.cross2_0325092654 (right). Blue level – water-mud interface, dark red level – sharp density contrast in seismic data, green level – 1.2 kg/l (density), bright red level – 1.17 kg/l (density) level, orange level – 1.15 kg/l (density) level. Blue vertical line shows density profiles

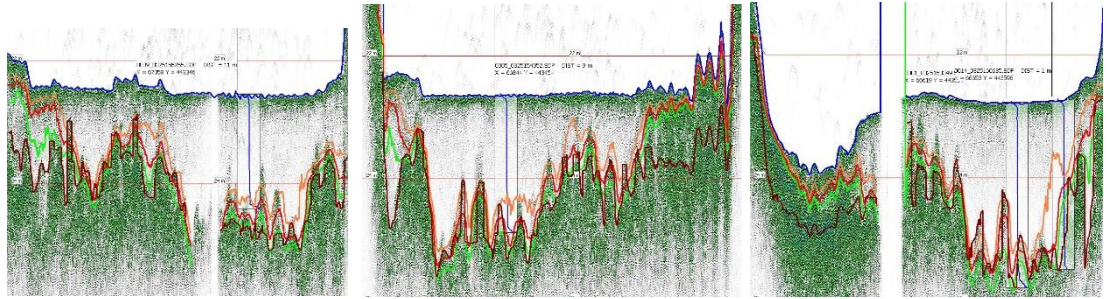


Figure A119. Fluid mud detection at the Calandkanaal on 25-03-2020: lines Cal.kan.cross_3_0325093328 (left), Cal.kan.cross_4_0325093756 (middle), Cal.kan.cross_5_0325094318 (right). Blue level – water-mud interface, dark red level – sharp density contrast in seismic data, green level – 1.2 kg/l (density), bright red level – 1.17 kg/l (density) level, orange level – 1.15 kg/l (density) level. Blue vertical line shows density profiles

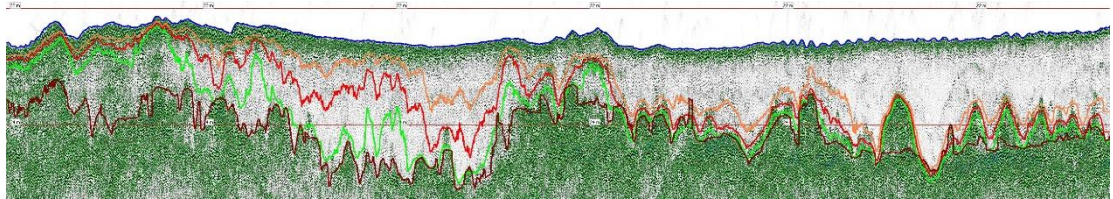


Figure A120. Fluid mud detection at the Calandkanaal on 25-03-2020: line Calandkanaal_1_0325084642. Blue level – water-mud interface, dark red level – sharp density contrast in seismic data, green level – 1.2 kg/l (density), bright red level – 1.17 kg/l (density) level, orange level – 1.15 kg/l (density) level. Blue vertical line shows density profiles

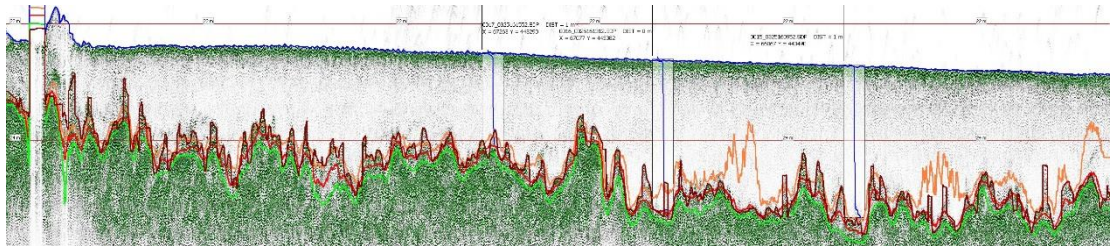


Figure A121. Fluid mud detection at the Calandkanaal on 25-03-2020: line Calandkanaal_2_0325085924. Blue level – water-mud interface, dark red level – sharp density contrast in seismic data, green level – 1.2 kg/l (density), bright red level – 1.17 kg/l (density) level, orange level – 1.15 kg/l (density) level. Blue vertical line shows density profiles

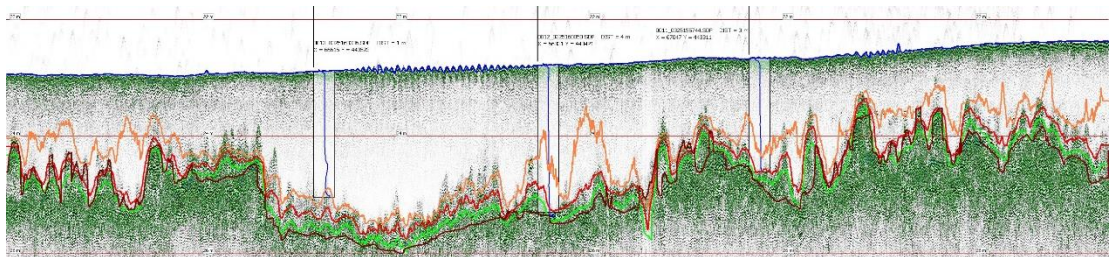


Figure A122. Fluid mud detection at the Calandkanaal on 25-03-2020: line Calandkanaal_4_0325082102. Blue level – water-mud interface, dark red level – sharp density contrast in seismic data, green level – 1.2 kg/l (density), bright red level – 1.17 kg/l (density) level, orange level – 1.15 kg/l (density) level. Blue vertical line shows density profiles

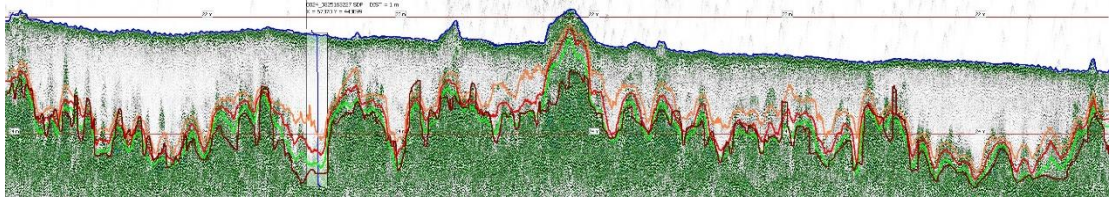


Figure A123. Fluid mud detection at the Calandkanaal on 25-03-2020: line Calandkanaal 5_0325080845. Blue level – water-mud interface, dark red level – sharp density contrast in seismic data, green level – 1.2 kg/l (density), bright red level – 1.17 kg/l (density) level, orange level – 1.15 kg/l (density) level. Blue vertical line shows density profiles

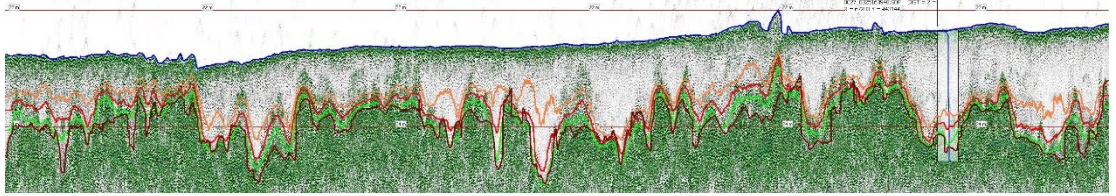


Figure A124. Fluid mud detection at the Calandkanaal on 25-03-2020: line Calandkanaal 6_0325075525. Blue level – water-mud interface, dark red level – sharp density contrast in seismic data, green level – 1.2 kg/l (density), bright red level – 1.17 kg/l (density) level, orange level – 1.15 kg/l (density) level. Blue vertical line shows density profiles

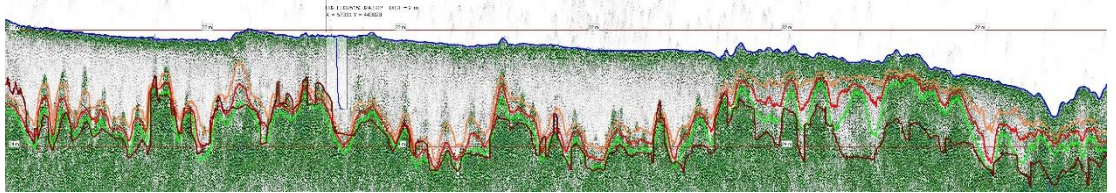


Figure A125. Fluid mud detection at the Calandkanaal on 25-03-2020: line Calandkanaal 7_0325074315. Blue level – water-mud interface, dark red level – sharp density contrast in seismic data, green level – 1.2 kg/l (density), bright red level – 1.17 kg/l (density) level, orange level – 1.15 kg/l (density) level. Blue vertical line shows density profiles

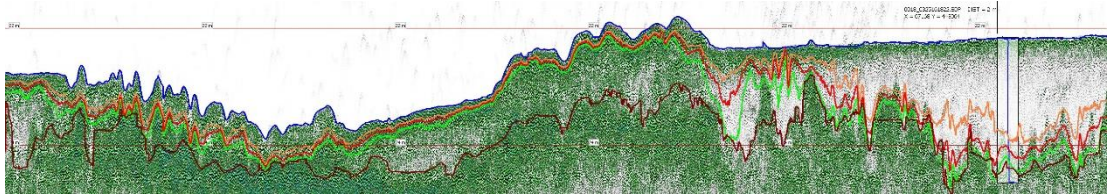


Figure A126. Fluid mud detection at the Calandkanaal on 25-03-2020: line Calandkanaal 8_0325072940. Blue level – water-mud interface, dark red level – sharp density contrast in seismic data, green level – 1.2 kg/l (density), bright red level – 1.17 kg/l (density) level, orange level – 1.15 kg/l (density) level. Blue vertical line shows density profiles

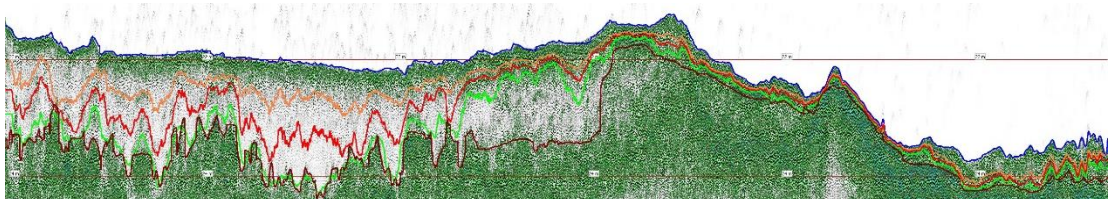


Figure A127. Fluid mud detection at the Calandkanaal on 25-03-2020: line Calandkanaal 9_0325071837. Blue level – water-mud interface, dark red level – sharp density contrast in seismic data, green level – 1.2 kg/l (density), bright red level – 1.17 kg/l (density) level, orange level – 1.15 kg/l (density) level.

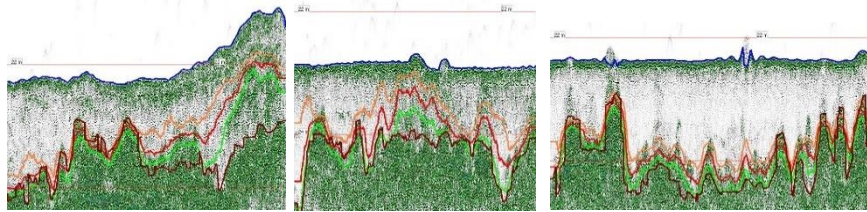


Figure A128. Fluid mud detection at the Calandkanaal on 25-03-2020: lines Calandkanaal 1_0325084642_1 (left), Calandkanaal 2_0325085924_1 (middle), Calandkanaal 4_0325082102_1 (right). Blue level – water-mud interface, dark red level – sharp density contrast in seismic data, green level – 1.2 kg/l (density), bright red level – 1.17 kg/l (density) level, orange level – 1.15 kg/l (density) level.

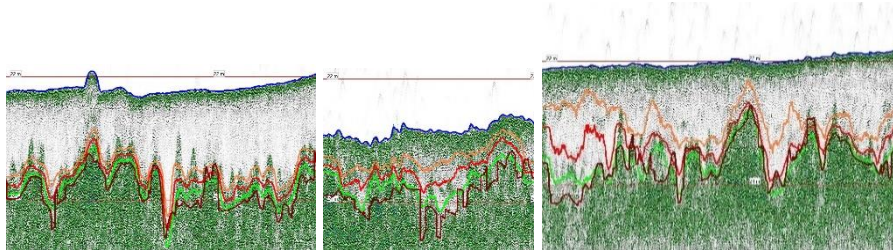


Figure A129. Fluid mud detection at the Calandkanaal on 25-03-2020: lines Calandkanaal 6_0325075525_1 (left), Calandkanaal 7_0325074315_1 (middle), Calandkanaal 8_0325072940_1 (right). Blue level – water-mud interface, dark red level – sharp density contrast in seismic data, green level – 1.2 kg/l (density), bright red level – 1.17 kg/l (density) level, orange level – 1.15 kg/l (density) level.

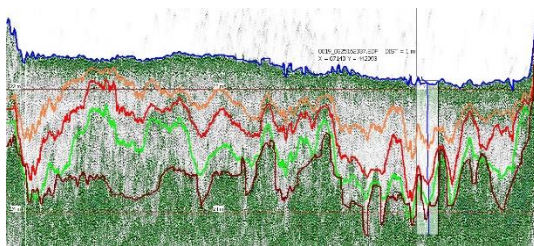


Figure A130. Fluid mud detection at the Calandkanaal on 25-03-2020: line Calandkanaal 10_0325070848. Blue level – water-mud interface, dark red level – sharp density contrast in seismic data, green level – 1.2 kg/l (density), bright red level – 1.17 kg/l (density) level, orange level – 1.15 kg/l (density) level. Blue vertical line shows density profiles

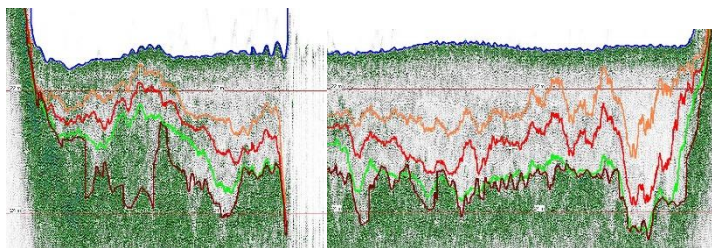


Figure A131. Fluid mud detection at the Calandkanaal on 25-03-2020: line Calandkanaal 11_0325070443. Blue level – water-mud interface, dark red level – sharp density contrast in seismic data, green level – 1.2 kg/l (density), bright red level – 1.17 kg/l (density) level, orange level – 1.15 kg/l (density) level

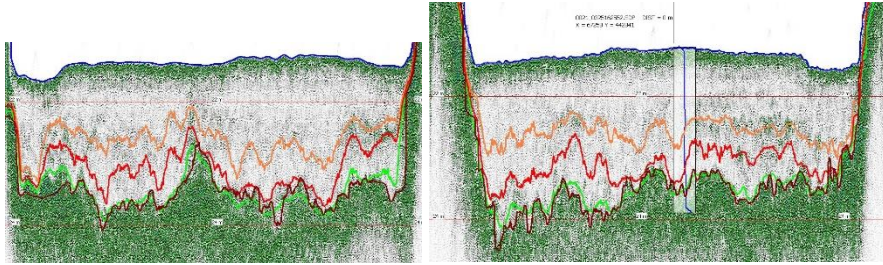


Figure A132. Fluid mud detection at the Calandkanaal on 25-03-2020: line Calandkanaal 13_0325065540. Blue level – water-mud interface, dark red level – sharp density contrast in seismic data, green level – 1.2 kg/l (density), bright red level – 1.17 kg/l (density) level, orange level – 1.15 kg/l (density) level. Blue vertical line shows density profiles

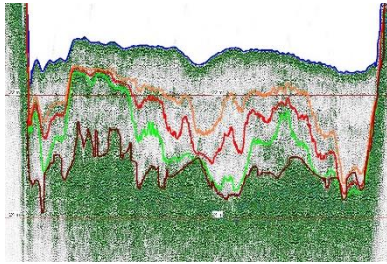


Figure A133. Fluid mud detection at the Calandkanaal on 25-03-2020: line Calandkanaal 14_0325065152. Blue level – water-mud interface, dark red level – sharp density contrast in seismic data, green level – 1.2 kg/l (density), bright red level – 1.17 kg/l (density) level, orange level – 1.15 kg/l (density) level.

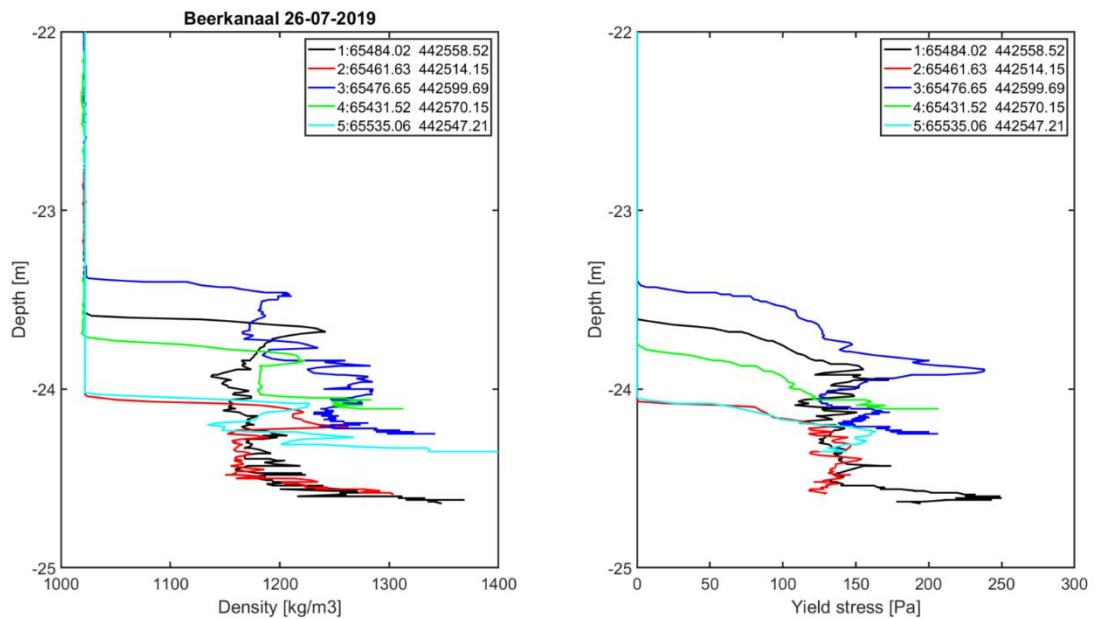


Figure A134. Fluid mud detection at the Beerkanaal on 26-07-2019: density (left) and yield stress (right) profiles

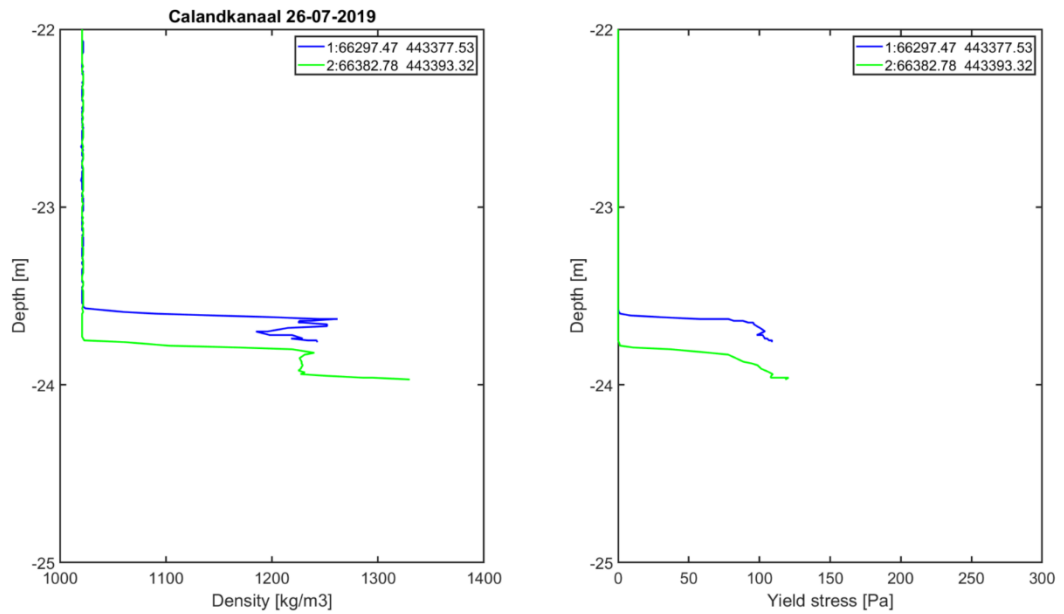


Figure A135. Fluid mud detection at the Calandkanaal on 26-07-2019: density (left) and yield stress (right) profiles

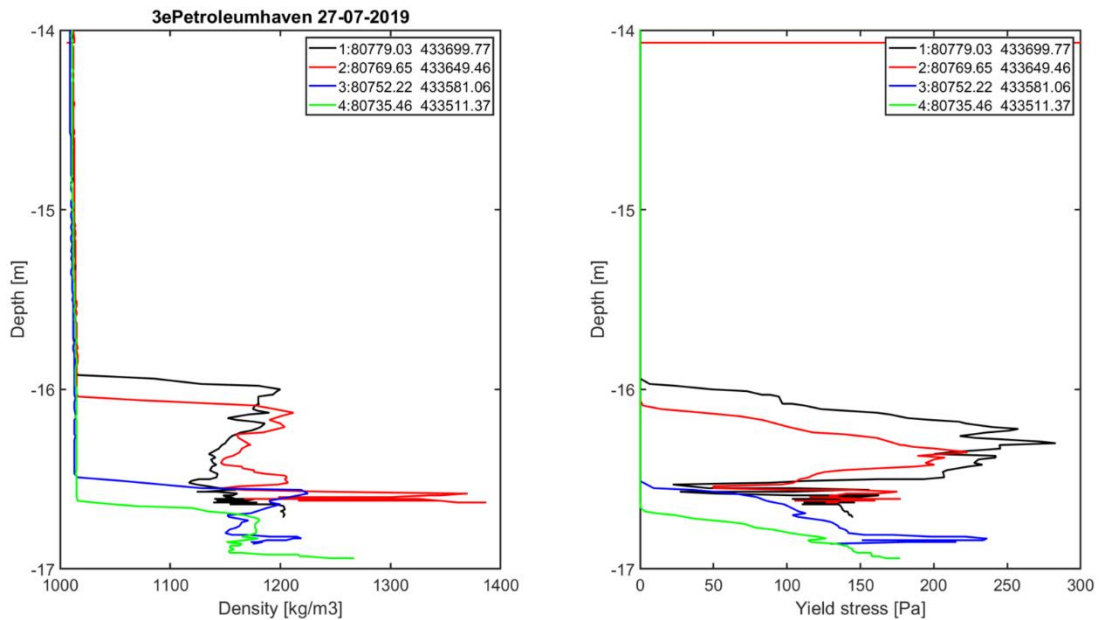


Figure A136. Fluid mud detection at the 3e Petroleumhaven on 27-07-2019: density (left) and yield stress (right) profiles

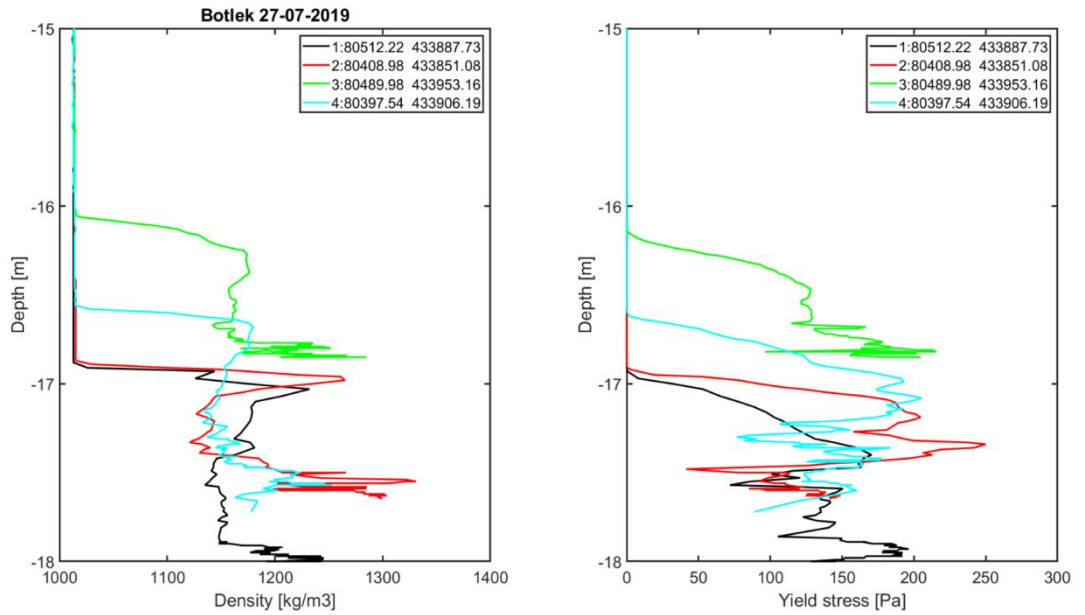


Figure A137. Fluid mud detection at Botlek on 27-07-2019: density (left) and yield stress (right) profiles

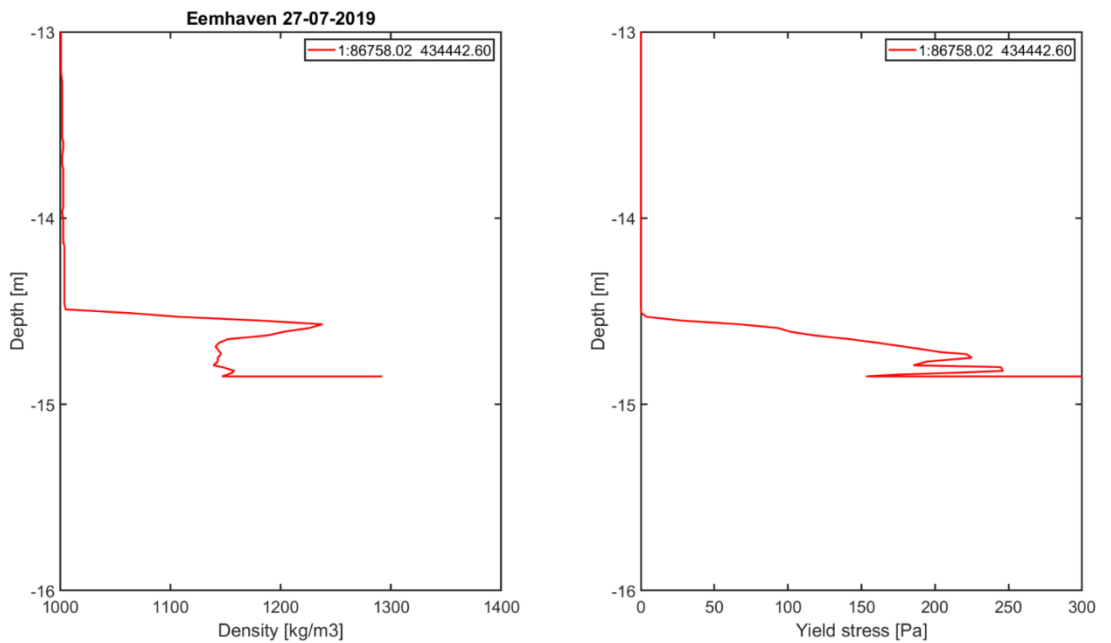


Figure A138. Fluid mud detection at the Eemhaven on 27-07-2019: density (left) and yield stress (right) profiles

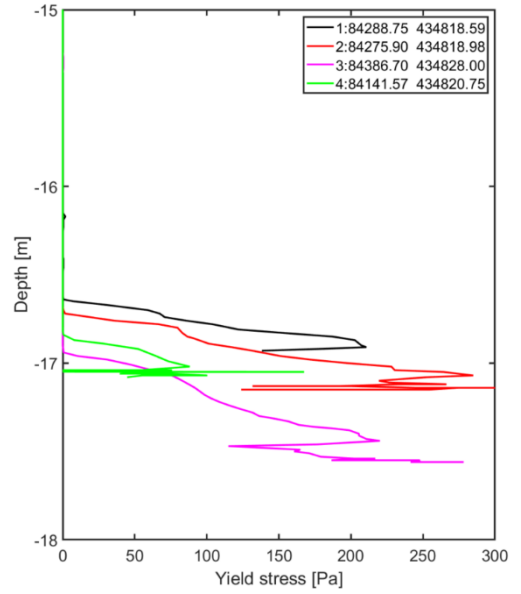
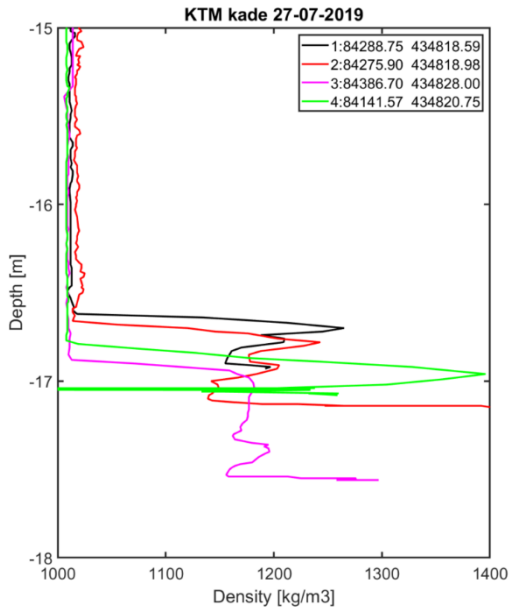


Figure A139. Fluid mud detection at the KTM kade on 27-07-2019: density (left) and yield stress (right) profiles

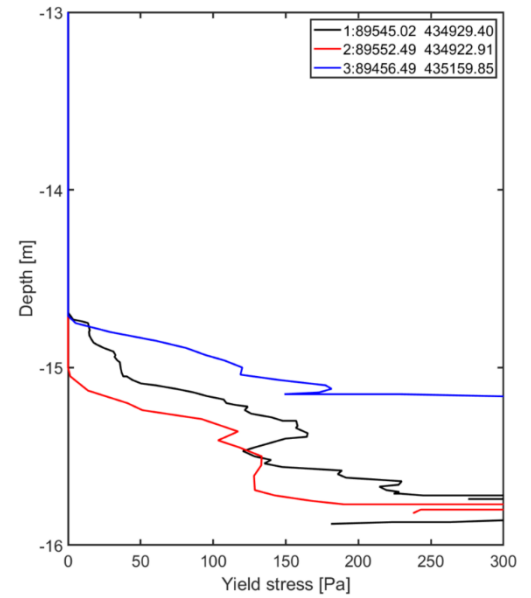
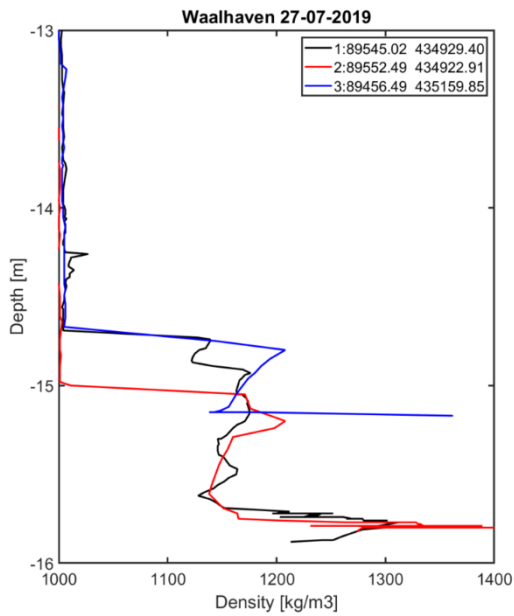


Figure A140. Fluid mud detection at the Waalhaven on 27-07-2019: density (left) and yield stress (right) profiles

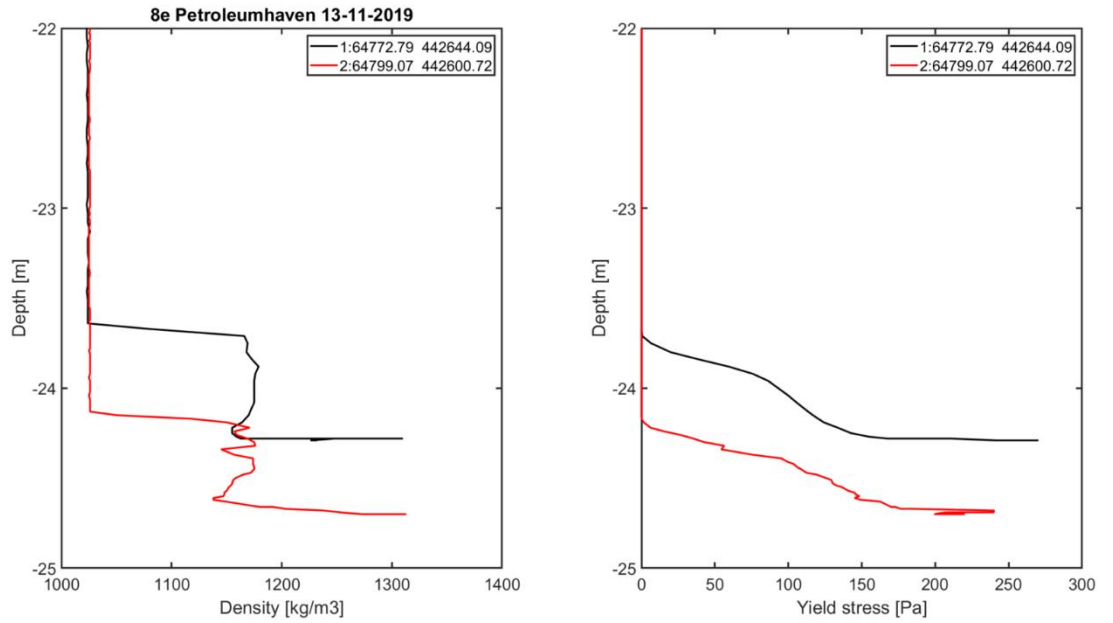


Figure A141. Fluid mud detection at the 8e Petroleumhaven on 13-11-2019: density (left) and yield stress (right) profiles

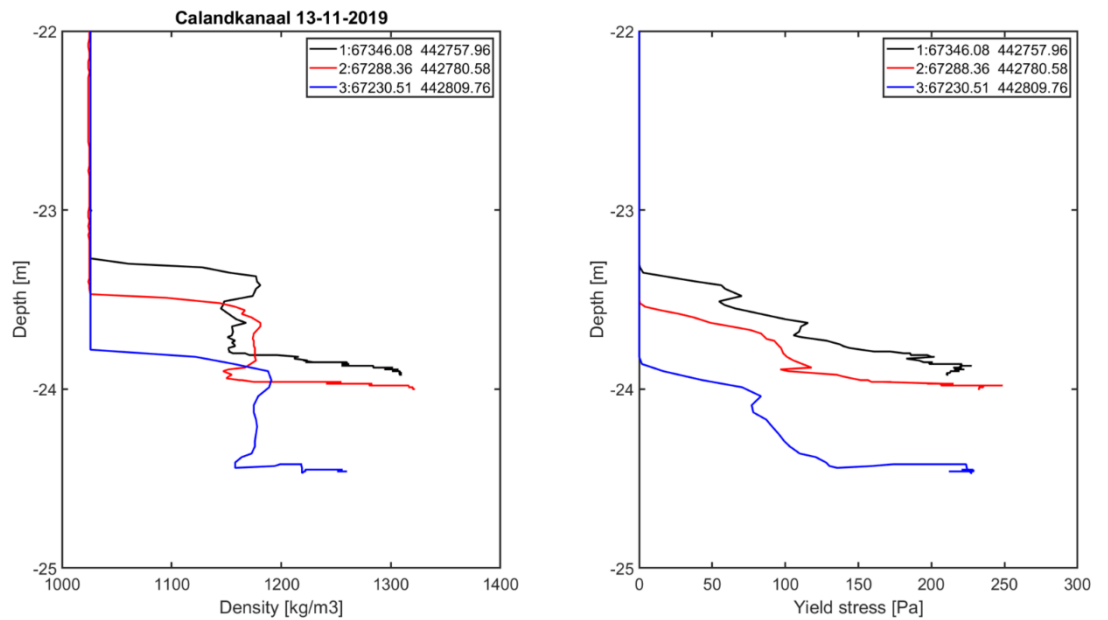


Figure A142. Fluid mud detection at the Calandkanaal on 13-11-2019: density (left) and yield stress (right) profiles

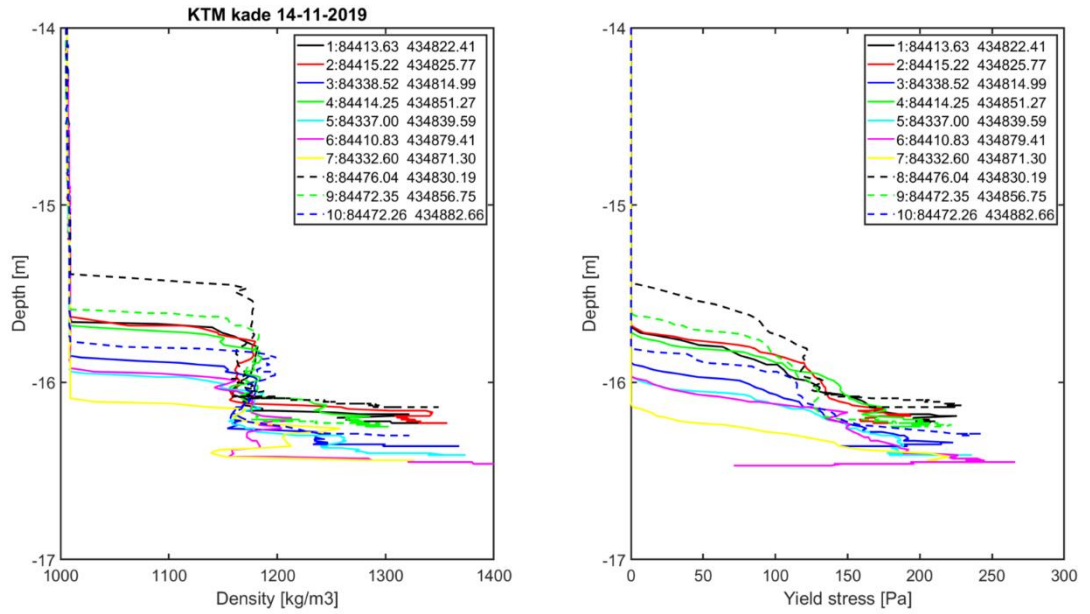


Figure A143. Fluid mud detection at the KTM kade on 14-11-2019: density (left) and yield stress (right) profiles

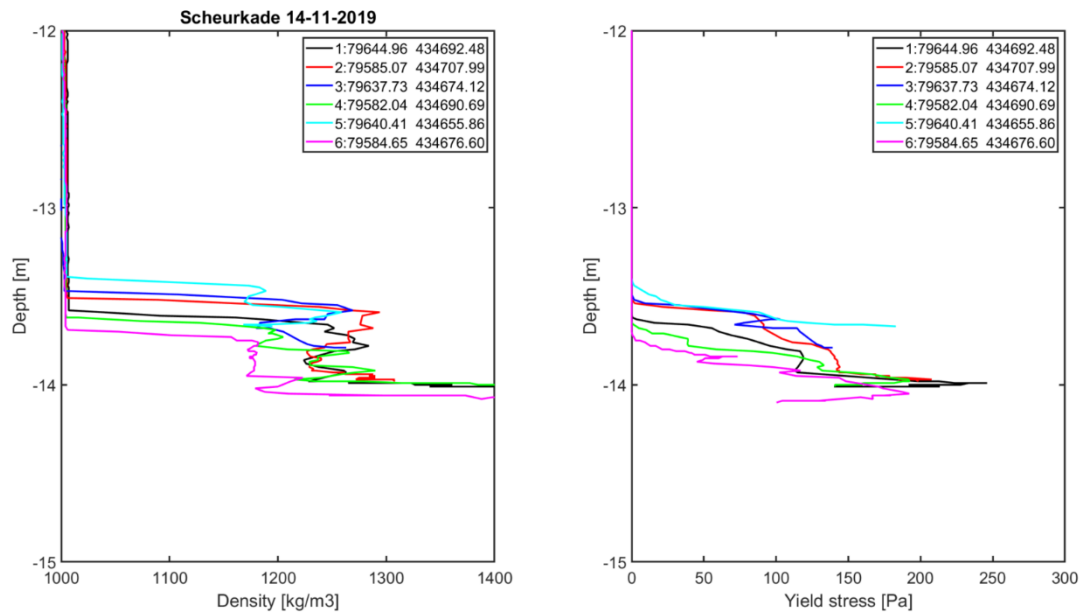


Figure A144. Fluid mud detection at the Scheurkade on 14-11-2019: density (left) and yield stress (right) profiles

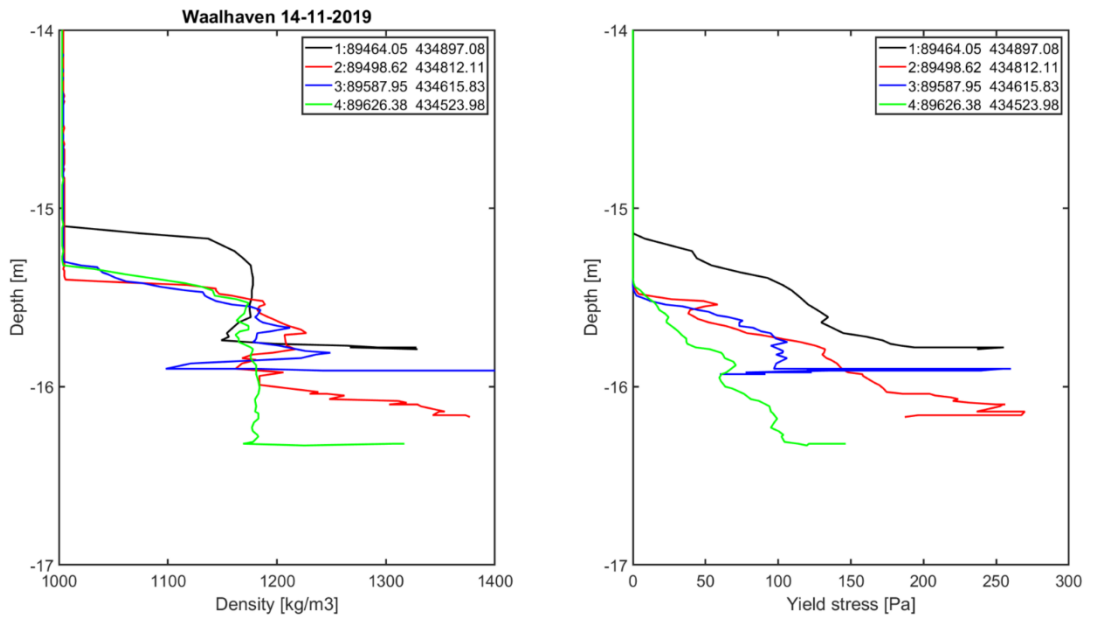


Figure A145. Fluid mud detection at the Waalhaven on 14-11-2019: density (left) and yield stress (right) profiles

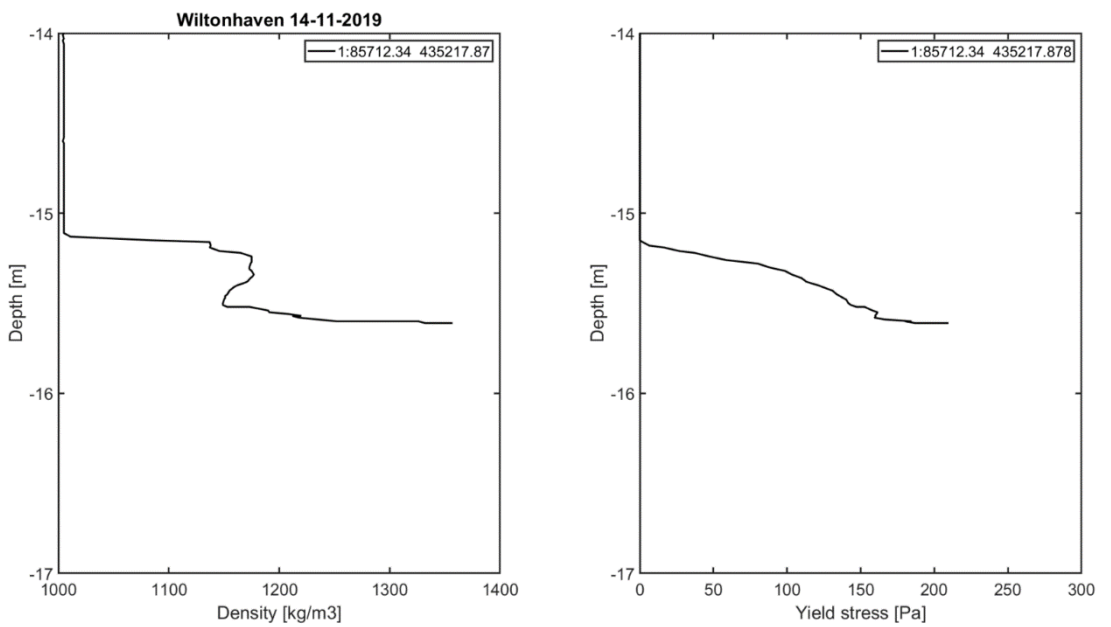


Figure A146. Fluid mud detection at the Wiltonhaven on 14-11-2019: density (left) and yield stress (right) profiles

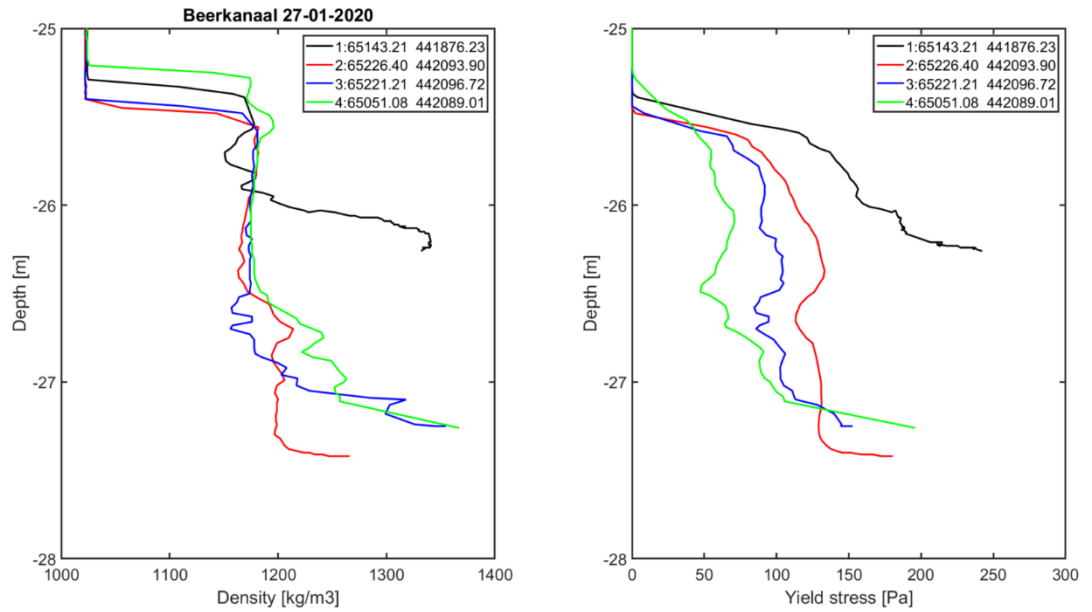


Figure A147. Fluid mud detection at the Beerkanaal on 27-01-2020: density (left) and yield stress (right) profiles

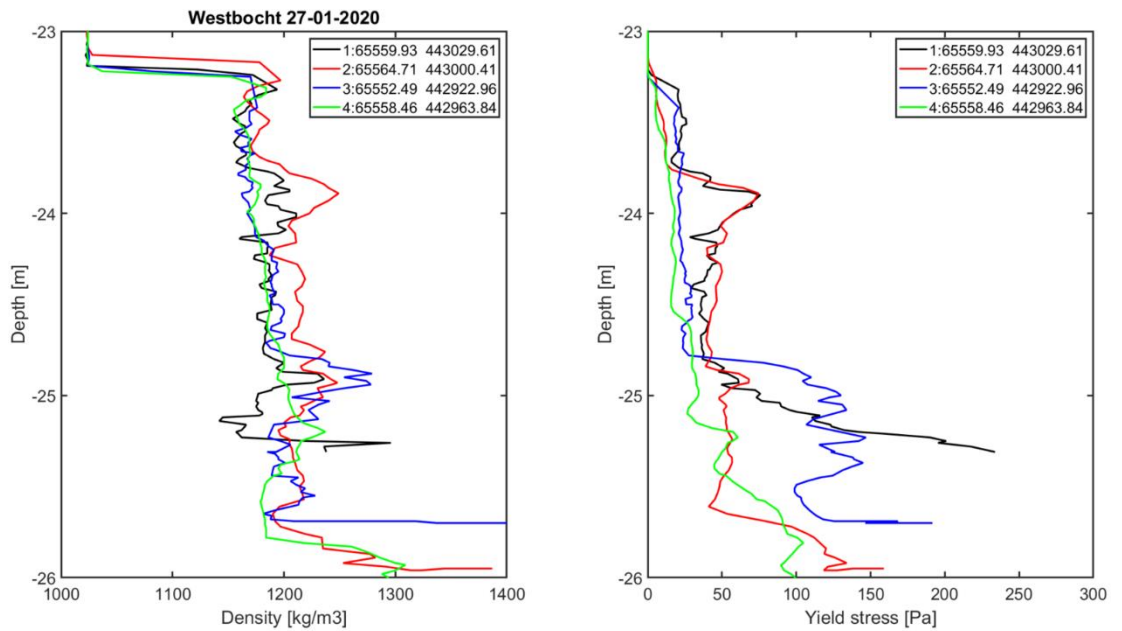


Figure A148. Fluid mud detection at the Westbocht on 27-01-2020: density (left) and yield stress (right) profiles

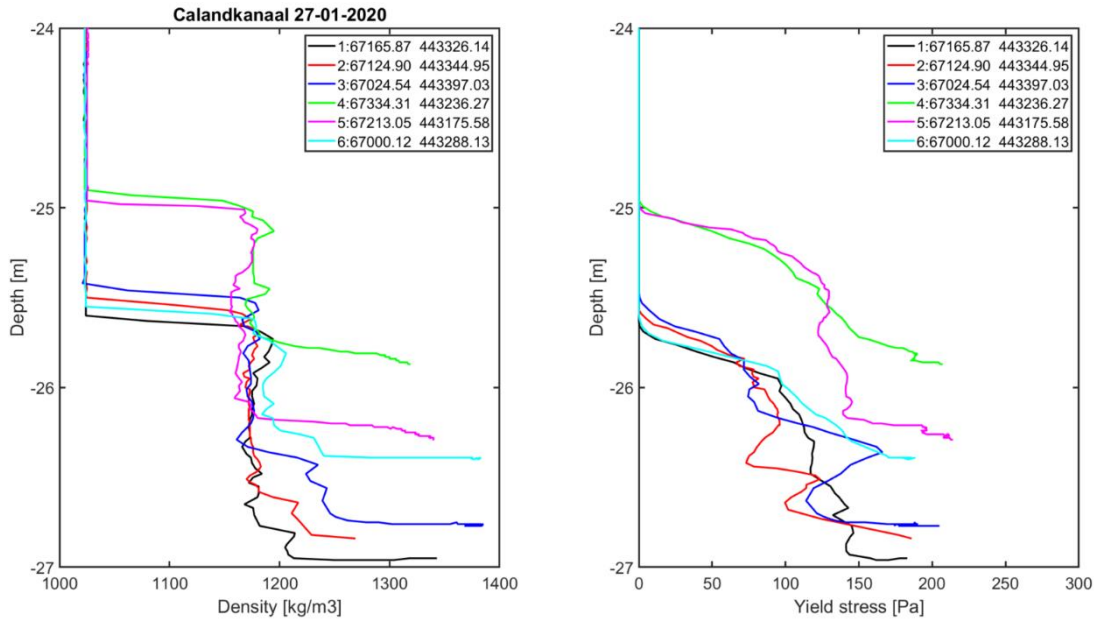


Figure A149. Fluid mud detection at the Calandkanaal on 27-01-2020: density (left) and yield stress (right) profiles

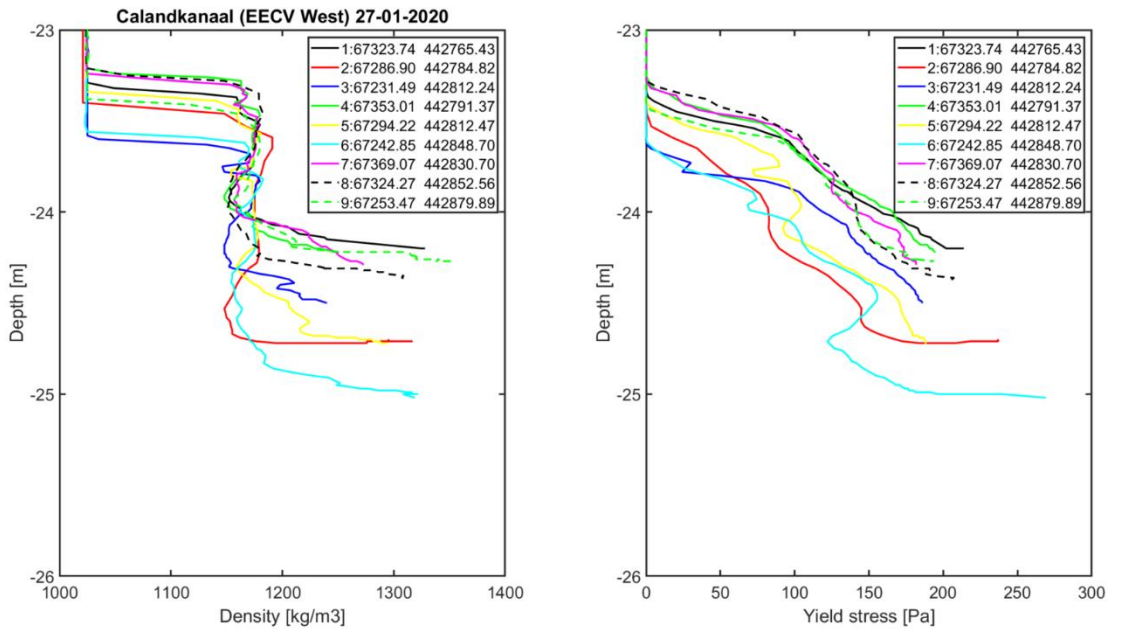


Figure A150. Fluid mud detection at the Calandkanaal (EECV West) on 27-01-2020: density (left) and yield stress (right) profiles

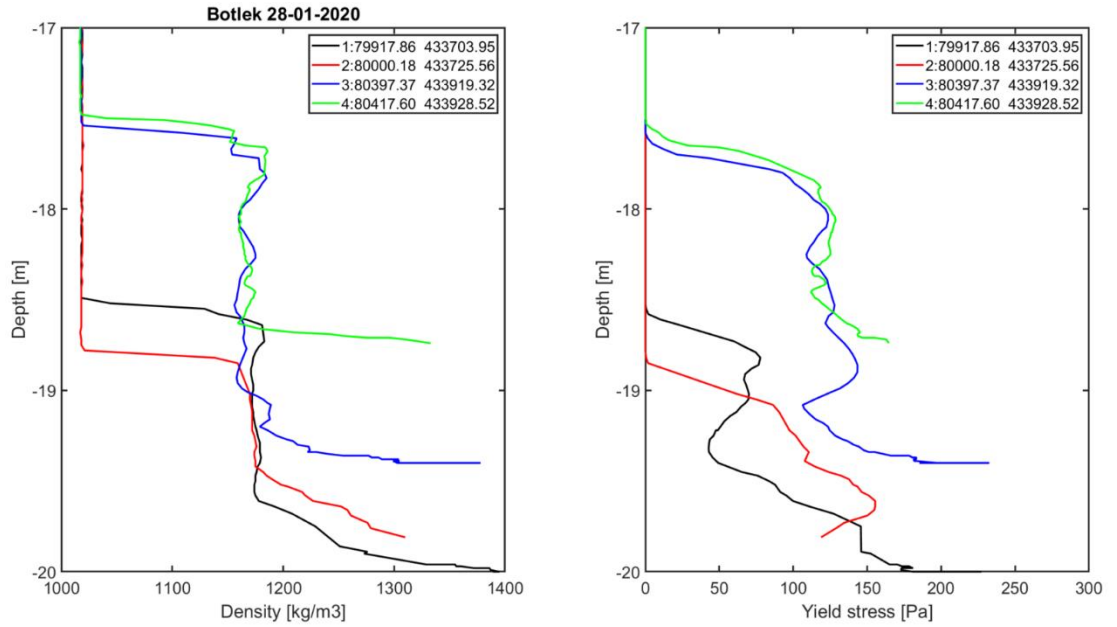


Figure A151. Fluid mud detection at Botlek on 27-01-2020: density (left) and yield stress (right) profiles

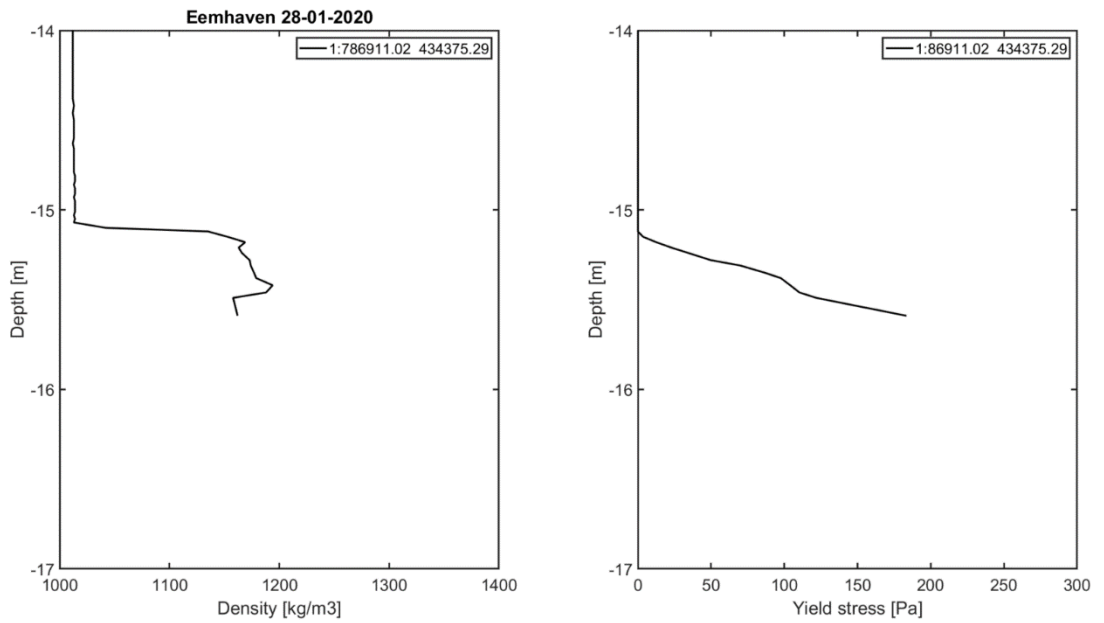


Figure A152. Fluid mud detection at Botlek on 27-01-2020: density (left) and yield stress (right) profiles

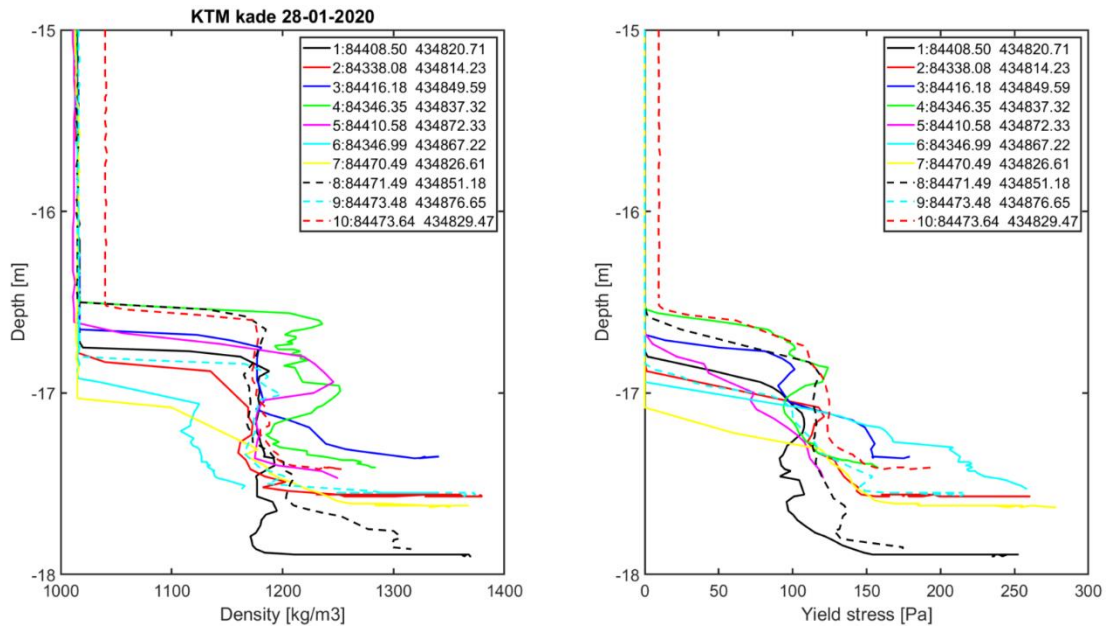


Figure A153. Fluid mud detection at the KTM kade on 28-01-2020: density (left) and yield stress (right) profiles

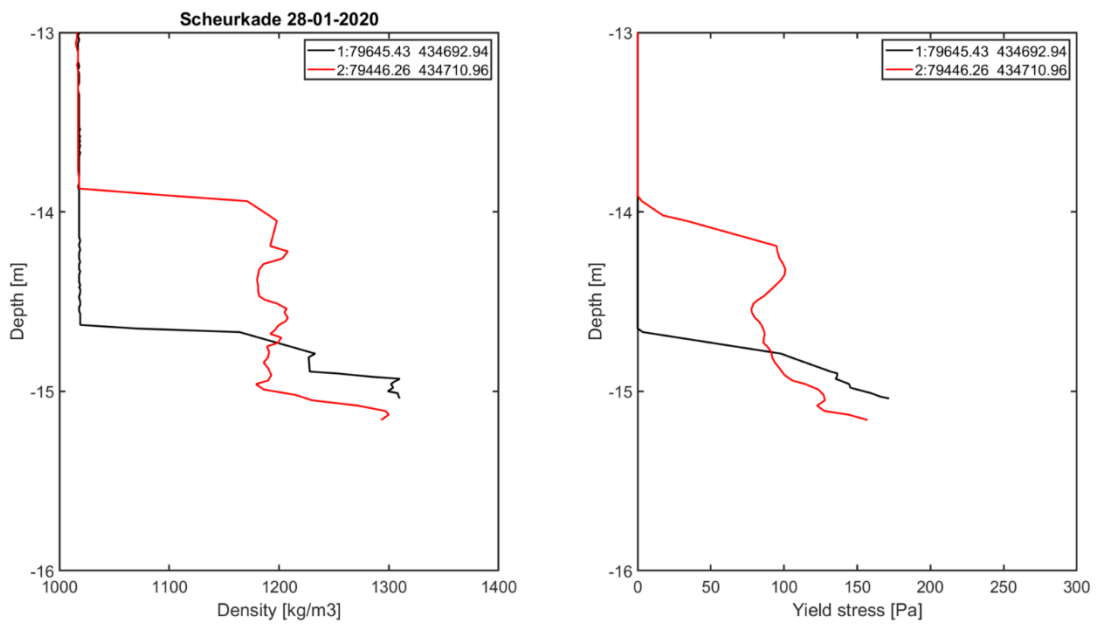


Figure A154. Fluid mud detection at the Scheurkade on 28-01-2020: density (left) and yield stress (right) profiles

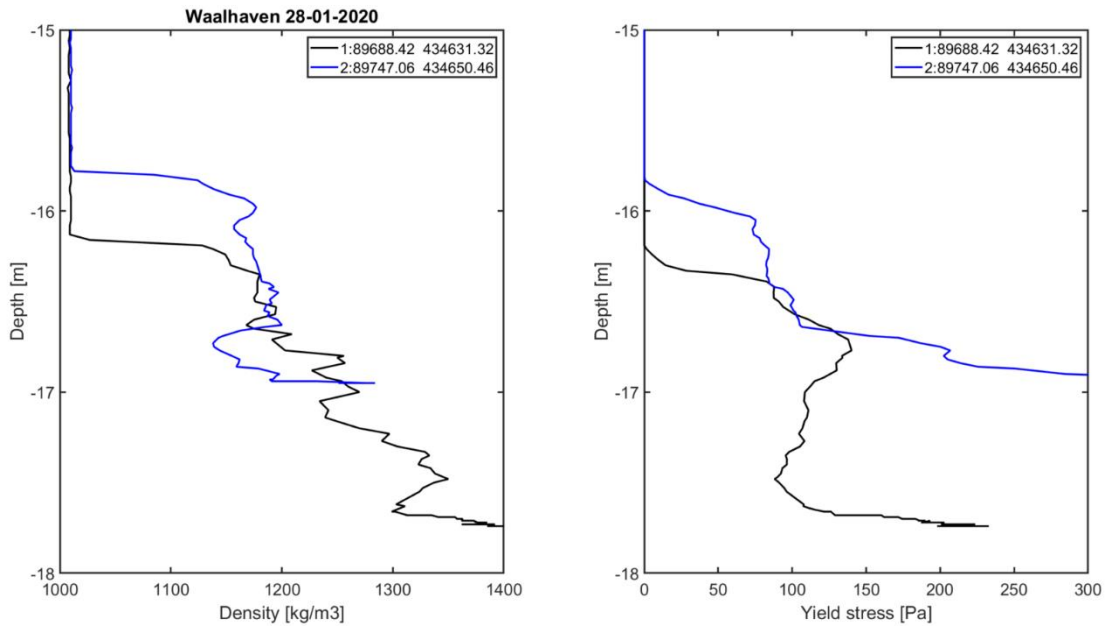


Figure A155. Fluid mud detection at the Waalhaven on 28-01-2020: density (left) and yield stress (right) profiles

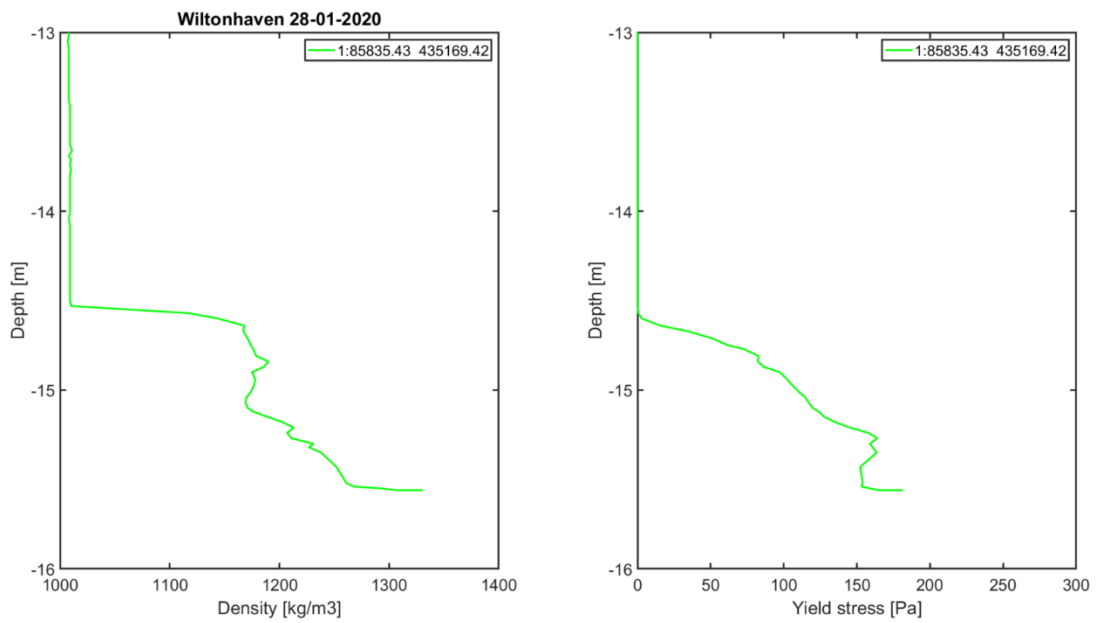


Figure A156. Fluid mud detection at the Wiltonhaven on 28-01-2020: density (left) and yield stress (right) profiles

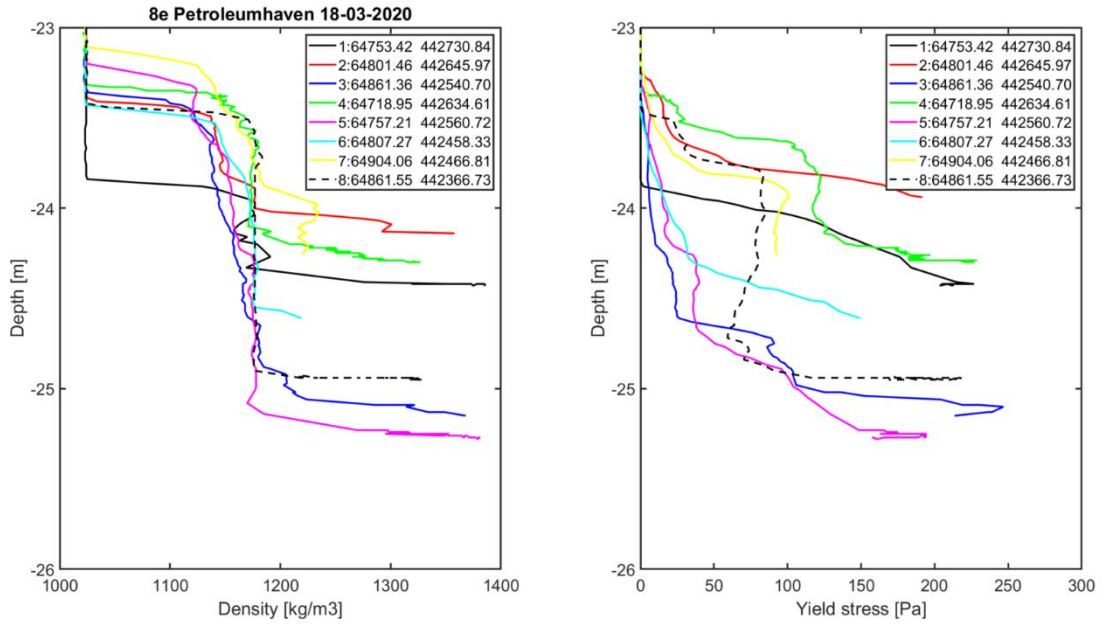


Figure A157. Fluid mud detection at the 8e Petroleumhaven on 18-03-2020: density (left) and yield stress (right) profiles

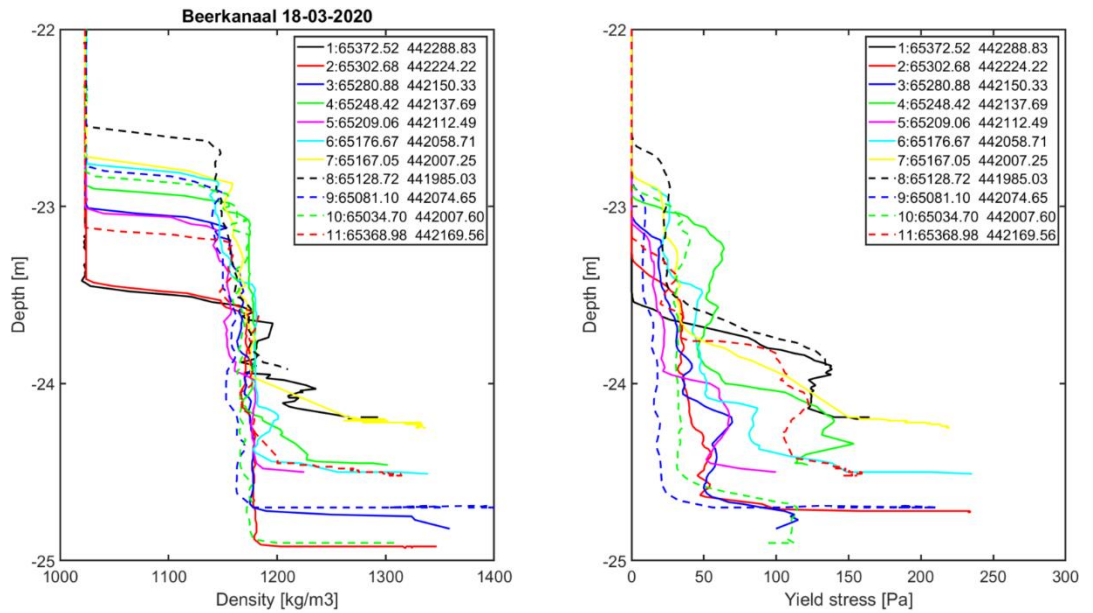


Figure A158. Fluid mud detection at the Beerkanaal on 18-03-2020: density (left) and yield stress (right) profiles

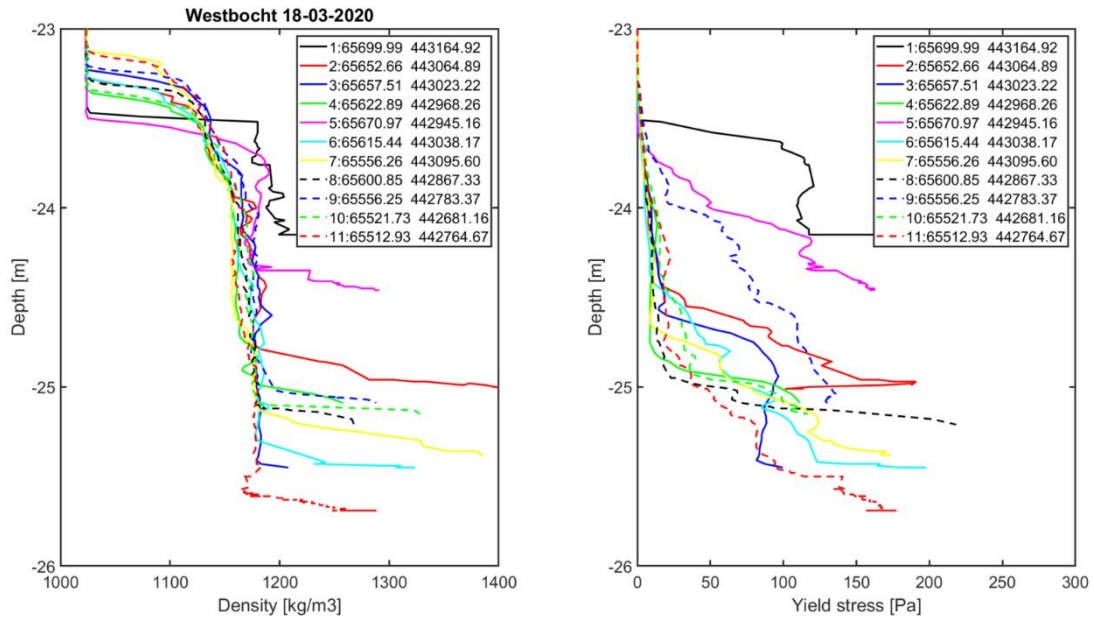


Figure A159. Fluid mud detection at the Westbocht on 18-03-2020: density (left) and yield stress (right) profiles

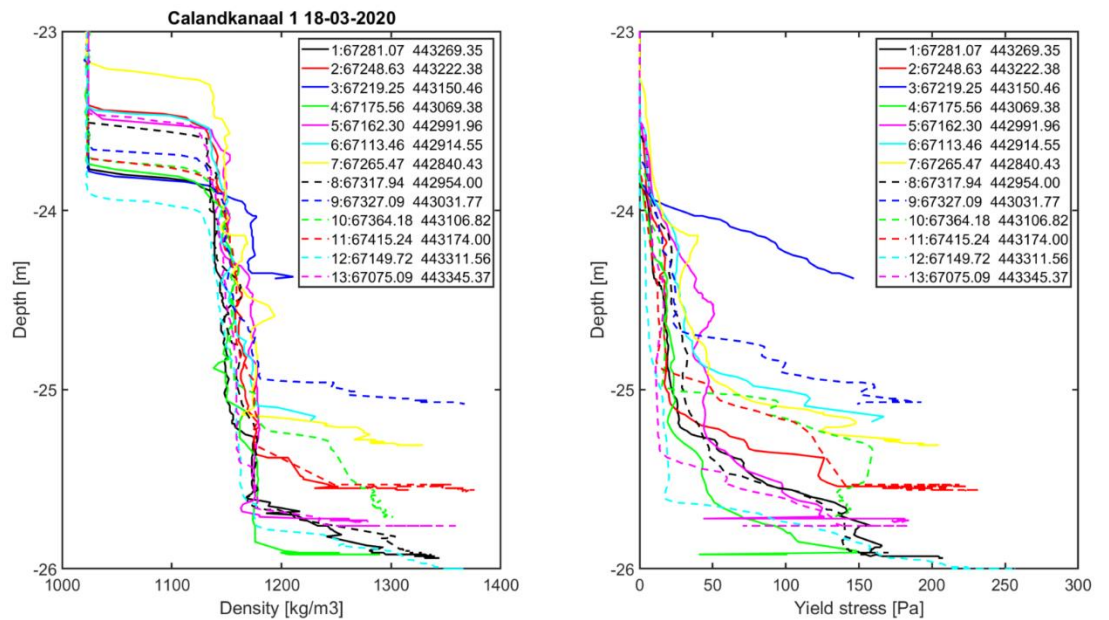


Figure A160. Fluid mud detection at the Calandkanaal on 18-03-2020: density (left) and yield stress (right) profiles, part 1

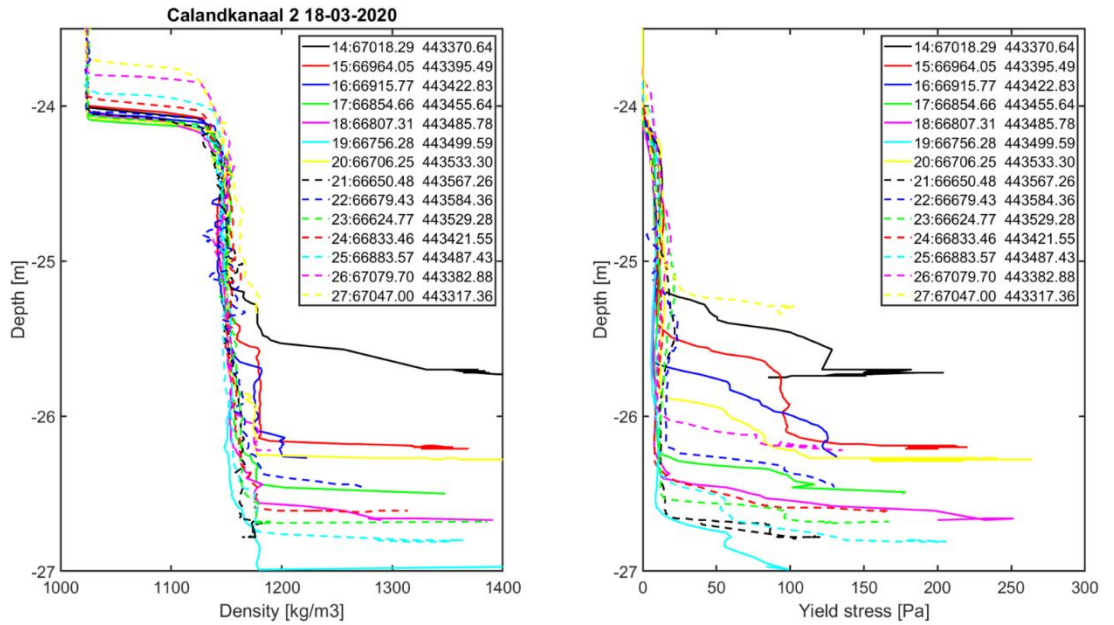


Figure A161. Fluid mud detection at the Calandkanaal on 18-03-2020: density (left) and yield stress (right) profiles, part 2

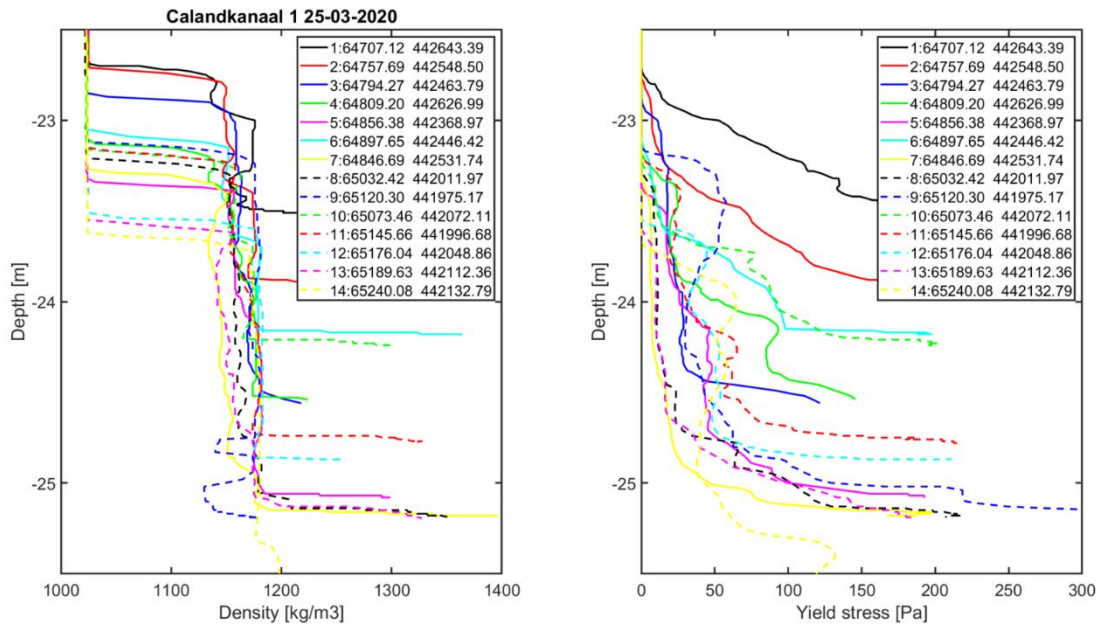


Figure A162. Fluid mud detection at the Calandkanaal on 25-03-2020: density (left) and yield stress (right) profiles, part 1

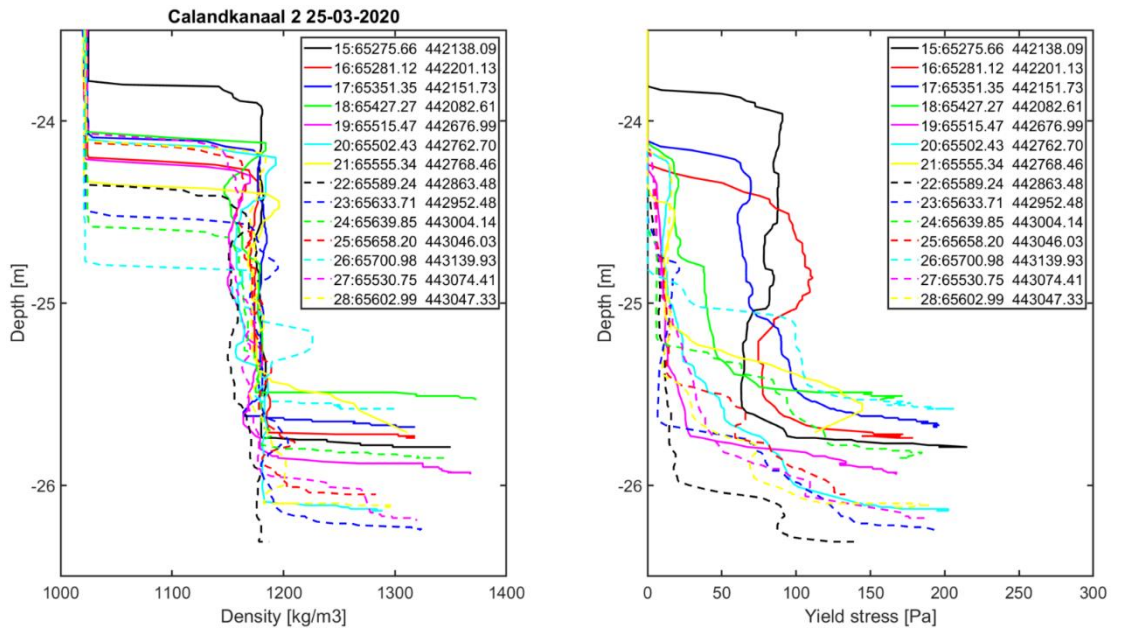


Figure A163. Fluid mud detection at the Calandkanaal on 25-03-2020: density (left) and yield stress (right) profiles, part 2

Table A1. Zeta-potential, pH and conductivity measurements

Sample Name	Zeta-potential	Conductivity	pH
CK1	-10,29	47,2	7.3
CK2	-7,60	30,98	7.3
3PH	-9,54	33,83	7.4
8PH1	-10,52	45,61	7.4
8PH2	-7,11	48,91	7.4
EH1	-8,41	33,27	7.3
KK1	-7,49	31,38	7.5
KK2	-6,98	30,46	7.3
SK1	-9,88	26,2	7.5
SK2	-8,75	30,17	7.5
WH1	-8,57	24,65	7.4
WH2	-11,66	22,8	7.4

Table A2. Organic matter degradation measurements (conducted by TU Delft)

		CK	CK	CK	BK	KK	TS	WH	WB
Coordinates	Location	51,9724722	51,9724722	51,9724722	51,964011	51,897481	51,971722	51,898966	51,973961
Coordinates fm: fluid mud,	Location	4,1104722	4,1104722	4,1104722	4,085257	4,361255	4,096286	4,436281	4,085735
ps: pre-consolidated sediment	Layer	fm	ps	ps	fm	fm	fm	ps	ps
sampling	Sampling	Frahmplot	Frahmplot	Frahmplot	Grab	Grab	Grab	Grab	Grab
start layer in depth profile	Layer-top	0	40	50	0	0	0	0	0
end layer in depth profile	Layer-bottom	40	50	90	25	25	25	25	25
sampling date	Date	31-10-2018	31-10-2018	31-10-2018	28-1-2020	28-1-2020	28-1-2020	28-1-2020	23-1-2020
total nitrogen, EN 16168:2012-11	TN	0,3	0,3	0,4	0,3	0,4	0,3	0,4	0,3
TOC, ISO 10694:1996-08	TOC	2,4	2,4	2,4	2,4	3,5	2,3	3,8	2,3
anaerobic incubation from 10 to 250 days, left, per total organic carbon (TOC)	G10	1	2	6	1	2	0	2	1
	G21	2	3	7	3	5	1	4	2
	G50	3	6	12	5	12	2	9	3
	G100	6	10	18	8	23	2	16	5
	G150	9	14	23	11	29	2	21	7
	G250	12	20	30	17	41	2	29	12
	% degr after 250 days	1	2	3	2	4	0	3	1
anaerobic incubation from 10 to 250 days, left, right: per dry matter (DM)	G10	0,0	0,1	0,1	0,0	0,1	0,0	0,1	0,0
	G21	0,0	0,1	0,2	0,1	0,2	0,0	0,2	0,0
	G50	0,1	0,1	0,3	0,1	0,4	0,0	0,3	0,1
	G100	0,2	0,2	0,4	0,2	0,8	0,0	0,6	0,1
	G150	0,2	0,3	0,6	0,3	1,0	0,0	0,8	0,2
	G250	0,3	0,5	0,7	0,4	1,4	0,0	1,1	0,3
water content at the start of incubation, can vary from in-situ water content	WC	277	237	149	250	275	597	219	289
redox potential	Redox	-220	-235	-250	-220	-250	-120	-270	-210
ph value measured from TU Delft	pH				7,3	7,5	7,3	7,4	7,3
water content at the time of yield stress measurement	WC-fresh				253,2	282,9	700,0	215,7	293,8
static yield stress of fresh sediment	SYS-fresh				15	9	0	23	6
fluidic yield stress of fresh sediment	FYS-fresh				54	30	1	81	22

B GraviProbe and Rheotune

B.1 Working Principle of Measurement and Monitoring Tools

The two probes which were used were the GraviProbe and RheoTune. Additionally, mud samples were taken with a Beaker sampler (shown in Figure B1) for reference measurements of density and strength profiles.



Figure B1: Overview of the used tools. From left to right: the GraviProbe, RheoTune and Beaker Sampler.

B.1.1 GraviProbe 2.0

The GraviProbe 2.0 is a torpedo-shaped free-fall penetrometer of 960 mm in length and 50 mm in diameter. Its mass is about 8 kg (the equivalent weight underwater is approximately 6.1 kg). It is equipped with accelerometers, and a pressure sensor at the cone tip and at the tail. The probe is released in the water column, a minimum of 4 meters above mudline to guarantee it reaches terminal velocity before hitting the mudline. When it hits the mudline, it will decelerate in the mud layer. The free fall is monitored with two accelerometers, one for large accelerations and one for accurate measurements of small accelerations. Integration of the acceleration allows to obtain the velocity and integration of the velocity leads to the displacement. The acceleration measured by GraviProbe is a function of gravity acceleration, flow resistance and the undrained shear strength of the medium in which it penetrates e.g. mud. When the influence of gravity and flow resistance are known, the undrained shear strength can be calculated.

The undrained shear strength of the mud leads to both tip resistance and shaft resistance. Both shaft resistance and tip resistance depend on the penetration velocity. The model described in Bezuijen et al. (2018) does not include the flow resistance. This was added to Bezuijen et al (2018) model to achieve a more accurate calculation of the fall velocity in the water column and the mud setup used in this study. This yields the following equation for undrained shear strength s_u at point n . Note that authors don't have access to the exact equations dotOcean uses to obtain s_u . The equation below is used only to back calculate the s_u and compare it with the output of GraviProbe. It was found that there is an excellent agreement between the back calculated s_u and the output of GraviProbe.

$$s_{u,n} = \frac{W_g - ma - F_D - F_B - \alpha \cdot \sum_{i=1}^{n-1} s_{u,i} O_p \Delta z_i}{R_f N_{kt} A_p}$$

where W_g is the weight of the probe in air, m is the mass, a is the acceleration at point n , F_D is the drag resistance, F_B is the upward buoyancy force due to Archimedes' law, α is the friction

factor (i.e. the ratio of remoulded to undisturbed shear strength), followed by a summation of the undrained shear strength over the probe surface area (i.e. probe circumference O_p multiplied by the depth increment Δz_i). R_f is the rate factor for correction of rate effects, N_{kt} is an empirical factor relating tip resistance to undrained shear strength and A_p is the probe face area.

Viscosity is not included in the equation, because it is assumed that during of the trajectory of the fall the velocity is high enough to cause turbulent flow (Reynolds number above 2100 up to 7000 depends on the velocity and plastic viscosity of medium).

In the above equation only one average density for mud is used, although it could be extended to varying densities when known. The variation in the density of the mud is relatively limited and the density of the probe is much higher than that of the mud. Therefore, the error made by using just one average density value for the mud is relatively small. In addition, the drag coefficient is found by fitting the calculated s_u to the measured s_u , thus, the effect of variation in density is already considered in the drag coefficient.

As can be seen, this model has multiple assumptions, such as the mud density, sensitivity, drag coefficient, tip correlation factor and rate effects. Each of these input parameters is associated with its own uncertainty, contributing to uncertainty in the derived undrained shear strength. It will be useful to cross check with dotOcean to evaluate how they deal with these uncertainties.

- The reported accuracy is 0.01% for the depth measurement, likely this number is based on the accuracy of the accelerometer in the probe. There is no reported accuracy for shear strength (dotOcean, 2020). This study shows the depth measurement by GraviProbe is highly accurate. Investigating the accuracy of shear strength values from GraviProbe, however, was out of the scope of the current project. Having said that, as shown above, the back calculated shear strength and measured shear strength by GraviProbe are in a good agreement.

It should be noted that any GraviProbe data presented further-on in this report is directly produced by dotOcean and has not been re-processed other than producing the figures itself.

Conclusions and recommendations

The following conclusion is drawn and recommendations are made:

- It is unclear whether geotechnical assumptions (such as the N_{kt} factor and the applicability of the sensitivity) are fully applicable in fluid mud. It is therefore recommended to perform tests with the GraviProbe on clay with known properties and also with constant velocity.

B.1.2 RheoTune

The RheoTune is a self-weight penetrating probe, 750 mm in length and 150 mm in diameter. The mass is about 15 kg, but additional weights are optional. It outputs both (Bingham) yield stress and density. The measurement principle is based on a tuning fork which is positioned at the tip. The high-level working principle of RheoTune is discussed below.

Rheology

A flow curve, in rheology, depicts the relation between shear rate of deformation and shear stress of a non-Newtonian fluid e.g. natural mud from harbours. Such a relation is necessary to quantify the flow properties of mud layers. Different rheological models are available in the literature to characterize shear rate- shear stress relationship of materials. One of the most used models is Bingham model. In case of Bingham characterization, the rheological properties

of a flowing mud can be described by two main parameters of Bingham yield stress and plastic viscosity, Figure B2. In case deformations are small and the material does not fail (unremoulded state), we are in the so-called Linear Visco-Elastic regime (LVE) regime where the main governing rheological parameters are shear modulus and linear dynamic viscosity, Figure 2.4.

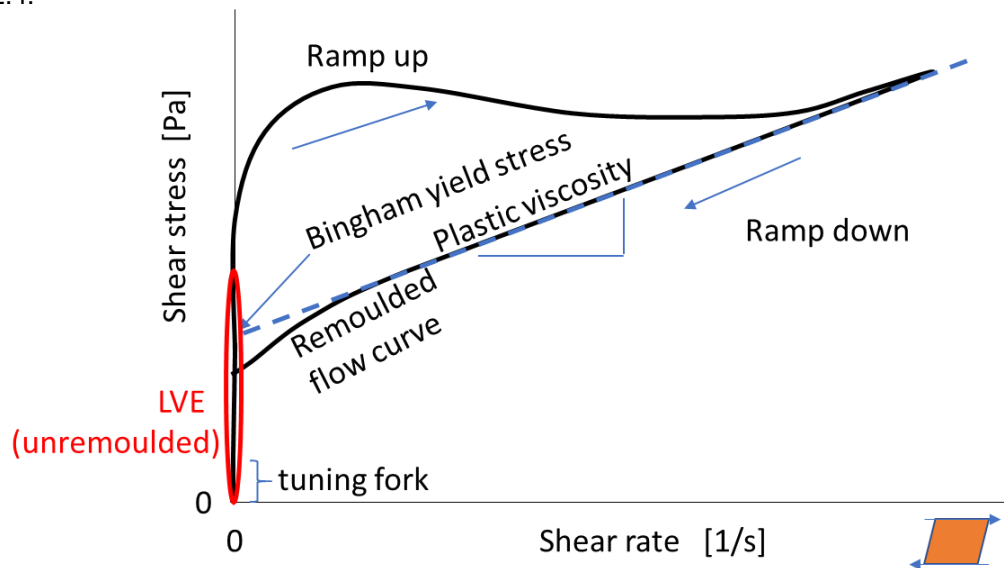


Figure B2: Rheology sketched: flow curve (in black), Bingham parameters (in blue), Visco-Elastic regime (in red).

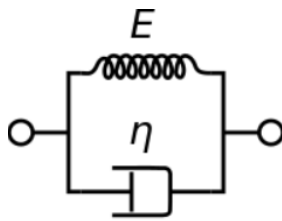


Figure B3: Mechanical representation of linear visco-elastic Voight model. (Wikipedia).

In general, in case of tuning fork-based measurement devices, the fluid's response to very small amplitudes of vibration (in the order of 10 micron) is measured. One of the two tines (i.e. teeth) of the tuning fork is driven by a piezoelectric element in the root of the tine, producing a certain amplitude of vibration with a given frequency. Another piezoelectric element in the root of the other tine measures the remaining amplitude of vibration and the phase shift in the frequency under the influence of fluids between two tines. Piezoelectricity is the electricity generated by piezo element by effect called the piezoelectric effect. It is the ability of certain materials to generate an AC (alternating current) voltage when subjected to mechanical stress or vibration, or to vibrate when subjected to an AC voltage, or both. The theoretical base of similar transducers is described in Allwright 2002 (Newtonian) and Fonseca et al. 2015. The response of a tuning fork is a function of its mechanical properties and the material properties of fluid (such as density, viscosity and shear modules) in which it is submerged. To mathematically describe the fluid's response to vibration of a tuning fork, theory of LVE should be applied in combination with theory of tines's oscillatory motion. There are different sources in the literature explaining how the transducer is driven, namely at two different operational schemes: natural frequency, or at a 45 degrees phase shift between forcing and response (Pedocchi et al. 2015 and Groposo et al. 2015). Put it simply, it is easy to get an object to vibrate at its natural frequencies, and contrarily hard to get it to vibrate at other frequencies.

For the latter (45 degrees phase shift), in case of Newtonian fluids, viscosity does not influence oscillation frequency (Allwright 2002), and the oscillation frequency is only determined by fluid mass, resulting in density values. In case of other transducer, it switches between +45 degrees phase shift and -45 degrees phase shift, which in case of Newtonian fluids produces information on viscosity too. The mentioned phase shifts are situated at the -3 dB point of the frequency response diagram, Figure B4. In case of non-Newtonian fluids, the outputs of the instrument have to be processed differently to obtain the fluid properties.

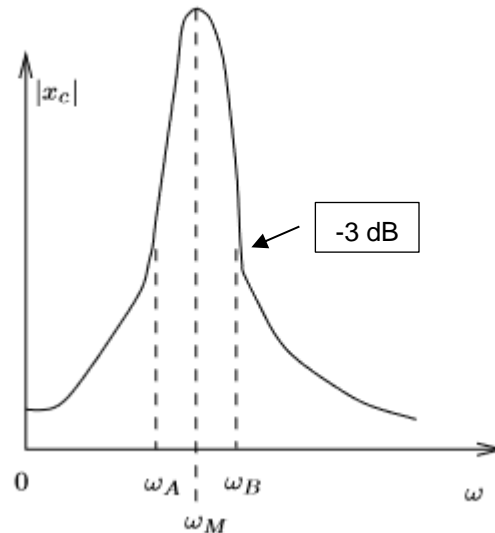
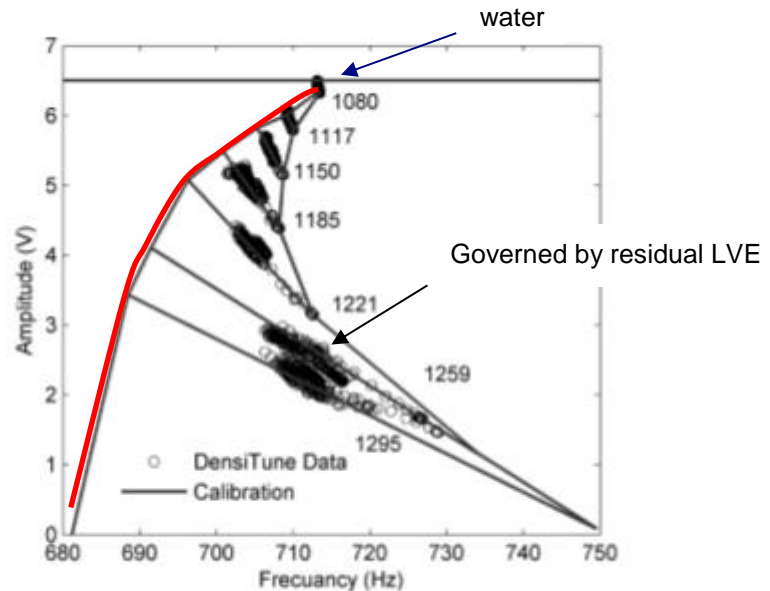


Figure B4: Frequency response curve tuning fork (Allwright 2002)

Calibration:

A one-time calibration is necessary to quantify 4 mechanical/electrical parameter groups of the tuning fork (mass of tines/elasticity tines, volume of fluid's added mass/elasticity tines, contact area fluid/elasticity tines, amplification of vibration/output voltage). Such data is around, but calibration for voltage output is missing in our experiments and in literature. Since the fluid mechanical parameters (viscosity/density, shear modulus/density) are different for each mud, the 7826 transducer needs to be calibrated each time. This is done with the aid of a so-called density calibration domain graph, Figure B5, containing oscillation frequency and amplification voltage (=driving voltage to keep the amplitude of the measuring element constant, driving voltage is equal to the shear stress, Allwright 2002) recorded when the tuning fork is gently pulled through e.g. 20 litres of mud (prepared at different densities), responding to residual LVE properties of the mud. At the top of the calibration domain there is one point representing water. At the left-hand side of the figure the theoretical viscous boundary of a Newtonian fluid with the same density as the mud is shown, which has lost all its non-Newtonian properties (high shear rate asymptote). With frequency theoretically known, the position of this boundary is constructed by extrapolating the data points obtained in the 20-litre test. The elastic properties are dominant at the right-hand side of the graph.



RheoTune calibration diagram, numbers refer to densities in kg/m^3 .

Figure B5: Calibration domain, with theoretical viscous boundary in red. (Densi/Rheotune is gently moved through mud from one area, but prepared at different densities), Pedocchi et al 2015.

Yield stress:

A tuning fork can give at most the LVE parameters (density, shear modulus and linear dynamic viscosity). The Densi/Rheotune outputs density via the density domain calibration procedure (actual or from data base). The Rheotune addresses a data-base in which mud properties from different locations are stored, by which outputs such as density, yield stress (and viscosity,) without the need to apply the density calibration is produced. But the density calibration procedure can still be applied at will. We do not know the accuracy of the yield stress from the data base and we do not know which yield stress is outputted. Fonseca et al. 2015 describe a correlation between Bingham yield stress and voltage output at the theoretical viscous boundary of the calibration domain, unifying muds from 4 different Latin American ports. This seems not logical since the least sheared conductions are on the right-hand side of calibration diagram.

Evaluation:

A distinction is made between what can be measured by tuning fork and how to establish a link with flow curve parameters like yield stress. A tuning fork responds to LVE properties. For the transducer, residual LVE parameters can be manually back-calculated from calibration domain plots in the calibration procedure (if the density of mud is known plus 2 output parameters (frequency & voltage) to back calculate shear modulus and linear dynamic viscosity). The transducer can give LVE parameters directly. The transducer has 3 output parameters (2 frequencies and driving voltage) to quantify the 3 LVE parameters: density, viscosity and shear modulus.

The shear modulus is dominant for high density muds, in that case only two parameters need to be determined (density and shear modulus). This will however not be the case for the lower mud densities, since asymptotically viscous Newtonian conditions apply. One can already see this convergence in Figure B5 for densities $<1150 \text{ kg/m}^3$. Viscosity lowers the oscillation frequency and elasticity increases the oscillation frequency.

Dynamic and standard rotoviscometry might provide the link between (residual) LVE parameters & yield stress.

Conclusions and recommendations:

It is concluded that:

- The tuning fork responds to density, shear modulus and linear dynamic viscosity of the fluid.
- Rheotune does not directly measure the properties of the flow curve (i.e. yield stress and viscosity).
- Rheotune outputs yield stress via a data base correlation, on what this is based remains to be further investigated.

It is recommended that:

- all mechanical parameters of the Rheotune are calibrated;
- a virtual twin of the Rheotune is created to reproduce the density calibration domain in order to estimate associated LVE parameters;
- and that a transparent (mud independent?) relation between visco-elasticity parameters and yield stress (+ flow curve) in (dynamic) rotoviscometer experiments is quantified.

B.1.3 Beaker Sampler

Subsamples of the mud were taken with a so-called Beaker sampler. This is a manually operated piston type sediment sampler. The piston remains stationary at mudline, while a liner is pushed in manually to the desired sampling depth. A cutting shoe at the tip of the liner ensures minimal sample disturbance. A balloon-type seal is inflated at the cutting shoe during recovery in order to prohibit any sample material from escaping the liner. After retrieval the liner is extruded and sub-sampled in containers of 100 mm length. The deployment is illustrated in Figure B6, a schematic overview is shown in Figure B7.



Figure B6: Deployment of the Beaker Sampler.

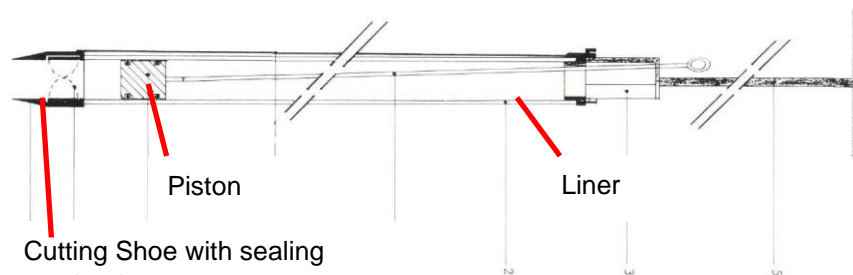


Figure B7: Schematic representation of the Beaker Sampler (adopted from Beeker, 1989).

Rheological Measurements

The rheological protocol described in Shakeel et al., 2019 is used for measuring Fluidic Yield Stress (FYS). It should be mentioned that the output of GraviProbe is undrained shear strength which should have an agreement with FYS. For this project, only the data from accelerometer is used to drive S_u . By incorporating the information from sensors located at the tip and shaft of the probe, estimation of other rheological parameters can be possible. GraviProbe also provides an accurate depth and S_u measurement.

The sub-samples obtained by the Beeker sampler are tested in a HAAKE MARS rheometer (Thermo Fisher, Karlsruhe, Germany) according to a protocol developed by Shakeel et al. (2019). This protocol comprises a stress-controlled sweep. Two yield stresses (i.e. two-step yielding) can be identified when plotting the apparent viscosity versus the shear stress, characterized by two sharp declines. These yield stresses are referred to as “static yield stress” (SYS) and “fluidic yield stress” (FYS), for the first and second decline, respectively. Figure shows an example. The presented example data is for multiple sub-samples (i.e. at different depths) from mud of the Port of Rotterdam, at a density of $1.25 \text{ g}\cdot\text{cm}^{-3}$. The red dots are the FYS values, and on average approximately 80 Pa. The SYS values are about 15 Pa.

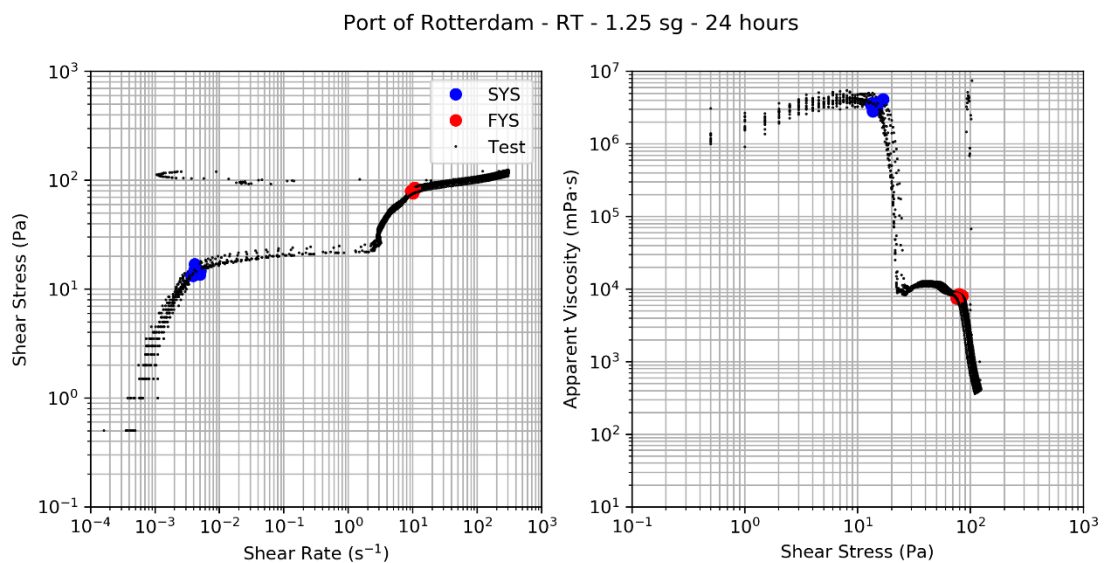


Figure B8: Data of stress-controlled sweep and derived Fluidic Yield Stress (FYS) and Static Yield Stress (SYS) for Port of Rotterdam mud, at a density of $1.25 \text{ g}\cdot\text{cm}^{-3}$.

Density Measurements

Density measurements are performed with an Anton Paar DMA 35. It is a handheld density meter, which is based on the oscillating U-tube principle. A glass tube containing the sample is excited to oscillate to a certain frequency, which depends on the density of the sample (Anton Paar, 2020a). The stated accuracy is $0.001 \text{ g}\cdot\text{cm}^{-3}$ (Anton Paar, 2020b). Additional measurements such as water content, organic content and particle density have not been performed specifically for this project.

C Far-field modelling

C.1 Analysis of the turbulent-laminar transition

The Effective Reynolds number is given by:

$$\frac{1}{Re^E} = \frac{1}{Re^{Visc} + Re^{Tau}}$$

and

$$Re^{Visc} = \frac{4\bar{\rho}UH}{\mu}$$

and

$$Re^{Tau} = \frac{8\bar{\rho}U^2}{\tau_y}$$

Here $\bar{\rho}$ is the layer-averaged density, U the velocity of the density plume, H the height of the plume and μ is the viscosity and τ_y is the yield stress. Effective Reynolds number between 2000 – 3000 indicate the onset of the turbulent-laminar transition.

Figure C1 shows the effective Reynold number for different velocities of the sediment plume. The vicious (ReynoldsVisc) and cohesive (ReynoldsTau) part are determined from mud properties obtained during field campaigns and laboratory experiments (see Chapter 3).

For the simulation in which we used a production rate of 800 kg/s the maximum near bed density of the fluid (at the sediment trap) was ~1036 kg/m³. This translates to an SSC of ~20.0 g/l, assuming a density of 1024 kg/m³ for water (brackish) and a specific density of 2560 for the sediment. The salinity near the sediment trap varied between 26 – 30 ppt. If 1036 kg/m³ is the maximum density that is reached in the sediment plume; the plume remains turbulent under almost all conditions (Figure C1.) and D3D is indeed capable of simulating the plume spreading.

The experiment which were initialized with an initial path of sediment (37.5, 75 and 150 kg/m³) started with an initial density of ~1048, 1070 and 1116 kg/m³. From Figure C1. it is visible that at the initiation and first hours of the experiment the plume/initial patch of sediment is below the turbulent-laminar transition. For the experiment with an initial concentration of 150 kg/m³ the density remained above 1050 kg/m³ during the first 1.5 h of the experiment with U below < 0.4 m/s.

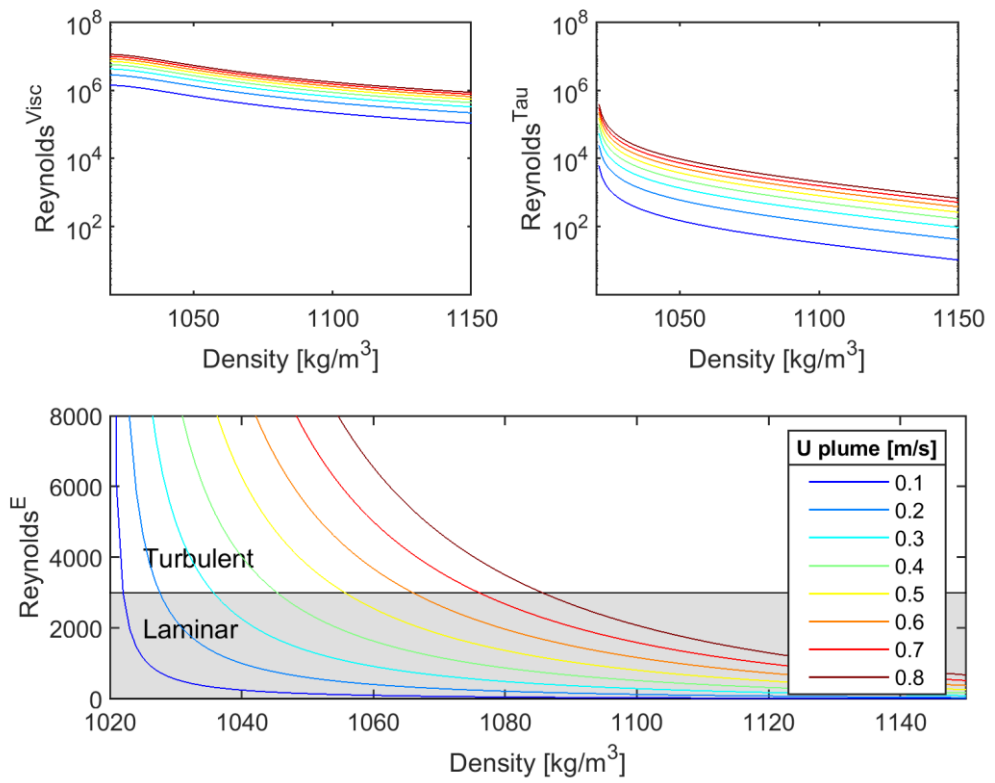


Figure C1. Effective Reynolds number for different flow velocities of the sediment plume.

C.2 LW and HW mid column plume spreading

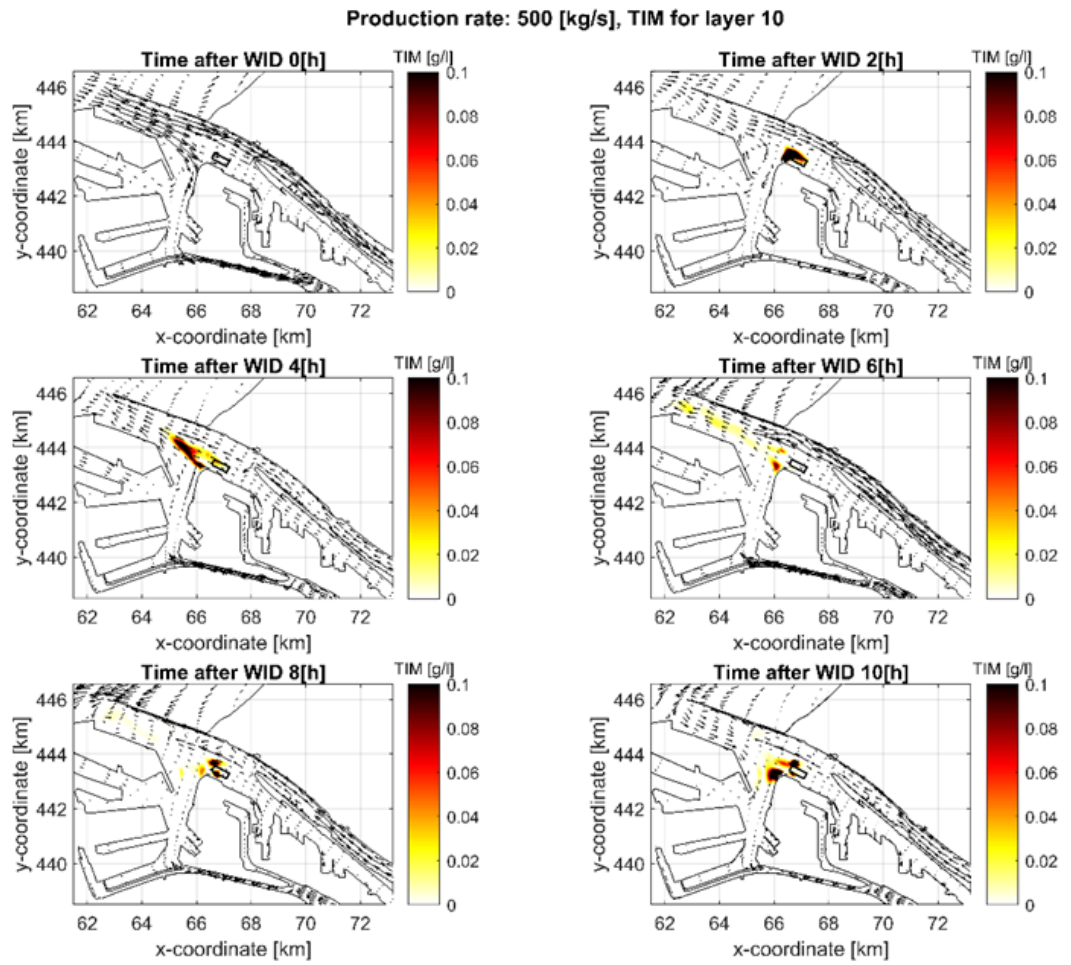


Figure C2. Horizontal near bed plume spreading, WID starts 1h before HW with a production rate of 500 kg/s in layer 10 (mid column).

Production rate: 500 [kg/s], TIM for layer 10

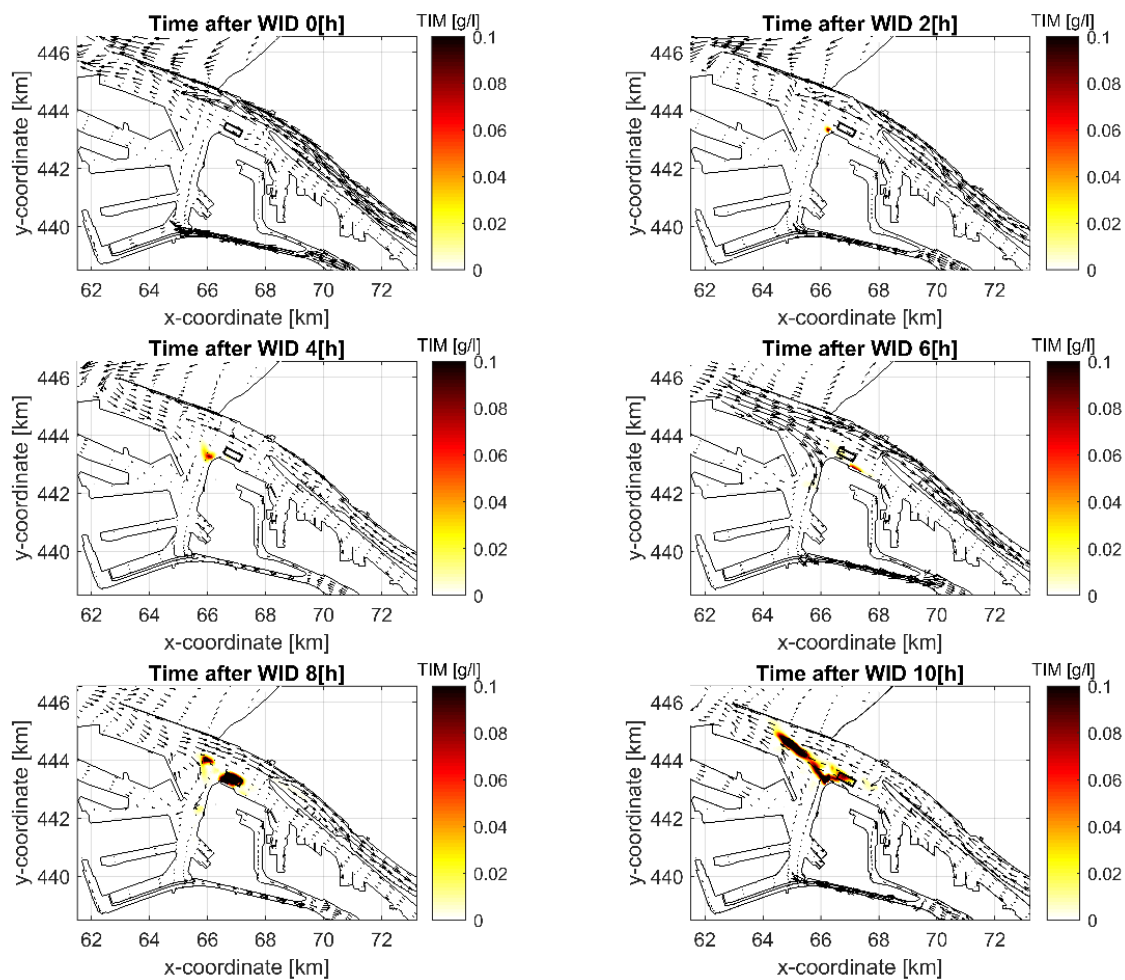


Figure C3. Horizontal near bed plume spreading, WID starts 1h before LW with a production rate of 500 kg/s in layer 10 (mid column).

C.3 Near bed plume spreading - One week of WID

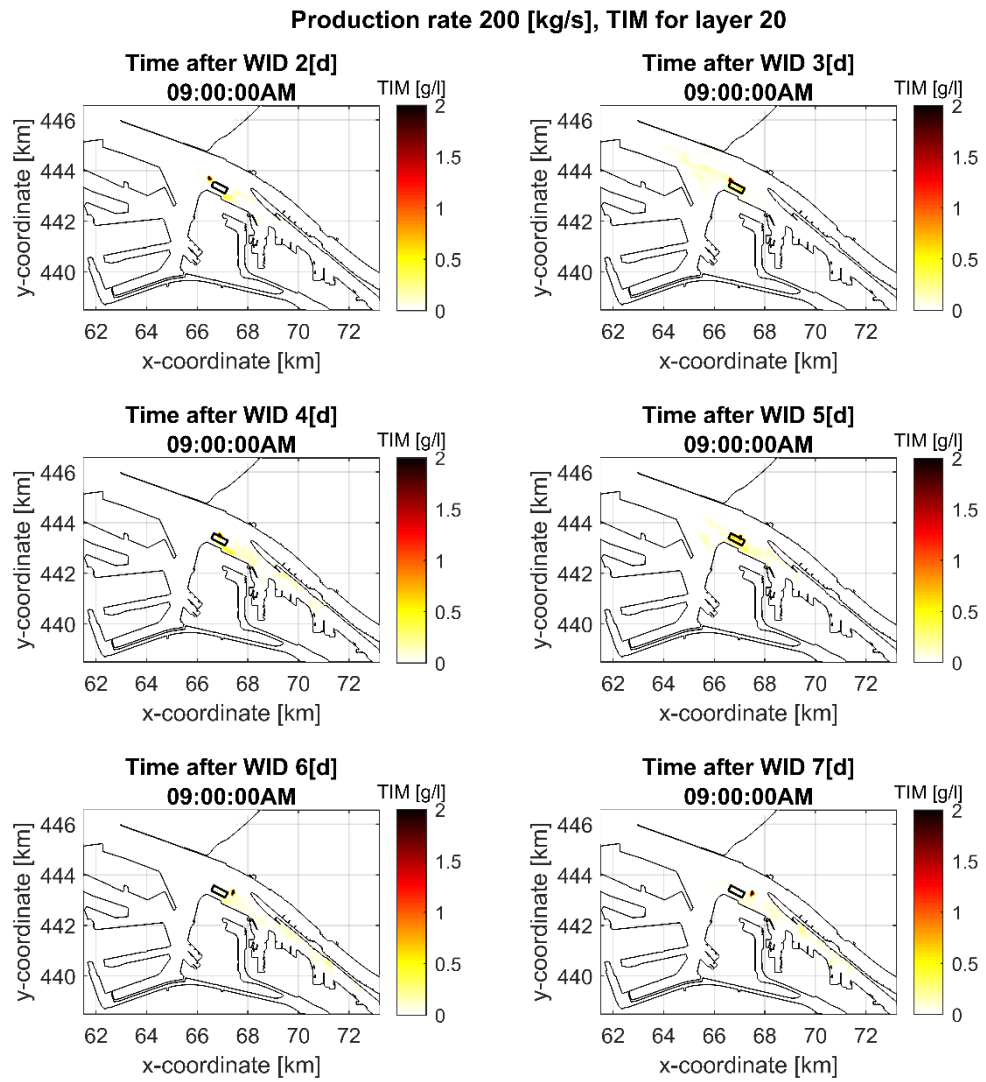


Figure C4. Near-bed plume concentration at the start of each WID day in the near bed layer for the lowest production rate

Production rate 200 [kg/s], TIM for layer 20

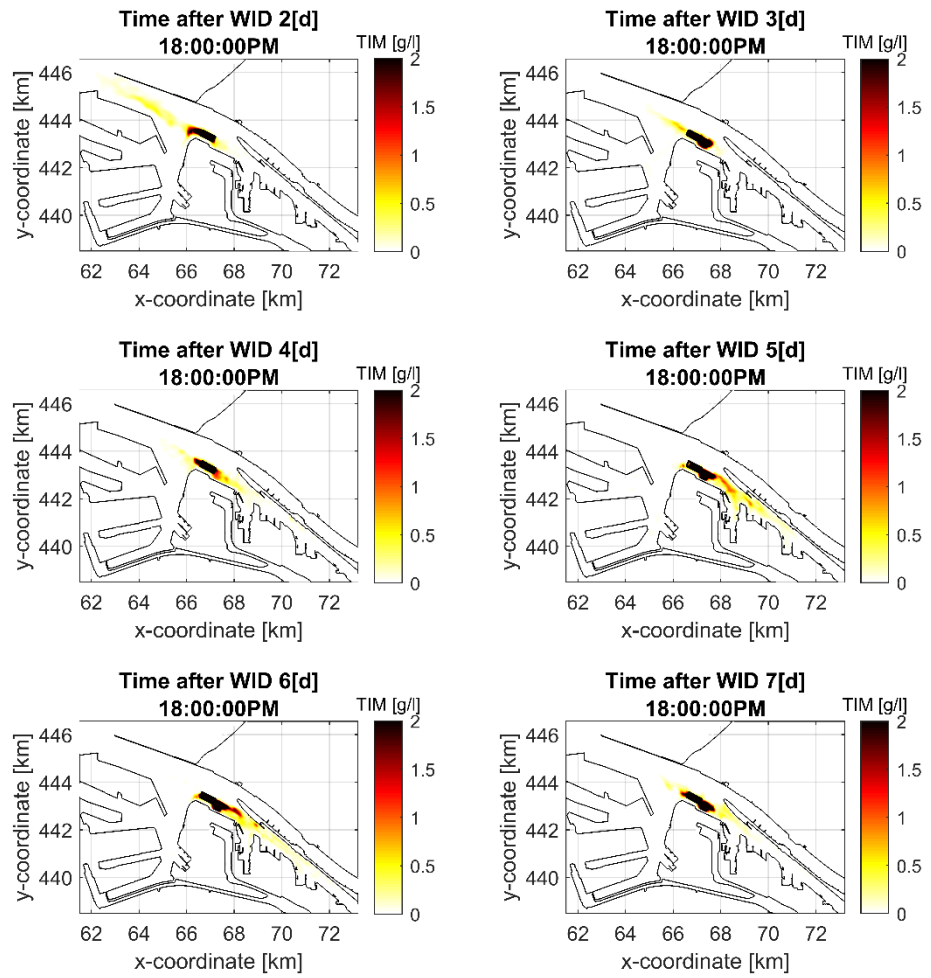


Figure C5. Near-bed plume concentration at the start of each WID day in the near bed layer for the lowest production rate

Production rate 800 [kg/s], TIM for layer 20

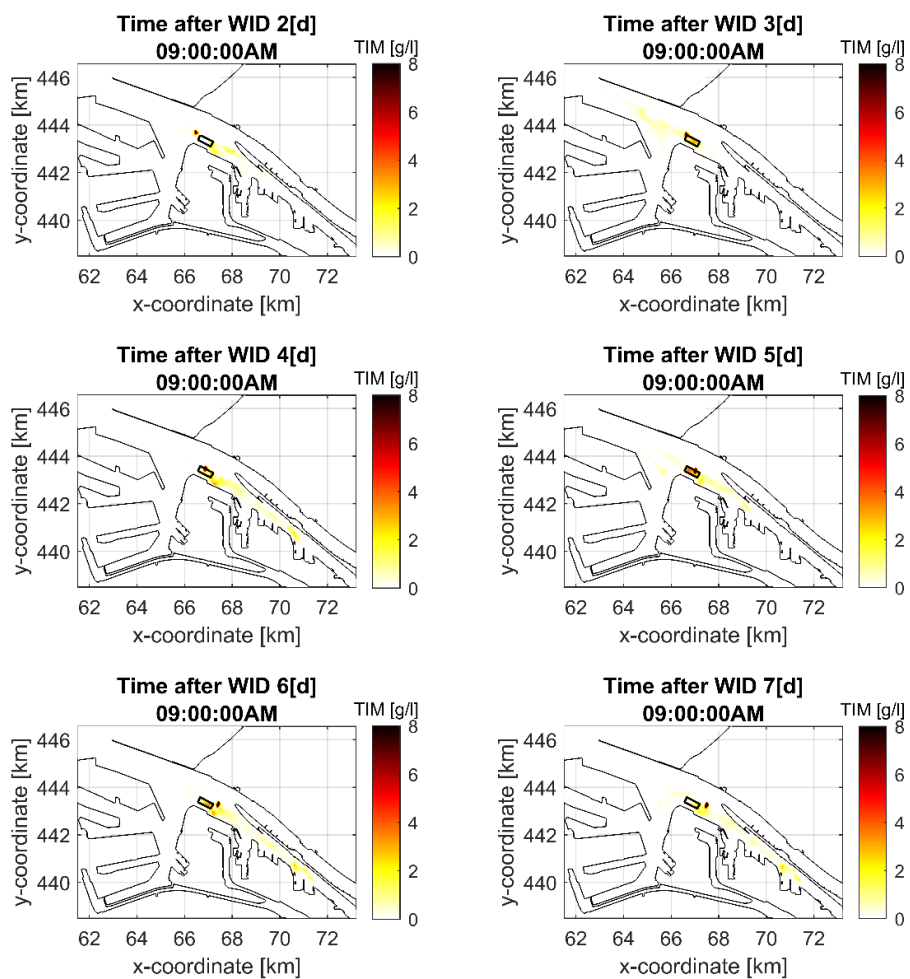


Figure C6. Near-bed plume concentration at the start of each WID day in the near bed layer for the highest production rate

Production rate 800 [kg/s], TIM for layer 20

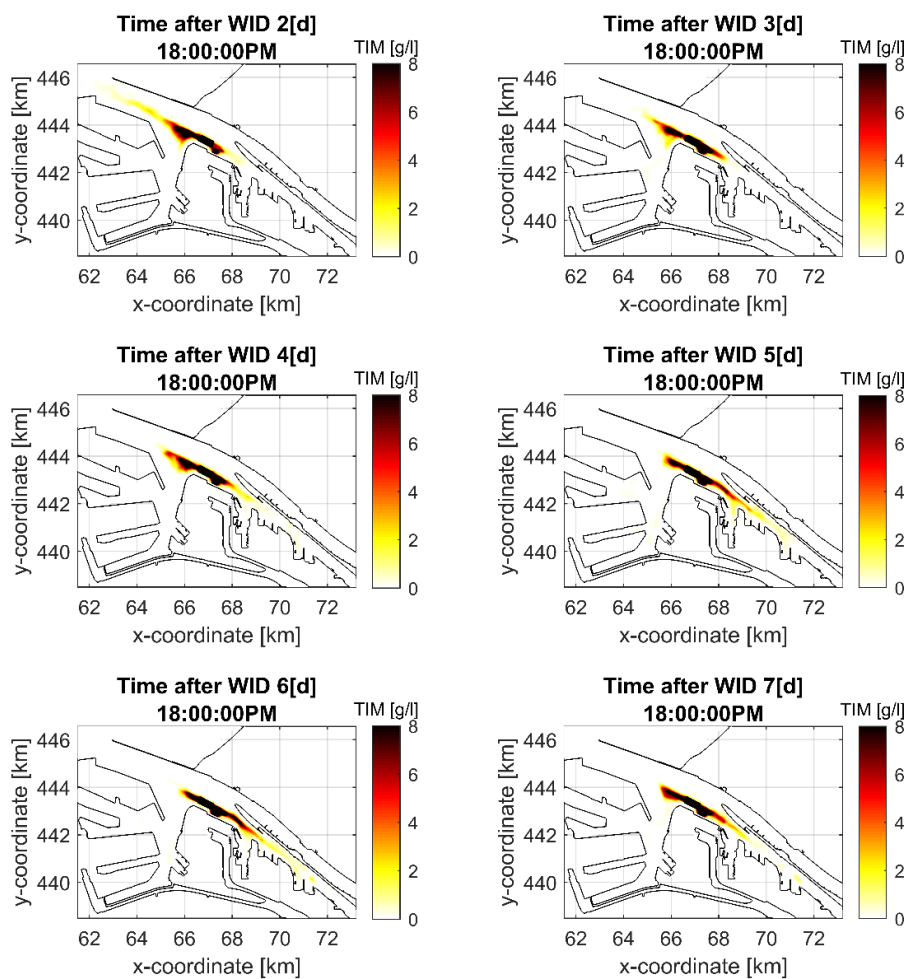


Figure C7. Near-bed plume concentration at the end of each WID day in the near bed layer for the highest production rate

C.4 Influence of HW or LW release on the sediment footprint of individual fractions

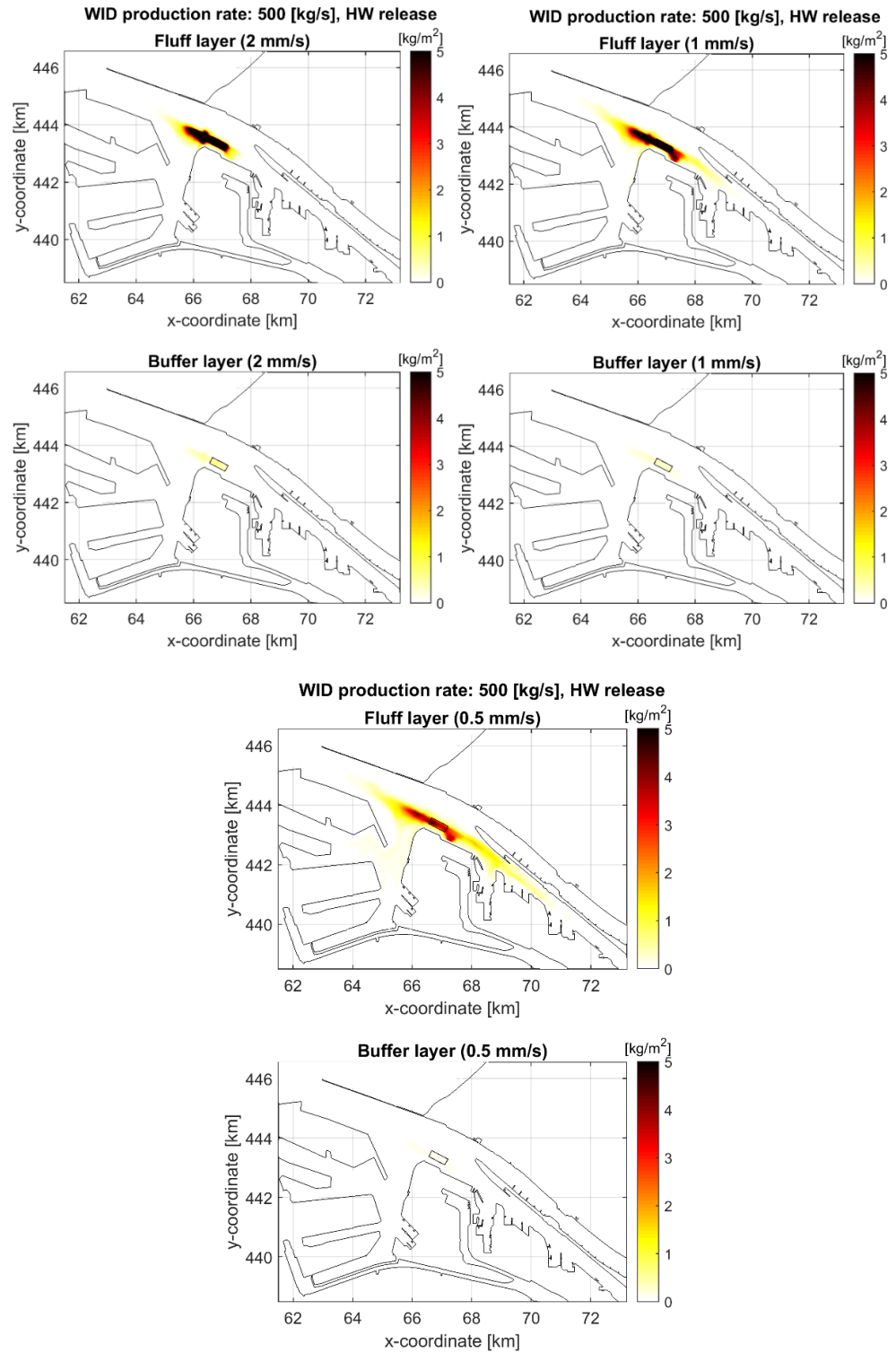


Figure C8. Sediment footprint for the individual sediment fractions. Here the results for the HW release experiment are shown three days after WID.

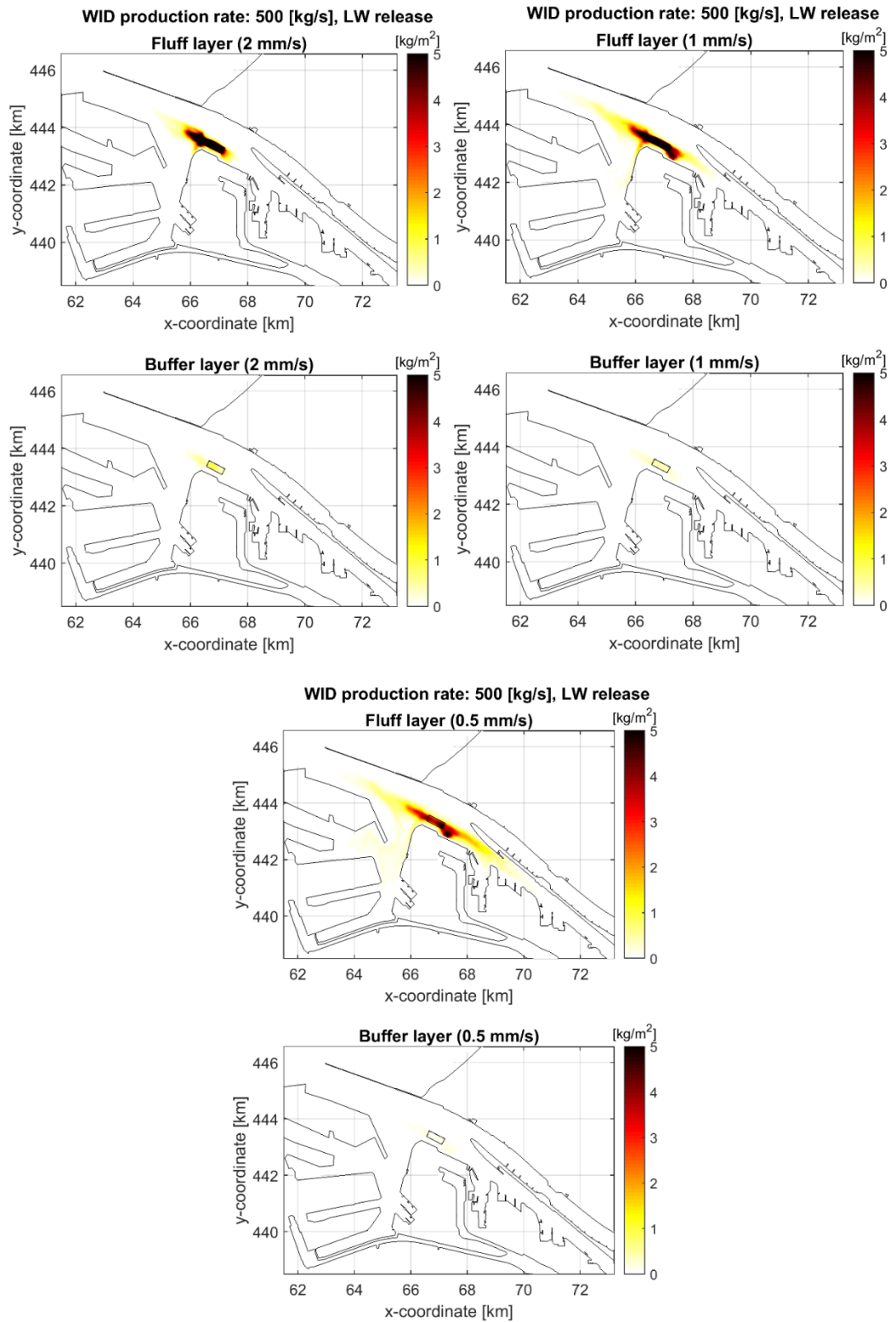


Figure C9. Sediment footprint for the individual sediment fractions. Here the results for the LW release experiment are shown three days after WID.

C.5 Influence of the production rate on the sediment footprint

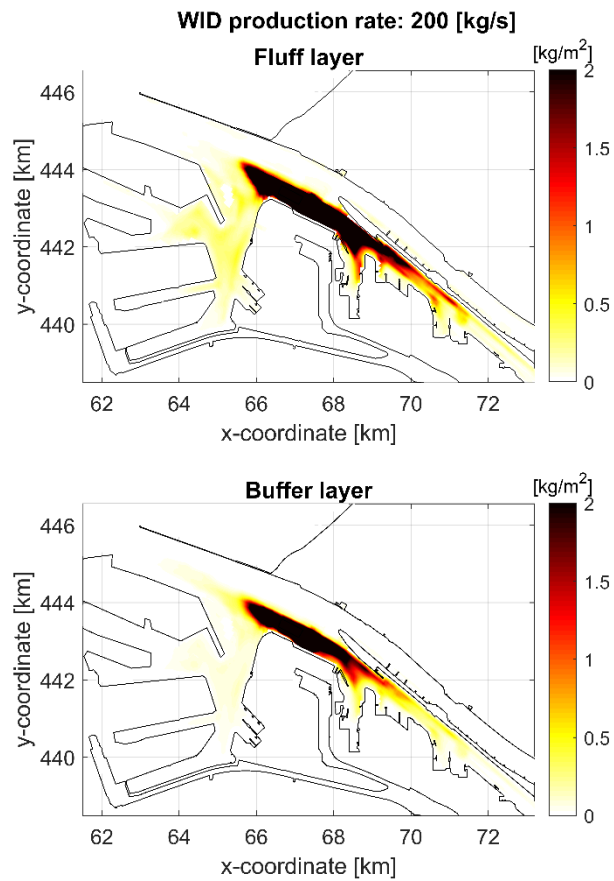


Figure C10. WID sediment deposited in the fluff and buffer layer at the end of the simulation (after 3 weeks), production rate of 200 kg/s is used in this run.

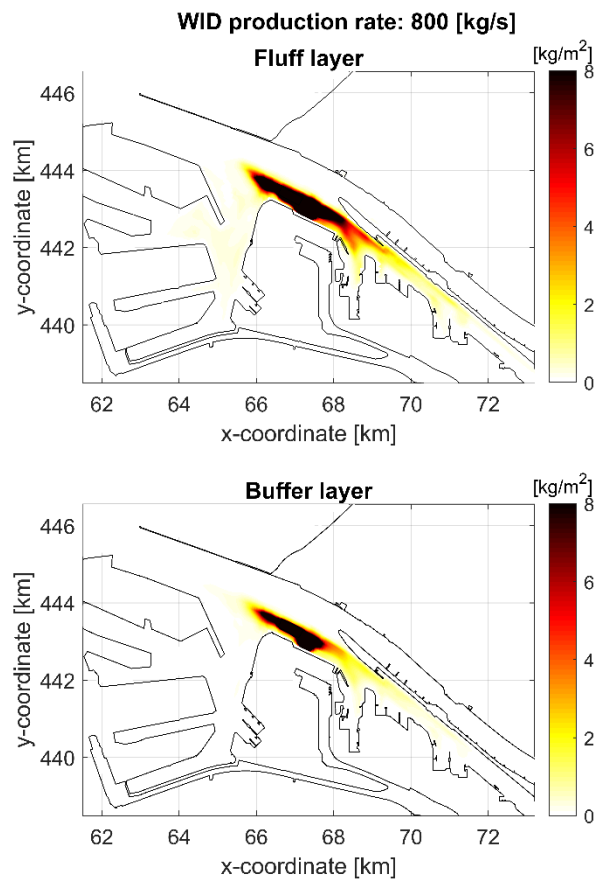


Figure C11. WID sediment deposited in the fluff and buffer layer at the end of the simulation (after 3 weeks), production rate of 800 kg/s is used in this run.

C.6 Influence of the production rate on the sediment footprint of individual fractions

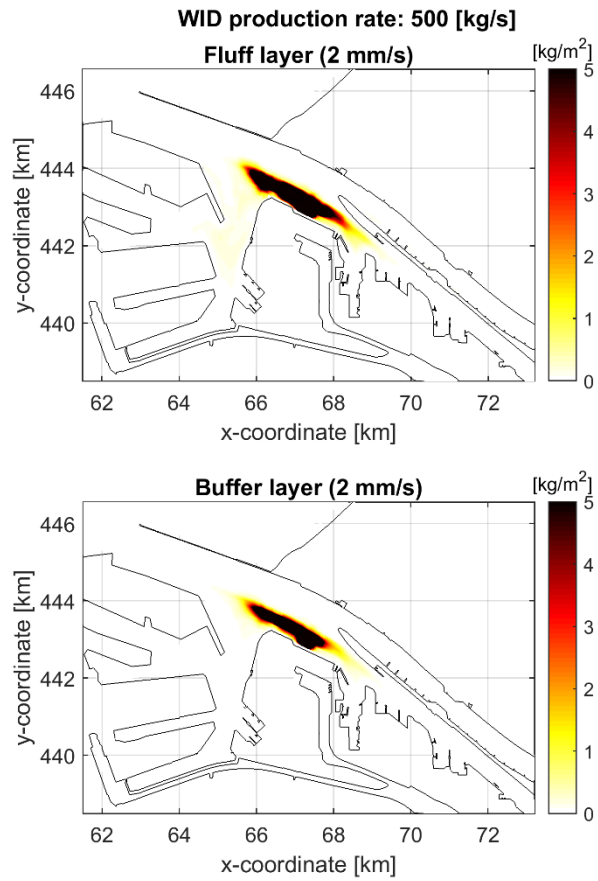


Figure C12. WID sediment with a fall velocity of 2 mm/s deposited in the fluff and buffer layer at the end of the WID activities, production rate of 500 kg/s is used in this run.

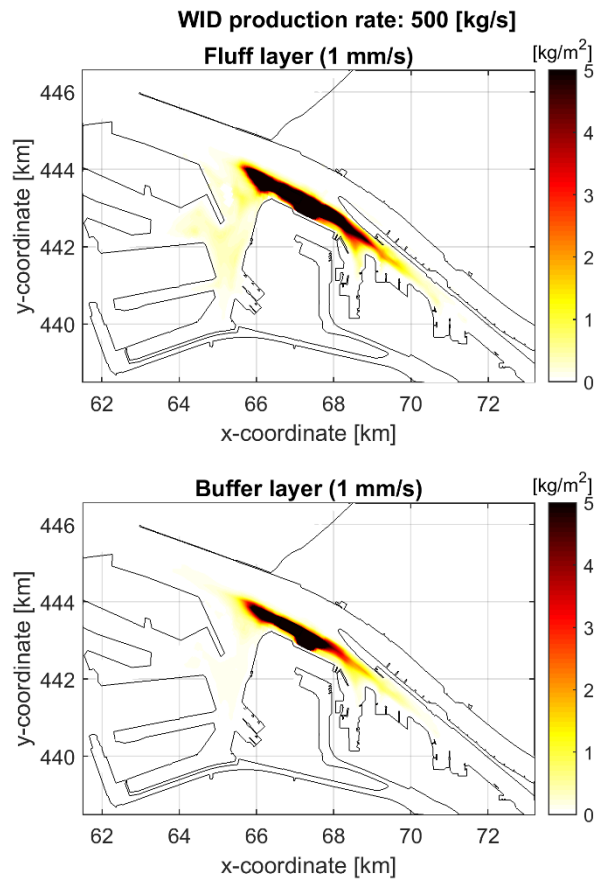


Figure C13. WID sediment with a fall velocity of 1 mm/s deposited in the fluff and buffer layer at the end of the WID activities, production rate of 500 kg/s is used in this run.

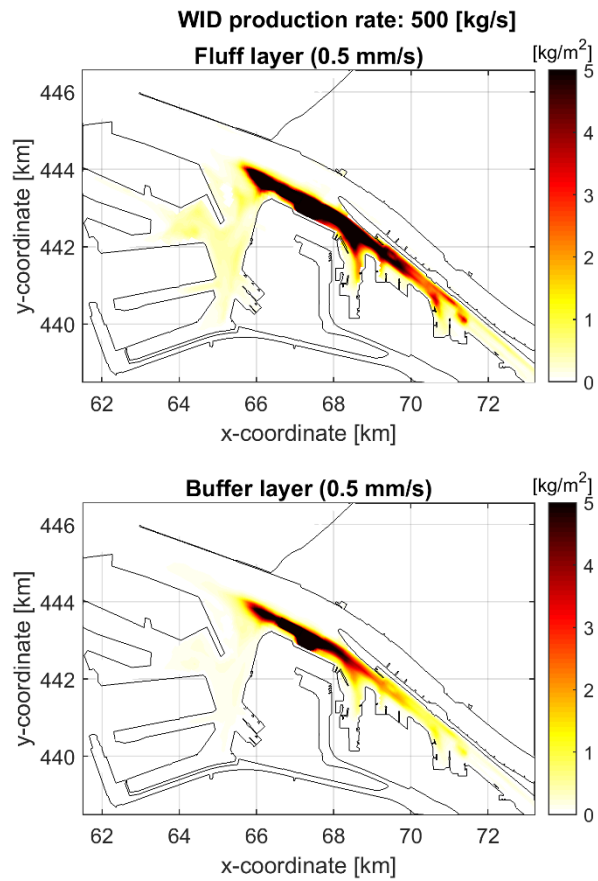


Figure C14. WID sediment with a fall velocity of 0.5 mm/s deposited in the fluff and buffer layer at the end of the WID activities, production rate of 500 kg/s is used in this run

Production rate 200 [kg/s], TIM for layer 20

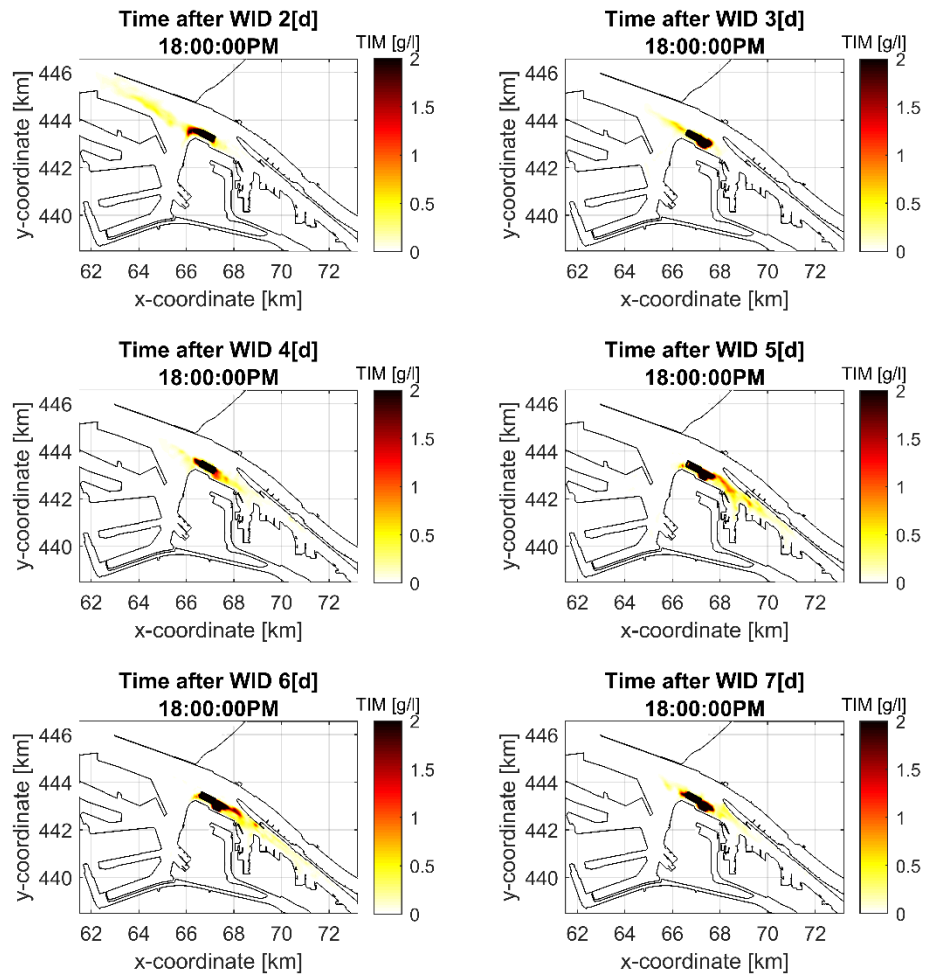


Figure C15. Horizontal near bed plume spreading. Panels show the TIM model evaluated at 18:00 PM (start of WID) for day 2 – 7 of WID period.

D Description and validation TUDflow3d

D.1 Introduction

TUDflow3d is an open source 3D CFD model (<https://github.com/openearth/tudflow3d>) and has originally been developed for accurate near field simulations of TSHD (Trailing Suction Hopper Dredger) overflow plumes on real scale. It has also been used for WID (Water Injection Dredging) plumes, MFE (Mass Flow Excavation) plumes, deep sea mining tailing plumes and salinity driven density flows. TUDflow3d has been validated for a wide range of flows where turbulence and/or density differences and/or interaction with objects are important. TUDflow3d can deal with sediment bed update (morphological change: erosion and sedimentation) within reasonable run times (hours-days). The CFD model is fully 3D with variable density taken into account in all three dimensions (not just in the vertical), non hydrostatic pressure and turbulence captured by the accurate LES (Large Eddy Simulation) approach or by a RANS (Reynolds Averaged Navier Stokes) model.

D.2 TUDflow3d

D.2.1 Flow Equations

In the CFD model TUDflow3d the full Navier Stokes equations with variable density are solved:

$$\frac{\partial \rho}{\partial t} + \nabla \cdot (\rho u) = 0, \quad (1)$$

$$\frac{\partial \rho u}{\partial t} + \nabla \cdot (\rho u \otimes u) = -\nabla P + \nabla \cdot \tau + (\rho - \rho_a)g, \quad (2)$$

where ρ, ρ_a is respectively mixture density and ambient water density, u is the velocity vector, t is time, P is the dynamic pressure, $\nabla \cdot \tau$ is the viscous shear stress tensor and g is the acceleration vector due to body forces like gravity. The eddy viscosity approach is used in which the total eddy viscosity consists of the sum of the molecular viscosity of water and the modelled turbulent viscosity: $\mu_e = \mu_{mol} + \mu_t$. The viscous shear stress tensor is given by:

$$\nabla \cdot \tau = \mu_e (\nabla u + (\nabla u)^T - \frac{2}{3} \nabla \cdot u)$$

The simulations are carried out using a second order accurate finite volume method on a structured grid with rigid lid. The use of structured grids allows the use of a rapid solver. The code runs parallel (domain decomposition via MPI) on multi core computers for maximum speed. The influence of suspended sediment on mixture density is captured by the mixture model approach (Manninen et al., 1996). The pressure correction technique is used to enforce incompressibility following from the mass balance. Time integration of the advective, viscous, old pressure and body force terms during the predictor step is carried out by a third order Adams Bashforth scheme. Momentum advection is simulated using a stable artificial viscosity scheme (De Wit 2014a). Obstacles and a sediment bed within the grid are treated with an immersed boundary technique.

D.2.2 Turbulence

D.2.2.1. LES

Most accurate manner to capture the influence of turbulence in TUDflow3d is by the Large Eddy Simulation (LES) technique. In LES all large eddies containing the majority of the turbulent energy are solved on the grid and a sub-grid-scale model captures the influence of the smallest eddies smaller than the grid size. An advantage of LES over RANS (Reynolds averaged Navier Stokes) is that it resolves the large coherent structures instead of relying on a large eddy viscosity mimicking the effect of those coherent structures on spreading and mixing of momentum and sediment. Also the influence of variable density on turbulence is captured automatically in LES rather than through fitted model constants as in RANS. Within TUDflow3d standard the WALE sub-grid-scale model is used with $C_s=0.325$ which gives satisfactory results over a wide range of applications. Other LES sub-grid-scale models available within TUDflow3d are Standard Smagorinsky, Dynamic Smagorinsky (Germano-Lilly), Sigma model.

D.2.2.2. RANS

For cases where the fine LES grid is too expensive a RANS type Mixing Length turbulence model is also available within TUDflow3d. It uses the standard Bakhmetev mixing length profile over the vertical as mixing length. Turbulence damping by sediment concentration gradients are taken into account via the Munk-Anderson type of damping functions defined in the COSINUS project (for more info see De Wit 2014b). Recently the Realizable K-Epsilon RANS model has been implemented in TUDflow3d. The realizable K-Epsilon RANS model is generally considered as an improvement over normal K-Epsilon as it exhibits better performance for the spreading rate of planar and round jets, flows involving boundary layers with strong adverse pressure gradients, separation, recirculation, rotation.

D.2.3 Sediment

Sediment is modelled by a multi fraction approach in which the sediment Particle Size Distribution (PSD) can be captured by several different sediment fractions each having different characteristics like particle diameter and settling velocity. For each individual sediment fraction a separate transport equation is solved for the sediment volume concentration C :

$$\frac{\partial C}{\partial t} + \nabla \cdot (uC) = \nabla \cdot (\Gamma \nabla C), \quad (3)$$

with the diffusion coefficient $\Gamma = \nu_e / Sc$, a Schmidt number $Sc = 0.7$ adopted in this study. LES results are not sensitive in the choice of Schmidt number as in LES turbulent advection via eddies is dominant over the influence of the eddy viscosity on diffusion of concentration. In vertical direction a drift velocity is used to account for polydisperse settling of the sediment (Manninen et al., 1996) with hindered settling according to the theory of Richardson and Zaki (1954). Effect of flocculation on settling velocity and hindered settling is taken into account in TUDflow3d. The fluid mixture density is determined from the total sediment concentration:

$$\rho = \rho_a + (\rho_s - \rho_a)C \quad (4)$$

$\rho_s = 2650 \text{ kg/m}^3$ is the sediment density, ρ_a is the ambient water density.

D.2.4 Bed update

At the bed erosion and sedimentation of suspended sediment takes place. Erosion of sand is determined with the standard VanRijn1984 pick up function. Erosion and deposition of mud is determined with the standard Krone-Parteniades functions. The shear stress used in the sediment pick up function is based on the fluid velocity in the second grid cell above the bed as the first grid cell is influence a bit by the immersed boundary approach to simulate a fixed bed within the computational grid. Sedimentation is determined with the same drift-flux hindered settling approach as applied within fluid computational cells. Bed update can be switched on or off. Also without bed update the model keeps track of the sedimentation / erosion footprint but the feedback on the position of the seabed will be neglected. This approach is allowable for flow cases in which the change in bed level from sedimentation / erosion is limited and no feedback on the flow is expected.

D.3 Verification TUDflow3d for WID plumes

D.3.1 Introduction verification

Several benchmarks have been simulated with TUDflow3d to test density driven flow which occurs in WID plumes. First three benchmark tests have been repeated here from (De Wit 2015) because they are very relevant for testing the processes occurring in WID plumes. The fourth benchmark is a new one and has also been tested in the 1Dv model. In the past the TUDflow3d has also been tested to simulate accurately general turbulent flow, flow past an obstacle, flow past a silt screen, suspended sediment transport, high concentration sediment flow, buoyant and non-buoyant jet in crossflow, TSHD overflow dredge plumes on lab and field scale, hopper sedimentation. Those tests are reported in De Wit (2015), Radermacher (2016), De Wit (2019) and will not be repeated here.

The following benchmarks are presented here specifically for WID plumes:

- Front speed of density current at sloping bed (experiment of Britter and Linden 1980)
- Radial spreading of density driven overflow plume at bed (experiment of Boot 2000)
- Density current including deposition (experiment of Hallworth et al. 1998)
- Turbidity current on erodible bed (experiment of Parker et al. 1987)

D.3.2 Front speed of density current at sloping bed (experiment of Britter and Linden 1980)

A density current at a sloping bed flows in downward direction under influence of gravity, see the sketch in Figure (left). When the Reynolds number is sufficiently large the front velocity is constant for slopes with $\theta \geq 5^\circ$ (Britter and Linden 1980). Friction and entrainment of ambient fluid balance gravitational acceleration. The front speed u_f is then given by:

$$\frac{u_f}{(g \Delta \rho / \rho q)^{1/3}} = 1.5 \pm 0.2 \quad (0.1)$$

with q as the discharge per unit width. It is verified whether TUDflow3d simulation results for three different slopes (5° , 10° and 20°) are shown in Figure D1 (right). The vertical resolution dz is approximately 15 cells over the height of the density current and the horizontal grid sizes dx, dy are double the vertical one. q is chosen as $0.01 \text{ m}^2/\text{s}$ and $\Delta \rho / \rho = 0.083$. The bed is simulated as hydraulic smooth. The simulated front speed takes some time to grow close to the expected value of Eq. 2.1. For steeper slopes it takes less time to arrive at the final front speed than for less steep slopes. TUDflow3d gives the correct front speed of a density current at a sloping bed for slopes of 5° , 10° and 20° .

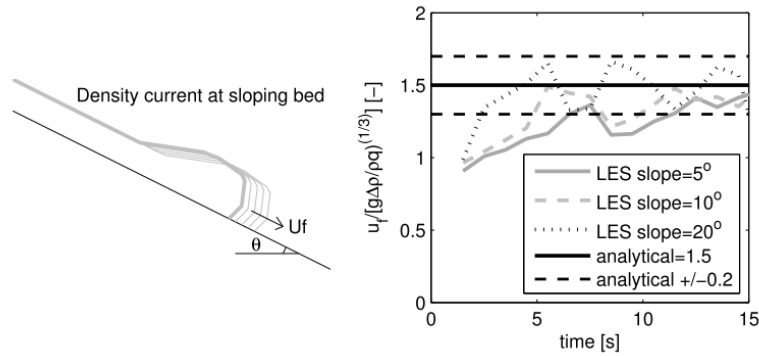


Figure D1. Sketch of moving front density current (left) and TUDflow3d LES result of simulated front speed (right)

D.3.3 Radial spreading of density driven overflow plume at bed (experiment of Boot 2000)

When an overflow plume touches the bed it will spread radially. Boot (2000) has studied the radial spreading of overflow plumes after impinging on a horizontal bed in an experimental set up. These experimental results are used by Winterwerp (2002) to derive a classification of density driven or mixing dominated behaviour of overflow plumes. Two cases in the density driven regime are used to validate the impingement of an overflow plume at the bed. First case has $\gamma = 0.78$, $Ri = 4.8$ ($\rho_{j0} = 1049 \text{ kg/m}^3$, $w_{j0} = 0.05 \text{ m/s}$, $\rho_{cf} = 1000 \text{ kg/m}^3$, $u_{cf} = 0.065 \text{ m/s}$, $D = 0.025 \text{ m}$) and second case $\gamma = 3.2$, $Ri = 0.30$ ($\rho_{j0} = 1049 \text{ kg/m}^3$, $w_{j0} = 0.2 \text{ m/s}$, $\rho_{cf} = 1000 \text{ kg/m}^3$, $u_{cf} = 0.065 \text{ m/s}$, $D = 0.025 \text{ m}$). In the experiments the density difference of the overflow plume is generated by using very fine China clay. The settling velocity is negligible ($w_s \approx 0.02 \text{ mm/s}$) and thus settling is switched off in the simulations. The bed is simulated as hydraulic smooth. The horizontal spreading is traced by following the progress in time of the edge of the plume at the bed.

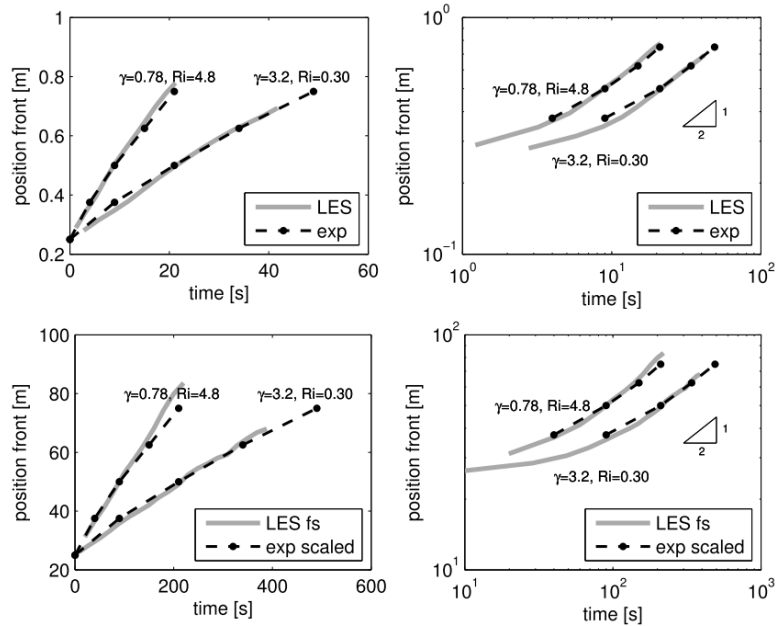


Figure D2. Radial spreading density driven overflow plume at bed as a function of time with linear axes (left) and log-log axes (right). The top row shows results at experimental scale, the bottom row shows results at full scale with Ri , γ similar to the experiment

The LES simulations follow the experimental results of Boot (2000) closely, see Figure D2 top row. The radial spreading progresses with the square root of time (2:1 slope in the log-log diagram of Figure D2).

Also full scale simulations are carried out where the length is multiplied by a factor 100, the velocity by a factor 10 and the density difference is kept at the experimental value to arrive at a realistic full scale TSHD with similar γ , Ri values as in the experiment. In order to arrive at similar crossflow velocity profiles for the experimental scale and full scale a Nikuradse roughness of $kn = 0.1$ m has been applied for the full scale case. With this roughness value the log velocity profiles of full scale and experimental scale are identical. The bottom row in Figure D2 shows the full scale results and they are similarly accurate as the simulation results at experimental scale. This shows that even for a full scale simulation, where all turbulent scales up to the inertial sub-range cannot be resolved on the grid as much as in a simulation on experimental scale, TUDflow3d LES is capable to simulate the correct front speed of the bed plume.

D.3.4 Density current including deposition (experiment of Hallworth et al. 1998)

The behaviour of a density current at a horizontal bed including deposition is validated with experimental measurements by Hallworth et al. (1998). In the experiment a fixed amount of particle loaded water is released through a vertical pipe at the free surface of an open flume. The particle loaded water flows through the water column almost instantaneously and then spreads horizontally at the bed as a density current. The front position of the density current is tracked in time and the final deposition amounts along the experimental flume are measured.

The flume length is 9.4 m, the flume width is 0.26 m and the water depth $H = 0.287$ m. 2 l water containing 50 g/l silicon carbide particles of $37 \mu\text{m}$ and $\rho_s = 3217$ kg/m³ is released at the water surface in the flume centre within 1 s. This release time is small compared to the total spreading time of the density current of more than 80 s. Exact inflow characteristics and exact release time in the experiment are not documented; in the model the particle loaded water is released in 1 s with a constant inflow discharge. Results with and without an ambient current of $U = 0.026$ m/s in the flume are used to validate the CFD model.

The simulations are carried out on a Cartesian computational domain. The computational grid with ambient current is 6.9 m long and has 670x40x40 cells; without ambient current it is 6.5 m long and has 645x40x40 cells. The horizontal grid size Δx varies between $0.02H$ and $0.05H$ with finer cells at the origin of the density current. The settling velocity of the silicon carbide particles is $w_s = 1.65$ mm/s. The bed is simulated as a hydraulic smooth wall and the sidewalls are simulated as no slip walls. There is one important difference between the simulation set up and the experimental set up: in the experiment the release of the particle loaded water leads to an increase in the total amount of water in the flume which causes a slightly larger water depth. In the model a rigid lid approach is followed and the total volume of water in the flume stays equal. The particle loaded water released in the model therefore leads to a flow in horizontal direction out of the computational domain. In order to prevent a significant flow in positive x -direction towards the outflow boundary during the 1 s release time, 50% of the influx is sucked out of the model domain at the inflow x -boundary. This fix does not completely solve the discrepancy in volume balance between the experimental and simulation set up, but at least the density current is not biased towards the positive x -direction in the model.

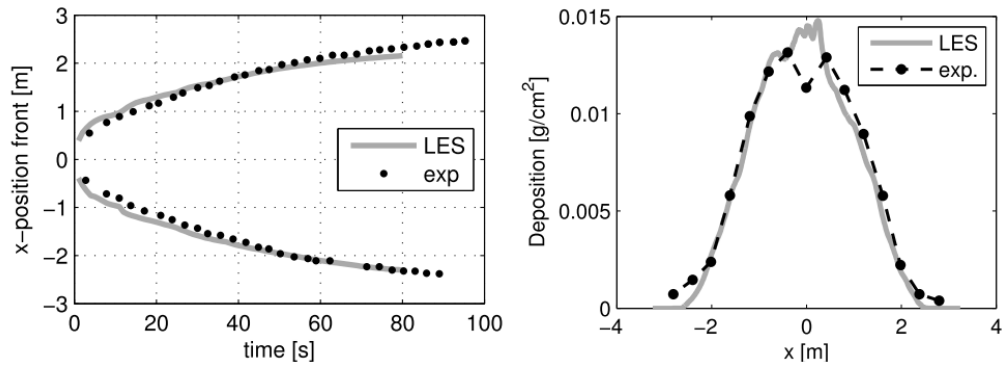


Figure D3. Symmetric spreading of density current at a bed without ambient current, position front (left) and final deposition at the bed (right).

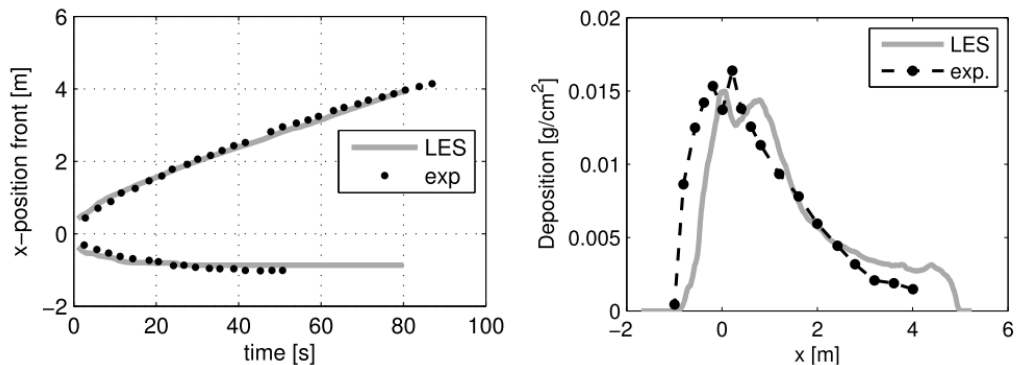


Figure D4. Asymmetric spreading of a density current at a bed with ambient current, position front (left) and final deposition at the bed (right).

Figure D3 shows the symmetric spreading of the density current in absence of an ambient current. The simulation results show the expected symmetric behavior and the position of the front and deposition are close to the measurements. The results in case of a small ambient current are shown in Figure D4. The simulation shows the expected asymmetric spreading towards the direction of the ambient current. The simulated position of the front is close to the measured position of the front. The simulated deposition is correct in shape and magnitude, but it is shifted in positive x direction compared to the experiment alone. This discrepancy might be caused by the aforementioned differences between model and experiment in volume balance and the unknown exact release characteristics of the particle loaded water in the experiment and therefore no further attempts to improve the TUDflow3d LES results are made. Overall the model shows the correct behavior of a density current with deposition at the bed both with and without ambient current; the front position is simulated accurately and the deposition profile has the correct shape and magnitude.

D.3.5 Turbidity current on erodible bed (experiment of Parker et al. 1987)

A series of experiments on the development of a density current over a sloping erodible bed has been executed by Parker et al (1987). See Figure D5 for the general setup. The flume had a constant width of 0.7m. Experiment 13 has been used to compare CFD results with measured profiles of SSC and velocity at $x=1.5\text{m}$; $x=4.5\text{m}$ and $x=8.5\text{m}$ from the inlet. The inlet height is 0.08m with an inlet discharge $Q=15\text{ l/s}$ (U inflow 0.27 m/s) and sediment flux of 164.6 kg/m^3 (C inflow $4.1\text{e-}4$) which are used as inflow conditions in the CFD model with block profiles for U inflow and C inflow. The bed slope is 1:20. Sediment d_{50} is $30\mu\text{m}$. During the experiment the erodible bed started flat but ended with bedforms of typically several cm long and several mm high. In the CFD model this is captured by a bed Nikuradse roughness of 5 mm, although sensitivity tests (not shown) proved that the results are not very dependent

on this value. Sediment pickup from the erodible bed is simulated by the VanRijn1984 pickup function (Van Rijn, 1984) calibrated to 0.25 of its original value to reproduce the measured near bed SSC profile as close as possible. During the experiment some flocculation seem to have occurred but this has not been taken into account in the simulations. Model input is summarized in Table D1.

Table D1 Input parameters CFD model for Parker 1987 experiment 13

Parameter	Value
Hinflow	0.08m
Uinflow (block profile)	0.27 m/s (Q inflow 21.4 l/s/m)
Cinflow (block profile)	4.1e-4 (SSC 164.6 kg/m ³)
Sinflow	3.53 kg/s/m
CFD domain LxHxW	13.5m x 1.32 m x 0.7m <i>Due to 1:20 sloping bed effectively H=0.65m at inflow and 1.32 m at outflow</i>
Bed slope	1:20
Sediment d50	30µm
Bed roughness	k _n =5mm
Pickup	Van Rijn 1984 pickup formula, calibration parameter 0.25

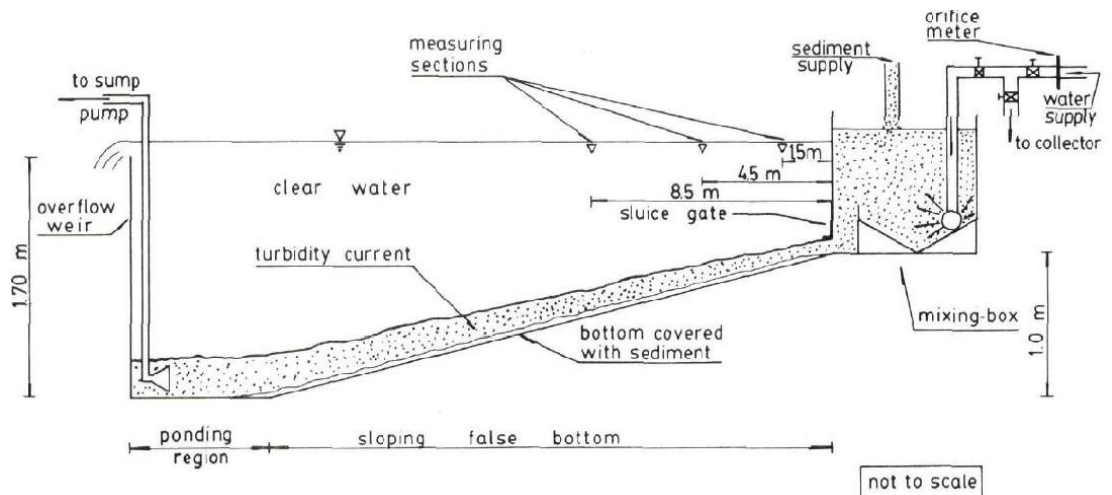


Figure D5. Sketch experimental set up Parker et al. 1987

An instantaneous snapshot of the modelled density current for experiment 13 (Parker et al. 1987) is shown in Figure . The individual turbulent eddies and whirls resolved on the grid in LES are clearly visible. Comparison for time averaged velocity and SSC profiles with measured ones is given in Figure . The vertical SSC profile and layer thickness of the density current is captured very well in the CFD LES model and the velocity profile is captured reasonably well with a small overprediction of the near bed velocity.

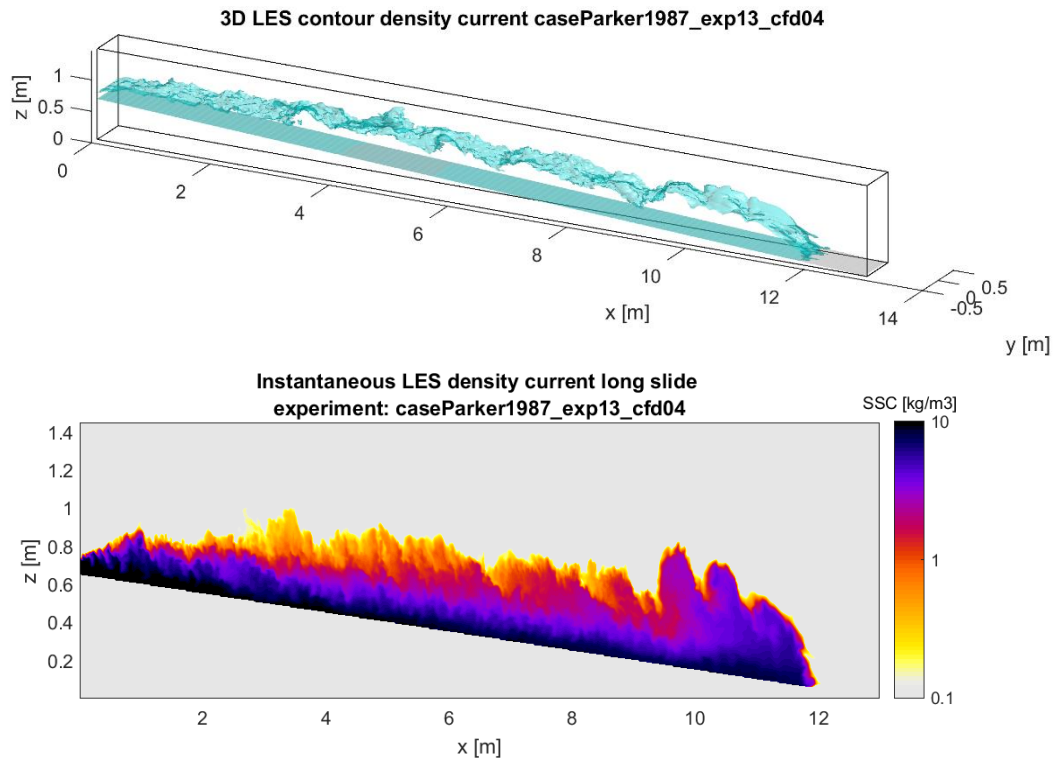


Figure D6. Instantaneous LES snapshot of 3D contour (top) of turbidity current and SSC at 2Dv slice through centre of turbidity current (bottom) for experiment 13 Parker et al. 1987

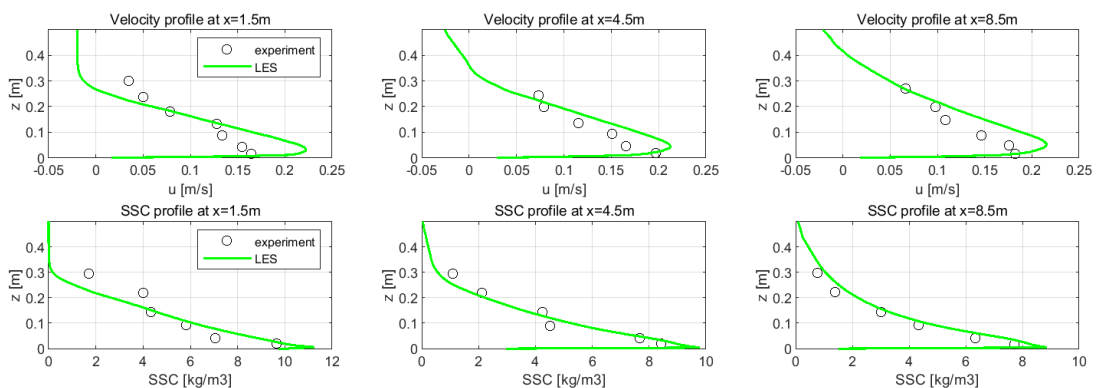


Figure D7 Comparison modelled time averaged LES velocity and SSC profiles and measurements for experiment 13 Parker et al. 1987

When LES simulation is unfeasible it is also possible to carry out a RANS Reynolds averaged simulation in TUDflow3d. For the Parker density current experiment simulations with the Mixing Length and the Realizable K-Epsilon model are performed. In the Mixing Length model damping of turbulence on the top edge of the density current is taken care of by Munk-Anderson type of damping functions defined in the COSINUS project (for more info see De Wit 2014b). In the Realizable K-Epsilon model there are specific terms in the K and Epsilon equations taking care of turbulence damping in the presence of density gradients.

Time averaged velocity and SSC profiles for experiment 13 of Parker et al. 1987 are shown in Figure for three different turbulence model settings: LES, Mixing Length and Mixing Length with reduced eddy viscosity near the bed. Figure 5-9 shows the same for LES, K-Epsilon and K-Epsilon with reduced eddy viscosity near the bed. The reduced near bed eddy viscosity option adjusts (effectively reduces) the simulated eddy viscosity of the turbulence model for

the first two grid cells from the bed by an eddy viscosity that exactly reproduces the required shear belonging to the modelled bed shear stress at that location. The near bed eddy viscosity is determined from the relation: $\tau = \nu_e \frac{\partial U}{\partial z}$.

Figure shows that the standard RANS Mixing Length model underpredicts the near bed velocity in the density current considerably. The RANS Mixing Length model with adjusted near bed viscosity improves the near bed velocities for this case, but still the near bed velocities are underpredicted a bit. The SSC profiles for both RANS Mixing Length models show SSC values which are higher than measured ones in the lower zone of the density current. Default RANS K-Epsilon also underpredicts the near bed velocity in the density current considerably, see Figure 5-9, but with adjusted near bed viscosity the near bed velocities improve a lot and become even a bit overpredicted. In fact, RANS K-Epsilon with reduced near bed viscosity is very close to the LES results. Simulated SSC profiles are very close to measured ones for RANS K-Epsilon with reduced near bed viscosity and with default K-Epsilon SSC profiles are overpredicted a little.

There is difference in simulation time between LES and RANS as LES uses a finer grid and therefore RANS is faster.

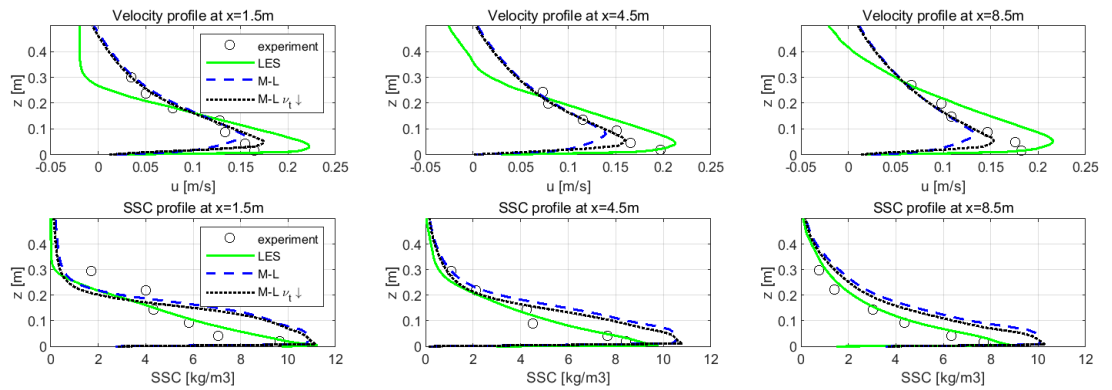


Figure D8 Comparison modelled time averaged velocity and SSC profiles with 3 different turbulence settings (LES; Mixing Length and Mixing Length with reduced near bed viscosity) and measurements for experiment 13 Parker et al. 1987

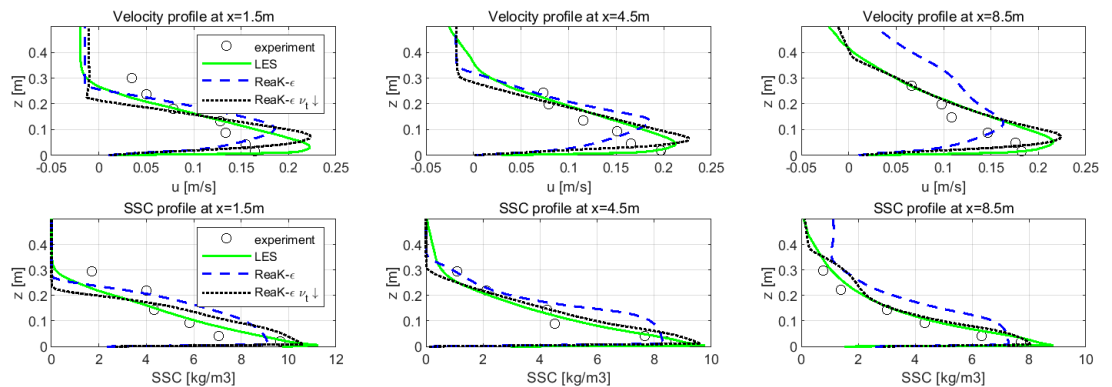


Figure D9 Comparison modelled time averaged velocity and SSC profiles with 3 different turbulence settings (LES; Realizable K-Epsilon and Realizable K-Epsilon with reduced near bed viscosity) and measurements for experiment 13 Parker et al. 1987

Conclusions TUDflow3d results experiment Parker et al 1987

The experiment of a density current along a sloping erodible bed of Parker et al. 1987 has been used as test case for the CFD model TUDflow3d. The experimental measured velocity and SSC profiles can be reproduced accurately. The choice in turbulence model settings has clearly visible influence on the outcomes. The adjusted near bed viscosity improved the results for both RANS models (Mixing Length and Realizable K-Epsilon) significantly. LES gives the best results, but Realizable K-Epsilon with adjusted near bed viscosity is very close. Because of the finer grid employed in LES runs RANS Realizable K-Epsilon is computationally faster. Between the two tested RANS models Realizable K-Epsilon shows better results as Mixing Length for this case.

D.3.6

Conclusions verification TUDflow3d for WID plumes

Four different benchmark simulations have showed that TUDflow3D can simulate density currents at a flat bed and sloping bed accurately. Deposition of sediment from such density current is simulated accurately as well as erosion of sediment from the bed by the density current giving it a self-containing character. This gives confidence in applying TUDflow3d for simulating WID plumes.

Deltares is an independent institute for applied research in the field of water and subsurface. Throughout the world, we work on smart solutions for people, environment and society.

Deltares

www.deltares.nl